



THE HONG KONG  
POLYTECHNIC UNIVERSITY

香港理工大學

Pao Yue-kong Library

包玉剛圖書館

---

## Copyright Undertaking

This thesis is protected by copyright, with all rights reserved.

**By reading and using the thesis, the reader understands and agrees to the following terms:**

1. The reader will abide by the rules and legal ordinances governing copyright regarding the use of the thesis.
2. The reader will use the thesis for the purpose of research or private study only and not for distribution or further reproduction or any other purpose.
3. The reader agrees to indemnify and hold the University harmless from and against any loss, damage, cost, liability or expenses arising from copyright infringement or unauthorized usage.

### IMPORTANT

If you have reasons to believe that any materials in this thesis are deemed not suitable to be distributed in this form, or a copyright owner having difficulty with the material being included in our database, please contact [lbsys@polyu.edu.hk](mailto:lbsys@polyu.edu.hk) providing details. The Library will look into your claim and consider taking remedial action upon receipt of the written requests.

**SEISMIC PERFORMANCE OF STRUCTURES  
EQUIPPED WITH INNOVATIVE SMA-BASED  
RESILIENT DAMPERS**

**PING ZHANG**

**PhD**

**The Hong Kong Polytechnic University**

**2025**

The Hong Kong Polytechnic University  
Department of Building and Real Estate

**Seismic performance of structures equipped  
with innovative SMA-based resilient dampers**

**Ping ZHANG**

A thesis submitted in partial fulfilment of the requirements for the degree  
of Doctor of Philosophy

September 2024

## **CERTIFICATE OF ORIGINALITY**

I hereby declare that this thesis is my own work and that, to the best of my knowledge and belief, it reproduces no material previously published or written, nor material that has been accepted for the award of any other degree or diploma, except where due acknowledgement has been made in the text.

Ping Zhang  
(Name of student)

## Abstract

The challenge of limited natural resources in the face of growing human populations emphasises the pressing need for sustainable development. Recent post-earthquake investigations in civil engineering have revealed that, although conventional structures designed to current seismic standards may withstand earthquakes, the resulting damage often leads to high repair costs or the demolition of structures due to residual deformation, compromising sustainable development principles. Consequently, the need to mitigate earthquake-induced damage to structures has driven the development of high-performance resilient structures. This thesis introduces a novel resilient slip damper featuring a multistage energy-dissipation mechanism, explores its structural applications, and evaluates its effectiveness in seismic mitigation compared to previous systems. Note that the multistage energy-dissipation mechanism shows promise in balancing the requirements for significant post-yielding stiffness and energy-dissipation capacity in structures, based on a literature review. The proposed damper is called shape-memory-alloy (SMA)-based variable friction and stiffness damper (SMA-VFSD). In this damper, it combines the characteristics (i.e., superelastic effect and phase transformation) of SMAs, disc spring systems, and a variable friction mechanism and integrate them into a specific configuration. Supported by the restoring force from the disc spring systems, the proposed damper decouples the interdependence between the friction coefficient and the sloping angle of friction pairs, a phenomenon known as self-locking in previous research. This decoupling enables the multistage energy-dissipation mechanism and enhances the design flexibility for the damper. To validate

the feasibility of the proposed damper following the multistage energy-dissipation capacity, a systematic investigation is needed.

In this study, eight damper specimens were tested under cyclic loadings. The test results, including experimental observations, hysteretic behaviour, and energy-dissipation capacities, were discussed, and the effects of the design parameters (i.e., SMA bolt type, sloping angle of friction pairs and preload of SMA bolts) on damper performance were investigated. Based on test data, the accuracy of the developed analytical model in predicting the hysteretic responses for the SMA-VFSD was confirmed. Utilising the analytical model, further exploration was conducted to investigate the effects of an extended range of the design parameters on the damper behaviour. To provide a further understanding of the damper's performance, a detailed refined and a simplified numerical model were developed and validated against test data. The test and numerical results confirmed the feasibility of the SMA-VFSD at the damper level, and as expected, the damper demonstrated a multistage energy-dissipation mechanism.

Further, an experimental programme investigating the cyclic behaviour of a one-bay and one-story braced frame equipped with the SMA-VFSD was conducted. Six frame tests were performed to study the effects of design parameters, including the preload of the SMA bolts and the sloping angle of the friction pairs, on structural behaviour. The frame test results demonstrated a multistage energy-dissipation behaviour with flag-shaped hysteretic curves at the sub-structure level, mirroring the findings from the previous damper test. This indicated that the frame's hysteretic characteristics was governed by the damper.

Finally, the seismic performance of braced structures equipped with the proposed damper was numerically assessed via a structural case study. The effect of fabrication

tolerances (i.e., clearance among pin connections) on structural performance was evaluated by comparing the seismic behaviour of structures with and without initial gaps in braces. In addition, utilising a self-developed calculation programme, nonlinear spectral analyses were performed on a Single Degree of Freedom (SDOF) system representing a low-to-medium structure showing multistage energy-dissipation characteristics. The analysis results demonstrated the viability of the SMA-VFSD in improving structural behaviour at the system level.

## Publications arising from the thesis

### Journal paper:

Zhang, P., Yam, M.C.H., Ke, K., Zhou, X.H., and Chen, Y.H. (2022). Steel moment resisting frames with energy-dissipation rocking columns under near-fault earthquakes: Probabilistic performance-based-plastic-design for the ultimate stage. *Journal of Building Engineering*, 54:104625.

Ke, K., Yam, M.C.H., Zhang, P., Shi, Y., Li, Y., and Liu, S. (2023). Self-centring damper with multi-energy-dissipation mechanisms: Insights and structural seismic demand perspective. *Journal of Constructional Steel Research*, 204: 107837.

Zhang, P., Yam, M.C.H., Ke, K., Song, Y.C., and Zhu, M. (2024). An experimental study on a self-centring damper with multistage energy-dissipation mechanism. *Journal of Structural Engineering*. (Accepted).

Zhang, P., and Yam, M.C.H. (2024). An SMA-based resilient slip damper with tri-stage energy-dissipation mechanism: hysteretic behaviour and structural performance. *Engineering Structures*. (Under preparation).

Zhang, P., and Yam, M.C.H. (2024). Feasibility validation of a novel self-centring damper with multistage energy-dissipation mechanism for structural applications: an experimental case study. *Journal of Structural Engineering*. (Under preparation).

### Conference paper:

Yam, M.C.H., Zhang, P., Huang Y., Zhao Q.Y., and Ke K. (2021). Preliminary study on

novel beam-to-column connection based on SMA plate. Proceedings of International Structural Engineering and Construction, 8(1).

Zhang, P., Yam, M.C.H., Ke K., Liu, Y.C., Chung, K.F. (2023). Performance investigations on steel-brass friction devices. The 2023 World Congress on Advances in Structural Engineering and Mechanics (ASEM23).

## Acknowledgements

First and foremost, I want to deliver my sincere gratitude to my chief supervisor, Prof. Michael C.H. Yam, for being his Ph.D. student. This thesis would not have been completed without his continuous supervision, insightful guidance, generous support, and the invaluable time and patience he dedicated to this research. I remember one instance when an expensive SMA bolt failed due to my unstandardised operation. I panicked, but Prof. Michael encouraged me, reminding me that everyone makes mistakes in research. He emphasised the importance of learning from these mistakes and not repeating them. I have learnt a lot from his meticulous attitude in academic research, and his rich experience in engineering projects, which will continue to benefit me in both my research and daily life. Prof. Michael also encouraged me not to blindly accept the findings of previous research and to learn to challenge existing conclusions. I would like to extend my thanks to my co-supervisor, Prof. K. Ke for providing professional advice and support to me during the past few years, especially during preparing journal papers.

The financial support provided by the Research Committee and the Chinese National Engineering Research Centre for Steel Construction (Hong Kong Branch) at PolyU is greatly appreciated. I am also grateful to PolyU for offering me a great research environment and providing me with research facilities.

I would like to thank the members of Prof. Yam's research group, and my friends made during my Ph.D career, including Dr. Y.C. Song, Dr. J.Z. Zhang, Dr Y.W. Li, Dr. Z.Y. Zhou, Dr. X.Z. He, Dr. J.J. Wang, Dr. Q. He, Mr. H.Y. Zhang, Mr. Y.L. Zhang, Miss. Q.Y. Zhao, Miss M. Zhu, Miss Y.C. Liu, Miss M.Y. Zhang, Mr. J.W.

## Acknowledgements

---

Liu, and Miss S.X. Li.

I would like to express my gratitude to my lab assistant Mr. I.K. Chen for his valuable suggestions and support during the tests of my dampers and frame specimens. Additionally, I extend my thanks to Professors Y.Z. Fang, C. Fang, and G.H. Sun for their invaluable guidance and instructions on my research topics during our discussions.

Last but not the least, I would like to deliver sincere gratitude to my devoted family, my father, mother and sisters for their unwavering support and patience throughout the long-time span. I want to tell them that I love them forever in Chinese. (我爱你们，我的父母).

# Table of Contents

<b>Abstract.....</b>	<b>I</b>
<b>Acknowledgement .....</b>	<b>VI</b>
<b>List of Tables.....</b>	<b>XII</b>
<b>List of Figures.....</b>	<b>XIII</b>
<b>List of Notations .....</b>	<b>.XIX</b>
<b>Chapter 1 Introduction.....</b>	<b>1</b>
1.1 Overview and research background.....	1
1.2 Scope and objectives.....	5
1.3 Significance of the research project.....	6
1.4 Outline of the thesis .....	7
<b>Chapter 2 Literature review .....</b>	<b>11</b>
2.1 Introduction.....	11
2.2 PT-based and SMA-based connections and structures .....	11
2.2.1 PT-based connections and their structural applications .....	12
2.2.2 SMA-based connections and their structural applications.....	14
2.3 Self-centring rocking systems.....	17
2.4 Hybrid-strength steel structures .....	20
2.5 Resilient dampers or braces and their structural applications.....	21
2.6 Seismic demands for self-centring structures .....	25
2.7 Summary.....	26
<b>Chapter 3 Concept design and analytical model of the proposed damper .....</b>	<b>34</b>
3.1 Introduction.....	34

## Table of Contents

---

3.2 Concept design.....	34
3.2.1 Configuration of SMA-VFSD.....	34
3.2.2 Working principles and deformation modes .....	36
3.3 Analytical hysteretic model of SMA-VFSD.....	37
3.4 Summary.....	41
<b>Chapter 4 Experimental programme for SMA-VFSD .....</b>	<b>48</b>
4.1 Introduction.....	48
4.2 Material- and constituent component-level tests .....	49
4.2.1 Material level tests .....	49
4.2.2 Constituent component-level tests .....	50
4.2.2.1 SMA bar test .....	50
4.2.2.2 Test of friction system.....	51
4.2.2.3 Disc spring group test .....	53
4.3 Test of SMA-VFSD test.....	54
4.3.1 Test specimen design .....	54
4.3.2 Test setup and instrumentation.....	55
4.3.3 General observation .....	56
4.3.4 Cyclic behaviour .....	56
4.3.5 Hysteretic characteristics .....	58
4.3.6 Energy-dissipation Capacity .....	59
4.4 Analytical validation and parametric study.....	60
4.5 Numerical analyses of SMA-VFSD.....	63
4.5.1 Refined numerical analysis of SMA-VFSD .....	64
4.5.1.1 Establishment of refined numerical model .....	64
4.5.1.2 Numerical results .....	65

4.5.2 Simplified numerical analysis of SMA-VFSD .....	66
4.6 In summary .....	68
<b>Chapter 5 Experimental programme for braced frame equipped with SMA-VFSD</b> .....	<b>101</b>
5.1 Introduction.....	101
5.2 Engineering applications of SMA-VFSD .....	102
5.3 Test of braced frame equipped with SMA-VFSD.....	102
5.3.1 Material test .....	102
5.3.2 Specimen design .....	103
5.3.3 Test setup and instrumentation.....	106
5.3.4 General observation .....	107
5.3.5 Cyclic behaviour .....	108
5.3.6 Energy-dissipation capacity .....	110
5.3.7 Self-centring behaviour.....	112
5.4 Numerical analysis.....	112
5.4.1 Establishment of simplified numerical model .....	113
5.4.2 Numerical results .....	114
5.5 In summary .....	115
<b>Chapter 6 Seismic performance evaluation and demand analysis on braced frames</b> .....	<b>140</b>
6.1 Introduction.....	140
6.2 Seismic performance evaluation on braced frame equipped with SMA-VFSD .....	141
6.2.1 Design of prototype building .....	141
6.2.2 Numerical model of prototype building and results .....	143

Table of Contents

---

6.2.3 Effect of initial gaps on performance of braced frames equipped with SMA-VFSD .....	147
6.3 Seismic demand analysis on braced frames equipped with SMA-VFSD.....	150
6.3.1. Energy modification factor demand.....	154
6.3.2. Acceleration factor demand .....	155
6.4 Summary.....	156
<b>Chapter 7 Summary and conclusions .....</b>	<b>172</b>
7.1 Summary.....	172
7.2 Conclusions.....	174
7.3 Future work.....	177
<b>Appendix A Codes for MGSC material in OpenSees .....</b>	<b>179</b>
<b>Appendix B Copyright of the publications used in this thesis. ....</b>	<b>190</b>
<b>References .....</b>	<b>194</b>

## List of Tables

Table 4.1 Material constants for tested SMA bolts .....	71
Table 4.2 Information on friction tests.....	71
Table 4.3 Specimen details .....	71
Table 4.4 Hysterical characteristics of the specimens .....	72
Table 4.5. Information on each combination of design parameters .....	73
Table 5.1 Material constants for longer SMA bolt.....	117
Table 5.2 Information on frame specimens.....	117
Table 6.1. Mechanical design parameters of dampers for case structure.....	158

## List of Figures

Fig. 1.1 Framework of the thesis .....	10
Fig. 2.1 PT beam-to-column connection.....	28
Fig. 2.2 Beam-through frame with self-centring modular panels.....	28
Fig. 2.3 Thermal-mechanical characteristics of SMA .....	29
Fig. 2.4 Steel rocking braced frame with butterfly-shaped steel plates.....	29
Fig. 2.5 Steel MRF with EDBs .....	30
Fig. 2.6 Steel MRF with tension-only braces .....	31
Fig. 2.7 Self-centring damper using disc springs.....	31
Fig. 2.8 Self-centring damper using SMA bars.....	31
Fig. 2.9 Self-centring brace using SMA wires.....	32
Fig. 2.10 Resilient slip damper .....	32
Fig. 2.11 Flowchart of constant-ductility spectral analysis of an equivalent SDOF system .....	33
Fig. 3.1 Configuration of SMA-VFSD .....	43
Fig. 3.2 Assembly process of SMA-VFSD.....	43
Fig. 3.3 Deformation modes and expected hysteretic behaviour.....	44
Fig. 3.4 Free body diagrams (FBDs) of SMA-VFSD.....	44
Fig. 3.5. Simplified model of SMA-VFSD.....	45
Fig. 3.6. Hysteretic skeleton of S1 under tension and release .....	45
Fig. 3.7. Hysteretic behaviour of S2 .....	46
Fig. 3.8. Hysteretic behaviour of the SMA-VFSD .....	47
Fig. 4.1 Material coupons before and after tests.....	74

List of Figures

---

Fig. 4.2 Test results of coupon tests .....75

Fig. 4.3 Test of SMA bolts .....75

Fig. 4.4 Typical test results of NiTi/NiTiCo SMA bolts .....76

Fig. 4.5 Hysteretic parameters for SMA bolts .....76

Fig. 4.6 Comparison between test results and Auricchio's approach.....77

Fig. 4.7 Friction test of steel-brass combination.....77

Fig. 4.8 Results of friction tests .....78

Fig. 4.9 Surface wears after friction tests .....78

Fig. 4.10. Test of disc spring groups .....78

Fig. 4.11 Fabricated components of SMA-VFSD.....79

Fig. 4.12 Dimensions of the damper components.....79

Fig. 4.13 Test of SMA-VFSD .....80

Fig. 4.14 Test phenomenon of SMA-VFSD test.....80

Fig. 4.15 Fracture of a NiTiCo SMA bolt for specimen DH20V16-13-NiTiCo.....80

Fig. 4.16. Hysteretic curves of test specimens.....83

Fig. 4.17. Comparisons of the hysteretic curves of test specimens .....84

Fig. 4.18. Measured axial elongation of SMA bolts .....85

Fig. 4.19 Symbols of hysteretic parameters of SMA-VFSD .....85

Fig. 4.20 Definition of equivalent viscous damping ( $\zeta$ ) .....85

Fig. 4.21 Cumulative energy dissipation and  $\zeta$  of test specimens .....87

Fig. 4.22. Comparisons of the cumulative energy dissipation and  $\zeta$  of test specimens  
.....89

Fig. 4.23. Detailed comparisons of analytical prediction and test data for specimen  
DH20V16-10-NiTiCo .....89

Fig. 4.24. Results of parametric study .....92

## List of Figures

---

Fig. 4.25. Refined numerical model for SMA-VFSD.....	93
Fig. 4.26. Deformation state under maximum displacement amplitude for specimen DH20V16-10-NiTiCo .....	93
Fig. 4.27. Stress contour of each component for specimen DH20V16-10-NiTiCo under maximum positive displacement amplitude .....	94
Fig. 4.28. Comparisons of hysteretic curves between refined numerical results and test data for specimen DH20V16-13-NiTiCo and its constituent systems.....	96
Fig. 4.29. OpenSees framework.....	97
Fig. 4.30. Usage and input parameters of uniaxial MGSC material .....	97
Fig. 4.31. Simplified model in OpenSees .....	98
Fig. 4.32. Comparisons of hysteretic curves between simplified numerical model and test data .....	100
Fig. 4.33. Comparisons of hysteretic curves between various methods and test data for specimen DH20V16-10-NiTiCo .....	100
Fig. 5.1. Engineering applications of SMA-VFSD.....	118
Fig. 5.2. Braced frame equipped with SMA-VFSD.....	119
Fig. 5.3. Material test .....	120
Fig. 5.4. Result of coupon test .....	120
Fig. 5.5. Stiffness of disc spring group .....	121
Fig. 5.6. SMA bolt test.....	121
Fig. 5.7. Dimension of the frame specimen .....	123
Fig. 5.8. Diagram of test setup for braced frame test.....	123
Fig. 5.9. Photo of braced frame test .....	124
Fig. 5.10. Visible gap due to fabrication tolerances.....	124
Fig. 5.11. Measurement plan.....	125

List of Figures

---

Fig. 5.12. Loading protocol.....125

Fig. 5.13. Deformation states of the damper and frame at the maximum drift  
amplitudes in the pull and push directions.....126

Fig. 5.14. Gap formation of the damper in the specimens.....127

Fig. 5.15. Hysteretic curves for test specimens .....129

Fig. 5.16. Hysteretic curves of the SMA-VFSD for the test specimens .....131

Fig. 5.17. Comparisons of the hysteretic curves of test specimens .....133

Fig. 5.18. Loss of total preloads of the SMA bolts during the last loading cycle of  
specimens FH20V8-10 and FH20V16-10 .....133

Fig. 5.19. Comparison of hysteretic curves of the brace and SMA-VFSD for the test  
specimens.....135

Fig. 5.20 Cumulative energy dissipation and  $\zeta$  of test specimens .....136

Fig. 5.21. Comparisons of the cumulative energy dissipation and  $\zeta$  of test specimens  
.....137

Fig. 5.22. Development of residual drift of test specimens .....138

Fig. 5.23. Simplified numerical model for test specimens .....138

Fig. 5.24. Material behaviour.....138

Fig. 5.25. Comparison of hysteretic curves obtained by numerical models and test  
data for specimen FH20V16-10.....139

Fig. 6.1. Information on case structure .....159

Fig. 6.2. Numerical model of braced frame .....159

Fig. 6.3. Spectral acceleration of earthquake records .....160

Fig. 6.4. Comparisons of cyclic pushover for structures equipped with SMA-VFSD  
and PD.....160

Fig. 6.5. Distributions of mean maximum interstorey drifts.....161

## List of Figures

---

Fig. 6.6. Hysteretic responses of brace at 1 <sup>st</sup> storey .....	162
Fig. 6.7. Distributions of mean maximum interstorey residual drifts .....	162
Fig. 6.8. Distributions of mean maximum interstorey PFAs .....	163
Fig. 6.9. Floor acceleration responses of 3rd storey in both structures .....	164
Fig. 6.10. Comparisons of calculated overstrength of brace at each storey under earthquakes for two structures .....	165
Fig. 6.11. Comparisons of cyclic pushover for BF-SMA-VFSD with and without initial gaps .....	165
Fig. 6.12. Comparisons of distributions of mean maximum interstorey drifts for structures with and without the initial gaps .....	166
Fig. 6.13. Comparisons of distributions of mean maximum interstorey PFAs .....	166
Fig. 6.14. Information on LA28 .....	167
Fig. 6.15. Comparisons of relative FAs of each storey for structure with and without the initial gaps .....	167
Fig. 6.16. Comparisons of relative FV of each storey for structure with and without the initial gaps .....	167
Fig. 6.17. Comparisons of interstorey drift responses of each storey for structure with and without the initial gaps .....	168
Fig. 6.18. Comparisons of hysteretic damper behaviour at each storey for structure with and without the initial gaps .....	168
Fig. 6.19. Hysteretic behaviour of structure equipped with SMA-VFSD and implications of hysteretic parameters. ....	169
Fig. 6.20. Energy balance concept of systems .....	169
Fig. 6.21. Spectral analyses .....	169
Fig. 6.22. Comparison results of BTESPEC and OpenSees under Kocaeli record ...	170

## List of Figures

---

- Fig. 6.23. Comparison of the mean energy modification factor spectra.....171
- Fig. 6.24. Comparison of the mean acceleration factor spectra.....171

## List of Notations

$\theta_a$	Sloping angle of friction pairs
$\mu_a$	Friction coefficient of friction pairs
$F_{S1}$	Force sustained by the disc spring systems
$F_{DSS,pre}$	Preload of the disc spring systems
$k_{DSS}$	Axial stiffness of the disc spring systems
$k_{steel}$	Axial stiffness of the steel bars
$k_{dg}$	Axial stiffness of the disc groups
$N_a$	Number of the disc spring systems
$n_p$	Number of disc springs in each paralleled unit
$n_s$	Number of units in series
$k_{disc}$	Stiffness of one disc spring
S1	Disc spring systems and its hysteretic behaviour
S2	Variable friction system and its hysteretic behaviour
S3	Elastic behaviour of each damper component when loaded
$F_{f,pre}$	Friction force of S2 induced by $F_{pre,SMA}$
$F_{pre,SMA}$	Preload of the SMA bolts
$\delta_p$	Relative displacement of S2 corresponding to the initiation of SMA phase transformation
$\delta_{max}$	Relative displacement of S2 corresponding to the maximum loading
$F_{f,p}$	Friction force of S2 corresponding to the initiation of SMA phase transformation
$F_{f,max}$	friction force of S2 corresponding to the maximum loading

## List of Notations

---

$F_{f,res}$	Residual force when S2 returns to its initial position
$F_{f,rev}$	Reversed force corresponding to the initiation of reversed slip of S2 at the maximum deformation
$k_{SMA}$	Axial stiffness of the total SMA bolts before SMA phase transformation
$k_{SMA,a}$	Axial stiffness of the total SMA bolts after SMA phase transformation
$E_A$ and $E_M$	Austenite and martensite modulus of the SMA bolts, respectively
$A_{SMA}$	Sum of cross section area of the SMA bolts
$l_{SMA}$	Work length of the SMA bolts
$\mu_1$ and $\mu_2$	Friction coefficients of the contact interfaces of the exterior friction plates vs the interior friction plates and the exterior tube, respectively
$l_{d,c}$	Dynamic reference line for S2
$k_f$ and $k_{fa}$	Stiffness contributed by S2 before and after phase transformation of the SMA bolts, respectively
$k_{f,un}$	Second unloading stiffness of S2
$k$	Initial stiffness of the damper
$F_y$ and $F_p$	1 <sup>st</sup> and 2 <sup>nd</sup> yielding force of the damper, respectively
$F_{rev}$ and $F_{res}$	Reverse force associated with the onset of unloading at the peak displacement and the residual force corresponding to the closure of the damper gap
$\Delta_{rev}$ and $\Delta_{res}$	Reverse displacement associated with the onset of unloading at the peak displacement and the residual displacement corresponding to the closure of the damper gap

## List of Notations

---

$\Delta_y$ and $\Delta_p$	1 <sup>st</sup> and 2 <sup>nd</sup> yielding displacement of the damper, respectively
$l_d$	Dynamic reference line for the damper behaviour
$k_1, k_2, k_3,$ and $k_4$	1 <sup>st</sup> post-yielding stiffness, 2 <sup>nd</sup> post-yielding stiffness and 1 <sup>st</sup> unloading stiffness and 2 <sup>nd</sup> unloading stiffness of the damper, respectively
$\Delta_b$ and $\Delta_t$	x-coordinates (i.e., x) of two intersections (i.e., dynamic key points) of the current dynamic reference line with either the reference lines
Ra	Roughness index of surface
$\zeta$	Energy-dissipation sequence
$\beta$	Energy-related factor
$W_d$	Absolute cumulative energy consumption
$EVD, \xi$	Equivalent viscous damping
$W_e$	Energy absorbed by the corresponding linear elastic system
$V/W$	Dimensionless ratio of base force to seismic weight
BF-SMA-VFSD	Braced frame equipped with the SMA-VFSD
BF-PD	Braced frame equipped with the PF
FOE	Frequently occurred earthquake
DBE	Design basis earthquake
MCE	Maximum considered earthquake
PFA	Peak floor acceleration
PFV	Peak floor Velocity
$\Omega$	Ratio of the maximum force of dampers to the 1 <sup>st</sup> yielding force of dampers under earthquakes
$\mathbf{m}$	mass matrix of the structure
$\phi_1$	1 <sup>st</sup> mode vector of the designed structure

List of Notations

---

$\mathbf{c}$	Damping matrix of the structure
$\mathbf{k}$	Stiffness matrix of the structure
$T$	Structural period
$\zeta$	Damping ratio
$K$	Initial stiffness of the structure
$\bar{\alpha}_1$	1 <sup>st</sup> post-yielding stiffness factor
$\bar{\alpha}_2$	2 <sup>nd</sup> post-yielding stiffness factor
$\bar{\alpha}_3$	1 <sup>st</sup> post-yielding unloading stiffness factor
$\bar{\alpha}_4$	2 <sup>nd</sup> post-yielding unloading stiffness factor
$\bar{\zeta}$	Energy-dissipation sequence of structures
$\bar{\beta}$	Energy-related factor of structures
$\bar{\mu}$	Ductility of structures
$E_a$	Peak nominal energy of the equivalent SDOF system
$E_{ae}$	Peak nominal energy of the corresponding elastic SDOF system
$M$	Total mass of the equivalent SDOF system
$\chi$	Damage-control coefficient
$V_e$	Base force of the corresponding elastic system
$R$	Strength reduction factor
$\bar{\delta}_y$ and $\bar{\delta}_p$	Displacement where the 1 <sup>st</sup> and 2 <sup>nd</sup> pseudo yielding of the equivalent SDOF system starts, respectively
$\bar{\delta}_e$	Maximum displacement of the corresponding elastic SDOF system
$\gamma$	Energy modification factor
$\eta$	Acceleration factor
S-SMA-VFSD	Structures equipped with the SMA-VFSD
S-BFS	Structures equipped with the damper showing bi-linear flag-shaped

## List of Notations

---

	hysteretic behaviour
S-IBFS	Structures equipped with the damper showing improved bi-linear flag-shaped hysteretic behaviour

# Chapter 1 Introduction

## 1.1 Overview and research background

Conventional structures, designed in accordance with ductility-based seismic codes, have proven effective in achieving predetermined seismic performance target (e.g., life-safety) during earthquakes (ANSI/SISC 341-10; ASCE7-16; FEMA-355C; GB50011-2010; PEER/ATC-72-1). However, the satisfactory behaviour of these structures depends on seismic energy dissipation through material nonlinearity in main structural elements, such as beams, columns, and braces. Structures that sustain damage during earthquakes, often displaying significant residual deformation, compromise their seismic resilience (Kazantzi et al. 2008; Zhao et al. 2009; Erochko et al. 2011; Ke and Chen 2016; Hu et al. 2022a; Hu et al. 2022b; Hu et al. 2022c). Recently, the research community has established a residual story drift of 0.5% as the drift target for structures that can be economically repaired. Beyond this threshold, the proposed repair strategies for structures may prove uneconomical compared to the alternative of rebuilding (McCormick et al. 2008; Chen and Ke 2019). As a result, damaged structures may require demolition, resulting in service interruptions, economic losses and waste of natural resources, thereby jeopardising sustainable development.

The enhancement of structural resilience against earthquakes has emerged as a promising solution to reduce seismic damage to both structural and non-structural members, improve repairability, and consequently mitigate the impact on society. Recently, driven by damage-control mechanisms as strategies towards structural resilience (Ricles et al. 2002; Ke and Chen 2016; Chen and Ke 2019; He et al. 2022), various self-centring members or systems have been proposed and investigated to

enhance structural resilience (e.g., reduce residual deformation and acceleration responses). These include post-tensioned (PT)-based or material-based (e.g., shape memory alloy (SMA)) connections and structures (i.e., beam-to-column connections and column bases and their structural applications) (Ricles et al. 2001; Ricles et al. 2002; Christopoulos et al. 2002a; Christopoulos et al. 2002b; Garlock 2002; Garlock et al. 2003; Garlock et al. 2005; Rojas et al. 2005; Garlock et al. 2007; Kim and Christopoulos 2009; Clayton et al. 2012; Dowden et al. 2012; Fang et al. 2015; Wang et al. 2023), self-centring rocking systems (Eatherton 2010; Eatherton et al. 2010; Eatherton et al. 2014a; Eatherton et al. 2014b; Eatherton et al. 2014c; Hu et al. 2022a), hybrid-strength steel structures (Charney and Atlayan 2011; Malakoutian et al. 2013; Li et al. 2018; Li et al. 2019a; Li et al. 2019b; Li et al. 2019c; Ke and Chen 2016; Chen and Ke 2019; Zhai et al. 2019), and structures utilising resilient dampers or braces (Christopoulos et al. 2008; Ke et al. 2023c; Zhou et al. 2023; Hu and Zhu 2022b).

Among these options, structures utilising resilient dampers or braces have garnered significant interest within the academic community due to advantages, such as shop fabrication and ease of installation. In the past decades, a variety of innovative dampers and braces have been investigated, and their potential structural applications have also been explored. Notably, PT-based dampers and braces have been proposed and demonstrated reliable flag-shaped hysteretic behaviour (Christopoulos et al. 2008). Typically, the PT elements and dissipaters are arranged in parallel within such devices, to allow for flexible adjustment of damper performance to meet different engineering demands through rational proportioning. However, concerns have been raised in their structural applications, such as the limited deformability of PT elements and the overstrength (defined by the ratio of ultimate strength to yielding strength) of the dampers and braces (Christopoulos et al. 2008). Efforts, including the use of double-

core configurations (Chou and Chen 2015; Zhou et al. 2015) or disc springs as PT systems (Chen et al. 2023; Xu et al. 2016a; Xu et al. 2016b), have been made to address these concerns and optimise damper/brace performance. In parallel, due to the unique characteristics of shape memory alloys (SMAs), namely superelasticity and phase transformation, SMA-based PT elements have been also recognised as an alternative solution, while further enriching the energy-dissipation capacity of dampers or braces (Eatherton et al. 2014c; Fang et al. 2015; Qiu and Zhu 2017; Qiu et al. 2017; Sun et al. 2022). A recoverable strain (between 8% - 10%) and the phase transformation feature of SMAs could effectively enhance damper deformability and reduce the overstrength of the previous PT-based dampers or braces, respectively. However, the extensive use of SMA-based PT elements, which are the primary contributors to the strength and self-centring behaviour of dampers and braces, results in an obvious increase in construction costs.

More recently, a resilient slip damper (RSD) based on a variable friction mechanism has been investigated (Hashemi et al. 2017; Hashemi et al. 2019). The proposed damper addresses the issue of insufficient deformability and enhances energy-dissipation capacities through the variable friction mechanism. However, the overstrength issue remains in the RSD. In response, an improved resilient slip damper (IRSD) combining the variable friction mechanism and SMA bolts has been introduced and systematically examined (Chen et al. 2022; Qiu et al. 2022; Ke et al. 2023a). In the IRSD, the contribution of energy dissipation and strength is attributed to friction mechanism, consequently reducing SMA usage. By leveraging the phase transformation of SMA bolts, the IRSD exhibits a multistage energy dissipation characteristic, showcasing a trilinear flag-shaped hysteretic curve with a two-stage stiffness reduction mechanism. This mechanism holds promise in decoupling the

interdependence of the strength and stiffness of the damper, effectively addressing the overstrength concerns. Nevertheless, the observed self-locking phenomenon, arising from the interdependence of the design parameters of the IRSD (i.e.,  $\tan\theta_a \geq \mu_a$ ,  $\theta_a$ ,  $\mu_a$  = sloping angle and friction coefficient of wedge-shaped friction pairs, respectively), may hinder the application of the multistage energy-dissipation mechanism. Specifically, if the relationship between the  $\theta_a$  and  $\mu_a$  is not satisfied, the dampers' self-centring behaviour will not activate automatically. Therefore, previous research did not recommend using a large friction coefficient with a small sloping angle, as this combination fails to fully utilise the multistage energy-dissipation mechanism (Chen et al. 2022; Qiu et al. 2022; Ke et al. 2023a). Ke et al. (2023a) noted that a small friction coefficient and a large sloping angle may be unfavourable for the efficiency of frictional energy dissipation and could increase the deformation demands on the SMA bolts. Hence, further endeavours are required to improve the behaviour of the dampers following the multistage energy-dissipation mechanism and to assess the seismic performance of structures equipped with such devices.

Additionally, applying the multistage energy-dissipation mechanism to self-centring structures (e.g., structures equipped with self-centring dampers based on this mechanism) may offer a potential solution to the seismic challenge of balancing peak floor acceleration and overstrength (benefiting from lower post-yielding stiffness) with controlling high-mode effects (benefiting from higher post-yielding stiffness). Specifically, based on a literature review, it was found that insufficient energy-dissipation capacity, as a common issue, in current self-centring structures can result in severe high-mode effects and high peak acceleration responses, posing potential risks to soft-storey integrity and causing damage to non-structural elements. Increasing the post-yielding stiffness of self-centring structures may reduce high-mode effects but also

introduces overstrength issues and decreases energy-dissipation capacity. The reduced energy-dissipation capacity of self-centring structures typically leads to higher peak accelerations, especially when other structural hysteretic parameters remain unchanged.

## 1.2 Scope and objectives

The main objective of this thesis is to propose an innovative SMA-based resilient slip damper (SMA-VFSD) following the multistage energy-dissipation mechanism, addressing the concerns raised in section 1.1. The conceptual design of the damper was given and then validated through a series of cyclic test. Subsequently, at the sub-structure level, an experimental study was conducted to explore the seismic performance of a braced frame equipped with the SMA-VFSD. Finally, a comprehensive investigation was carried out on the seismic demand model and performance evaluation of low-to-medium braced frames equipped with the SMA-VFSD at the system level. In summary, the major research objectives of the thesis were listed as below:

1) To propose an innovative SMA-based resilient slip damper (SMA-VFSD) following the multistage energy-dissipation mechanism.

2) To analytically, experimentally and numerically investigate the hysteretic behaviour of the SMA-VFSD.

3) To analytically, experimentally and numerically examine the seismic performance of a one-storey-one-bay braced frame equipped with the SMA-VFSD.

4) To evaluate the seismic performance of low-to-medium braced frames equipped with the SMA-VFSD (labelled as BF-SMA-VFSD) and examine the viability of the damper in controlling seismic structural responses under earthquakes. Additionally, the seismic demands of BF-SMA-VFSD were comparably investigated via Single Degree

of Freedom (SDOF)-based theory.

### **1.3 Significance of the research project**

The research community has explored various strategies to optimise the damage-evolution mode of structures and enhance their resilience during seismic events. Among these works, structures utilising resilient dampers or braces have garnered significant interest. However, research findings have also highlighted several concerns in current dampers or braces, including the insufficient deformability (resulting from the limited elastic deformation of PT strands), the overstrength, and the coupling of design parameters of such devices. These issues compromise the overall performance and engineering applicability of the devices. For example, significant overstrength in the dampers or braces can increase the strength demand on their adjacent structural members or connections, which may pose the risk of local failures of the above positions (connection failure occurs first) at extreme cases.

Considering the above, this thesis aims to improve seismic performance of structures by introducing a novel damper (SMA-VFSD) featuring the multistage energy-dissipation mechanism. Note that self-centring structures utilising the multistage energy-dissipation mechanism may effectively balance the need to control peak floor acceleration and overstrength (which benefits from lower post-yielding stiffness) with mitigating high-mode effects (which benefit from higher post-yielding stiffness). Firstly, the working mechanisms of the SMA-VFSD were clarified. Subsequently, a systematic investigation was conducted to evaluate the viability of the SMA-VFSD in controlling seismic responses by addressing the aforementioned concerns. In this context, the research outcomes of the thesis are believed to provide a promising alternative for structural engineers when enhancing structural seismic

performance. Additionally, it was anticipated that these outcomes will advance the engineering applications of novel materials, such as SMA, and effective energy-dissipation technology, such as the variable friction mechanism, in practical engineering.

## 1.4 Outline of the thesis

This thesis is organised into seven chapters. Fig. 1.1 illustrates the framework of the thesis.

**Chapter 1** presented an introduction for this research, summarising the research background, research gaps, research objectives, significance of the research project, and the outline of this thesis.

**Chapter 2** reviewed the related literature on various strategies for structures resilience, particularly on the development of resilient dampers or braces.

**Chapter 3** introduced the conceptual design of the SMA-VFSD, along with its analytical hysteretic model. Firstly, the configuration of the damper was described. Subsequently, the deformation modes of the damper and the expected hysteretic responses were presented. Following this, a simplified spring model denoting the working principles of the damper was described. Finally, an analytical hysteretic model, capable of predicting the hysteretic responses, was developed and can be used for the damper design.

**Chapter 4** presented the test results of the SMA-VFSD and its constituent components (i.e., SMA bolts, friction pairs and disc spring groups). Using the test data, the developed analytical model in Chapter 3 was validated and utilised to investigate the effects of an expanded design parameter space on the hysteretic behaviour of the damper. Subsequently, numerical models, both refined and simplified, were developed

and calibrated against the test data to further investigate the damper performance. The results demonstrated that the SMA-VFSD exhibited a multistage energy-dissipation behaviour with flag-shaped hysteretic curves, where the key hysteretic parameters can be flexibly adjusted by varying the design parameters (i.e., preloads of disc spring systems and SMA bolts, SMA bolt type and sloping angle of friction plates), making the damper adaptable to different engineering demands.

**Chapter 5** investigated the seismic performance of one-storey-one-bay braced frame equipped with the SMA-VFSD. Firstly, a novel brace comprising of a SMA-VFSD, and a steel segment was proposed. Cyclic tests were then conducted to examine the feasibility of the SMA-VFSD at sub-structural level. Additionally, a macro numerical model which could consider initial gaps due to fabrication tolerances was developed to predict the hysteretic behaviour and energy-dissipation capacities of the frame specimens.

**Chapter 6** evaluated the viability of the SMA-VFSD in mitigating structural seismic responses from the perspectives of both structural demands and capacities. An illustrative prototype structure equipped with the SMA-VFSD was designed and evaluated through dynamic analyses. Subsequently, the effect of the initial gaps among the pin connections of braces (due to fabrication tolerances) on the seismic performance of structures (i.e., seismic drift and floor acceleration responses) was examined. Finally, based on the energy balance notion, nonlinear constant-ductility-based spectral analyses of equivalent nonlinear Single-Degree-of-Freedom (SDOF) systems representing low-to-medium structures equipped with the SMA-VFSD were performed. According to the established database, the seismic demand model of structures equipped with SMA-VFSD was examined.

**Chapter 7** summarised the main conclusions of the thesis as well as suggestions

for future work.

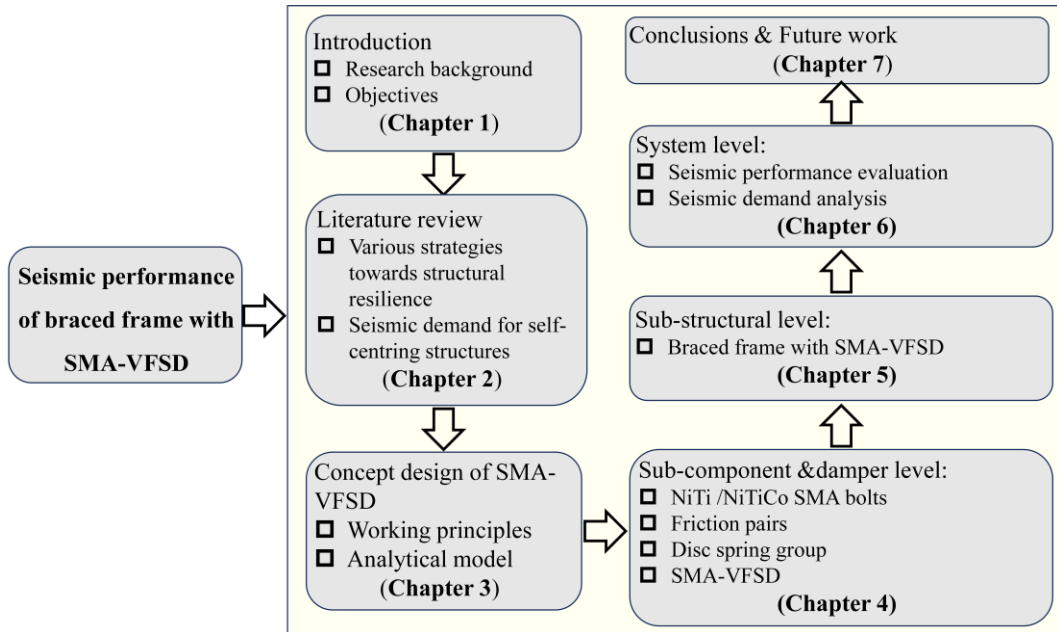


Fig. 1.1 Framework of the thesis

## **Chapter 2 Literature review**

### **2.1 Introduction**

This chapter reviewed the literature on various strategies to enhance structural resilience, with a focus on the development of resilient dampers or braces. Section 2.2 reported on the research progress regarding PT-based and SMA-based connections, including beam-to-column connections and column bases, and their structural applications. Section 2.3 briefly examined structural response control using a self-centring rocking mechanism. The development of novel dampers and braces was discussed in Section 2.4, while Section 2.5 and Section 2.6 revisited research studies on self-centring rocking systems and seismic demand analyses and performance evaluations for self-centring structures, respectively.

### **2.2 PT-based and SMA-based connections and structures**

In steel moment resisting frames (MRFs) structures, the ductile behaviour of beam-to-column connections is expected to dissipate seismic energy during earthquakes according to current seismic codes under earthquakes (ANSI/SISC 341-10; ASCE7-16; FEMA-355C; GB50011-2010; PEER/ATC-72-1). However, previous studies have indicated that the anticipated performance of these connections has not been achieved satisfactorily. (Engelhardt et al. 1995; Gupta et al. 1999). Premature fracture failure modes in beam-to-column connections, often attributed to substandard welding quality, may occur before the formation of beam plastic hinges, highlighting the need for an improved design philosophy in connection design.

In response, the section of beams away from the welding zones is reduced and this reduced zone act as dissipaters for absorbing plastic energy, thereby promoting ductile connection behaviour over brittle fracture. In general, implementing this damage-control strategy (from the welding zone to the reduced beam section) enhances the seismic performance of connections. However, connections designed according to current ductile standards may survive earthquakes but exhibit significant permanent deformation, undermining both structural resilience and sustainable development goals. To enhance structural resilience, various novel connections have been investigated, employing either PT technology or SMAs, and relevant findings are reviewed here.

### **2.2.1 PT-based connections and their structural applications**

PT-based beam-to-column connections, shown in Fig. 2.1, were initially used to optimise the seismic behaviour of precast concrete structures (Priestley et al. 1999), and then were later extended to steel MRFs (Ricles et al. 2001; Christopoulos et al. 2002a; Christopoulos et al. 2002b; Garlock 2002; Garlock et al. 2003; Garlock et al. 2005; Rojas et al. 2005; Garlock et al. 2007; Kim et al. 2009). In PT-based connections and their structural applications, main structural members (such as beams and columns) are designed to remain elastic, while seismic energy is dissipated by predetermined energy-dissipation elements (such as steel angles, steel plate shear walls, and steel bars). During unloading, the recentring force provided by PT connections can return connections or structures to their initial position (Garlock et al. 2007; Kim et al. 2009). Previous numerical and experimental studies have shown that both connections and structures exhibit flag-shaped hysteretic behaviour, with plastic energy dissipated in easily replaceable energy-dissipation elements and recentring force supported by PT elements. Compared to ductile connections (e.g., welded beam-to-column connections with

reduced beam sections), one conclusion can be drawn that PT-based connections decouple the coupling relationship between energy dissipation and elastic restoring force elements. This allows for flexible adjustment of connection performance through rational proportions of energy dissipation and restoring force elements, achieving resilience with controllable damage, low residual deformation, and sufficient strength/stiffness.

To further improve the lateral resisting capacity of PT-based MRFs, self-centring steel plate shear walls (SC-SPSW) combining the advantages of thin SPSWs, and PT technology were proposed and investigated (Clayton et al. 2012; Dowden et al. 2012). Experimental and analytical analyses revealed that SC-SPSWs possess high lateral resistance and moderate energy-dissipation capacities. However, challenges persist, notably the "beam-growth" phenomenon observed in previous PT-based MRFs, which could adversely affect the seismic performance of SC-SPSWs. To address this issue, Dowden *et al.* optimised previous PT connections to mitigate beam-growth. Additionally, ensuring reliable anchorage of tension fields in thin SPSWs increases the strength and stiffness demands on columns in SC-SPSWs. In previous studies (Nakamura et al. 1997; Eatherton 2010; Eatherton et al. 2010; Ma et al. 2010), researchers have indicated that SPSWs with openings (e.g., slit web plates, butterfly-shaped web plates) can enhance the overall seismic performance of SPSWs and reduce strength and stiffness demands on their adjacent members. Although PT-based structures can enhance structural resilience, their widespread adoption may be hindered by the need for specialised technical expertise and extensive on-site construction.

Recently, building on prior research into beam-through steel frames (Wang et al. 2013), self-centring modular panels with slit steel plate shear walls or tension-only braces were developed and systematically examined in beam-through steel frames

(Wang et al. 2017a; Wang et al. 2017b; Wang et al. 2018; Chu et al. 2020). The self-centring modular panel serves as a structural component to enhance the performance of beam-through steel frames, as shown in Fig. 2.2. Note that the self-centring modular panel can be prefabricated in factories and bolted to beam-through steel frames at construction sites, reducing the need for a professional technical team. Additionally, the modular panels help mitigate adverse effects caused by beam growth on structural performance. The experimental and numerical analysis results revealed that self-centring modular panel embraces notable energy-dissipation capacity and excellent self-centring behaviour. This makes it an effective choice for integration into steel beam-through frames in low-intensity regions.

It is essential to note that the design principles for enhancing resilience in PT-based connections or their structural applications are similar. Typically, elements or systems related to energy dissipation and those related to restoring force are arranged in parallel and can be flexibly adjusted to achieve satisfactory structural performance, striking a balance between energy dissipation and self-centring behaviour.

### **2.2.2 SMA-based connections and their structural applications**

In parallel with PT technology, the use of SMAs in connections and structures has emerged as a promising alternative for achieving resilience. This is due to the notable characteristics of SMAs, namely the shape memory effect (SME) and superelastic effect (SE), as depicted in Figure 2.3 (Auricchio et al. 1997; Auricchio et al. 2003; DesRoches et al. 2004; McCormick et al. 2005; McCormick 2006; Bellouard 2008; Guo et al. 2013; Chang and Araki 2016; Cladera et al. 2016). As illustrated in Fig. 2.3, SMAs have two thermo-related grain states (i.e., austenite( $A$ ) and martensite( $M$ )). Martensite can be further categorised into twinned and detwinned crystal structures.  $M_s$  denotes the

critical temperature for triggering the stress-induced martensite phase transformation under zero stress level, while  $M_f$  represents the finished temperature for completing the transformation from  $A$ -to- $M$ .  $A_s$  and  $A_f$  denote the start and finished temperatures for completing the transformation from  $M$ -to- $A$ , respectively. The previous research (Otsuka et al. 1997a; Otsuka et al. 1997b; Fang et al. 2015; Ke et al. 2022) showed that the mechanical properties of SMAs are dependent on the alloy composition, crystal structure, heat treatment and fabrication process (i.e., different SMA products have different forging strategies (e.g., cold work)). Thus, understanding the mechanical properties of SMAs can provide comprehensive guidance for designing SMA-based products/devices. Recently, various SMA-based products, such as SMA rings, SMA bolts, SMA U dampers, and SMA disc washers, have been utilised in structural engineering and systematically studied to enhance structural resilience.

Among these, SMA bars of various dimensions can flexibly and easily meet different strength demands and have been introduced to enhance the seismic performance of structural connections. The feasibility of steel beam-to-column connections using SMA bolts was experimentally examined (Ocel et al. 2004). The test results confirmed excellent seismic performance and capacity for rehabilitation, with reduced residual deformation achieved by heating SMA bars above the transformation temperature. Abolmaali et al. (2006) evaluated the seismic behaviour of connections joined by T-stub connectors using superelastic SMA bolts. While the connections demonstrated satisfactory self-centring behaviour, deficiencies in ductility were also noted, possibly due to inadequate design details of the SMA bolts. Following this, a series of test programmes was conducted to evaluate the cyclic performance of several connection types equipped with SMA bars (Fang et al. 2014; Yam et al. 2015; Fang et al. 2017). The tested connections exhibited flag-shape hysteresis curves and stable

energy-dissipation capacities. Additionally, preliminary design considerations for beam-to-column connections were provided based on test observations and numerical parametric studies.

To further enhance beam-to-column connections, SMA washers were integrated into the connections to improve their seismic performance (Fang et al. 2018). The test results of the connections utilising SMA bolts and washers showed that the connections exhibited flag-shaped hysteretic behaviour, demonstrating good self-centring ability. Additionally, satisfactory ductility and moderate energy dissipation capacities were confirmed. Therefore, the SMA components significantly contributed to the strength, stiffness, and energy dissipation of the connections as anticipated.

While SMAs offer desirable characteristics such as superelasticity and energy dissipation capacity, their high cost poses a barrier to their widespread use in structures. Therefore, the utilisation of SMAs in structures should strike a balance between cost and performance. Recently, a hybrid beam-to-column connection combining SMA bolts with various energy-dissipation elements (such as steel bars, steel angles, shear tab friction and web hourglass steel pins (WHPs)) was proposed, and its feasibility was examined (Wang et al. 2015; Wang et al. 2017a; Wang et al. 2017b; Mohammad et al. 2017). In the hybrid beam-to-column connections, the energy-dissipation elements provide supplementary energy dissipation and shear capacities for connections. The results indicated that SMA bolts and energy-dissipation elements absorbed the inelastic deformation of connections, while the beams and columns remained elastic. Moreover, by proportioning the SMA bolts and additional energy-dissipation elements rationally, the hybrid beam-to-column connections demonstrated satisfactory self-centring behaviour and energy-dissipation capacities.

Similar to beam-to-column connections, the seismic performance of novel column

bases equipped with SMA bolts and dissipaters was investigated (Tamai et al. 2004; Wang et al. 2019). The results demonstrated that column bases enhanced by SMA bolts exhibited satisfactory and stable flag-shaped hysteresis curves, confirming excellent self-centring behaviour and moderate energy-dissipation capacities.

At the structural system level, to verify the effectiveness of SMA-based beam-to-column connection in structural resilience, numerical models of such structures were established, and their dynamic behaviour were examined (Taftali 2007; DesRoches et al. 2010; Ke et al. 2017; Zhou et al. 2021; Ke et al. 2020; Nia et al. 2023; Hassanzadeh et al. 2024). The seismic demand and performance evaluations of such structures were systematically examined. The analysis results showed that structures equipped with these connections exhibited satisfactory self-centring behaviour, albeit with reduced energy dissipation capacity compared to conventional structures. However, insufficient energy dissipation could lead to severe high-mode effects and increased peak floor acceleration (PFA) responses for structures equipped with these connections. This may pose soft-storey risks and cause damage to non-structural members which were sensitive to PFA. Therefore, additional efforts may be required to enhance energy-dissipation capacities and effectively reduce the risks associated with concentrated soft storeys.

### **2.3 Self-centring rocking systems**

As stated in section 2.2, self-centring structures equipped with PT and SMA connections may encounter soft-storey risks during earthquakes, resulting from severe high-mode effects due to their lower energy dissipation capacity compared to conventional structures. A potential solution involves enhancing the post-yielding stiffness of structures. A notable increase in post-yielding stiffness can efficiently

alleviate the adverse effects induced by high-mode responses (Christopoulos et al. 2002a; Charney et al. 2011; Malakoutian et al. 2013; Ke and Chen 2016; Ke and Yam 2018; Ke et al. 2018; Chen and Ke 2019; Ke et al. 2023a). Another promising strategy to address the soft-storey issues is to introduce rocking systems to control the overall drift pattern for the main structures.

Similar to structures with PT-based connections, PT technology is also utilised in rocking frames. The advantage of the rocking behaviour in assisting structure to resist earthquakes was first highlighted by Housner (Housner 1963). A precast seismic structural system research programme was conducted for 10 years by Priestley et al. to extend the utilisation of precast concrete structure in seismic zones (Priestley et al. 1978; Priestley and Tao 1993; Priestley and MacRae 1994; Priestley et al. 1999). This programme paved the way for the development of rocking concrete systems (e.g., rocking concrete shear wall system). Based on the research findings in concrete structures, this strategy was also introduced in steel structures to improve their performance. Using the rocking mechanism, self-centring steel concentrically braced frames was proposed and demonstrated to mitigate seismic damage by absorbing lateral drifts in rigid body mode, while seismic energy is dissipated through easily replaceable dissipators (Roke et al. 2006; Roke et al. 2010; Chancellor et al. 2017). Utilising this rocking mechanism, a range of replaceable dissipators providing stable energy dissipation and good ductility were investigated both experimentally and numerically. Among these dissipators, butterfly-shaped steel plates were demonstrated to be effective and stable, emerging as a promising option, as shown in Fig. 2.4 (Eatherton 2010; Eatherton et al. 2010; Deierlein et al. 2011; Ma et al. 2011; Eatherton et al. 2014a; Eatherton et al. 2014b). Recently, partial rocking concept was proposed to improve the

seismic performance and limit excessive yielding of the braces for buckling-strained braced frames and the feasibility was subsequently confirmed.

The rocking mechanism has been extended to timber structures as a promising approach to improve their seismic performance. A novel concept for rocking timber frames has been developed, involving the refinement and adaptation of jointed ductile connections with PT steel. These beam-to-column connections consist of laminated veneer lumber post-tensioned using unbonded tendons, along with external or internal energy dissipaters (Newcombe et al. 2008). Drawing from a similar concept, a 3D, three-storey timber structure was designed, incorporating a combination of rocking timber beam-column joints and replaceable dampers. The seismic performance of this structure was experimentally evaluated. Additionally, rocking timber wall panels were introduced, and their effectiveness in mitigating soft-storey risks for timber frame structures was demonstrated through full-scale shaking table tests (Sarti et al. 2016; Ganey et al. 2017; Moroder et al. 2018; Di Cesare et al. 2020).

Based on the discussions above, the design philosophy for various self-centring rocking structures (concrete, steel, and timber structures) aligns with that of structures using PT connections. The approach involves partially releasing boundary constraints to enable rigid rotation of the main structural members during large deformations, thereby reducing damage. Seismic energy is absorbed by pre-designated dissipaters. PT-based rocking systems can provide restoring force to return structures to their initial positions. In summary, elastic restoring-force-related rocking main structural members and energy dissipation-related dissipaters are generally arranged in parallel and combined in appropriate proportions to jointly determine the seismic performance of such structures. Additionally, compared to structures using PT connections, rocking

systems can effectively mitigate soft-storey risks induced by high-mode effects due to continuous stiffness along structural height.

## **2.4 Hybrid-strength steel structures**

Recently, hybrid dual structural systems have emerged as a promising strategy to enhance the seismic performance of structures. These systems employ a damage-control mechanism, comprising high-strength main structural systems alongside secondary systems or fuse systems (Dusicka and Iwai 2007; Charney and Atlayan 2011; Mohammad 2012; Dougka et al. 2014; Tenchini et al. 2014; Ke and Chen 2014; Dimakogianni et al. 2015; Ke and Chen 2016; Ke and Yam 2018; Ke et al. 2018a; Ke et al. 2018b; Li et al. 2018; Li et al. 2019a; Li et al. 2019b; Chen and Ke 2019; Zhai et al. 2019; Ke et al. 2023a; Ke et al. 2023b). During earthquakes, inelastic damages are confined to the sacrificial fuse systems, ensuring minimal impact on the main structural systems. Recent investigations confirmed the shared advantages of the performance of dual steel systems: inelastic damages are limited to fuse systems under an expected earthquake and fuse systems can be easily repaired after earthquakes (Charney and Atlayan 2011; Mohammad 2012; Ke and Chen 2016; Ke and Yam 2018; Ke et al. 2018a; Ke et al. 2018b; Li et al. 2018; Li et al. 2019a; Li et al. 2019b). In addition, dual systems can exhibit recentring behaviour at a certain level under an expected earthquake. Various secondary fuse systems applicable to steel MRFs have been examined by the research community. Steel frames with linked columns were proposed by Dusicka and Iwai (2007), and the seismic performance of this effective structure was examined by Mohammad (2012). Ke and Chen (2016), Ke and Yam (2018), Ke et al. (2018a, b) developed seismic resistant energy dissipation bays for steel MRFs, shown in Fig. 2.5.

Additionally, Ke and Chen (2016) also systematically investigated the hysteretic behaviour of hybrid steel moment-resisting frames (MRFs) with steel slit shear walls.

In parallel, Li et al. (2018, 2019a, b) developed an innovative dual steel moment-resisting frame (MRF) known as the steel MRF with energy dissipation rocking columns (MRF-EDRCs), making use of the advantages of the rocking mechanism. The EDRC system comprises distributed steel strip fuses (SSF), rigid links at the floor level, and dual columns. Experimental and numerical analyses confirmed the effectiveness of the EDRC system. However, the self-centring capability provided by elastic steel MRFs may not effectively reduce residual drift for structures, even during the damage-control stage. This unsatisfactory self-centring behaviour is attributed to the fact that EDRC systems contribute strength and stiffness comparable to or higher than that of the main steel frames. Consequently, the elastic restoring force provided by the main frame is insufficient to reduce residual deformation. Therefore, enhancing the self-centring force is necessary to improve its recentring ability.

## **2.5 Resilient dampers or braces and their structural applications**

Compared to self-centring steel MRFs, steel braced frames which utilise resilient dampers or braces have garnered significant attention in the academic community due to their advantages, such as shop fabrication, ease of installation, and good repairability. In addition, braced frame systems, serving as a more effective lateral resisting system, can further enhance the seismic performance of structures in various aspects, including better control of peak floor drift responses during earthquakes, flexible design under various seismic demands and less challenges associated with connections to the adjacent gravity systems. Based on the mechanical characteristics of previous dampers

or braces, two categories are summarised: tension-only braces and tension-compression braces.

The feasibility of tension-only braces using SMA bars for steel frames was demonstrated via a 1/3 scale quasi-static and shaking table tests, shown in Fig. 2.6 (Araki et al. 2014). The tests showed that the SMA brace system effectively controlled the behaviour of the whole steel frame, with strong recentring capability. In subsequent research, the brace was optimised by incorporating a stopper as a simple failsafe mechanism to restrain the deformation of SMA bars under strong earthquakes (Araki et al. 2016). This approach helped prevent premature fracture of SMA bars under strong seismic intensities. Experimental results demonstrated that the steel frame equipped with the brace exhibited a flag-shaped hysteresis with minimal residual deformation upon load release. A novel configuration of tension-only brace was introduced, and its effectiveness in enhancing the seismic response of deficient reinforced concrete squat walls as a retrofit device was systematically investigated (Leonardo and Cortes 2017). The brace comprises two rigid steel elements and an SMA link. The rigid steel elements are required to remain elastic and undergo minimal deformation throughout all loading stages.

In tension-compression dampers or braces, PT technology is employed to enable self-centring ability. As discussed in chapter 1, by combining PT elements (e.g., high-strength steel and composite tendons) with various energy-dissipation mechanisms (e.g., metal yielding and friction mechanism), the hysteretic performance of dampers and their adjustability in performance through rational proportions of PT elements and energy-dissipation-related elements were explored. Flag-shaped hysteretic curves with excellent recentring behaviour were observed, demonstrating their effectiveness in minimising residual deformation in structures (Christopoulos et al. 2008; Zhou et al.

2015; Xie et al. 2016; Xie et al. 2020; Haide and Lee 2021; Ghowsi and Celik 2022). These studies also highlighted concerns regarding the implementation of such devices in structural application, such as the limited deformability of PT elements and the overstrength (defined as the ratio of ultimate strength to yielding strength). Recently, a new configuration involving dual cores deforming in series has been proposed to enhance deformability (Chou and Chen 2015; Zhou et al. 2015; Xie et al. 2016; Xie et al. 2020). Additionally, disc spring groups have been utilised as restoring force systems to replace the PT elements, shown in Fig. 2.7. It is noteworthy that the flexibility of disc spring groups achieved by combining them in series or parallel can meet various deformation and strength requirements during earthquakes (Xu et al. 2016; Chen et al. 2023).

In addition, SMAs are also adopted in tension-compression dampers or braces to address above-mentioned issues related to insufficient deformation and overstrength. Due to their superelasticity and phase transformation. The seismic performance of a self-centring tension-compression bracing system using SMA bars, shown in Fig.2.8, was experimentally examined (Issa and Alam 2019). The test results confirmed that the proposed damper exhibited negligible permanent deformation with stable energy dissipation capacity throughout the entire testing procedure. The cyclic behaviour of self-centring tension-compression brace using SMA wires was investigated, as depicted in Fig. 2.9 (Qian et al. 2013; Qiu et al. 2017). The results demonstrated that the developed braces using SMA wires exhibited a typical flag-shaped hysteretic curve, suggesting satisfactory self-centring behaviour. However, anchorage reliability poses significant challenges and may lead to failure risks under cyclic loading. As an alternative, an innovative self-centring damper utilising buckling restrained SMA bars was proposed, and its feasibility was confirmed by experimental programme (Qiu et al.

2020a). Additionally, to enhance energy dissipation for these SMA-based dampers or braces, other energy-dissipation mechanisms were incorporated in such devices, such as low-yielding steels and friction mechanisms (Qiu et al. 2020b). As discussed in Chapter 1, the use of SMA bars or wires as core components in dampers or braces can substantially increase construction costs.

Recently, a resilient slip damper (RSD) employing a variable friction mechanism (illustrated in Fig. 2.10) was developed, and its structural applications were extensively investigated (Hashemi et al. 2017; Hashemi et al. 2019). The RSD not only addresses insufficient deformability but also enhances energy dissipation capacities, although it still encounters overstrength issues. To address this issue, SMA bolts were utilised as a replacement for the combination of high-strength steel and disc washers in subsequent improved resilient slip damper (IRSD) (Chen et al. 2022; Qiu et al. 2022; Ke et al. 2023a). The stress-induced phase transformation of SMA bolts can decrease their axial stiffness when the damper experiences significant deformation levels. Therefore, the IRSD exhibited a trilinear flag-shaped hysteretic curve with a two-stage stiffness reduction mechanism. The two-stage stiffness reduction mechanism holds promise in decoupling the interdependence of the strength and stiffness of the damper, effectively addressing the overstrength concerns. Note that in the IRSD, the contribution of energy dissipation and strength is attributed to friction mechanism, consequently reducing SMA usage. Although such advantages, the observed self-locking phenomenon, arising from the interdependence of design parameters of the IRSD (i.e.,  $\tan\theta_a \geq \mu_a$ ,  $\theta_a$ ,  $\mu_a$  = sloping angle and friction coefficient of wedge-shaped friction pairs), may significantly reduce the design flexibility and overall performance. Moreover, lateral instability issues also compromise the cyclic performance of current IRSDs under compression.

Hence, further endeavours are required to address the issues related to instability under compression for such dampers.

## **2.6 Seismic demands for self-centring structures**

Inspired by the damage-control mechanisms, various members, connections, and systems with different hysteretic behaviour have been developed to enhance structural resilience, as given in previous sections. In general, compared to traditional structures displaying a full hysteretic curve, self-centring structures exhibit a flag-shaped hysteretic curve with no or negligible residual deformation. However, while demonstrating excellent self-centring behaviour, inadequate energy dissipation may result in other undesirable outcomes, including severe high-mode effects, high peak floor acceleration and drift demands, as well as increased energy demands for structures. Constant-ductility or constant-strength nonlinear spectral analyses of single-degree-of-freedom (SDOF) systems were often utilised to assess the seismic inelastic demands of emerging structures, such as, strength demand (quantified by a strength reduction factor), energy demand (quantified by a modified energy factor) and acceleration demand (quantified by an acceleration factor). Dynamic analyses of SDOF systems with flag-shaped hysteretic curves have shown that increasing either the post-yielding stiffness or the energy dissipation capacity of self-centring structures can mitigate issues caused by high-mode effects. (Christopoulos et al. 2002a; Christopoulos et al. 2002b). Furthermore, by adjusting combinations of hysteretic parameters, a flag-shaped hysteretic system could be quantitatively matched or even surpassed by the response of an elasto-plastic system in terms of displacement ductility. However, the former system may need higher peak strength to control drift responses. Additionally, constant-ductility-based spectral analyses of SDOF systems, representing self-centring

structures with different hysteretic behaviour, were conducted to compare seismic demands under various far-fault earthquakes, as depicted in Fig. 2.11. It was found that the seismic demand of self-centring structures is sensitive to hysteretic parameters of structures.

Notably, designing structures or structural members (such as dampers or braces) to maintain a substantial post-yielding stiffness throughout the entire loading stage is generally undesirable. The substantial post-yielding stiffness of such structural members may lead to overstrength issues and result in increased construction costs. Moreover, the significant post-yielding stiffness also compromises energy-dissipation capacity of structures, posing potential risks to non-structural members during strong earthquakes (Zhang et al. 2022b).

## **2.7 Summary**

To identify research gaps in design strategies for structural resilience, this chapter reviewed the literature on various self-centring technologies and their impact on the seismic performance of self-centring structures.

Insufficient energy-dissipation capacity, as a common issue, in current self-centring structures can result in severe high-mode effects and high peak acceleration responses. This poses potential risks to soft-storey integrity and can cause damage to non-structural elements. Increasing the post-yielding stiffness of self-centring structures may reduce high-mode effects but also introduces overstrength issues and decreases energy-dissipation capacity. The reduced energy-dissipation capacity of self-centring structures typically leads to higher peak accelerations, especially when other hysteretic parameters remain unchanged. Therefore, the interdependence between controlling peak floor acceleration and overstrength (which benefits from lower post-

yielding stiffness) and managing high-mode effects (which benefits from higher post-yielding stiffness) in self-centring structures requires further exploration. To address this, the thesis explored the potential of the multistage energy-dissipation mechanism in self-centring structures. Note that applying the multistage energy-dissipation mechanism to self-centring structures (e.g., structures equipped with self-centring dampers based on this mechanism) may offer a potential solution to the seismic challenge of balancing peak floor acceleration and overstrength (benefiting from lower post-yielding stiffness) with controlling high-mode effects (benefiting from higher post-yielding stiffness).

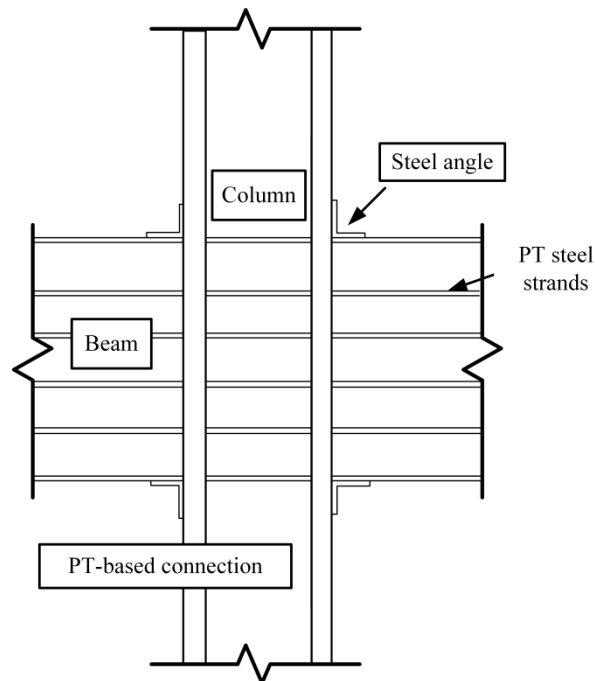


Fig. 2.1 PT beam-to-column connection (Garlock et al. 2005)

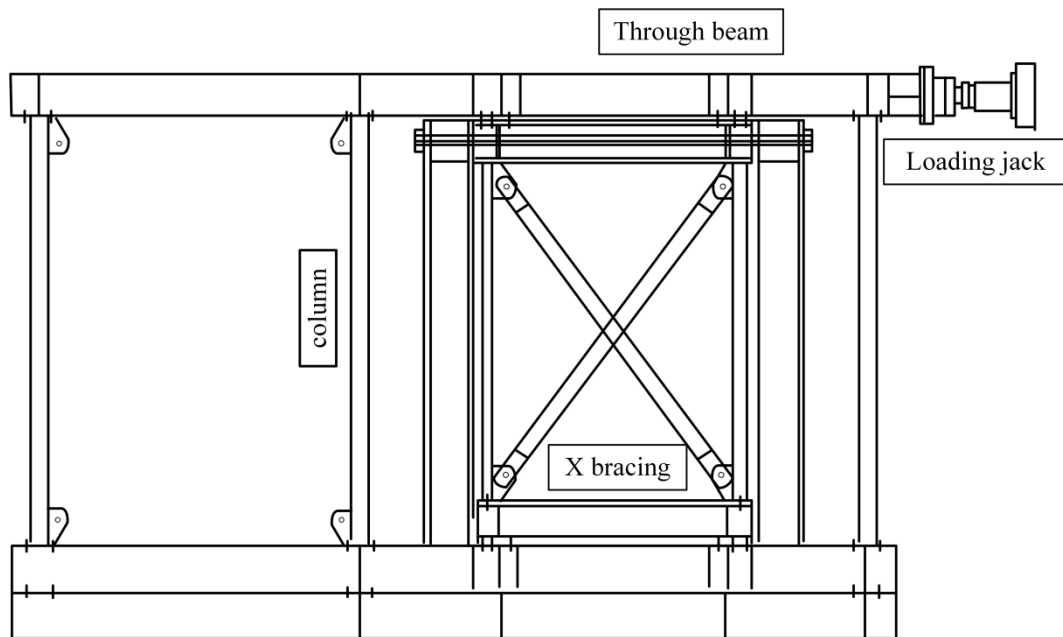


Fig. 2.2 Beam-through frame with self-centring modular panels (Wang et al. 2017)

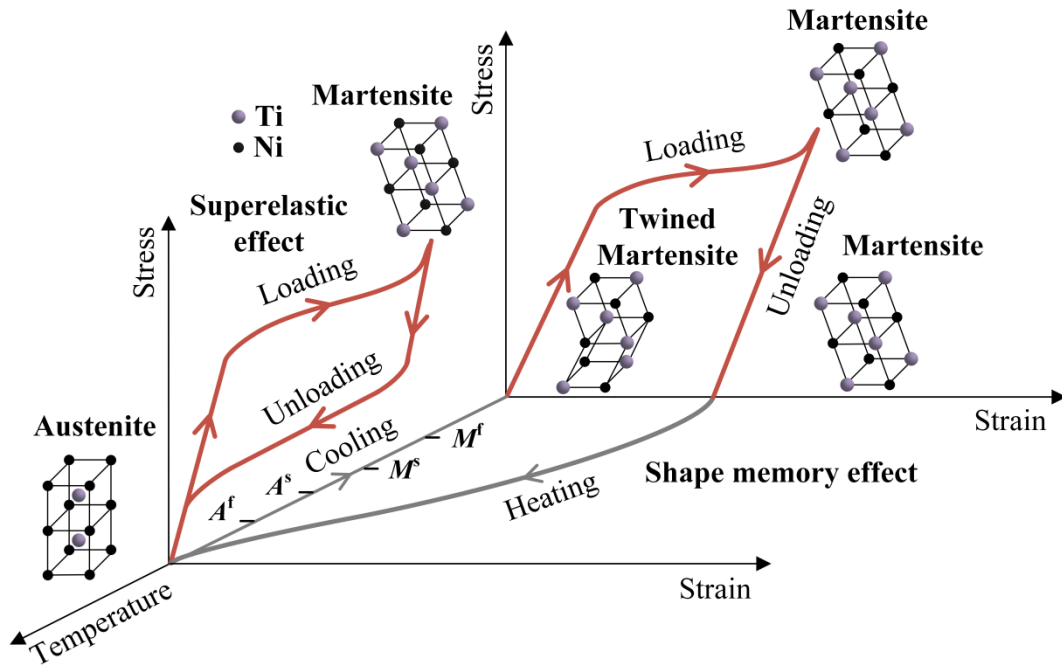


Fig. 2.3 Thermal-mechanical characteristics of SMA

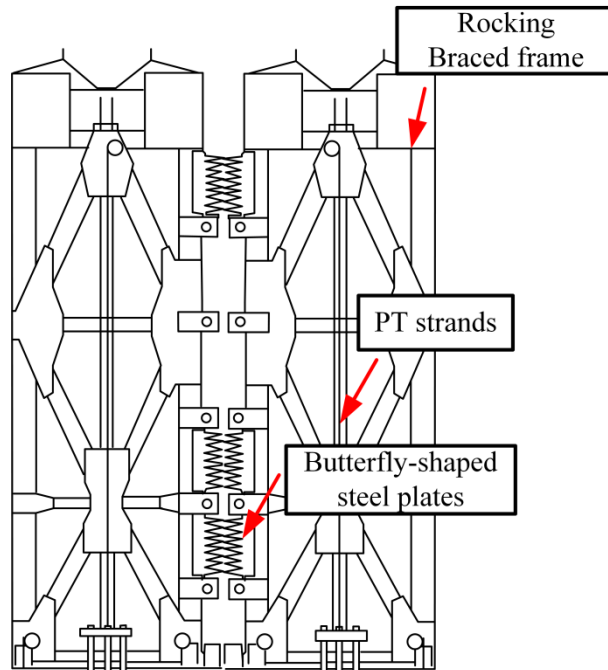


Fig. 2.4 Steel rocking braced frame with butterfly-shaped steel plates (Eatherton et al. 2014)

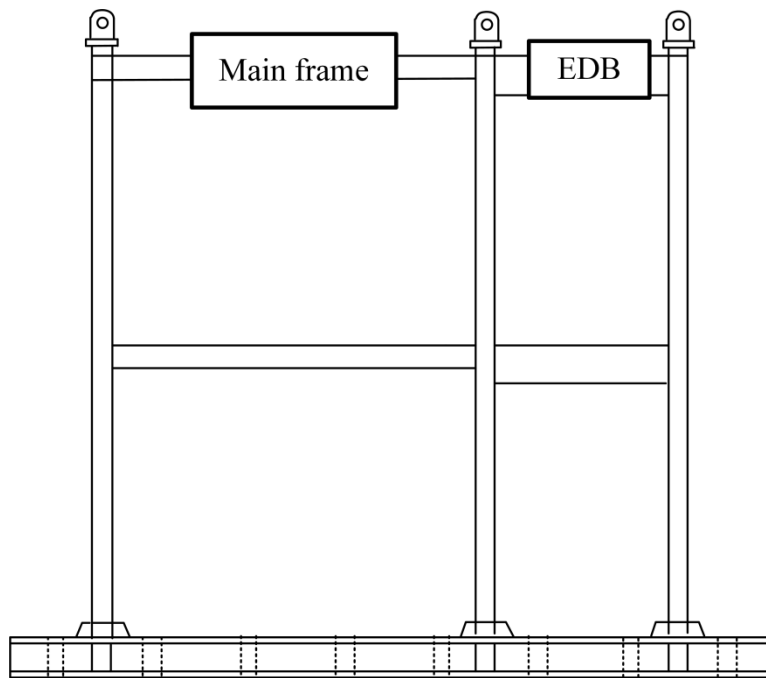


Fig. 2.5 Steel MRF with EDBs (Ke and Chen 2016)

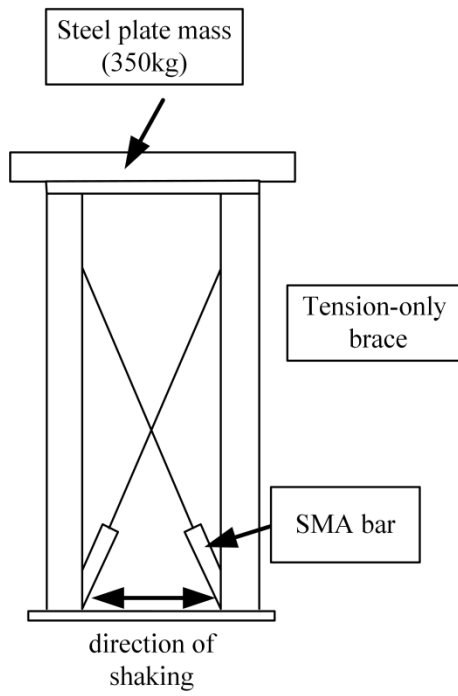


Fig. 2.6 Steel MRF with tension-only braces (Araki et al. 2016)

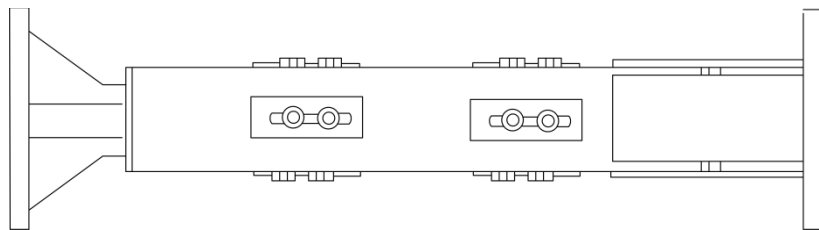


Fig. 2.7 Self-centring damper using disc springs (Xu et al. 2016)

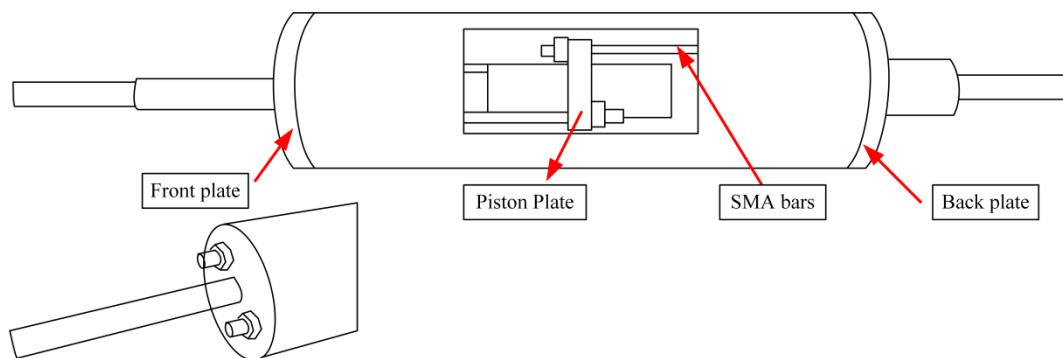


Fig. 2.8 Self-centring damper using SMA bars (Issa and Alam 2019)

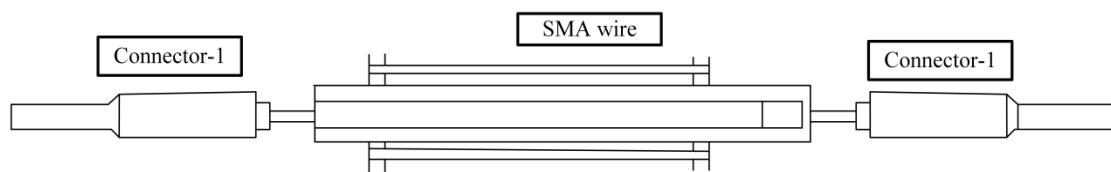


Fig. 2.9 Self-centring brace using SMA wires (Qiu et al. 2017)

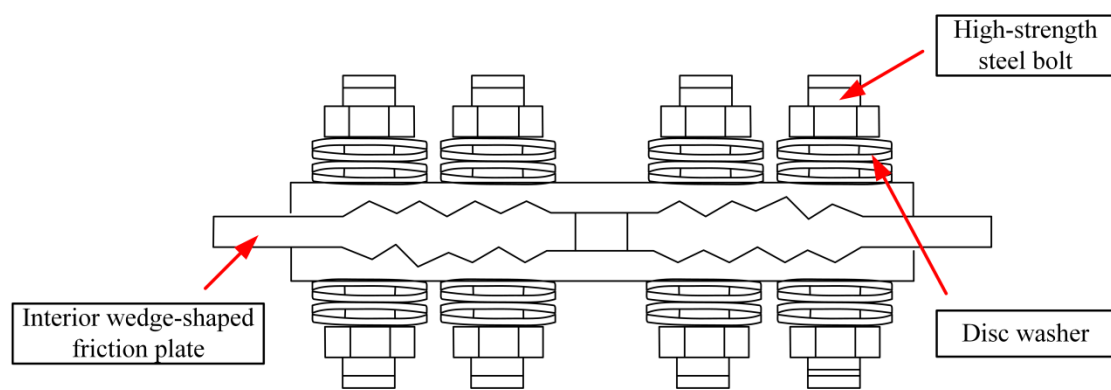


Fig. 2.10 Resilient slip damper (Hashemi et al. 2017)

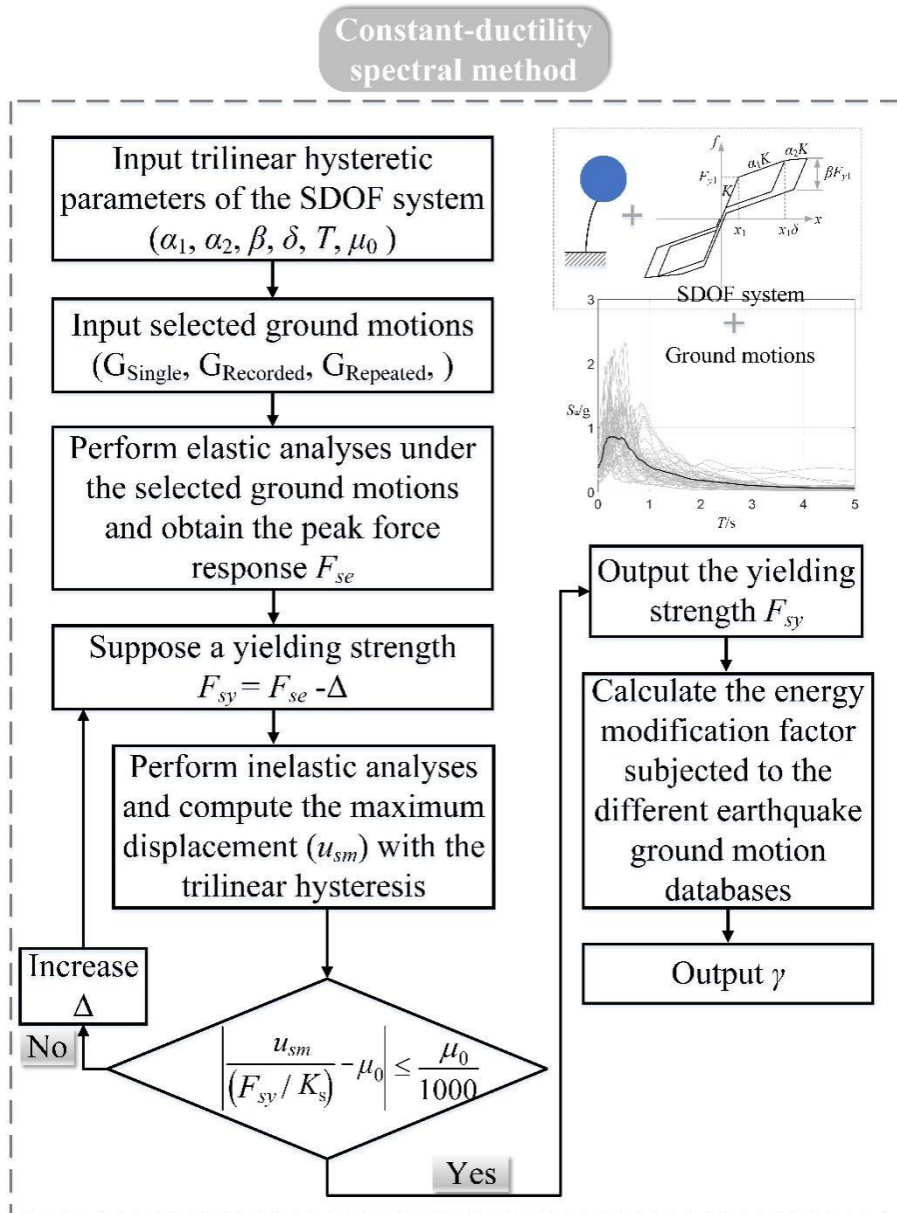


Fig. 2.11 Flowchart of constant-ductility spectral analysis of an equivalent SDOF system (Ke et al. 2022)

## **Chapter 3 Concept design and analytical model of the proposed SMA-VFSD<sup>1</sup>**

### **3.1 Introduction**

This chapter introduced the conceptual design, which encompassed configuration, working principles and deformation modes, of the SMA-VFSD, along with its analytical hysteretic model. Firstly, the configuration of the damper was described, and the damper assembly process was explained step by step. Subsequently, the deformation modes of the damper and the expected hysteretic responses were presented. Following this, based on the force analysis of the SMA-VFSD, a simplified spring model denoting the working principles of the damper was described. At last, an analytical hysteretic model capable of predicting the hysteretic responses was developed and validated against the test results provided in Chapter 4.

### **3.2 Concept design**

#### **3.2.1 Configuration of SMA-VFSD**

---

<sup>1</sup>Chapter 3 is based on a published study and is being reproduced with the permission of ASCE publications. Zhang, P., Yam, M.C.H., Ke, K., Song, Y.C., and Zhu, M. (2024). An experimental study on a self-centring damper with multistage energy-dissipation mechanism. *Journal of Structural Engineering*.

As shown in Fig. 3.1, the SMA-VFSD consists of eight main components: (1) SMA bolt, (2) exterior friction plate, (3) interior friction plate, (4) interior core, (5) preloaded disc system, (6) endplate-2, (7) exterior tube, (8) endplate-1, along with other accessories (e.g., bolts and nuts). The exterior friction plates with wedge-shaped friction surfaces are installed through the customised openings cut on the top and bottom walls of the exterior tube, hence ensuring that the movements of the exterior friction plates occur only in the transverse direction. Furthermore, the stability of the damper under compression are enhanced due to the constraints from the exterior tube, while lateral instability of dampers was observed in previous research (Hashemi et al. 2017; Hashemi et al. 2019; Chen et al. 2022; Qiu et al. 2022 and Ke et al. 2023a). Two narrow openings are cut on the side walls of the exterior tube, for visual examination of the internal working state of the damper. Two dog bone-shaped SMA bolts connect the exterior friction plates to the interior friction plates and the interior cores. Specifically, the bolt holes of the interior core and friction plates are slotted to allow relative movements against the exterior friction plates. The disc spring systems, comprising steel bars and a group of disc springs, are anchored to the endplates at both ends of the exterior tube. Note that the adopted disc spring systems can be flexibly adjusted to meet the strength and deformation demands for the damper (Xu et al. 2016a; Xu et al. 2016b). Preloads are applied to the SMA bolts and disc spring systems to assemble the damper and provide the initial restoring forces. The detailed assembly process (shown in Fig. 3.2) of the damper was outlined below (the number in the bracket corresponds to the component number shown in Fig. 3.1(b)):

**Step 1)** install the interior friction plates (i.e., 3) into the interior core (i.e., 4);

**Step 2)** place the assembled part from step 1 into the exterior tube (i.e., 7);

**Step 3)** install the endplates (i.e., 6 and 8) at each side of the exterior tube;

**Step 4)** incorporate the disc spring system (i.e., 5) to clamp the two endplates in step 4;

**Step 5)** insert the exterior friction plates (i.e., 2) into the customised openings of the exterior tube and install the SMA bolts (i.e., 1) to clamp the exterior friction plates, interior friction plates and interior core.;

**Step 6)** apply pre-stress to the SMA bolts and disc spring systems.

### 3.2.2 Working principles and deformation modes

The expected deformation modes and hysteretic response of the SMA-VFSD under cyclic tension and compression are shown in Fig. 3.3(a)-(d), respectively. During both tension and compression, the relative slip between the exterior and the interior friction plates occurs once the external loads exceed the sum of the disc spring systems' preloads and the static friction force between the friction plates. An obvious stiffness degradation of the damper is triggered (termed as the 1<sup>st</sup> pseudo yielding point) due to this sliding mechanism. Subsequently, with the increase of external loads, the transverse movement of the exterior friction plates occurs due to slip between the wedge-shaped friction pairs. This leads to the elongation of the SMA bolts and a resulting increase in the normal force between the friction pairs. The augmented normal force increases the friction force, and thus the “variable friction mechanism” concept is achieved. With a further increase in external loads, the increased rate of the friction force degrades after the SMA bolt phase transformation (i.e., from austenite state to martensite state, the stiffness of the SMA bolts is reduced) is reached. In this stage, a subsequent degradation of damper stiffness occurs (termed as the 2<sup>nd</sup> pseudo yielding point). Thereby, by combining the variable friction mechanism and the SMA features (i.e., phase transformation), a multistage-energy-dissipation mechanism of the SMA-VFSD is

developed. Notably, the phase transformation and superelastic characteristics of the SMA bolts enabled an approximately bilinear hysteretic behaviour, which facilitated the development of the 2<sup>nd</sup> yielding feature and the realisation of self-centring behaviour for the damper. Moreover, the energy dissipation capacity of the SMA bolts was not required in the proposed damper, as the majority of energy dissipation was provided by the friction mechanism. In the entire deformation range, the preloaded disc springs and steel bars deform in the elastic range, offering recentring force upon unloading and adjust the strength for the damper as discussed before.

The self-locking phenomenon, observed in previous research, which arises from the interdependence of design parameters (i.e.,  $\tan\theta_a \geq \mu_a$ , where  $\theta_a, \mu_a$  = sloping angle and friction coefficient of friction pairs), may significantly compromise the design flexibility and overall performance of the damper (Chen et al. 2022; Qiu et al. 2022 and Ke et al. 2023a). However, this design constrain can be overcome by incorporating the disc spring systems in the SMA-VFSD. Thus, a large friction coefficient and a small sloping angle can be used in the SMA-VFSD. It is noteworthy that when the same friction force is designed, a higher friction coefficient can significantly reduce the demand for normal force in the friction pairs. This, in turn, lowers the risk of material wear and enhances the life of friction pairs compared to a smaller coefficient. In addition, a smaller sloping angle can reduce the deformation demands of SMA bolts and enlarges the intervals of two yielding points of the damper. It should be mentioned that the interval between the two yielding points of the damper was quantified by the yielding sequence in previous research (Ke and Chen 2016; Chen and Ke 2019; Zhang et al. 2022a; Zhang et al. 2022b). This yielding sequence serves as a crucial hysteretic parameter for fine-tuning damper performance in multi-performance-based designs, thus making its adjustability highly desirable. In general, the expected hysteretic

response of the damper is given in Fig. 3.3(d). An analytical hysteretic model predicting the hysteretic behaviour of the damper is developed for the damper design in next section.

### 3.3 Analytical hysteretic model of SMA-VFSD

Considering the mechanical symmetry of the SMA-VFSD, the hysteretic behaviour under tension was illustrated herein. Fig. 3.4 provides the free body diagrams (FBDs) of the SMA-VFSD under loading and release in pull direction, respectively. The implications of the symbols are also given in Fig. 3.4. Drawing upon force analysis, a simplified spring model is depicted to enhance comprehension of the working principles of the SMA-VFSD, as depicted in Figure 3.5. S1 and S2 describe the hysteretic behaviour of the disc spring systems and the variable friction system, respectively, where S3 accounts for the elastic deformation of each damper component when loaded. Usually, the elastic deformation of S3 is minimal, and it was treated as a rigid body in previous research (Chen et al. 2022; Qiu et al. 2022 and Ke et al. 2023a). In this study, the stiffness of S3 is accounted for, approximating it to the average measured initial stiffness of the specimens, as detailed in Chapter 4. Notably, S1 and S2 operate independently but both contribute to the damper's load-carrying capacity, meaning a parallel relationship can be assumed between them, as shown in Fig. 5.5. For S1, it exhibits a bilinear elastic response, resulting in coincidence between the loading and unloading paths. The arbitrary loading and unloading paths of S1 is depicted in Fig. 3.6 and the force of S1 at arbitrary position can be determined by:

$$F_{S1} = F_{pre,DSS} + k_{DSS} \delta \quad \delta > 0 \quad (3.1)$$

$$k_{DSS} = \frac{k_{steel} + k_{dg}}{k_{steel} k_{dg}} \quad (3.2)$$

$$k_{\text{steel}} = \frac{E_s A_s}{l_s} \quad (3.3)$$

$$k_{\text{dg}} = N_a \frac{2n_s k_{\text{disc}}}{n_p} \quad (3.4)$$

where  $F_{S1}$  = force sustained by the disc spring systems;  $F_{\text{DSS,pre}}$  and  $k_{\text{DSS}}$  = preload and axial stiffness of the disc spring systems, respectively;  $k_{\text{steel}}$  and  $k_{\text{dg}}$  = axial stiffness of the steel bars and disc groups;  $N_a$  = number of the disc spring systems;  $n_p$  and  $n_s$  = number of disc springs in each paralleled unit and number of units in series for each disc spring group; and  $k_{\text{disc}}$  = stiffness of one disc spring, determined according to Chinese standard (GB/T 1972-2005).

Leveraging the material properties of the SMA, S2 exhibits a multistage hysteretic skeleton curve. Note that the loading and unloading paths follows different paths due to energy dissipation. The cyclic pushover skeleton of S2 (shown in Fig. 3.7(a)) can be determined by five reference lines (i.e.,  $l_1$ - $l_5$ ) and five key points. The reference lines are given as below:

$$\left. \begin{array}{l} l_1: \\ l_2: \\ \{l_1 - l_5\} \\ l_3: \\ l_4: \\ l_5: \end{array} \right\} \begin{cases} \delta = 0 \\ F = \frac{F_{f,p} - F_{f,\text{pre}}}{\delta_p} \delta + F_{f,\text{pre}} \\ F = \frac{F_{f,\text{max}} - F_{f,p}}{\delta_{\text{max}} - \delta_p} (\delta - \delta_p) + F_{f,p} \\ \delta = \delta_{\text{max}} \\ F = \frac{F_{f,\text{rev}} - F_{f,\text{res}}}{\delta_{\text{max}}} (\delta - \delta_p) + F_{f,\text{res}} \end{cases} \quad (3.5)$$

The coordinates of the key points are calculated according to the design parameters of dampers (e.g.,  $\theta_a$ ,  $\mu_1$ ,  $\mu_2$  et al.), also as indicated in Fig. 3.7(a), where  $F_{f,\text{pre}}$  = friction force of S2 induced by  $F_{\text{pre,SMA}}$ , and  $F_{\text{pre,SMA}}$  = preload of the SMA bolts;  $\delta_p$  and  $\delta_{\text{max}}$  = relative displacement of S2 corresponding to the initiation of SMA phase transformation and maximum loading, respectively;  $F_{f,p}$  and  $F_{f,\text{max}}$  = friction force of S2 corresponding to the initiation of SMA phase transformation and maximum loading,

respectively;  $F_{f, \text{res}}$  = residual force when S2 returns to its initial position;  $F_{f, \text{rev}}$  = reversed force corresponding to the initiation of reversed slip of S2 at the maximum deformation;  $k_{\text{SMA}}$  and  $k_{\text{SMA}, a}$  = axial stiffness of the total SMA bolts before and after SMA phase transformation, respectively;  $E_A$  and  $E_M$  = austenite and martensite modulus of the SMA bolts, respectively;  $A_{\text{SMA}}$  = sum of cross section area of the SMA bolts;  $l_{\text{SMA}}$  = work length of the SMA bolts;  $\mu_1$  and  $\mu_2$  = friction coefficient of the contact interfaces of the exterior friction plates vs the interior friction plates and the exterior tube, respectively and  $\theta_a$  = slipping angle of S2. To describe the arbitrary loading and unloading paths for S2, a dynamic reference line (referred to as  $l_{d, c}$  for the current dynamic reference line and  $l_{d, u}$  for a potential updated dynamic reference line in the next calculation step) is employed, along with two dynamic points that need to be updated promptly. Considering the hysteretic characteristics (i.e., before and after SMA phase transformation), the arbitrary loading and unloading paths for S2 are shown in Fig. 3.7(b)-(c), respectively and the force of S2 at an arbitrary position can be determined by:

$$F_{S2} = \begin{cases} F_{f, \text{res}} + k_{f, \text{un}} \delta & 0 < \delta < \delta_b \\ F_{f, \text{pre}} + k_f \delta & \delta_b < \delta \ \& \ \delta_b < \delta_p \\ F_{f, \text{pre}} + k_f \delta_p + k_{fa} (\delta - \delta_p) & \delta_b < \delta \ \& \ \delta_b > \delta_p \end{cases} \quad (3.6)$$

where  $k_f$  and  $k_{fa}$  = stiffness contributed by S2 before and after phase transformation of the SMA bolts, respectively and  $k_{f, \text{un}}$  = second unloading stiffness of S2.

Finally, taking into account the deformation caused by S3 and the arrangement pattern of the three springs, the loading and unloading paths for the SMA-VFSD can be determined. Similarly, five reference lines (i.e.,  $la-l_e$ ) and five key points are utilised to delineate the cyclic pushover skeleton of the damper during tension and release. The reference lines can be written by:

$$\left. \begin{array}{l} l_a: \\ l_b: \\ \{l_a - l_e\} \\ l_c: \\ l_d: \\ l_e: \end{array} \right\} \begin{array}{l} F = k\Delta \\ F = \frac{F_p - F_y}{\Delta_p - \Delta_y} \Delta + F_{pre} \\ F = \frac{F_{max} - F_p}{\Delta_{max} - \Delta_p} (\Delta - \Delta_p) + F_p \\ F = k(\Delta - \Delta_{rev}) + F_{rev} \\ F = \frac{F_{rev} - F_{res}}{\Delta_{rev} - \Delta_{res}} (\delta - \delta_p) + F_{f,res} \end{array} \quad (3.7)$$

The coordinates of the key points are similarly obtained based on design parameters, as given in Fig. 3.8(a), where  $k$  = initial stiffness of the damper;  $F_y$  and  $F_p$  = 1<sup>st</sup> and 2<sup>nd</sup> yielding force of the damper, respectively;  $F_{rev}$  and  $F_{res}$  = reverse force associated with the onset of unloading at the peak displacement and the residual force corresponding to the closure of the damper gap;  $\Delta_{rev}$  and  $\Delta_{res}$  = reverse displacement associated with the onset of unloading at the peak displacement and the residual displacement corresponding to the closure of the damper gap and  $\Delta_y$  and  $\Delta_p$  = 1<sup>st</sup> and 2<sup>nd</sup> yielding displacement of the damper, respectively. Similar to S2, a dynamic reference line ( $l_d$ ) and two dynamic key points are utilised to describe the arbitrary loading rules. Specifically, two arbitrary loading and unloading paths before and after SMA phase transformation are depicted in Fig. 3.8(b)-(c), respectively. The force of the SMA-VFSD at arbitrary position can be derived by:

$$F = \begin{cases} F_{res} + k_4 \Delta & 0 < \Delta < \Delta_b \\ F_p + k(\Delta - \Delta_b) & \Delta_b < \Delta < \Delta_t \\ F_y + k_1(\Delta - \Delta_y) & \Delta_t < \Delta \text{ \& } \Delta_t < \Delta_p \\ F_y + k_1(\Delta_p - \Delta_y) + k_2(\Delta - \Delta_p) & \Delta_t < \Delta \text{ \& } \Delta_t > \Delta_p \end{cases} \quad (3.8)$$

where  $k_1$ ,  $k_2$ ,  $k_3$ , and  $k_4$  = 1<sup>st</sup> post-yielding stiffness, 2<sup>nd</sup> post-yielding stiffness and 1<sup>st</sup> unloading stiffness and 2<sup>nd</sup> unloading stiffness of the damper, respectively and  $\Delta_b$  and  $\Delta_t$  =  $x$ -coordinates of two intersections (i.e., dynamic key points) of the current dynamic reference line with either the reference lines  $l_b$  and  $l_e$  or  $l_c$  and  $l_e$ , as indicated in Fig. 3.8(b)-(c).

Building upon the above equations, an analytical model capable of quantifying arbitrary loading and unloading paths of the SMA-VFSD was developed. Its accuracy is calibrated in Chapter 4.

### 3.4 Summary

This chapter presented the concept design and analytical model capable of predicting the hysteretic behaviour for the proposed damper. The key findings were summarised as below:

- Through force analysis based on the FBD of the SMA-VFSD and a simplified spring model, it was shown that the hysteretic performance of the SMA-VFSD depends on the series and parallel arrangement of S1 (denoting the behaviour of the disc spring systems), S2 (representing the behaviour of the variable friction system) and S3 (accounting for the elastic deformation of each constituent component).
- The disc spring systems in the SMA-VFSD offered adaptable elastic force, meeting both self-centring and strength requirements of the damper. This addressed the interdependence of design parameters, as evidenced in literature (Chen et al. 2022; Qiu et al. 2022; Ke et al. 2023a), enhancing design flexibility.
- A reduced sloping angle in the SMA-VFSD minimises deformation demands on the SMA bolts and modifies the yielding sequence, a crucial hysteretic parameter for implementing the multistage energy-dissipation mechanism in the damper.
- A hysteretic analytical model predicting the hysteretic behaviour of the SMA-VFSD was developed, providing a tool for the damper design.

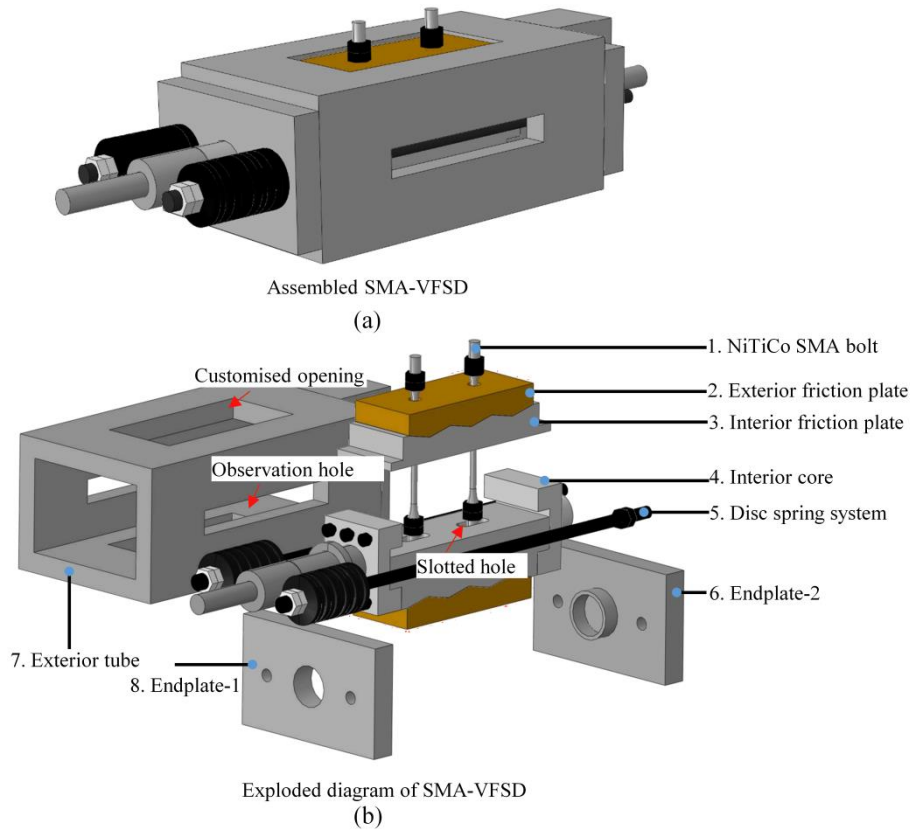


Fig. 3.1 Configuration of SMA-VFSD: (a) assembled diagram, (b) exploded diagram

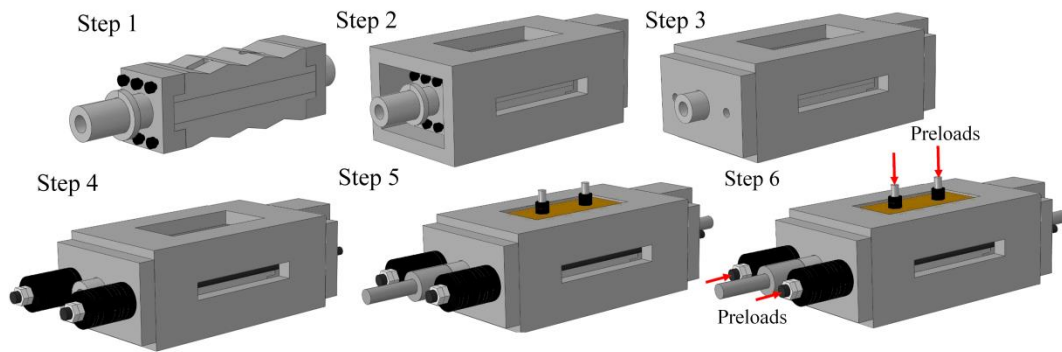


Fig. 3.2 Assembly process of SMA-VFSD

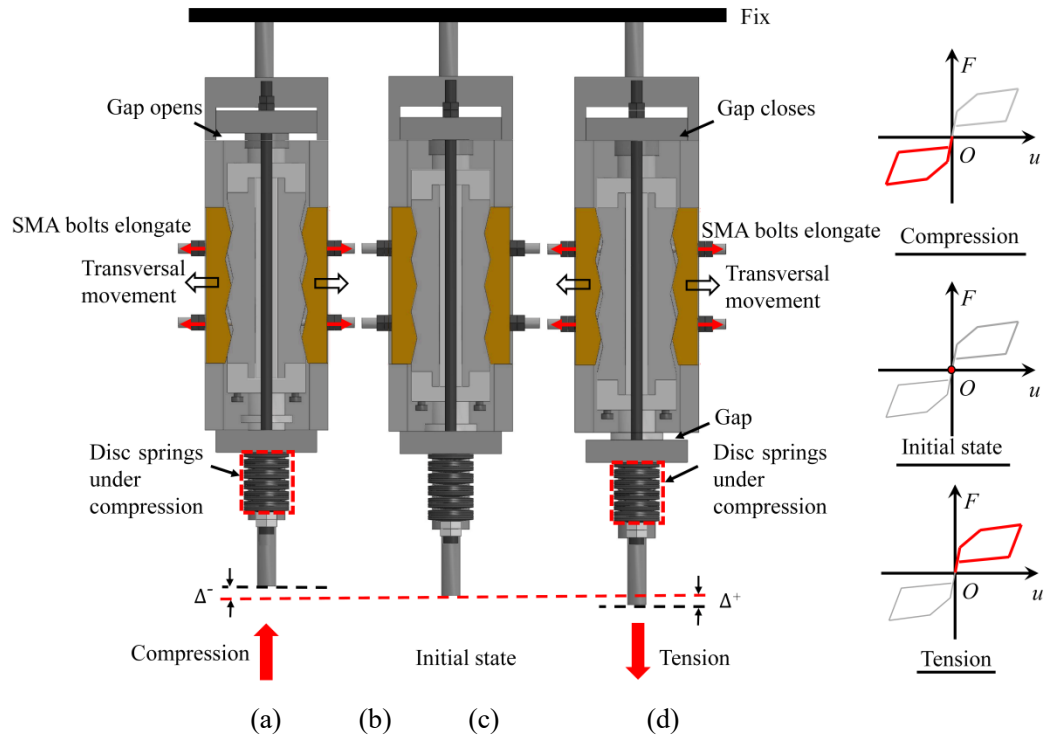


Fig. 3.3 Deformation modes and expected hysteretic behaviour: (a) under compression, (b) initial state, (c) under tension, and (d) hysteretic response

$F$  = load applied to the SMA-VFSD  
 $F_{SMA}$  = total force of the SMA bolts (note that the initial value is equal to the total preloads of the SMA bolts, that is,  $F_{pre}$ )  
 $F_{E,H}$  = contact force between the exterior friction plates and the exterior tube  
 $F_{E,V}$  = friction force between the exterior friction plates and the exterior tube in the vertical direction  
 $F_{DSS}$  = total force of the disc spring group system  
 $f$  = friction force between the wedge-shaped friction plates.  
 $N$  = normal force of contact surfaces  
 $\theta$  = slopping angle of the wedge-shaped friction plates

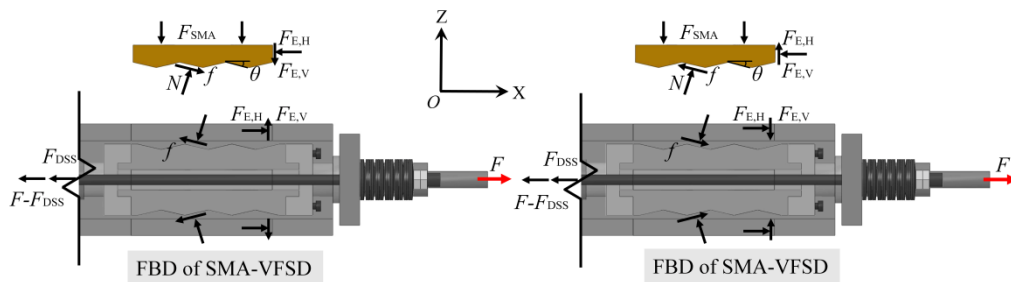


Fig. 3.4 Free body diagrams (FBDs) of SMA-VFSD: (a) under tension, and (b) under release

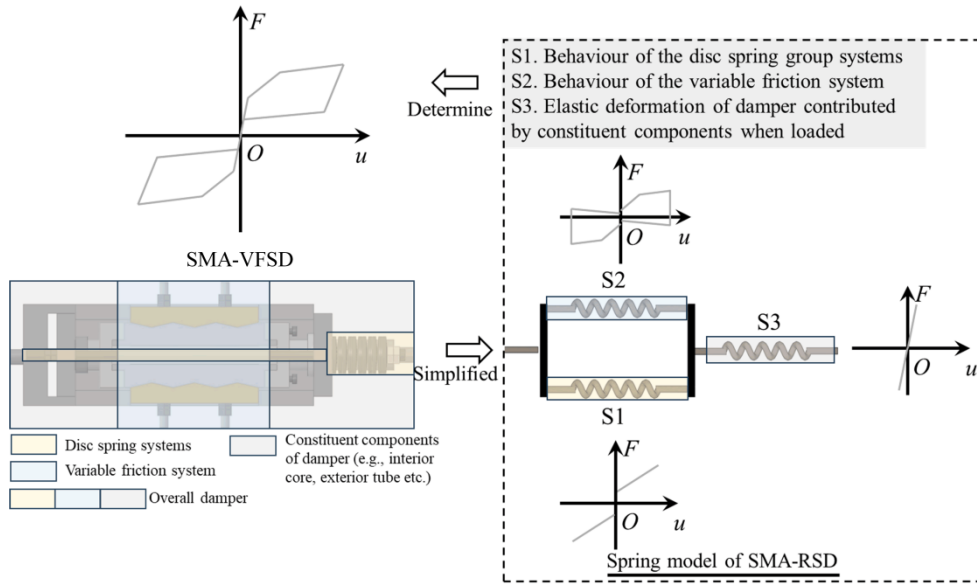


Fig. 3.5. Simplified model of SMA-VFSD

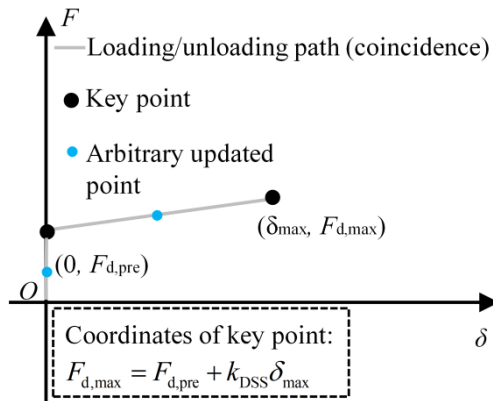


Fig. 3.6. Hysteretic skeleton of S1 under tension and release

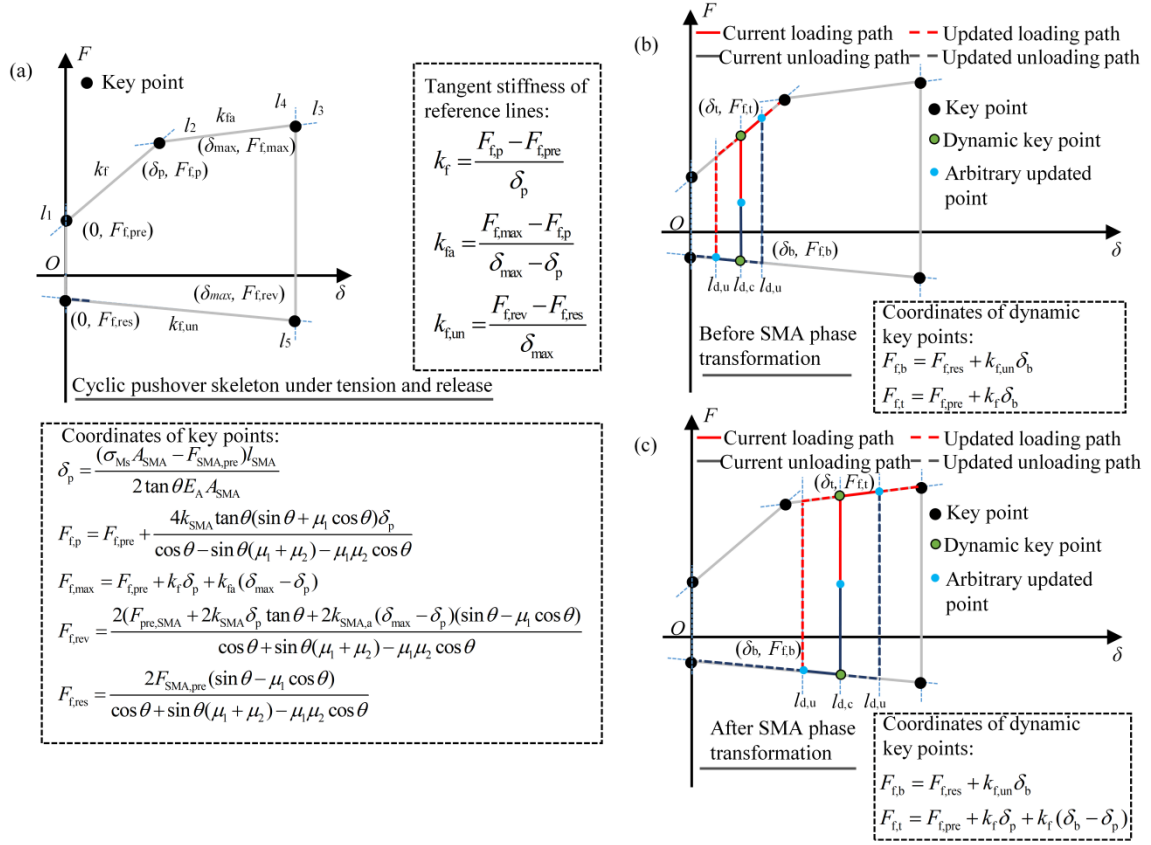


Fig. 3.7. Hysteretic behaviour of S2: (a) cyclic pushover skeleton and key points under tension and release, (b) arbitrary loading and unloading paths before SMA phase transformation, and (c) arbitrary loading and unloading paths after SMA phase transformation

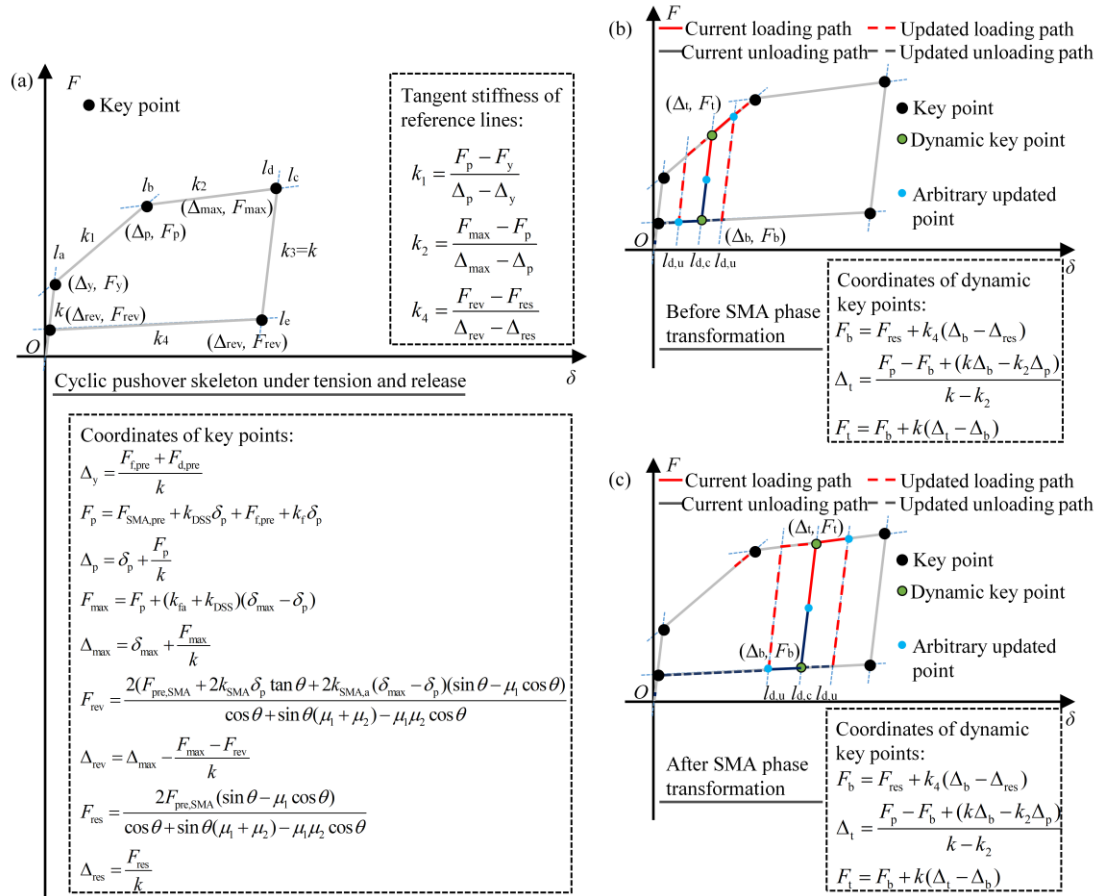


Fig. 3.8. Hysteretic behaviour of the SMA-VFSD: (a) cyclic pushover skeleton and key points under tension and release, (b) arbitrary loading and unloading paths before SMA phase transformation, and (c) arbitrary loading and unloading paths after SMA phase transformation

## Chapter 4 Experimental programme for SMA-VFSD<sup>1</sup>

### 4.1 Introduction

The working principles and analytical model of the SMA-VFSD were presented in Chapter 3. The SMA-VFSD employs a multistage energy-dissipation mechanism and excellent self-centring behaviour facilitated by the variable friction mechanism, SMA bolts, and disc spring group systems. This characteristic is desirable and advantageous for the multi-performance-based design of structures. To verify the concept and feasibility of the proposed damper, a comprehensive experimental programme was conducted, covering both the constituent component level and damper level. The results of these experiments were discussed in this chapter. The material coupon tests, and the damper constituent component tests were conducted and discussed in section 4.2. This chapter began by evaluating the stability of the hysteretic behaviour of each damper component under cyclic loading conditions. Subsequently, the damper tests were conducted and the test results, including experimental observations, hysteretic behaviour, and energy-dissipation capacities, were discussed in section 4.4. Based on the test data, the effectiveness

---

<sup>1</sup>Chapter 4 is based on a published study and is being reproduced with the permission of ASCE publications. Zhang, P., Yam, M.C.H., Ke, K., Song, Y.C., & Zhu, M. (2024). An experimental study on a self-centring damper with multistage energy-dissipation mechanism. *Journal of Structural Engineering*.

of the developed analytical model in predicting the hysteretic responses for the SMA-VFSD was confirmed. Utilising the analytical model, further exploration was conducted to investigate the effects of an extended range of design parameters on the damper behaviour. Following this, a detailed refined numerical model was established and validated against the test data, which was used to further understand and interpret the test results. Finally, to enhance computational efficiency and address convergence issues in the refined numerical model, a simplified numerical model for tracing the damper behaviour was developed and its accuracy was also demonstrated.

## **4.2 Material- and constituent component-level tests**

### **4.2.1 Material level tests**

As discussed in Chapter 3, the energy-dissipation capacity of the proposed damper is mainly contributed by the variable friction system. Therefore, all the constituent components of the damper (except for the SMA bolts, which are discussed in the next section) should be designed to remain elastic and free of damage. The proposed damper used three metal materials, namely: GCr15 steel for the interior friction plates, H62 brass for the exterior friction plates and 38CrMoAl for the remaining components. To determine the material properties (i.e., elastic modulus and yielding strength) of the three materials, the material coupon tests were conducted following the Chinese material coupon standard (GB/T228-2021). Each circular coupon specimen had a nominal gauge length of 50 mm and nominal radius of 7 mm, as per the standard specifications. For each material, three coupons were fabricated. The photos of the coupons before and after the tests are shown in Fig. 4.1. The strain along the loading direction was measured by an extensometer with a 50-mm gauge length and the results

are given in Fig. 4.2. The material constants were calculated as an average value of test results of three coupons. Note that, for the tested materials, no obvious yielding stage was observed, and thus the yielding strength was determined as  $\sigma_{0.2}$ . The measured elastic modulus and yielding strength for H62, 38CrMoAl, and GCr15 are 95 GPa and 153 MPa, 221 GPa and 829 MPa, and 2212 GPa and 721 MPa, respectively.

## 4.2.2 Constituent component-level tests

### 4.2.2.1 SMA bar test

As stated in Chapter 3, the phase transformation and superelastic characteristics of SMA bolts are crucial for developing the 2<sup>nd</sup> yielding mechanism of the damper. Therefore, the phase transformation start stress (the stress level at which the phase transformation begins) should be considered a critical design parameter for controlling the yielding intervals between the first and second yielding points. In the damper test programme, two types of SMA raw material (i.e., NiTi SMA and NiTiCo SMA, in the form of 32 mm-diameter bar) were used to fabricate the SMA bolts as shown in Fig. 4.3. The original SMA bars were machined to the dog-bone-shaped SMA bolts with a diameter of 8 mm, as shown in Fig.4.3(a). Six SMA bolts (i.e., three NiTi SMA bolts and three NiTiCo SMA bolts, respectively) were tested using an INSTRON machine (with a 500kN load capacity) at room temperature (i.e., around 25 degrees Celsius). A three-stage loading protocol was adopted to examine the pre-training, training, and post-training behaviour of the SMA bolts, as indicated in Fig. 4.3(b). The maximum strain magnitude of all the stages was conservatively set at a low level (3% or 4%) to ensure the reuse of the SMA bolts in the subsequent damper tests. Fig. 4.4 presents the typical experimental results of the NiTi SMA and NiTiCo SMA bolts. During the pre-

training stage, the variation of hysteretic behaviour was observed for both types of SMA bolts, and the residual deformation was recorded (approximately 0.5% and 0.3% for NiTi and NiTiCo SMA bolts, respectively). Training strategies are often employed to stabilise the hysteretic behaviour of SMA-based components (DesRoches et al. 2004; McCormick et al. 2005; Speicher et al. 2011; Fang et al. 2015; Yam et al. 2022). Throughout the training stage, both the stress level of phase transformation and energy-dissipation capacities were continuously decreased but converged by the end of training. After the training stage, the hysteretic behaviour of the two types of SMA bolt was stabilised, and the residual deformations were mitigated. The NiTiCo bolts, in comparison to the NiTi SMA bolts, demonstrated higher strength but lower energy-dissipation capacities. Additionally, one NiTiCo SMA bolt fractured during the training stage at a maximum strain of 4%, indicating the insufficient cumulative deformation of the material. Additionally, utilising the test data, the hysteretic parameters (shown in Fig. 4.5) in the SMA analytical model based on the Auricchio's approach (Auricchio et al. 1997) were fitted and are presented in Table. 4.1. The comparisons between the analytical model and the test results of the two types of SMA bolts are illustrated in Fig. 4.6. A notable consistency was observed, affirming the accuracy of the analytical model in depicting the cyclic responses of SMA bolts. It's worth mentioning that the Auricchio's approach has been incorporated into the ABAQUS material library and can be adopted to simulate SMA behaviour (ABAQUS version 2022) (see section 4.5).

#### **4.2.2.2 Test of the friction system**

As the main component of the SMA-VFSD, the variable friction system is central to the energy-dissipation capacity of the damper. The criteria for selecting suitable material combinations as friction pairs are that they should exhibit the following

mechanical characteristics: stability and predictability. These characteristics require the friction pairs to maintain a stable friction coefficient under various conditions, such as different temperatures and normal force levels. Additionally, the friction pairs should be able to withstand a certain stress level to resist fracture. After reviewing the literature (Grigorian et al. 1993; Rojas et al. 2005; Clifton 2005), it was recommended to use combinations of different metals with a significant difference in hardness. This combination allows for stable and predictable friction behaviour, with only a slight increase in the friction coefficient as slip accumulates, particularly for the steel-brass combination. Therefore, this metal combination was chosen as the friction pair for the proposed damper. To validate the consistent friction behaviour of the steel-brass friction behaviour under variable normal force levels (due to the wedged contact surfaces) in the SMA-VFSD, cyclic friction tests were conducted in this work. These tests included three normal force levels, corresponding to the contact stresses of friction surfaces at 5 MPa, 10 MPa, and 15 MPa, equivalent to the normal forces of 13.4 kN, 26.8 kN, and 40.3 kN, respectively. Two friction surface conditions (dry and lubricated) were considered. The detailed information on the friction tests is listed in Table. 4.2. The purpose of testing the condition of lubricated friction surfaces was to determine the friction coefficient of the contact areas in the damper that require lubrication for smooth movement, such as the interface between the exterior friction plates and the exterior tube. The test setup and dimensions of the friction plates are shown in Fig. 4.7. Two cap plates were made from the same high-hardness GCr15 steel as the interior friction plates in the SMA-VFSD, and the middle brass friction plate (with slotted holes) was of the same material with the exterior friction plates in the SMA-VFSD. The surfaces of both the cap plates and brass plates were polished to a designated roughness (with a  $R_a$  value in the range of 0.8-1.6  $\mu\text{m}$ ). An M16 high-strength bolt was used to apply the normal

contact force at a designed level. The initial normal force and its fluctuation were monitored by a 50 kN load cell before and throughout the testing. To reduce the normal force loss during testing, disc washers were installed underneath the bolt head and nut. The relative slip of the steel cap plates, and the brass friction plate was measured using two linear variable differential transformers (LVDTs).

Six friction tests, involving four specimens, were conducted using a loading rate of 2.4 mm/min, and 10 cycles were applied for each test with a displacement magnitude of 10 mm. The loading was applied by displacement method. The cyclic curves of the friction force ratio (the friction force of each surface divided by the normal force) with respect to the interfacial slip are given in Figs. 4.8(a)-(d). The average friction force ratio in the positive and negative directions of each loading cycle was taken as the friction coefficient,  $\mu_a$ . The monitored variations of the normal force and friction coefficient with respect to the cumulative slip are depicted in Figs. 4.8(e)-(f). Notably, the normal force of all specimens exhibited negligible fluctuations around their initial values throughout the tests. With the increase of the cumulative friction slip,  $\mu_a$  also fluctuated, and a slight increase was observed during the tests for all specimens. Additionally, it was observed that the value of  $\mu_a$  was not strongly sensitive to changes in the normal force level. Comparatively, F10-2 and F10-3 exhibited slightly greater  $\mu_a$  values than specimen F10-1, which might be attributed to material wears on the friction surfaces, as indicated in Fig. 4.9. Due to the significant difference in hardness between H62 brass and GCr15 steel, the material wears were concentrated on the surfaces of the brass friction plates. However, despite the wear that occurred, the friction performance of the steel and brass combination remained stable and predictable, with only a slight increase in the friction coefficient as the slip accumulated. Based on the measured data, for the dry friction in the steel-brass combination, the average of the test data was

adopted as the design value of  $\mu_1$ , specifically 0.46. In the lubricated friction condition (F10-Lub), the  $\mu_2$  value was approximately one-third of that observed under the dry friction condition.

### 4.2.2.3 Disc spring group test

In the SMA-VFSD tests, each disc spring group consisted of 22-disc springs (i.e., two in parallel as a unit and then 11 units in series), designed to satisfy the self-centring demand of the damper specimens. The disc spring group and the dimension of each disc spring are shown in Fig. 4.10(a). To examine the behaviour of the disc spring group, a cyclic compression-release test was conducted using a three-stage loading protocol, given in Fig. 4.10(b). The first stage employed an incremental loading protocol, aiming at examining the basic hysteretic behaviour of the disc spring group. The disc spring group was subjected to a constant-magnitude loading (with the magnitude equal to the peak displacement in the first stage) in the second stage to examine the stability of the cyclic behaviour at a high load level. Finally, a repeated incremental cyclic loading, consistent with the protocol in the first stage, was applied to assess the repeatability of the cyclic behaviour. The test results of the disc spring group are depicted in Fig. 4.10(c). Throughout the tests, the disc spring group exhibited a typical elastic response with no discernible degradation in strength and stiffness. The test results indicated that the disc springs can be confidently used in the dampers, offering self-centring capacity and reusability within the design range of cyclic deformation. Moreover, based on the test data, the stiffness of the disc spring group can be linearly fitted (refer to Fig. 4.10(c)) at 1.75 kN/mm, a value close to 1.71 kN/mm calculated according to GB/T 1972-2023(Chinese standard (GB/T1972-2023)).

## 4.3 Test of SMA-VFSD

### 4.3.1 Test specimen design

The main variables in the SMA-VFSD test included the preload of the SMA bolts, the material type of the SMA bolts, and the sloping angle of the wedge-shaped friction plates. The fabricated components of the SMA-VFSD specimens are shown in Fig. 4.11. The interior and exterior wedge-shaped friction plates with three different sloping angles (i.e.,  $\theta_a = 7^\circ$ ,  $10^\circ$  and  $13^\circ$ ) were fabricated. It should be mentioned that in the proposed damper, a relatively small sloping angle (e.g.,  $7^\circ$ ) and a large friction coefficient (e.g., 0.46) of the friction pairs can be utilised, which was not recommended by previous studies (Chen et al. 2022; Qiu et al. 2022). However, this constraint is successfully eliminated through the incorporation of the additional disc spring group systems. Thus, the novel configuration of the damper may create more design flexibility in practice. Notably, in the damper test, the maximum sloping angle of the friction pair was set at  $13^\circ$ . This choice was made to control the strain level of the SMA bolts at approximately 3%, ensuring that the bolts can be reused. The dimensions of the main damper components are illustrated in Fig. 4.12. The material and surface conditions of the wedge-shaped friction plates were consistent with those of the friction plates in the friction tests. In the damper test, the surface condition of the friction pairs was dry. The exterior tube, interior core and endplates were made from 38CrMoAl alloys, sized to remain elastic and free of damage during the test. Two M18 grade 8.8 high-strength threaded steel bars were employed for the installation of the disc spring group. The maximum displacement of the damper was designed based on the recoverable deformation capacity of the SMA bolts obtained in section 4.2.2.1. In practical applications, the allowable strain could be determined according to the SMA material

properties. In addition, to ensure the smooth outward movements of the exterior friction plates, their surfaces in contact with the exterior tube were lubricated and the friction coefficient can refer to section 4.2.2.2. A total of eight tests were conducted. Each specimen was assigned a specimen convention. Use specimen DH20V16-NiTi as example, D denoted damper specimen, and H20 and V16 represented that the preloads for disc springs and SMA bolts were 20kN and 16kN, respectively. The appended NiTi was used to show the SMA type (i.e., NiTi SMA and NiTiCo SMA). The information on the test specimens is listed in Table. 4.3. Note that no friction system was installed for specimen DH20, and it was used to examine the hysteretic behaviour of the bare disc spring systems. Specimen DH20V16-NiTi-R was a repeated test of specimen DH20V16-NiTi under a slightly increased loading rate.

### **4.3.2 Test setup and instrumentation**

Following the assembly procedure shown in Fig. 3.2 (Chapter 3), the assembled test specimen was installed in an INSTRON test machine. As depicted in Fig. 4.13, the two ends of the specimen were clamped vertically by the hydraulic wedge-shaped fixtures. A pair of vertical LVDTs (i.e., LVDT1 and LVDT2) was mounted on the specimen to monitor the relative displacement between the two endplates. The average reading from these two LVDTs was recorded as the axial deformation of the damper. Two more LVDTs (i.e., LVDT3 and LVDT4) were used to measure the outward movement of the exterior friction plates. Four donut load cells were employed to monitor the internal loads of the disc spring systems and the SMA bolts. The loading protocol for the damper tests is shown in Fig. 4.13(b), which consists of ten loading cycles with gradually increased displacement amplitudes at five levels (two cycles for each amplitude). The loading rates for the tests were 2.4 or 7.2 mm/min, as summarised

in Table 4.3.

### 4.3.3 General observation of test results

In general, the anticipated working mechanisms were achieved for all test specimens. Once the total preloads (i.e., the sum of the preload of the disc spring groups and the friction force of the friction system) were overcome, a gap between the endplate and the exterior tube gradually developed. As shown in Fig. 4.14(a), the disc springs were always compressed despite the loading direction of the damper (tension or compression), which was consistent with the designed working mechanism (shown in Fig. 3.3). The relative movement of the exterior and interior friction plates can also be visually identified, as shown in Fig. 4.14(b). Upon the removal of the external load, the damper specimens re-centred to their original position, confirming the self-centring behaviour. For specimen DH20V16-13-NiTiCo, the test was terminated during the 9th loading cycle (with a displacement amplitude of 10 mm) due to the sudden fracture of a NiTiCo SMA bolt, as shown in Fig. 4.15. This was attributed to the insufficient cumulative deformation capacity of the NiTiCo material, consistent with the findings in section 4.2.2.1.

### 4.3.4 Cyclic behaviour

Fig. 4.16 depicts the hysteretic responses of all test specimens. The expected trilinear flag-shaped hysteretic curves were observed. Specimen DH20 exhibited a bilinear feature without energy dissipation, confirming that the disc spring group system only provided restoring force. In contrast, for the other specimens, the initial portion of the curves was linear, corresponding to the decompression of the preload in the disc spring system and overcoming of the static friction force in the friction system.

The 1<sup>st</sup> “yielding point” (note that the value is predicted by the proposed analytical model in Chapter 3) in the curves (Figs. 4.16(b)-(g)) corresponded to the stage that the applied load reached the preload of the spring disc system and the friction force. Subsequently, relative sliding between the wedged friction plates occurred. At this stage, the stiffness of the damper degraded compared to the initial loading stage. With a further increase in the damper deformation, the SMA bolt phase transformation was triggered, marking a 2<sup>nd</sup> “yielding point” in the hysteretic curves. The stiffness of the damper was further reduced after the 2<sup>nd</sup> yielding.

Figs. 4.17 (a)-(c) compares the cyclic behaviour of the test specimens with different design parameters. It can be seen from Fig. 4.17(a) that increasing the preload of the SMA bolts can slightly widen the damper hysteresis and enhance the energy-dissipation capacity. Fig. 4.17(b) shows that the strength and energy-dissipation capacities remarkably enhanced with the increase of the sloping angle of the friction plates (7°, 10° and 13°). However, a larger sloping angle also led to a greater deformation demand for the SMA bolts subjected to the same damper deformation. As an illustration, Fig. 4.18 shows the relationships between the axial elongation of the SMA bolts (measured by the outward movement of the exterior friction plates) and the axial displacement of the damper. The figure shows that the specimen with a larger sloping angle of the friction plates experienced greater axial elongation of the SMA bolts for the same axial displacement of the damper. Therefore, Fig. 4.18 demonstrates that the deformation demand on the SMA bolts depended on the sloping angle of the friction plates. Fig. 4.17(c) compares the specimens with different SMA bolt material types (i.e., NiTi and NiTiCo). It can be seen that specimen with NiTiCo SMA bolts exhibited higher strength and energy-dissipation capacities than that of the one with NiTi SMA bolts. The improved performance of the damper was attributed to the higher

load capacity of the NiTiCo SMA bolts and a resulting enhanced friction force. In addition, a more obvious multistage energy-dissipation hysteretic behaviour was observed for the damper equipped with NiTiCo SMA bolts. This was because the transformation stress of the NiTiCo SMA bolts was higher than that of the NiTi SMA bolts (shown in Fig. 4.4), leading to a larger interval between the 1<sup>st</sup> (corresponding to initial sliding) and 2<sup>nd</sup> (corresponding to phase transformation) yielding points. Fig. 4.17(d) examines the results of specimen DH20V16-NiTi in two tests with different loading rates (2.4 mm/min versus 7.2 mm/min). The similarity of the hysteretic curves demonstrated the consistent performance of the damper with the reuse of the friction system under different loading rates. In general, the conducted tests confirmed that the proposed damper can achieve excellent self-centring behaviour, reliable energy-dissipation capacity, and the expected multistage energy dissipation mechanism.

### 4.3.5 Hysteretic characteristics

The strength, stiffness, and other parameters characterising the hysteretic behaviour of the test specimens are listed in Table 4.4, and their symbols are provided in Fig. 4.19. With the decrease of the preload in the SMA bolts,  $F_{res}$ , and  $\zeta$  increased obviously, while the other parameters remained relatively unchanged except for slight decreases in  $F_y$  and  $\beta$ . Especially,  $\beta$  for specimen DH20V8-10-NiTiCo was smaller than that of the other specimens. This can be explained by the fact that the decreased preload of the SMA bolts resulted in a smaller 1<sup>st</sup> yielding force  $F_y$  and a larger residual strength  $F_{res}$ , which, according to the equation (i.e.,  $\beta = 1 - F_{res}/F_y$ ), led to a noticeable reduction in  $\beta$ . As shown in the table, when comparing specimens DH20V16-7-NiTi, DH20V16-10-NiTi and DH20V16-13-NiTi, it was found that the strength-related and stiffness-related parameters (i.e.,  $F_y$ ,  $F_p$ ,  $F_{res}$  and  $\alpha_1 k$ ) gradually increased with the increase of

the sloping angle of the wedged friction plates. An opposite trend was observed for the energy-dissipation sequence,  $\zeta$ , indicating an earlier occurrence of the SMA bolt phase transformation when a greater sloping angle of the friction plates was employed. In addition, the 2<sup>nd</sup> unloading stiffness seemed not to be sensitive to the sloping angle of the friction plates. By employing NiTiCo SMA bolts instead of NiTi bolts, the energy-dissipation sequence,  $\zeta$ , and  $F_p$  were remarkably increased, while the 2<sup>nd</sup> unloading stiffness was decreased obviously (i.e., the value fluctuated from around 2 kN/mm to around 1 kN/mm). The remaining parameters were not essentially influenced by the SMA bolt type. Based on the above discussions, it is evident that the damper possesses an adjustable hysteretic parameter known as the energy-dissipation sequence (denoted as  $\zeta$ ). Moreover, previous research has substantiated that  $\zeta$  can be effectively employed to modulate structural energy demands and optimise structural performance, such as mitigating high-mode effects in structures (Qiu and Zhu 2017; Ke et al. 2023a). For all specimens, the measured 1<sup>st</sup> unloading stiffness was approximately equal to the initial stiffness, which was consistent with the theoretical expectation. Additionally, the hysteretic parameters obtained from the repeated tests of specimen DH20V16-10-NiTi were basically consistent, indicating that the damper could provide a consistent performance after experiencing earthquake excitations.

### 4.3.6 Energy-dissipation capacity

The energy-dissipation capacity of the specimens can be quantified by the absolute cumulative energy consumption  $W_d$  and the equivalent viscous damping ( $\xi$ ) per cycle.  $\xi$  is a dimensionless index, as shown in Fig. 4.20, and can be calculated by:

$$\xi = \frac{W_d}{4\pi W_e} \quad (4.1)$$

where  $W_e$  = the energy absorbed by the corresponding linear elastic system, and  $W_d$  =

the covered area of the hysteretic loop at certain deformation level. The calculated cumulative  $W_d$  and  $\zeta$  of the specimens and their comparisons are depicted in Fig. 4.21 and Fig. 4.22, respectively. Fig. 4.22(a) shows the influence of the preload of the SMA bolts on the cumulated  $W_d$ . It was found that the increased preload of the SMA bolts can improve the energy-dissipation capacity of the damper. As shown in Fig. 4.22(b), the cumulated  $W_d$  increased with the increase of the sloping angle of the friction plates. Fig. 4.22(c) illustrates that the use of NiTiCo SMA bolts instead of NiTi bolts can significantly enhance the energy-dissipation capacity. This enhancement can be attributed to the larger transformation stress and elastic modulus of the NiTiCo SMA bolts compared to the NiTi ones. Consequently, the friction system equipped with these SMA bolts widens its hysteresis, as echoed in Fig. 4.17(c). Additionally, the repeated tests on specimen DH20V16-10-NiTi demonstrated comparable amount of dissipated energy, suggesting the reliable energy-dissipation capacity of the damper under sequent excitations. It is worthy to note that the  $\zeta$  of the test specimens fluctuated only slightly over the loading history, indicating that the proposed damper can offer a consistent energy-dissipation capacity under different levels of deformation. The measured average  $\zeta$  of the test specimens ranged from 16%-20%, approximately half of the conventional buckling restrained braces (BRBs).

#### **4.4 Analytical validation and parametric study**

As explained in Chapter 3, the elastic deformation of each damper component is considered in the developed analytical model for the SMA-VFSD. However, accurately predicting the resulting initial stiffness of the damper poses a challenge. Previous investigations have revealed that various uncertainties, such as fabrication errors and stress concentrations at contact interfaces, resulted in difficulties in providing precise

design predictions for initial stiffness (Zhang et al. 2023b; Chen et al. 2023). In this study, an empirical value (i.e.,  $k = 457$  kN/mm) was used for the initial stiffness of the damper based on the measured average value from the damper tests. Figs. 4.16(a)-(g) illustrate the comparisons between the hysteretic curves obtained by the analytical model and the test measurements for each specimen. The comparisons of the cumulative  $W_d$  and  $\zeta$  of the tests and analytical predictions are shown in Figs. 4.21(a)-(f). Furthermore, the comparisons of the hysteretic curves for the constituent systems of specimen DH20V16-10-NiTiCo, namely the friction system and disc spring systems, are depicted in Fig. 4.23. For each specimen, the developed analytical model can well predict their hysteretic curves and corresponding cumulative energy dissipation and  $\zeta$ . Additionally, use specimen DH20V16-10-NiTiCo as example, the analytical model also can trace the cyclic behaviour of the constituent systems of the damper. Based on the above discussions, the proposed analytical prediction model in Chapter 3 can reliably and accurately trace the damper behaviour, including the shape of the hysteretic curve and the energy-dissipation capacity as well as the behaviour of its constituent systems. The validated analytical model can conveniently guide engineers in determining the mechanical parameters of the developed SMA-VFSD for structural design.

Building upon the validated analytical model, further exploration was conducted to investigate the effects of an extended range of design parameters on damper behaviour. Taking the design parameters of specimen DH20V16-10-NiTiCo as a base control, the considered parameter matrix included: 1) SMA bolt diameter (6 mm, 10 mm and 12 mm); 2)  $\sigma_{Ms}$  of the SMA bolts (300 MPa, 500 MPa and 600 MPa); 3) SMA bolt preload (8 kN, 24 kN, 32 kN ); 4) SMA bolt length ( $l_{SMA} = 88$  mm 188 mm and 238 mm); 5) preload of the disc spring systems (5 kN, 10 kN, 40 kN); 6) stiffness of

the disc spring system ( $0.5k_{DSS}$ ,  $1.5 k_{DSS}$  and  $2k_{DSS}$ , note the  $k_{DSS}$  was the value in the current damper specimen ); 7) friction coefficient ( $\mu_1 = 0.2, 0.3$  and  $0.6$ ); and 8) sloping angle ( $\theta_a = 4^\circ, 7^\circ, 13^\circ$ ). The label and detailed information of each design parameter combination are listed in Table. 4.5.

Figs. 4.24(a)-(d) compare the cyclic responses of the damper with variations in the SMA bolt-related parameters. According to Fig. 4.24(a), increasing the diameter of the SMA bolts enhanced the damper's load-carrying capacities and energy dissipation. However, improper matching with the restoring capacity provided by the disc spring systems may lead to self-locking issues. Elevating the  $\sigma_{Ms}$  of the SMA bolts widened the interval between the two yielding points and enhanced both energy dissipation and load-carrying capacities to a certain extent (Fig. 4.24(b)). Fig. 4.24(c) shows the effect of the SMA bolt preload on damper performance. Increasing the preload of the SMA bolts markedly increased the 1<sup>st</sup> yielding strength, but at the expense of reducing the interval between the two yielding points. Additionally, employing the longer SMA bolts effectively enlarged the interval between the two yielding points, despite a slight sacrifice in the damper's strength and energy dissipation capacities. Figs. 4.24(e)-(f) examine the cyclic responses of the damper with variations in the disc-spring-group-related parameters. The disc spring systems fine-tuned the damper performance by adjusting the initial preload and stiffness. This ensured the necessary strength and self-centring behaviour for the damper. An inadequate preload force and stiffness in the disc spring systems may result in unsatisfactory self-centring performance and the potential risk of self-locking during unloading (Figs. 4.24(e)-(f)), respectively. It should be mentioned that a higher the disc spring systems stiffness can cause the overstrength to the damper. According to Figs. 4.24(g)-(h)), increasing either the friction coefficient or the sloping angle of the friction system can significantly enhance the damper's load-

carrying capacities and energy dissipation. Increasing the former had no effect on the interval between the two yielding points, while increasing the latter significantly reduced the interval between the two yielding points. As highlighted in section 4.3.5, the energy-dissipation sequence quantifying the interval between the two yielding points serves as a crucial hysteretic parameter for modulating damper performance in multi-performance-based designs, thus making its adjustability highly desirable. In general, the extended parametric study suggested that the damper performance is highly dependent on the combination of various design parameters. Therefore, the target damper demand under different levels of excitations can be flexibly realised by different combinations of the above design parameters.

## **4.5 Numerical analyses of SMA-VFSD**

For the SMA-VFSD, the exterior tube obstructs a clear visual inspection of the internal operational state during testing. To fully comprehend the working principles and movement mechanisms of the damper under loads, a refined numerical model was developed using professional software (ABAQUS, version 2022). Comparisons of the working principles and cyclic behaviour of the damper between the refined numerical model and the test data are provided in section 4.5.1. However, developing a refined numerical model can be time-consuming and may encounter convergence issues, rendering it unsuitable for structural analyses at the system level. Therefore, a simplified modelling technique, efficiently tracing the damper behaviour, should be developed, and can be employed in subsequent structural-level analyses. This approach is given in section 4.5.2 in this chapter.

### **4.5.1 Refined numerical analysis of SMA-VFSD**

#### 4.5.1.1 Establishment of refined numerical model

The refined numerical model for the SMA-VFSD is depicted in Fig. 4.25. All the parts of the damper were meshed using solid elements (i.e., C3D8 elements), except for the disc spring systems. The disc spring systems exhibit complex contact nonlinearity during the compression-tension transition of the SMA-VFSD, which can lead to convergence issues. Recalling the observed elastic and predicted hysteretic behaviour for the disc spring systems, a simplified spring model featuring a linear elastic behaviour (shown in Fig. 4.25) was employed to describe the hysteretic response of the disc spring systems. These springs were fixed at the bolt holes of the two endplates by multi-point constraints (MPC). The geometric and material properties of the refined numerical model were determined according to the conducted test programme. For the steel and brass materials, a kinematic hardening rule with a 0.02 post-yielding stiffness ratio was used. Auricchio's model, integrated into ABAQUS was utilised for modelling the material behaviour of the SMA bolts, and its validation can be found in section 4.2.2.1. Surface-to-surface contacts were used to simulate the friction behaviour of all contact interfaces, with hard contact and penalty functions employed for the normal and tangential behaviour of all contact pairs. The corresponding friction coefficients (both dry and lubricated) can be found in section 4.2.2.2 for reference. To facilitate the convergence of the developed numerical model, the mesh size of the master and slave surfaces was controlled even, with the former (i.e., master surfaces) slightly larger than the latter (i.e., slave surfaces). To simulate the boundary conditions of the test specimens, multi-point constraints (MPCs) were used to couple all degrees of freedom of the clamped areas (i.e., those gripped by the wedge-shaped fixture of INSTRON machine) of the test specimens into two reference points. One reference point was fixed, while cyclic loads were applied to the other reference point. To ensure convergence at

the beginning of the analysis, the preloads of the SMA bolts and disc spring group systems were applied in two stages. Initially, a small magnitude of preloads was applied to establish contact between all potential interfaces, and subsequently, the remaining preloads was applied to achieve the target values.

#### **4.5.1.2 Numerical results**

To visualise the internal sliding mechanisms of the SMA-VFSD, Fig. 4.26 depicts the deformation states at the maximum displacement amplitudes for specimen DH20V16-10-NiTiCo. The observed deformation modes were consistent with the expectations presented in Fig. 3.3. Whether under tension or compression, a gap gradually formed between the endplate (either endplate-1 or endplate-2) and the exterior tube as the loading stages increased. The relative movement between the friction pairs, as shown in Fig. 4.26, resulted in the outward movement of the exterior friction plates. This outward movement elongated the SMA bolts, significantly increasing their internal force, which was in line with the theoretical expectation. Additionally, when unloaded, the damper was observed to recentre to its initial position. To verify that the main damper components remained elastic during the test, Fig. 4.27 illustrates the stress contour of each damper component under peak loading displacement amplitude (using tension as an example). While a relatively higher stress level was detected at some localised areas due to stress concentration caused by stiffness change or direct contact, overall speaking, a relatively low stress level was observed for these components. This suggests that all the damper components (except for the SMA bolts) remained undamaged during the test and can be tested repeatedly. For the SMA bolts, although a high stress level was detected, their strain can be recoverable, thus the resilience of the damper was not affected.

To validate the accuracy of the refined numerical model in tracing the hysteretic behaviour of the damper, the hysteretic curves between the numerical results and test data for specimen DH20V16-13-NiTiCo and its constituent systems is also compared in Fig. 4.23. Good agreement was observed at both the damper and its constituent system levels, confirming the reliability of the adopted refined numerical modelling techniques in reproducing the damper behaviour. Additional comparisons between the numerical results and the test data for the other specimens are presented in Fig. 4.28, demonstrating the reliability and applicability of the modelling approach for dampers with various design parameter combinations.

#### **4.5.2 Simplified numerical analysis of SMA-VFSD**

As discussed in the previous section, although the refined numerical model can accurately predict the hysteretic behaviour and sliding working mechanism of the damper, its high computational cost and potential convergence issues may compromise the computational efficiency. In addition, the process of establishing the refined model for the damper is time-consuming and may not be suitable for structural-level analyses in subsequent research. Therefore, an efficient and simplified model needs to be developed to predict the damper behaviour.

Based on the proposed analytical model given in Chapter 3, a new material or element for describing damper behaviour was developed within a mature software platform. OpenSees (Open System for Earthquake Engineering Simulation) is an open-source software framework for simulating the behaviour of structures subjected to earthquakes and other dynamic loads. It provides a platform for performing advanced finite element analysis (FEA) and has been widely used in earthquake engineering, structural dynamics, and other related fields. One of the key features of OpenSees is its

extensibility, allowing users to customise and enhance the software to suit their specific needs. The software framework is shown in Fig. 4.29. In this research, the C++ language was utilised to develop a new uniaxial material named multi-general self-centring (MGSC) material, which adhered to the proposed analytical guidelines for the damper. The input parameters and the implications of the MGSC material in OpneSees are shown in Fig. 4.30 and the source codes for the MGSC material are provided in the Appendix. It should be noted that all the material input parameters should be determined based on the test data or theoretical predictions. Based on the above discussions, a force-based beam-column element assigned with a fibre section which is defined by the developed MGSC material can be employed to simulate the damper behaviour.

To demonstrate the effectiveness of the newly developed material in predicting the damper behaviour, a simplified model was established in OpenSees. Specifically, a damper-length force-based beam-column element was assigned with a fibre section with MGSC material to represent the damper. The displacement load was applied at Node 2. Detailed information on the simplified model is provided in Fig. 4.31. Fig. 4.32 compares the hysteretic curves between the simplified model and the test data for all specimens. Good comparison was observed, demonstrating that the simplified model accurately captures the damper behaviour. Note that, the calculation only takes several seconds for each specimen, compared to several hours using the refined model in ABAQUS.

In addition, to compare the above-mentioned methods for predicting the damper behaviour, Fig. 4.33 illustrates the comparisons of the hysteretic curves predicted by the analytical model, the ABAQUS model and the OpenSees model to the test data for specimen DH20V16-10-NiTiCo. It can be seen that all the proposed methods were able

to predict the damper behaviour. It is worth noting that the simplified numerical analysis using the OpenSees can enable the assessment of the seismic performance of structures equipped with the damper, which is discussed in next two chapters in details.

#### **4.6 In summary**

This chapter experimentally and numerically investigated the cyclic performance of the proposed SMA-VFSD. The test programme was systematically conducted, covering material, constituent component, and damper levels. At the constituent component level, the hysteretic behaviour of the SMA bolts, friction pairs, and disc spring groups was examined. Subsequently, six SMA-VFSD test specimens underwent quasi-cyclic testing, and the obtained data was compared with the analytical predictions. To enhance the comprehension of the damper's performance, a refined numerical model was developed and validated using the test data. Furthermore, to enable the seismic performance evaluation of structures equipped with the SMA-VFSD, a new uniaxial material, named MGSC material, was developed and incorporated into the material library of OpenSees. Using this newly added MGSC material, a simplified damper model was proposed and validated against the test results. The main findings were summarised as below:

- After training, both NiTi SMA and NiTiCo SMA demonstrated stable hysteretic behaviour with minimal residual deformation but lower energy dissipation. Additionally, trinary SMA bolts exhibited greater strength compared to binary SMA bolts, albeit at the potential expense of deformability.
- The friction behaviour of the steel (GCr15)-brass(H62) friction pair under three normal force levels was consistent, confirming the reliable and predictable performance of the friction pair under varying normal forces.

- The mechanical behaviour of the tested dampers was consistent with the conceptual design. Furthermore, the decoupled relationship of design parameters was confirmed.
- The tested SMA-VFSD demonstrated a multistage energy-dissipation mechanism and exhibited a trilinear flag-shaped hysteretic curves. The key hysteretic parameters of the damper can be flexibly adjusted by varying the design parameters, such as preloads of disc spring systems and SMA bolts, SMA bolt type and sloping angle of friction plates.
- The hysteretic behaviour of the SMA-VFSD was basically not influenced by the loading history and loading rate, indicating that the proposed damper has stable and reliable performance.
- The SMA-VFSD demonstrated a full self-centring behaviour and good energy-dissipation capacity. The test results showed that equivalent viscous damping (EVD) of the specimens was around 16%-20% and remained consistent in all loading stages.
- The prediction of the developed analytical model agreed well with the experimental results. Therefore, the analytical model can be used to reliably determine the demands of the damper components in the design process.
- The refined numerical model accurately replicated the damper's behaviour, encompassing deformation modes and hysteretic responses. The refined mode can be utilised to optimise the damper configurations in their structural applications for engineers.
- The effectiveness of the simplified damper model in predicting damper behaviour was validated, which can offer a highly efficient tool for subsequent structural analyses.

Table. 4.1 Material constants for tested SMA bolts

Material Constants	NiTi SMA	NiTiCo SMA
Forward transformation stress in tension, $\sigma_{Ms}$ (MPa)	200	400
Forward transformation stress in tension, $\sigma_{Mf}$ (MPa)	820	920
Reverse transformation stress in tension, $\sigma_{As}$ (MPa)	410	750
Reverse transformation stress in tension, $\sigma_{Af}$ (MPa)	100	140
Poisson ratio at austenite state, $\nu_A$	0.33	0.33
Poisson ratio at martensite state, $\nu_M$	0.33	0.33
Maximum transformation strain, $\epsilon_L$	0.025	0.013
Austenite modulus of elasticity, $E_A$ (GPa)	35	40
Martensite modulus of elasticity, $E_M$ (GPa)	20	27

Table. 4.2 Information on friction tests

Test label	Specimen	Normal stress level (unit: MPa)	Surface condition	Loading rate (unit: mm/min)
F5	F5	5	Dry	
F10-1	F10	10	Dry	
F10-2	F10	10	Dry	2.4
F10-3	F10	10	Dry	
F10-Lub	F10-Lub	10	Lubricated	
F15	F15	15	Dry	

Table. 4.3 Specimen details

Specimens	Sloping angle( $\theta$ )	SMA type	Preload of SMA bolts(kN)	Preload of disc spring system(kN)	Loading rate(mm/min)
DH20	-	-	-		
DH20V16-7-NiTi	7				2.4
DH20V16-10-NiTi	10	NiTi	16		
DH20V16-13-NiTi	13				
DH20V16-13-NiTi-R	13			20	7.2
DH20V8-10-NiTiCo	10		8		
DH20V16-10-NiTiCo	10	NiTiCo	16		2.4
DH20V16-13-NiTiCo	13				

Table. 4.4 Hysterical characteristics of the specimens

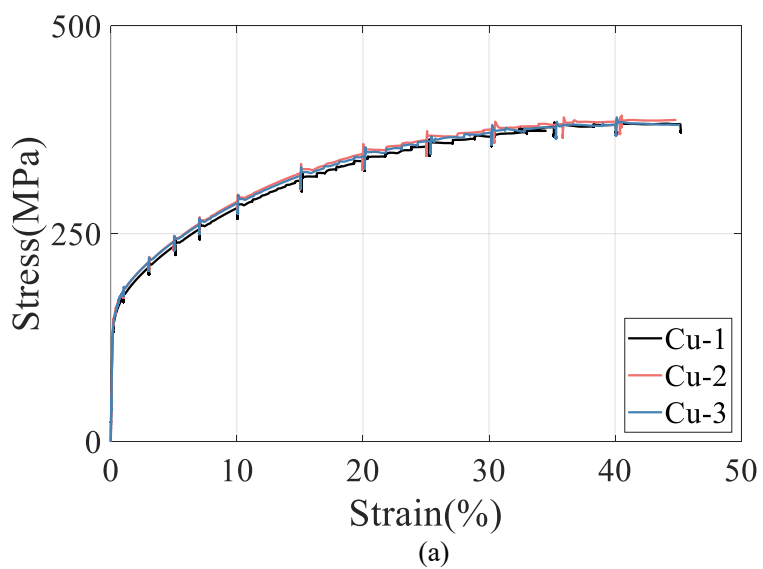
Specimen	$F_y$ (kN)	$F_p$ (kN)	$F_{res}$ (kN)	$k$ (kN/mm)	1 <sup>st</sup> post-yielding stiffness, $\alpha_1 k$ , (kN/mm)	2 <sup>nd</sup> post-yielding stiffness, $\alpha_2 k$ , (kN/mm)	1 <sup>st</sup> unloading stiffness, $\alpha_3 k$ , (kN/mm)	2 <sup>nd</sup> unloading stiffness, $\alpha_4 k$ , (kN/mm)	$\beta = 1 - F_{res}/F_y$	$\zeta = \delta_p / \delta_y$
DH20	21.3	-	-	420.2	3.5	-	-	-	-	-
DH20V16-7-NiTi	27.6	44.7	10.6	447.3	11.4	5.5	449.7	2.2	0.62	19.7
DH20V16-10-NiTi	31.1	48.4	13.6	477.7	15.8	7.9	441.1	1.9	0.56	14.8
DH20V16-13-NiTi	46.1	60.8	14.9	460.2	21.8	9.3	453.3	2.2	0.68	7.7
DH20V16-13-NiTi- R	44.2	58.4	15.1	452.1	20.1	9.1	438.2	2.3	0.66	8.1
DH20V8-10-NiTiCo	29.1	91.6	17.2	487.4	16.7	7.7	453.9	0.7	0.41	63.8
DH20V16-10- NiTiCo	40.2	91.5	13.1	472.1	16.9	7.6	451.8	1.1	0.67	36.6
DH20V16-13- NiTiCo	44.1	100.1	15.2	471.3	23.1	9.6	436.7	1.3	0.66	26.9

Table. 4.5. Information on each combination of design parameters

Label	SMA bolt diameter (mm)	$\sigma_{Ms}$	SMA bolt preload (kN)	SMA bolt length (mm)	Preload of disc spring system (kN)	Stiffness of disc spring system (kN/mm)	$\mu$	$\theta$
Base control	8	400	16	138	20	3.5	0.45	10
BC-D6	6	400	16	138	20	3.5	0.45	10
BC-D10	10	400	16	138	20	3.5	0.45	10
BC-D12	12	400	16	138	20	3.5	0.45	10
BC- $\sigma_{Ms}$ -300	8	300	16	138	20	3.5	0.45	10
BC- $\sigma_{Ms}$ -500	8	500	16	138	20	3.5	0.45	10
BC- $\sigma_{Ms}$ -600	8	600	16	138	20	3.5	0.45	10
BC-SMA-PL8	8	400	8	138	20	3.5	0.45	10
BC-SMA-PL24	8	400	24	138	20	3.5	0.45	10
BC-SMA-PI32	8	400	32	138	20	3.5	0.45	10
BC-SMA-Len88	8	400	16	88	20	3.5	0.45	10
BC-SMA- Len188	8	400	16	188	20	3.5	0.45	10
BC-SMA- Len238	8	400	16	238	20	3.5	0.45	10
BC-Disc-PI5	8	400	16	138	5	3.5	0.45	10
BC-Disc-PI10	8	400	16	138	10	3.5	0.45	10
BC-Disc-PI40	8	400	16	138	40	3.5	0.45	10
BC-Disc-S1.8	8	400	16	138	20	1.8	0.45	10
BC-Disc-S5.6	8	400	16	138	20	5.6	0.45	10
BC-Disc-S7.5	8	400	16	138	20	7.5	0.45	10
BC- $\mu$ -0.2	8	400	16	138	20	3.5	0.2	10
BC- $\mu$ -0.3	8	400	16	138	20	3.5	0.3	10
BC- $\mu$ -0.6	8	400	16	138	20	3.5	0.6	10
BC- $\theta$ -4	8	400	16	138	20	3.5	0.45	4
BC- $\theta$ -7	8	400	16	138	20	3.5	0.45	7
BC- $\theta$ -13	8	400	16	138	20	3.5	0.45	13



Fig. 4.1 Material coupons before and after tests



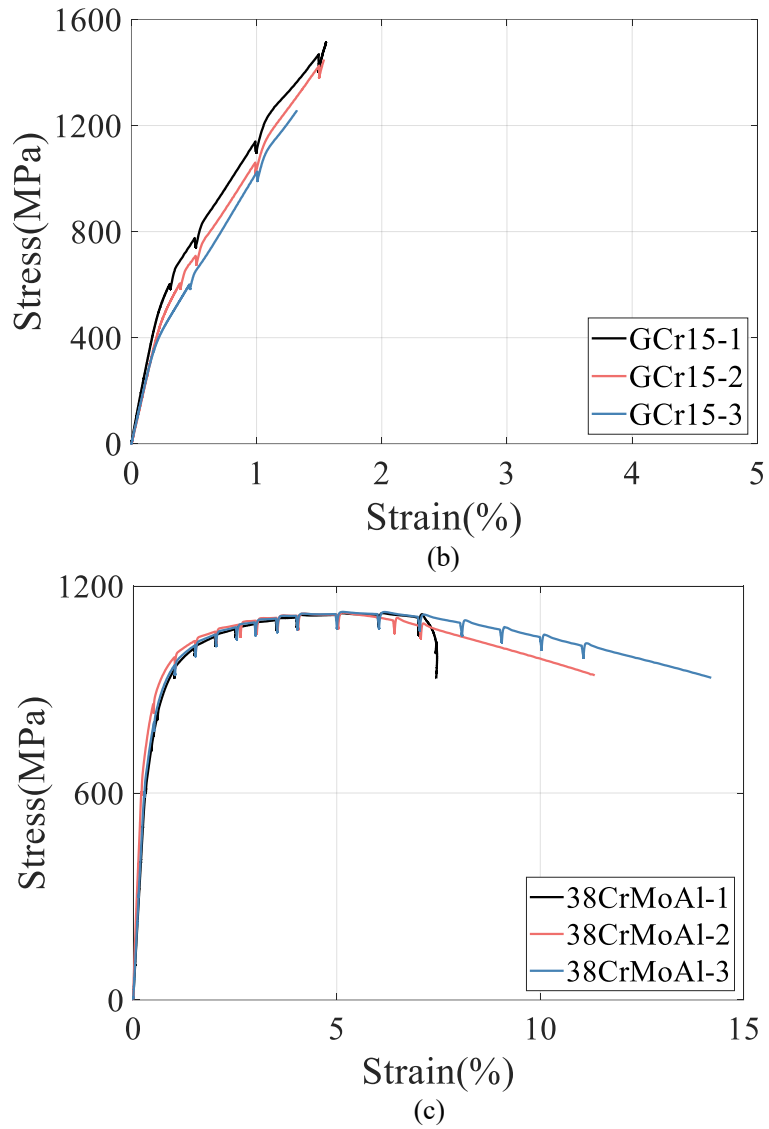


Fig. 4.2 Test results of coupon tests: (a) Cu, (b) GCr15; and (c) 38CrMoAl

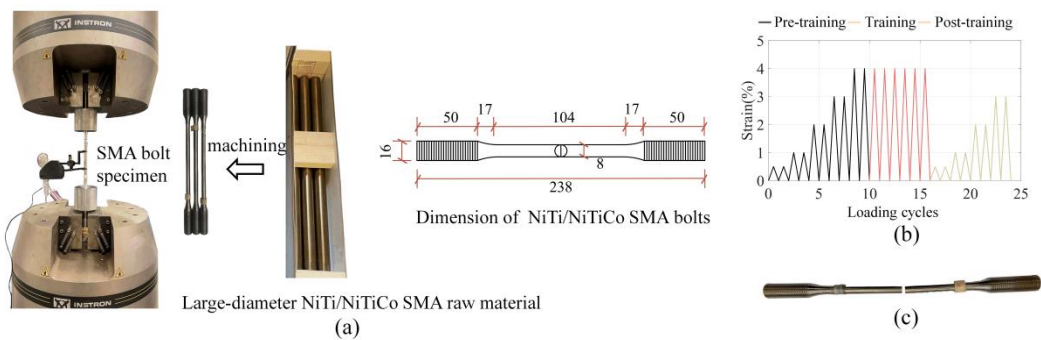


Fig. 4.3 Test of SMA bolts: (a) test setup and SMA bolt dimension, (b) loading protocol, and (c) fracture of a NiTiCo SMA bolt

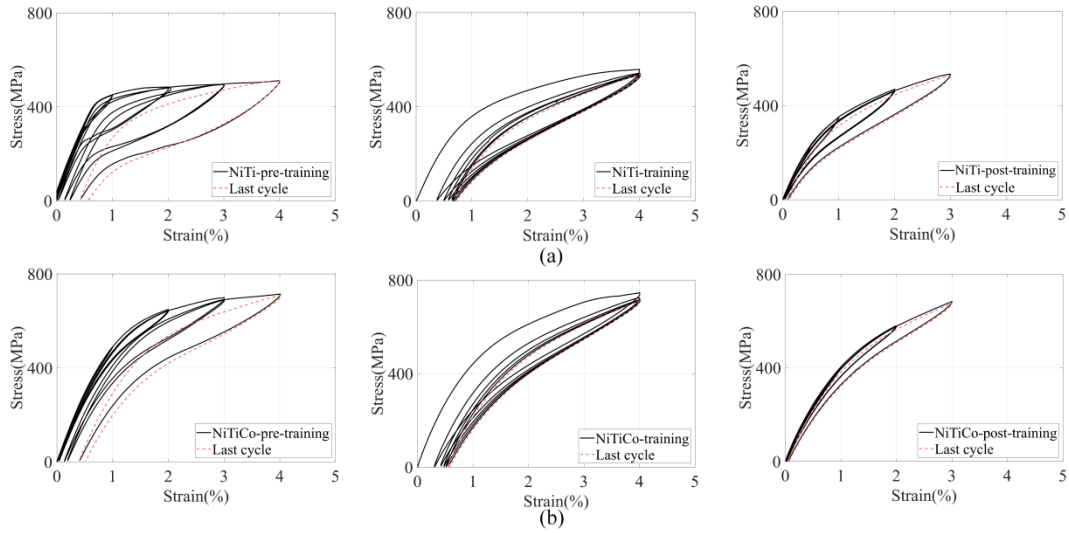


Fig. 4.4 Typical test results of NiTi/NiTiCo SMA bolts: (a) NiTi SMA bolt, and (b) NiTiCo SMA bolt

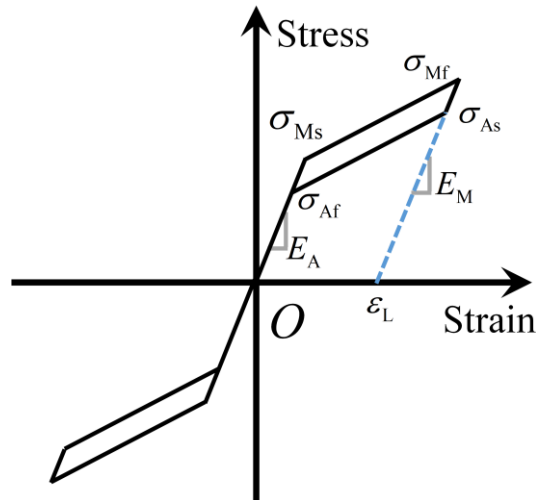
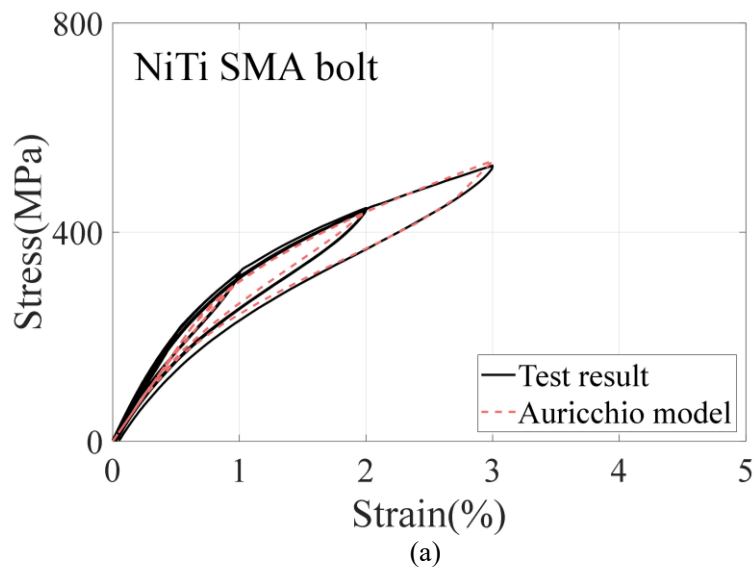


Fig. 4.5 Hysteretic parameters for SMA bolts





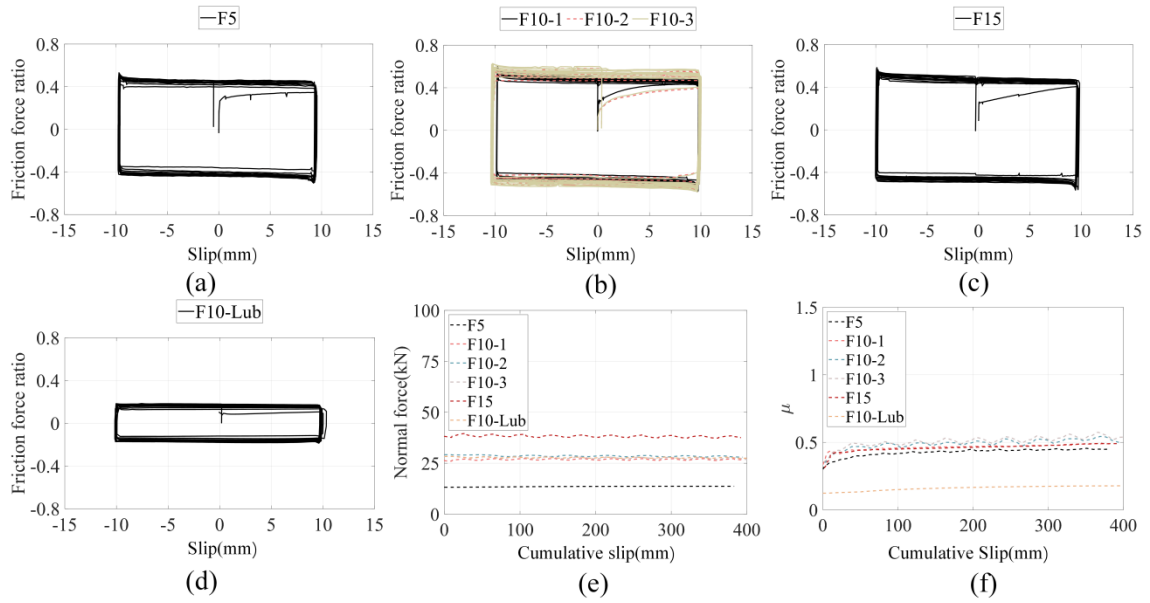


Fig. 4.8 Results of friction tests: (a) F5, (b) comparison results of repeated tests of F10, (c) F15, (d) F10-Lub, (e) normal force variation pattern, and (f) friction force variation pattern



Fig. 4.9 Surface wears after friction tests

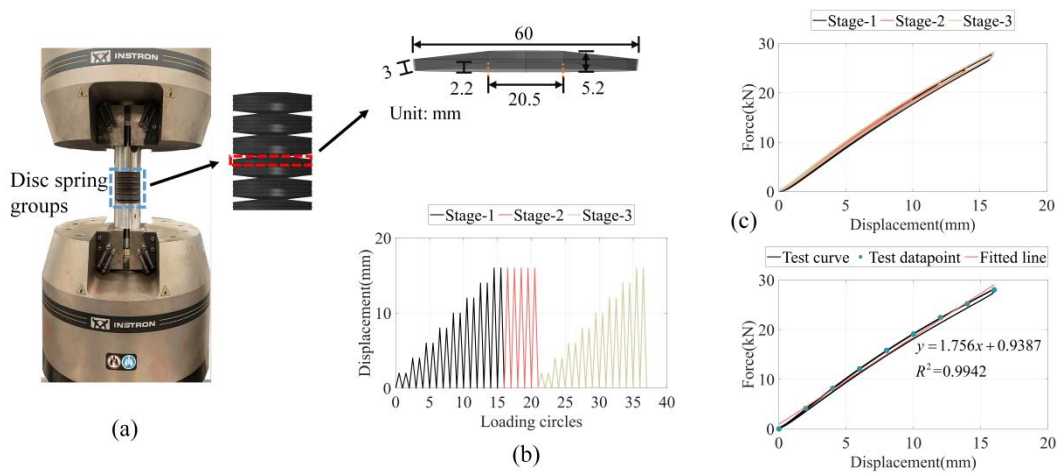


Fig. 4.10. Test of disc spring groups: (a) test setup and disc spring dimension, (b) loading protocol, and (c) test results

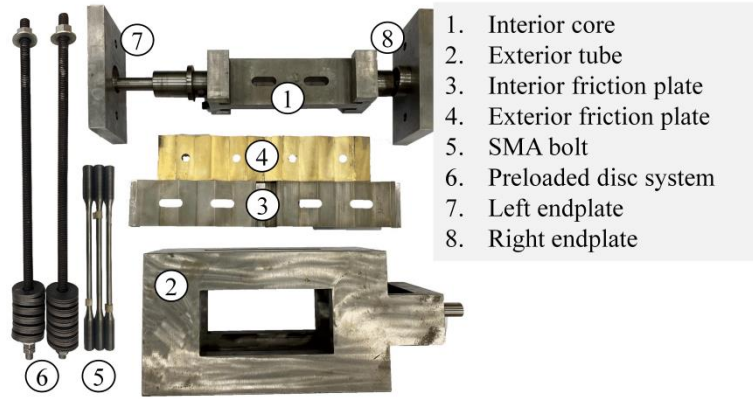


Fig. 4.11 Fabricated components of SMA-VFSD

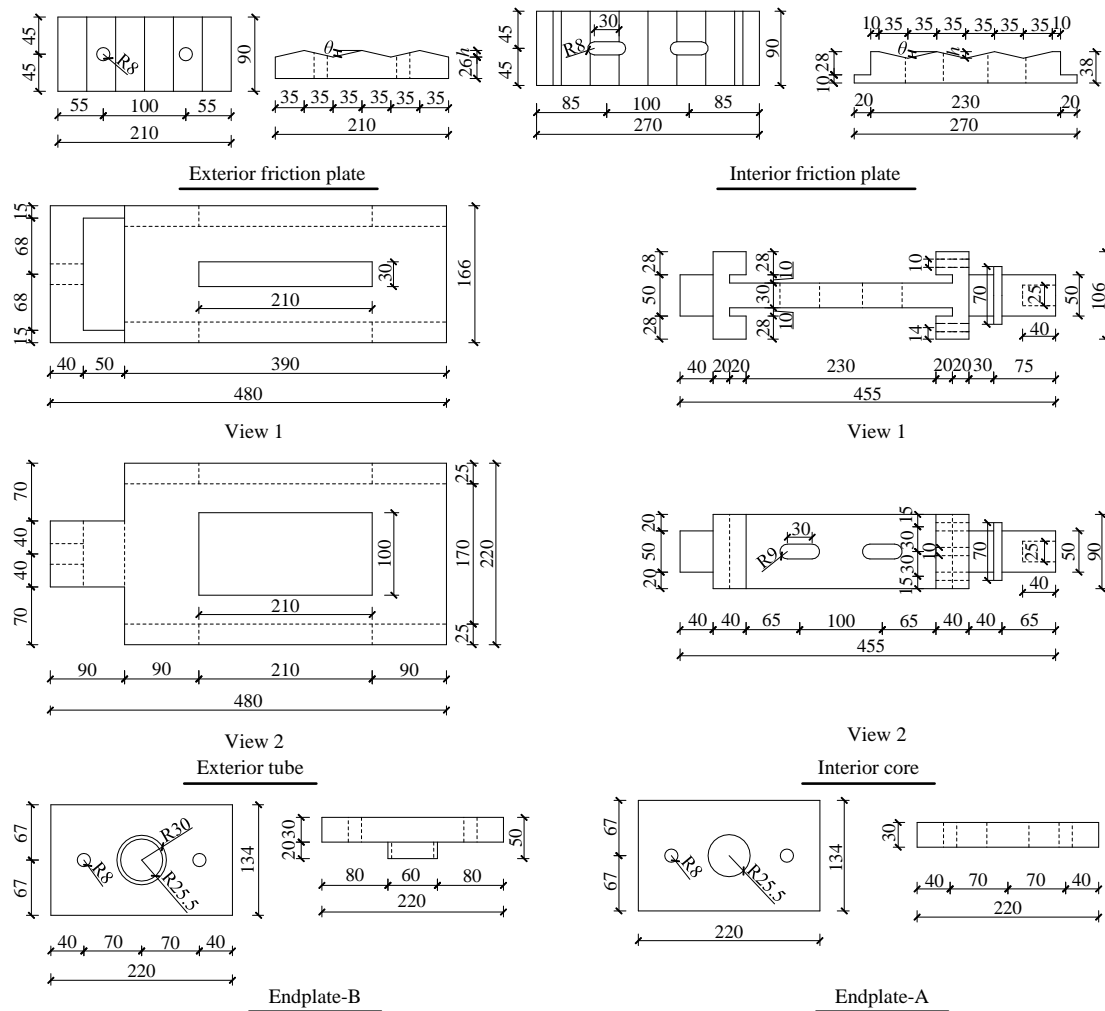


Fig. 4.12 Dimensions of the damper components

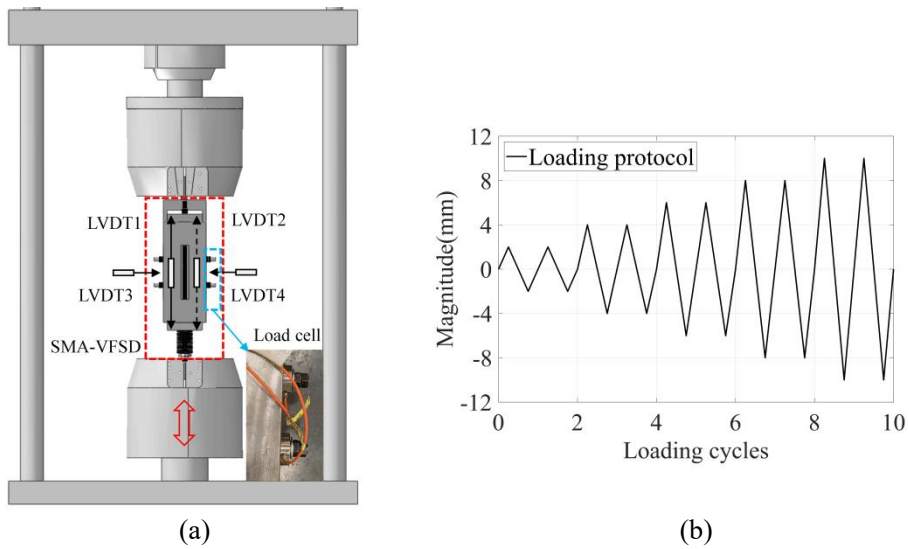


Fig. 4.13 Test of SMA-VFSD: (a) test arrangement, and (b) loading protocol

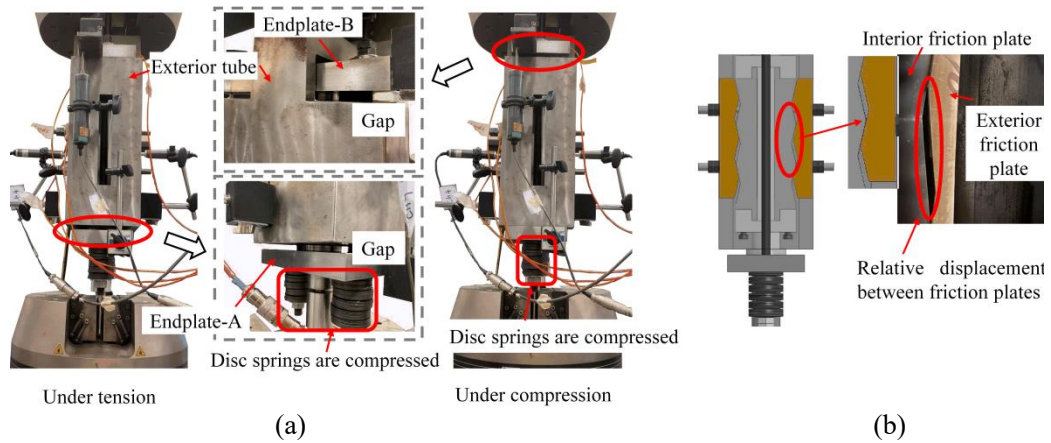


Fig. 4.14 Test phenomenon of SMA-VFSD test: (a) compressed disc spring group, and (b) relative movement of exterior/interior friction plates

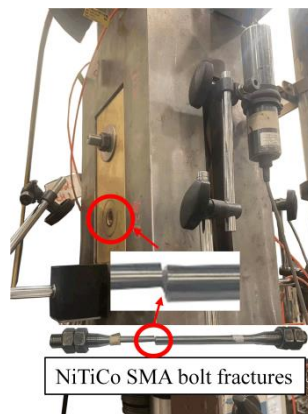
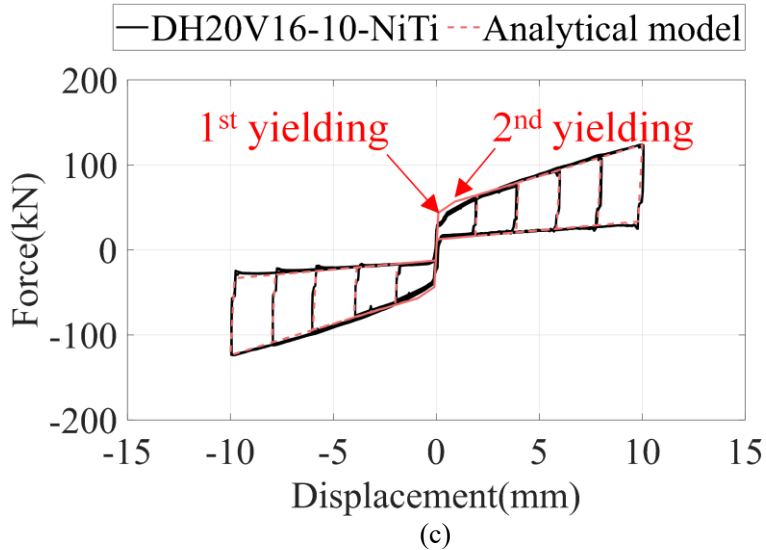
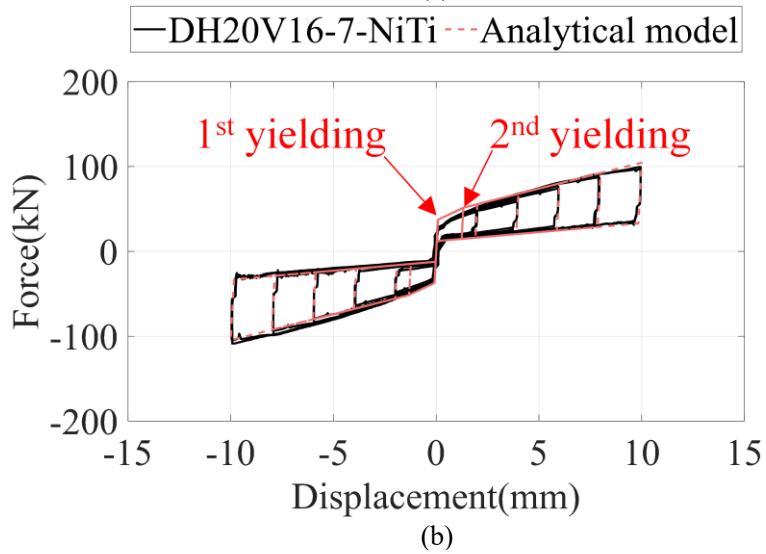
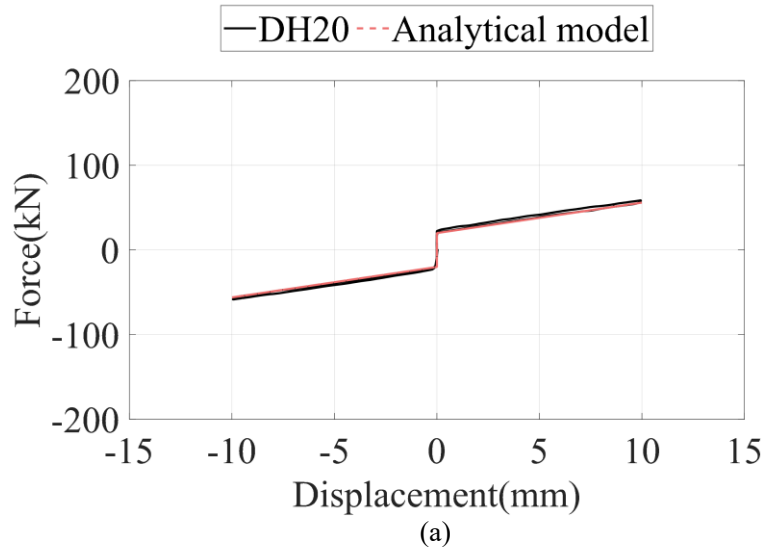
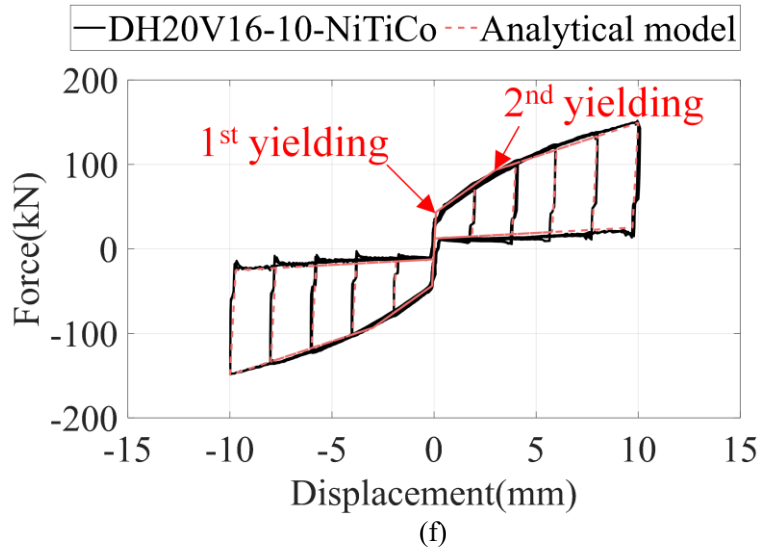
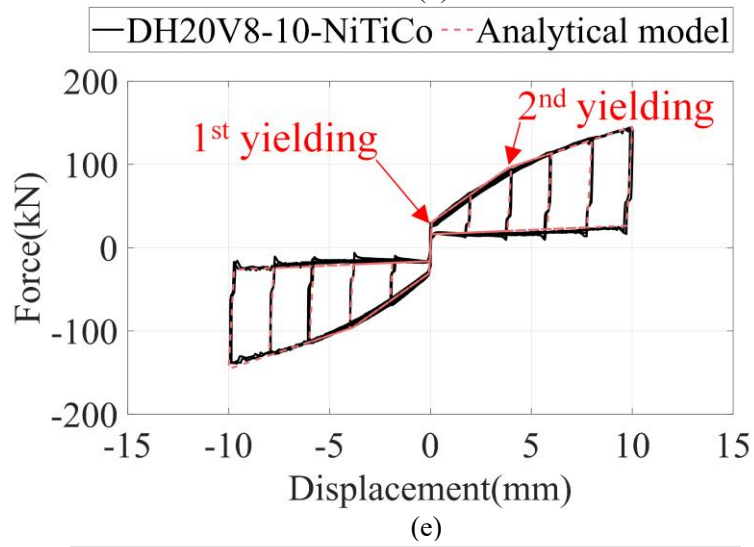
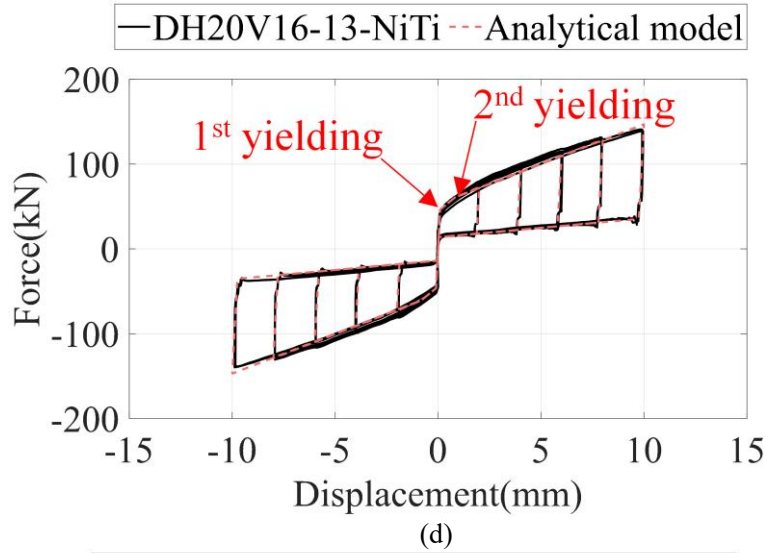


Fig. 4.15 Fracture of a NiTiCo SMA bolt for specimen DH20V16-13-NiTiCo





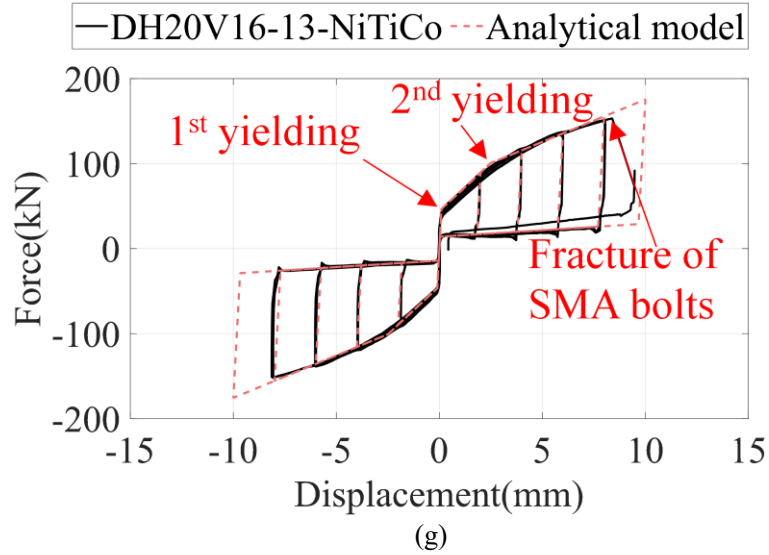
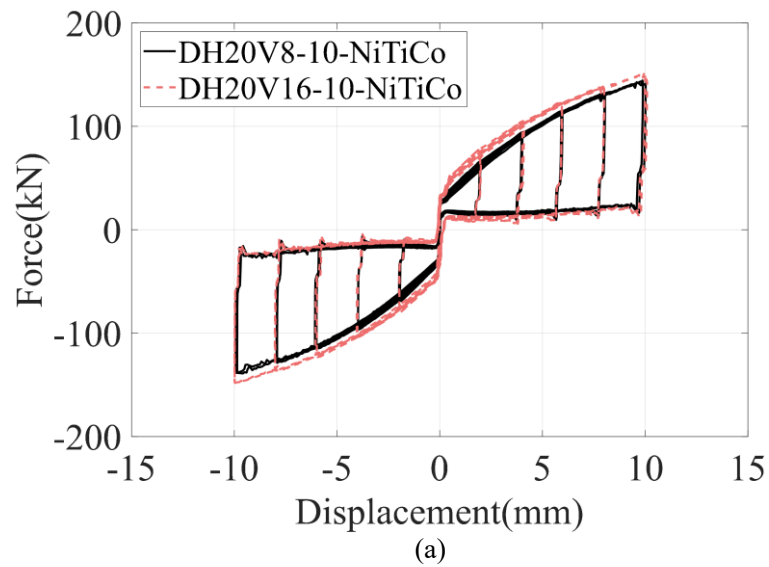
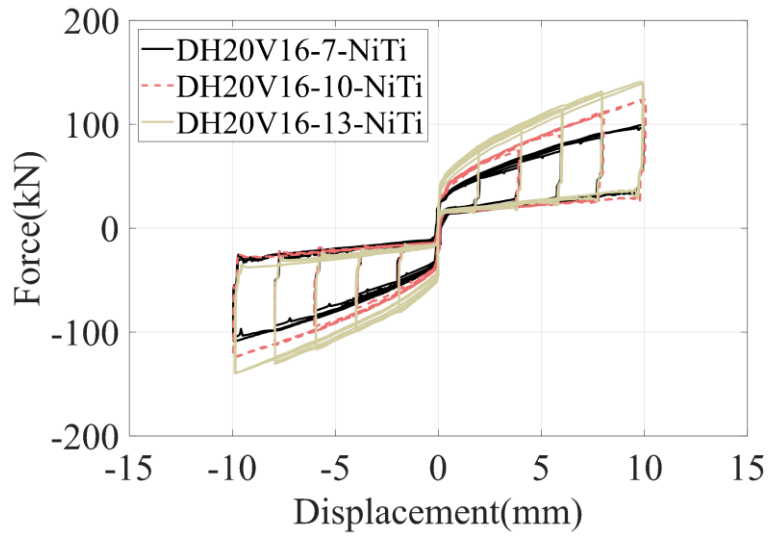
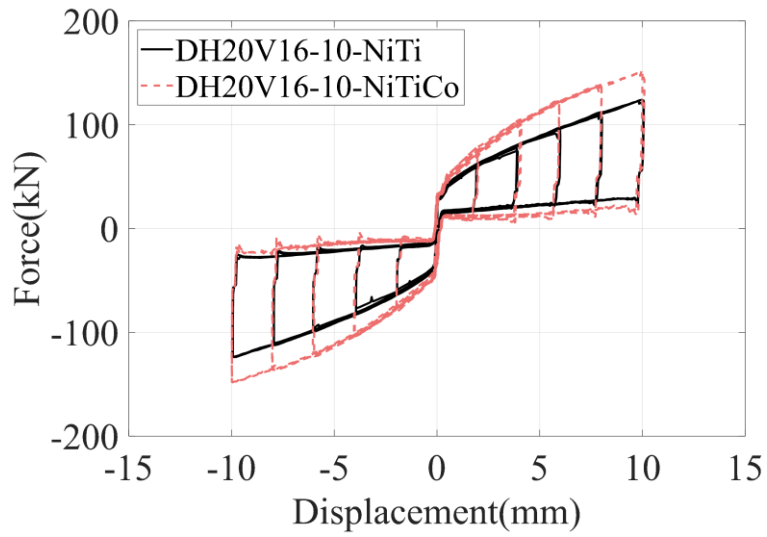


Fig. 4.16. Hysteretic curves of test specimens: (a) DH20, (b) DH20V16-7-NiTi, (c) DH20V16-10-NiTi, (d) DH20V16-13-NiTi, (e) DH20V8-10-NiTiCo, (f) DH20V16-10-NiTiCo, and (g) DH20V16-13-NiTiCo

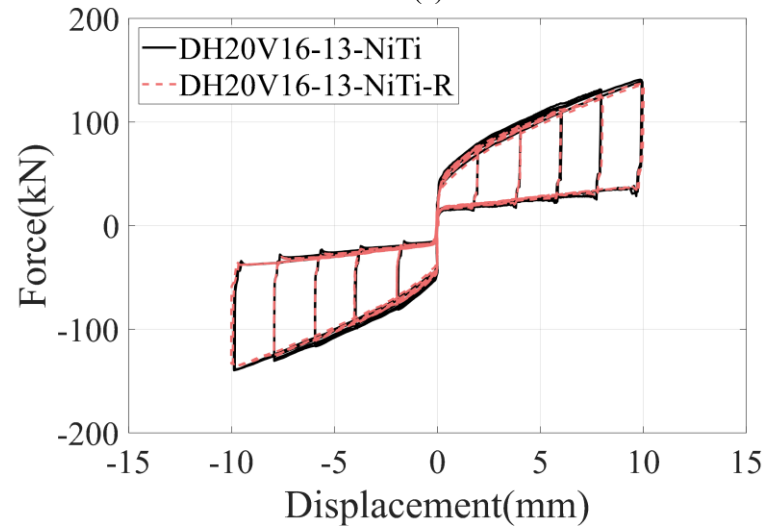




(b)



(c)



(d)

Fig. 4.17. Comparisons of the hysteretic curves of test specimens: (a) effect of preloads, (b) effect of sloping angles, (c) effect of SMA bolt type, and (d) effect of repeated tests under different loading rates

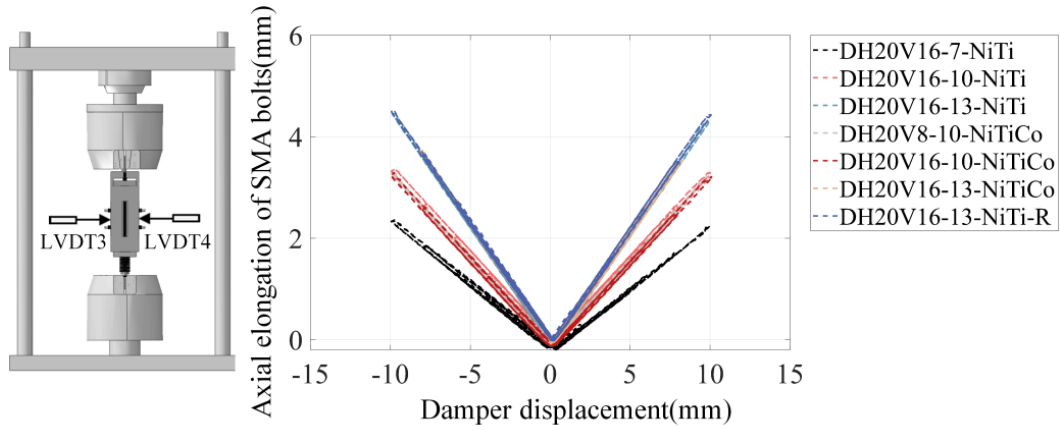


Fig. 4.18. Measured axial elongation of SMA bolts

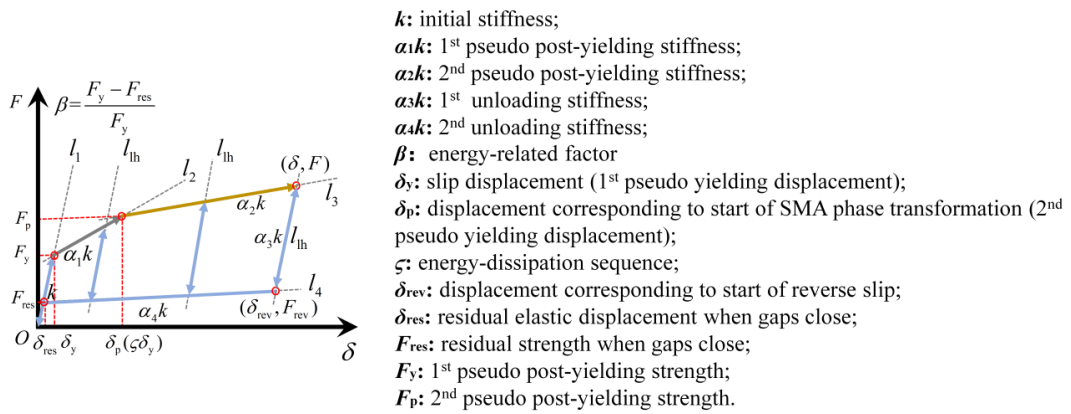


Fig. 4.19. Symbols of hysteretic parameters of SMA-VFSD

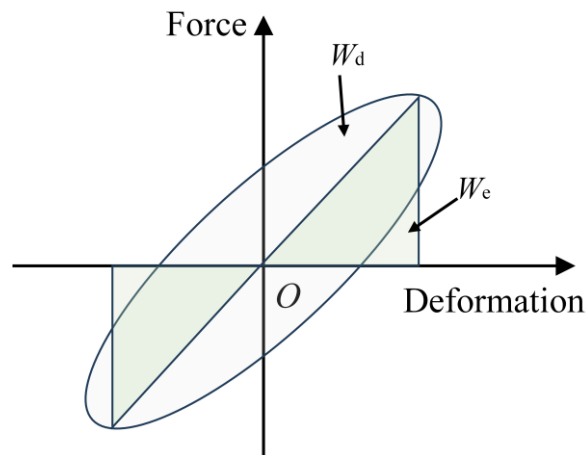
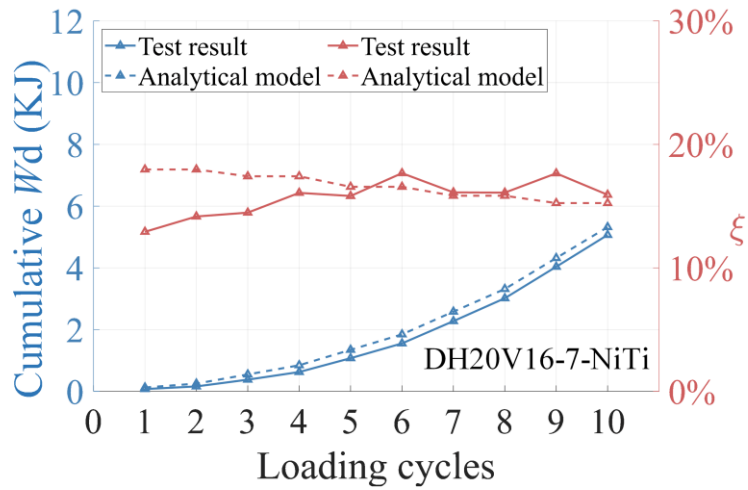
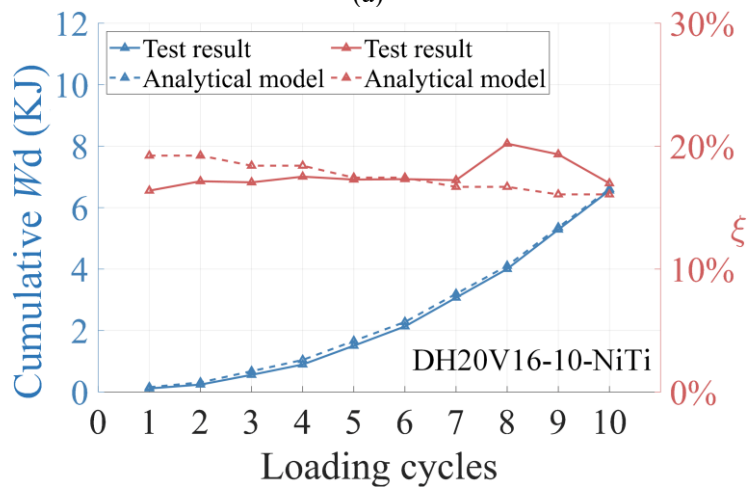


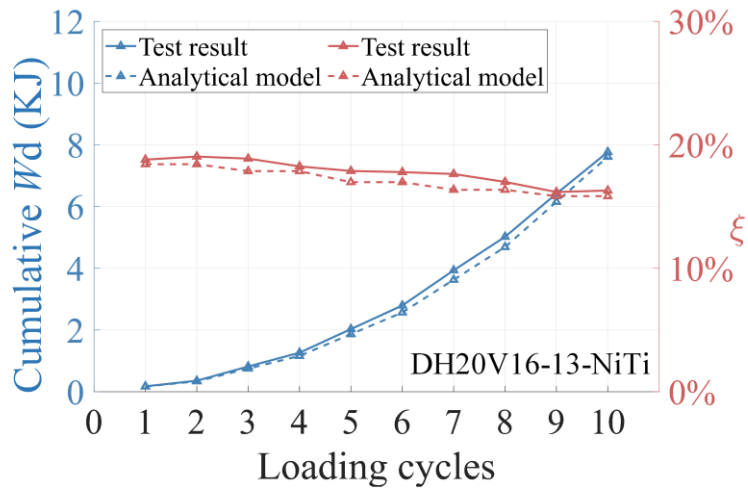
Fig. 4.20. Definition of equivalent viscous damping ( $\zeta$ )



(a)



(b)



(c)

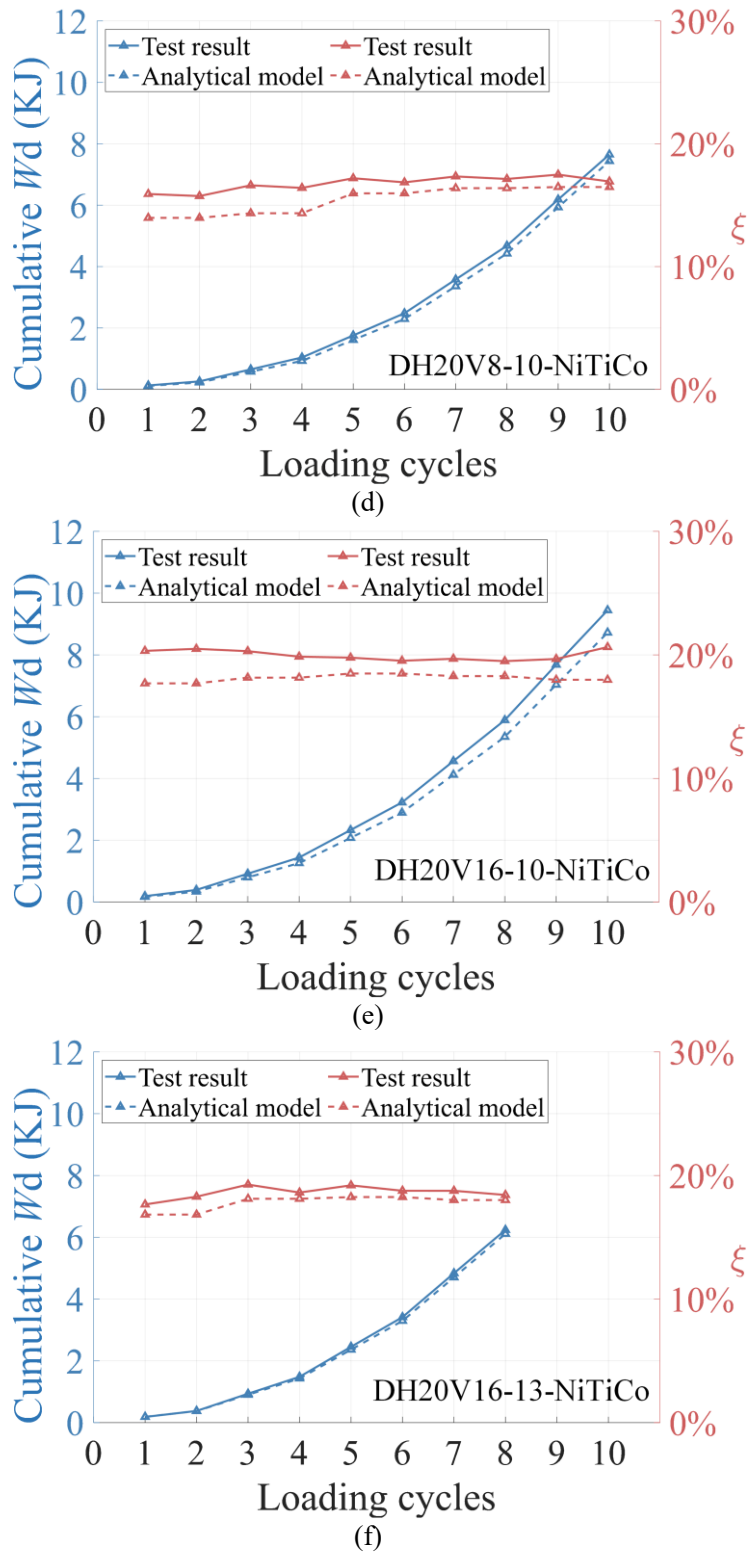
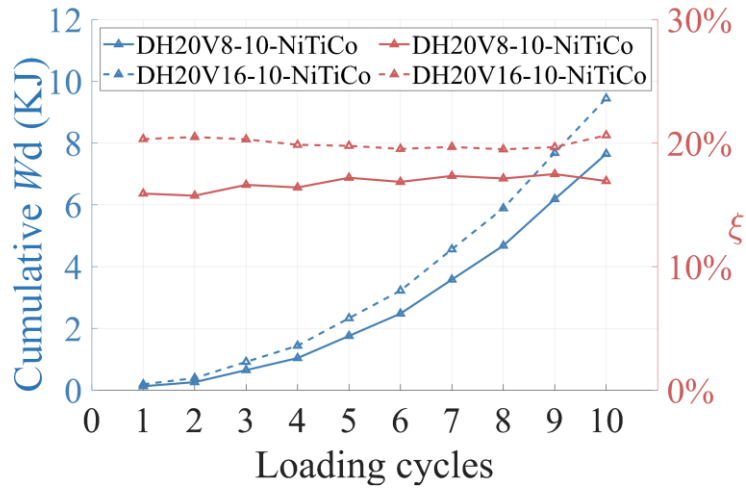
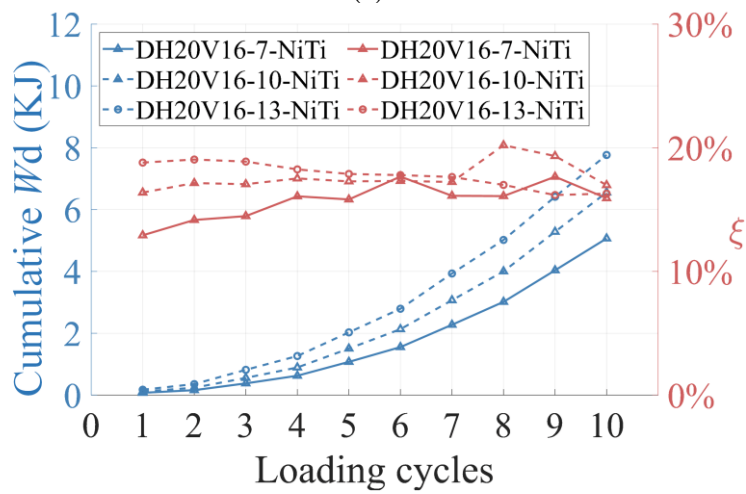


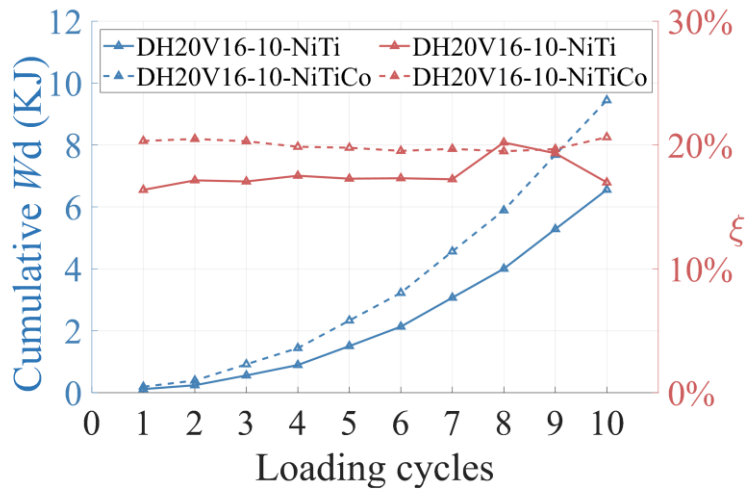
Fig. 4.21. Cumulative energy dissipation and  $\xi$  of test specimens: (a) DH20V16-7-NiTi, (b) DH20V16-10-NiTi, (c) DH20V16-13-NiTi, (d) DH20V8-10-NiTiCo, (e) DH20V16-10-NiTiCo, and (f) DH20V16-13-NiTiCo



(a)



(b)



(c)

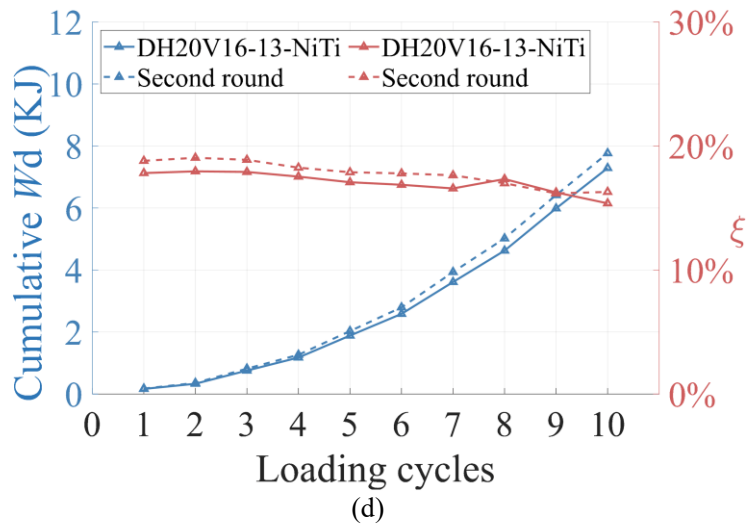


Fig. 4.22. Comparisons of the cumulative energy dissipation and  $\xi$  of test specimens: (a) effect of preloads, (b) effect of sloping angles, (c) effect of SMA bolt type, and (d) effect of repeated tests

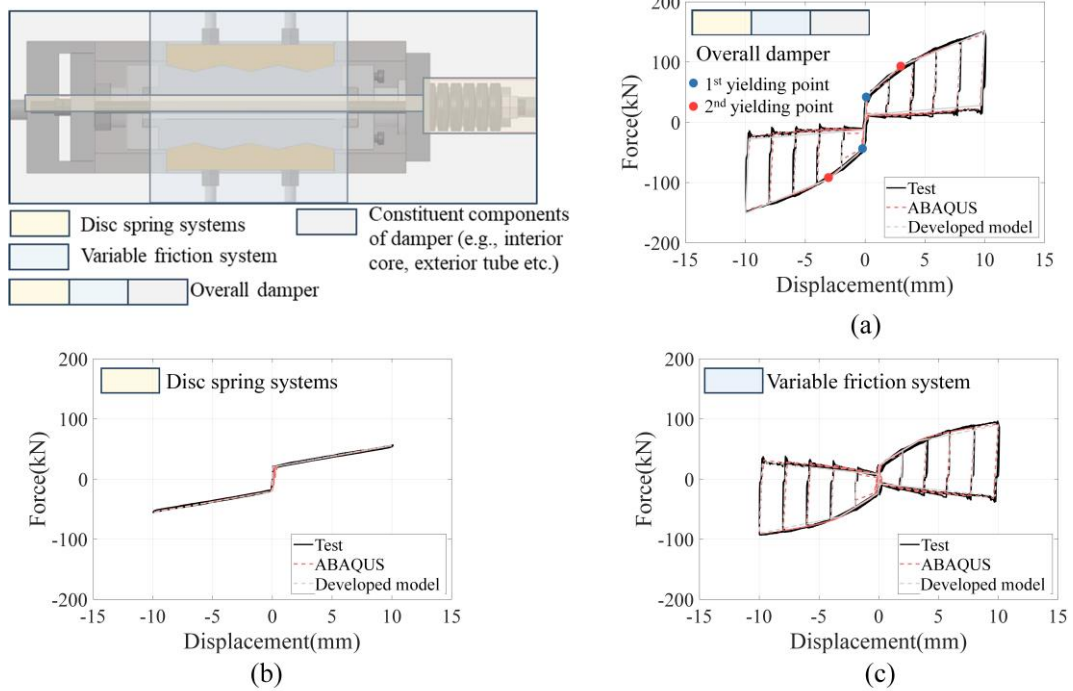
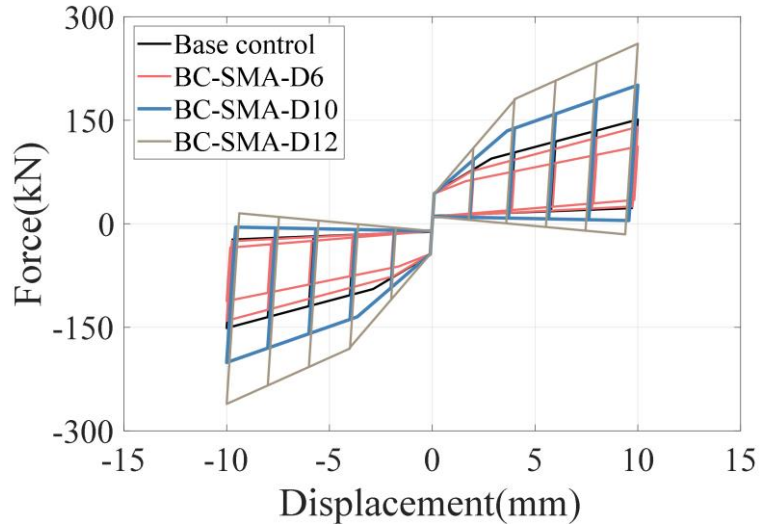
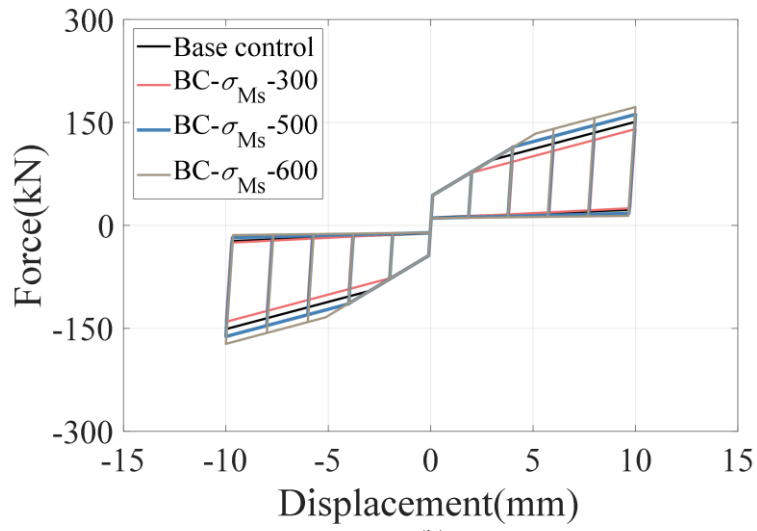


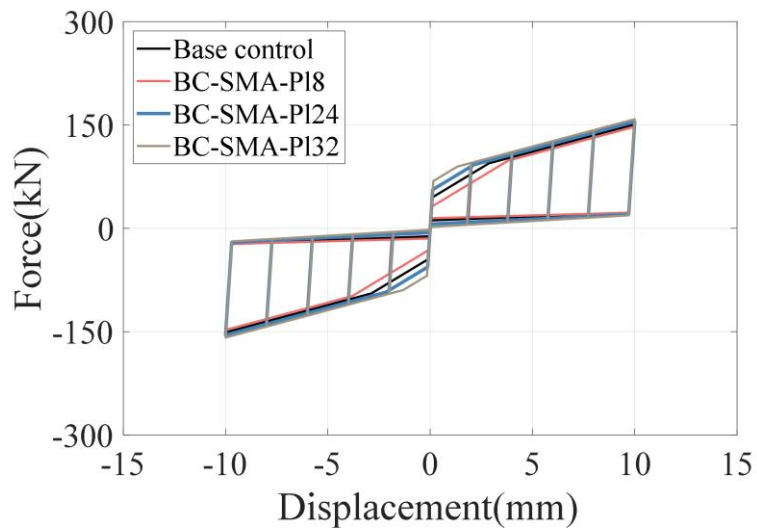
Fig. 4.23. Detailed comparisons of analytical prediction and test data for specimen DH20V16-10-NiTiCo: (a) cyclic curve of the damper specimen, (b) cyclic curve of the disc spring systems, and (c) cyclic curve of the variable friction system



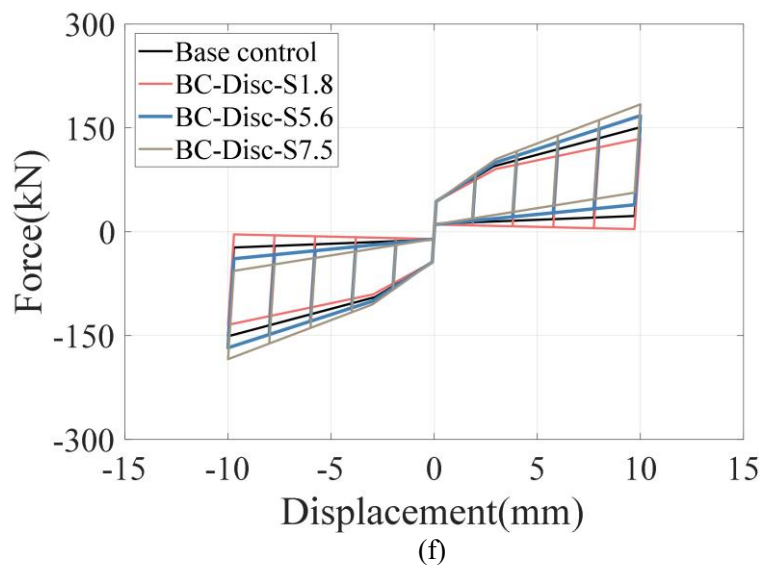
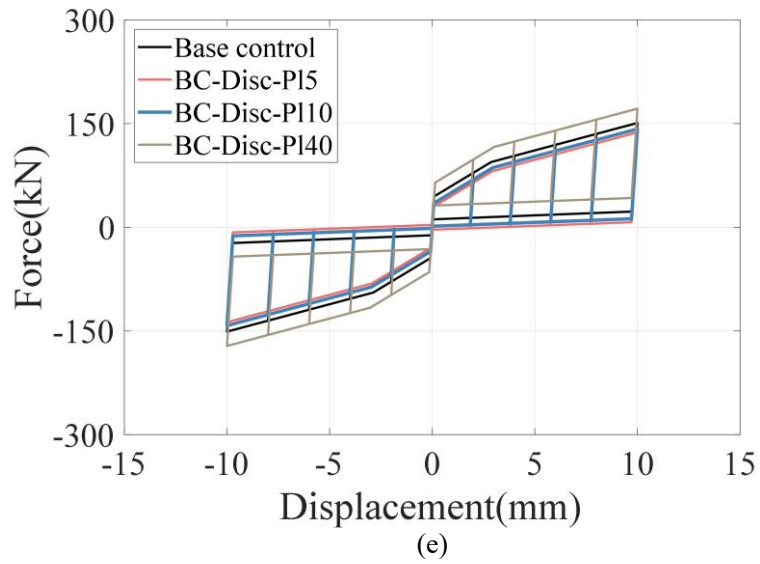
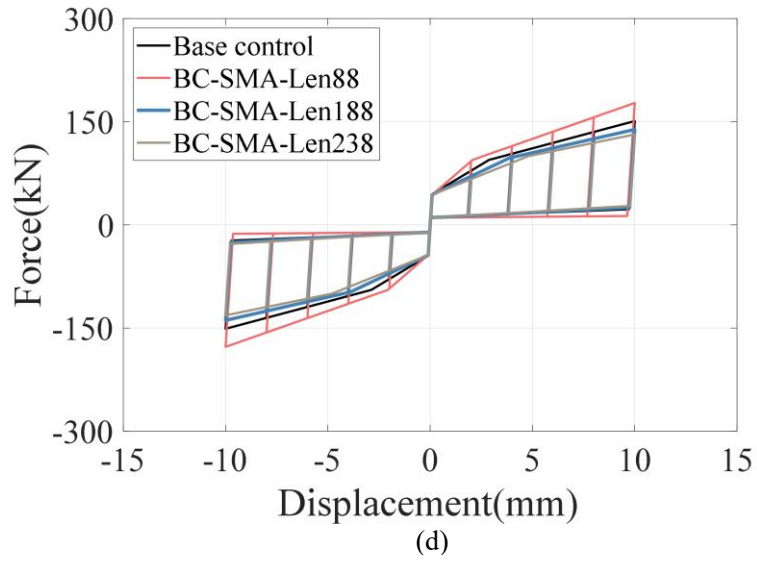
(a)

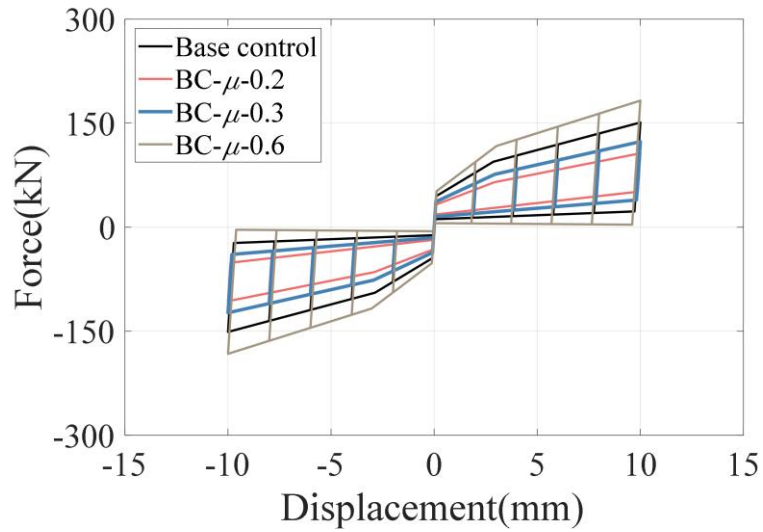


(b)

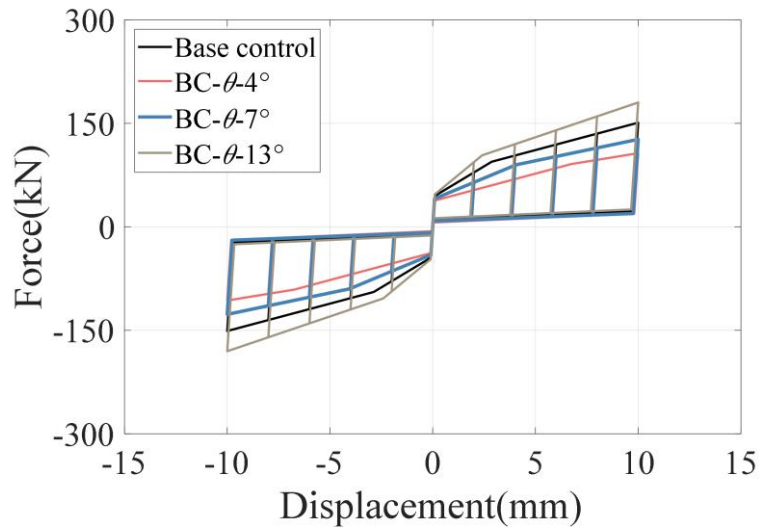


(c)





(g)



(h)

Fig. 4.24. Results of parametric study: (a) effect of SMA bolt diameters, (b) effect of  $\sigma_{Ms}$  of SMA bolts, (c) effect of SMA bolt preloads; (d) effect of effective SMA bolt work lengths, (e) effect of preloads of disc spring systems, (f) effect of stiffness of disc spring system, (g) effect of friction coefficients ( $\mu$ ), and (h) effect of sloping angles ( $\theta$ )

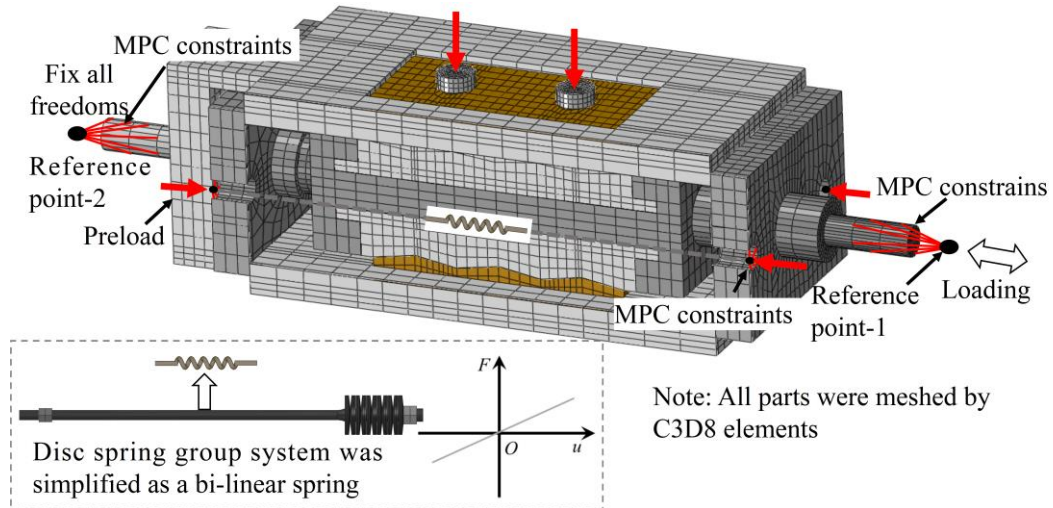


Fig. 4.25. Refined numerical model for SMA-VFSD

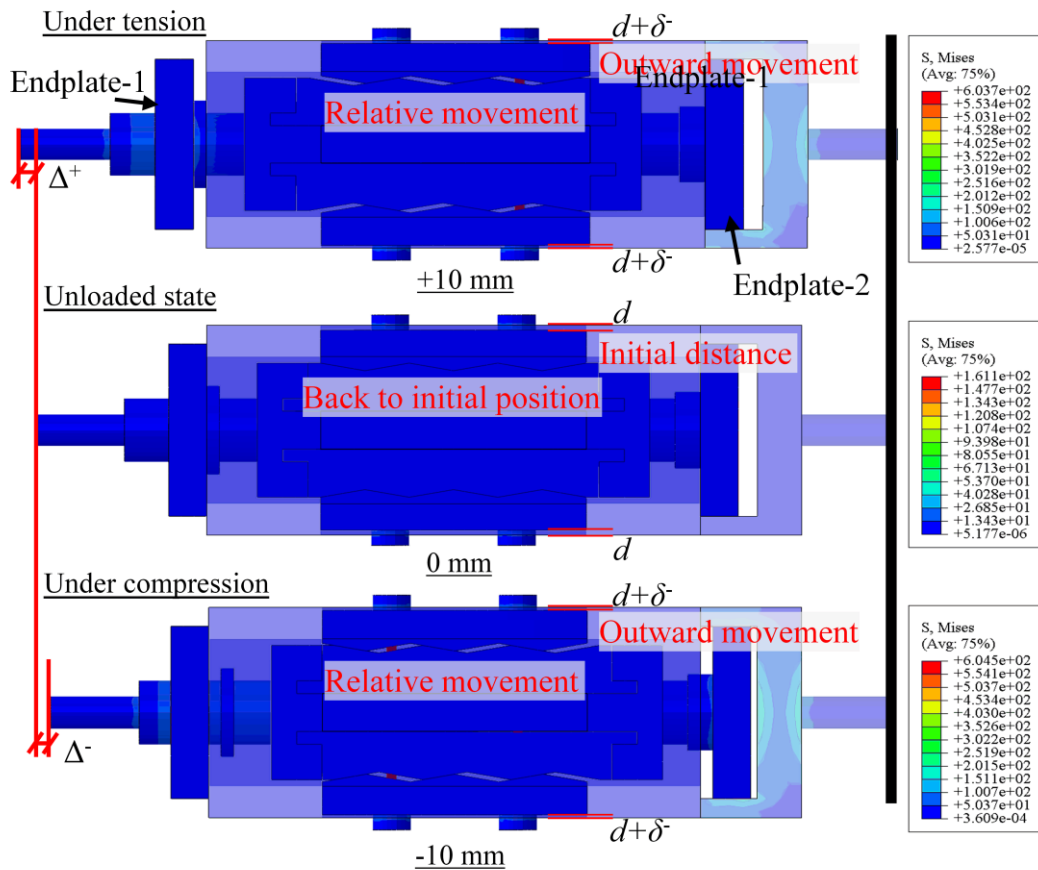


Fig. 4.26. Deformation state under maximum displacement amplitude for specimen DH20V16-10-NiTiCo

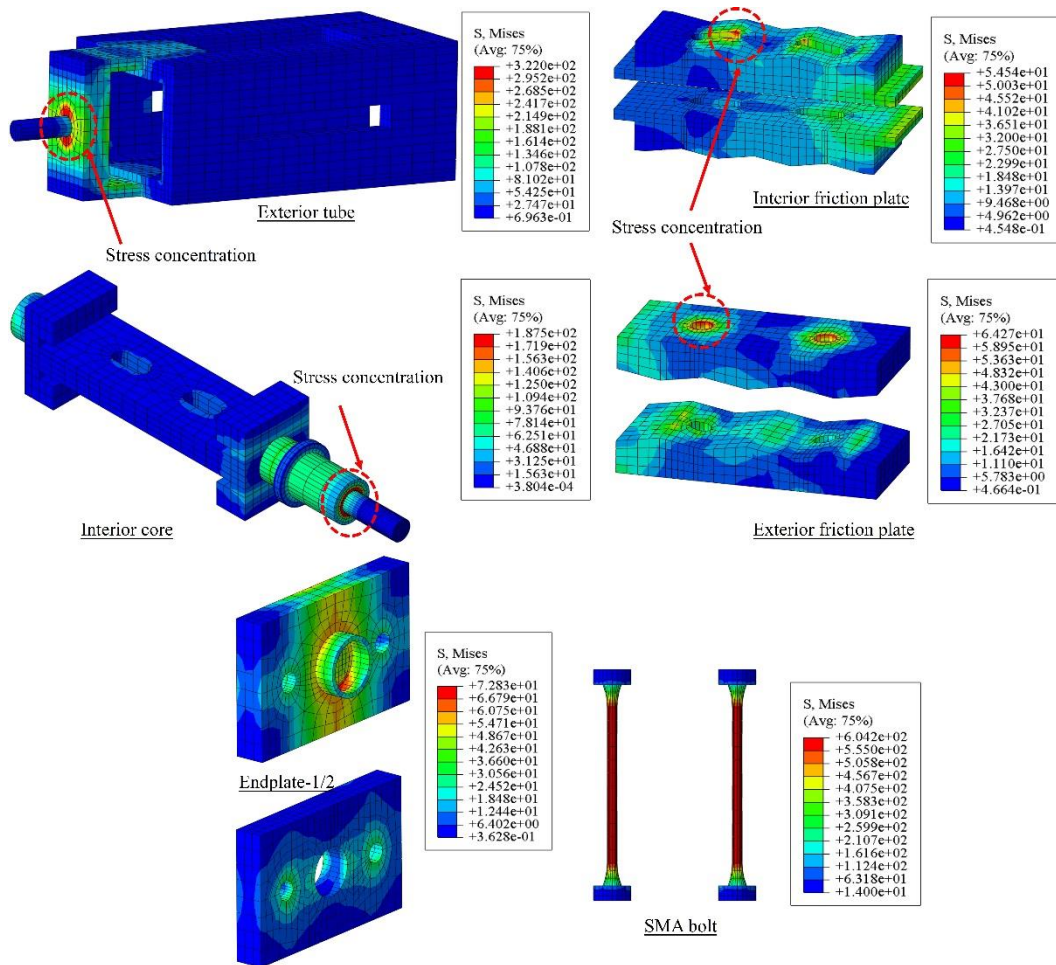
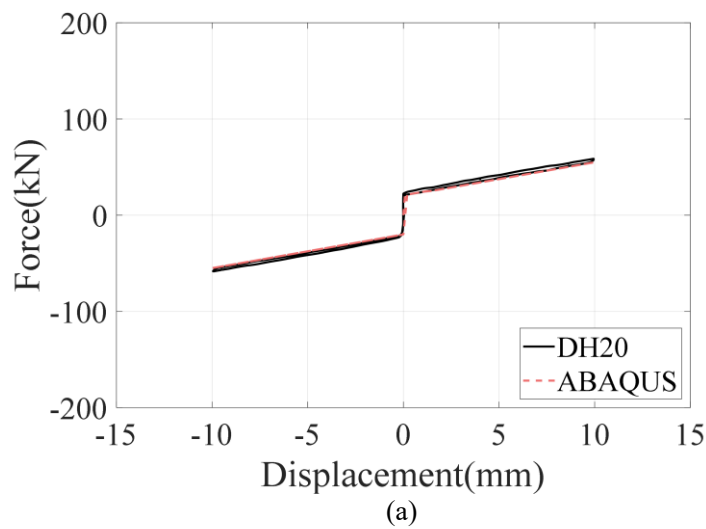
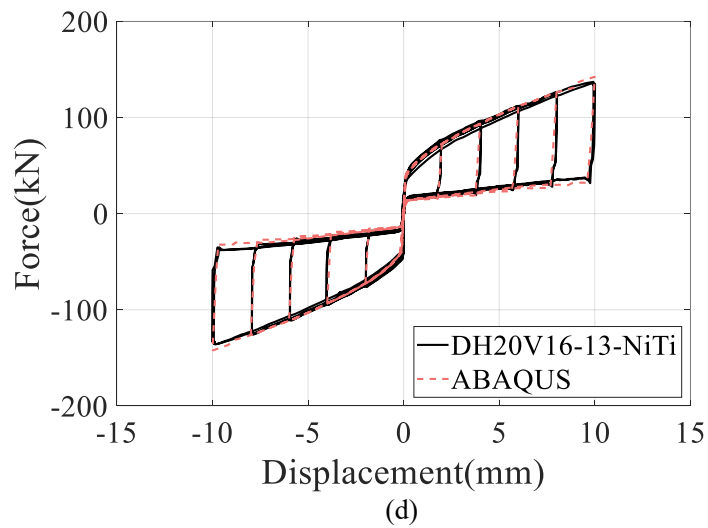
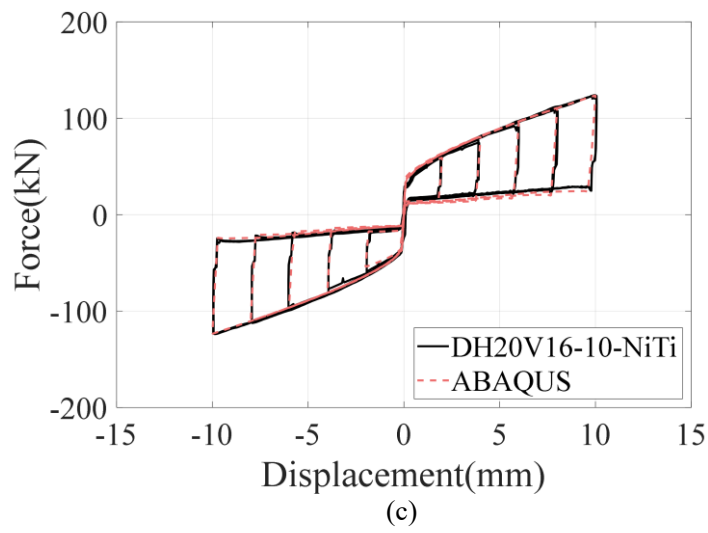
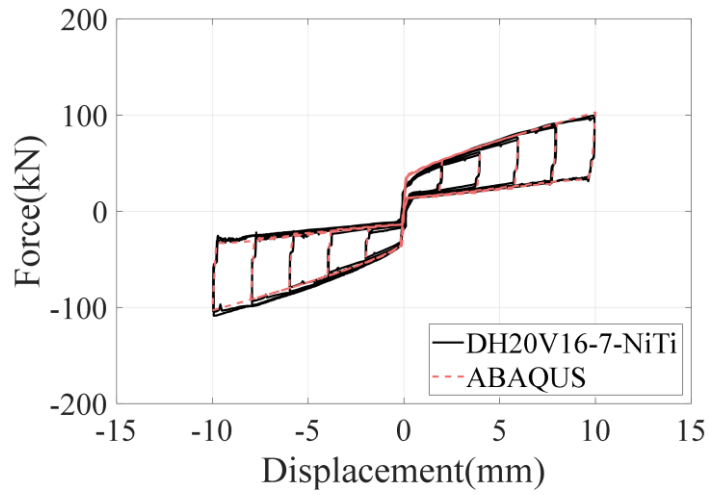
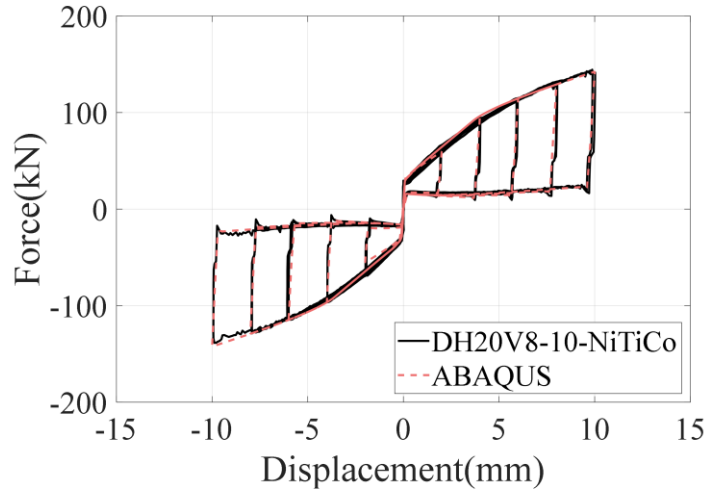


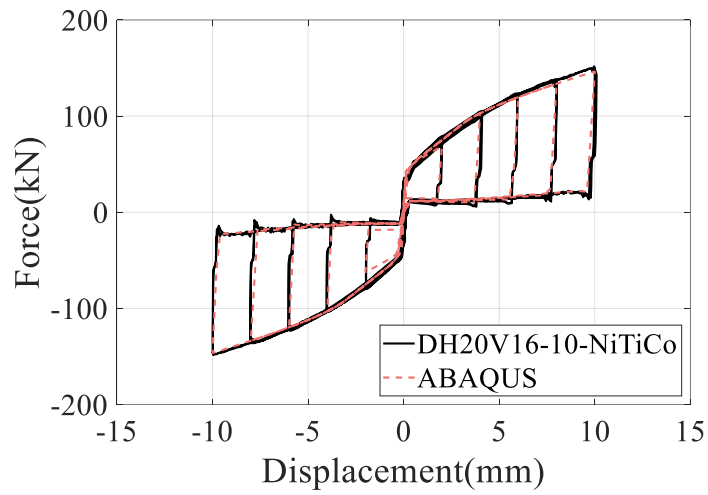
Fig. 4.27. Stress contour of each component for specimen DH20V16-10-NiTiCo under maximum positive displacement amplitude



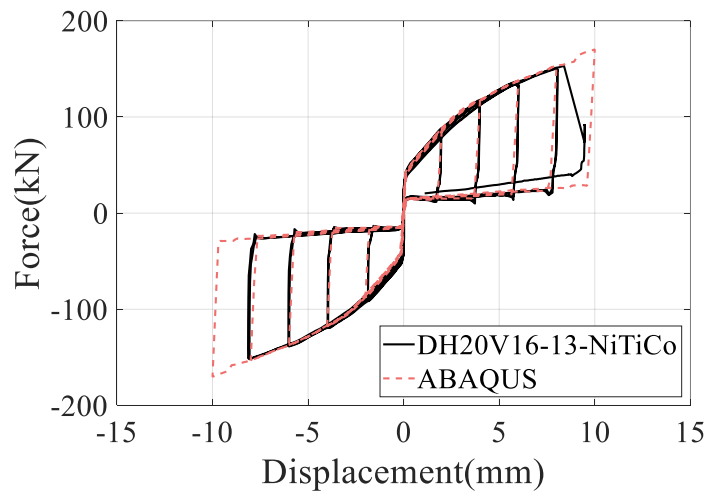




(e)



(f)



(g)

Fig. 4.28. Comparisons of hysteretic curves between refined numerical model and test data: (a) DH20, (b) DH20V16-7-NiTi, (c) DH20V16-10-NiTi, (d) DH20V16-13-NiTi, (e) DH20V8-10-NiTiCo, (f) DH20V16-10-NiTiCo, and (g) DH20V16-13-NiTiCo

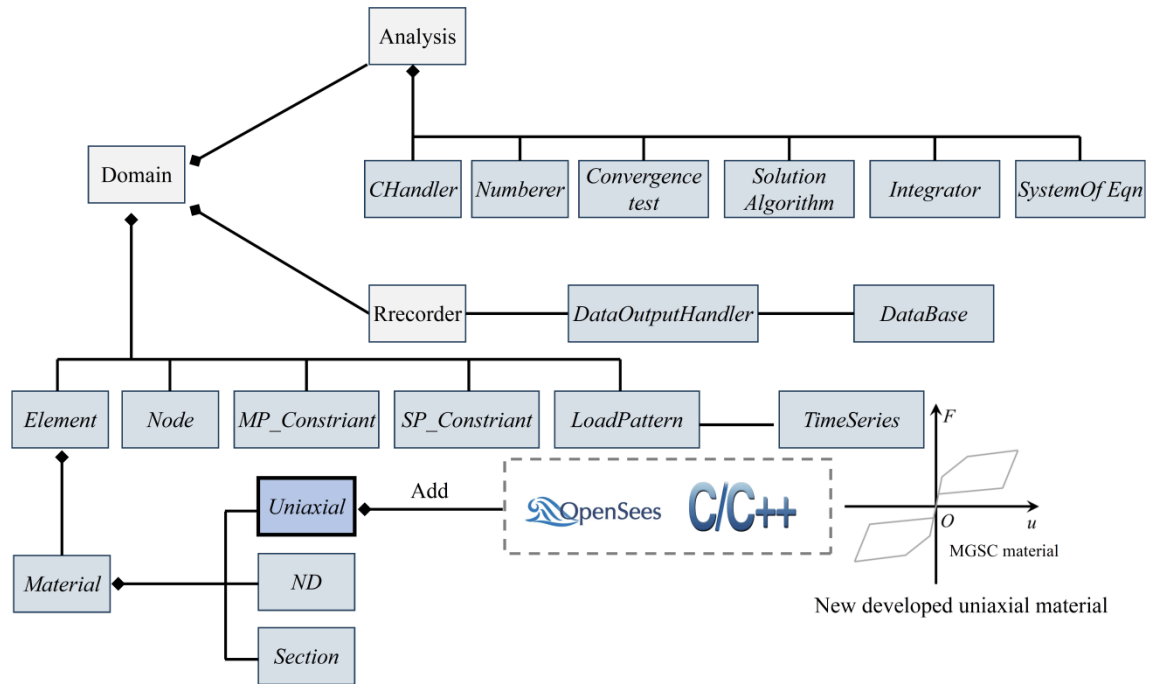


Fig. 4.29. OpenSees framework

The command of the added uniaxial material is shown below:

uniaxialMaterial MGSCMaterial \$matTag \$k<sub>1</sub> \$k<sub>2</sub> \$k<sub>3</sub> \$k<sub>4</sub> \$k<sub>5</sub> \$sigAct \$β \$ζ

\$matTag	Integer tag identifying material
\$k <sub>1</sub>	Initial Stiffness
\$k <sub>2</sub>	$k_2 = \alpha_1 k$ , 1 <sup>st</sup> pseudo-post-yielding stiffness
\$k <sub>3</sub>	$k_3 = \alpha_2 k$ , 2 <sup>nd</sup> pseudo-post-yielding stiffness
\$k <sub>4</sub>	$k_4 = \alpha_3 k$ , 1 <sup>st</sup> unloading stiffness
\$k <sub>5</sub>	$k_5 = \alpha_4 k$ , 2 <sup>nd</sup> unloading stiffness
\$sigAct	Yielding force/stress
\$β	Energy-related factor
\$ζ	Energy-dissipation sequence

Fig. 4.30. Usage and input parameters of uniaxial MGSC material

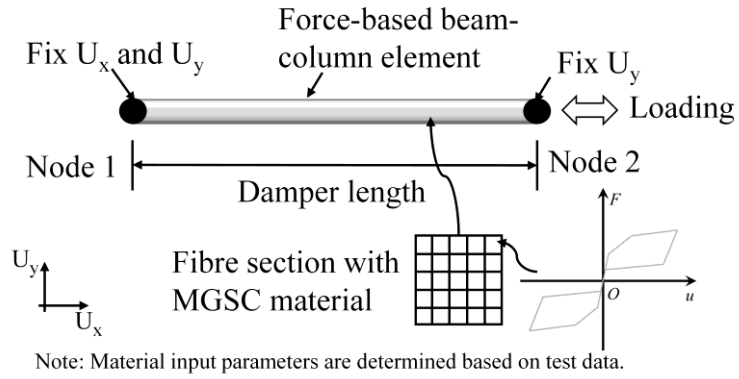
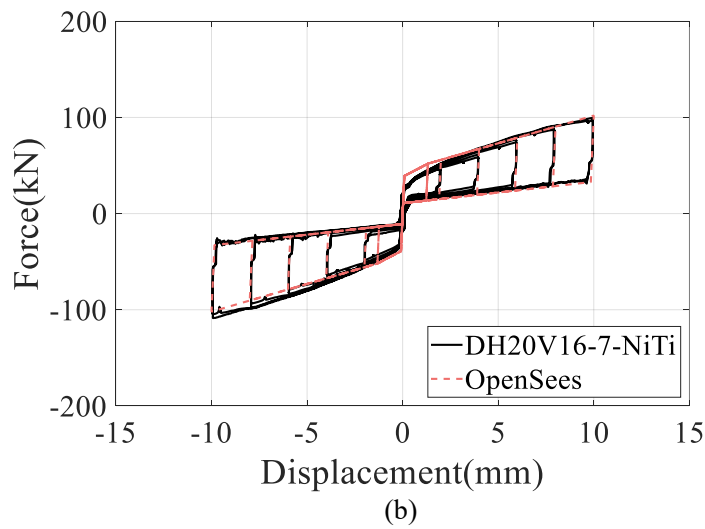
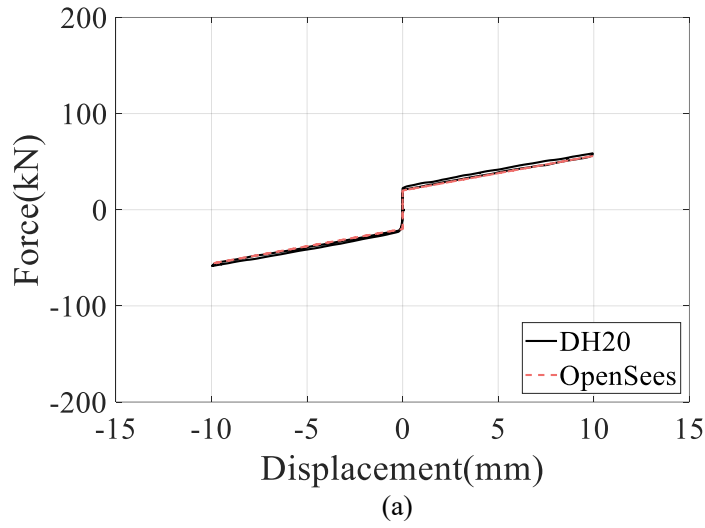
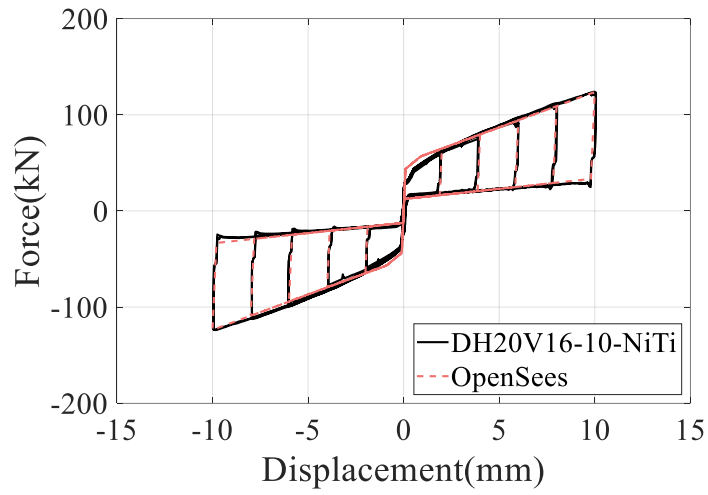
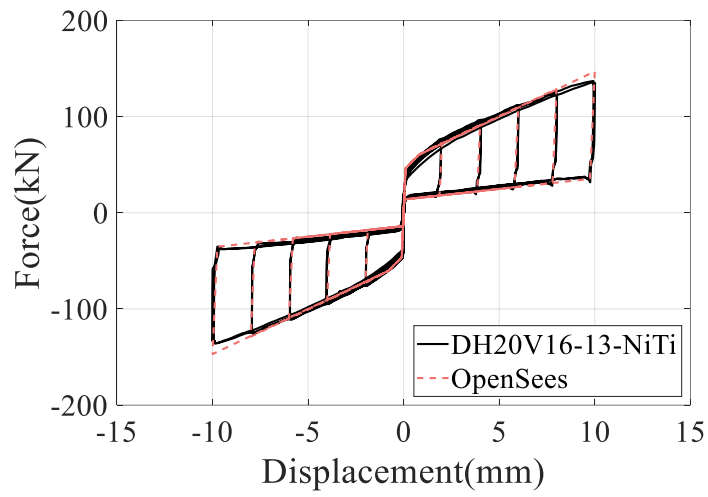


Fig. 4.31. Simplified model in OpenSees

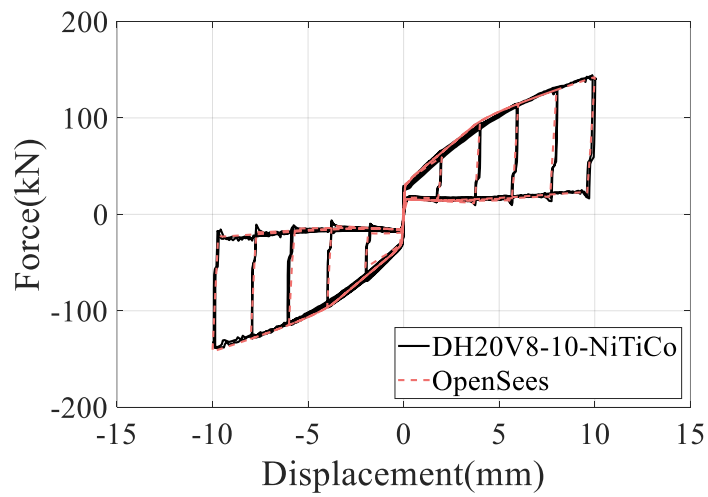




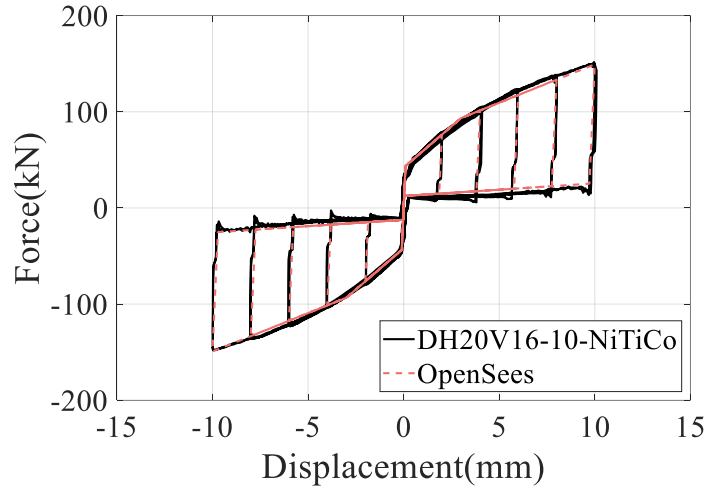
(c)



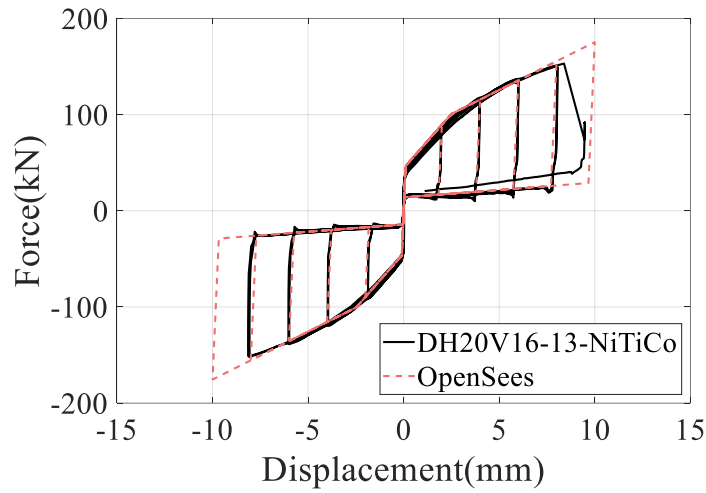
(d)



(e)



(f)



(g)

Fig. 4.32. Comparisons of hysteretic curves between simplified numerical model and test data: (a) DH20, (b) DH20V16-7-NiTi, (c) DH20V16-10-NiTi, (d) DH20V16-13-NiTi, (e) DH20V8-10-NiTiCo, (f) DH20V16-10-NiTiCo, and (g) DH20V16-13-NiTiCo

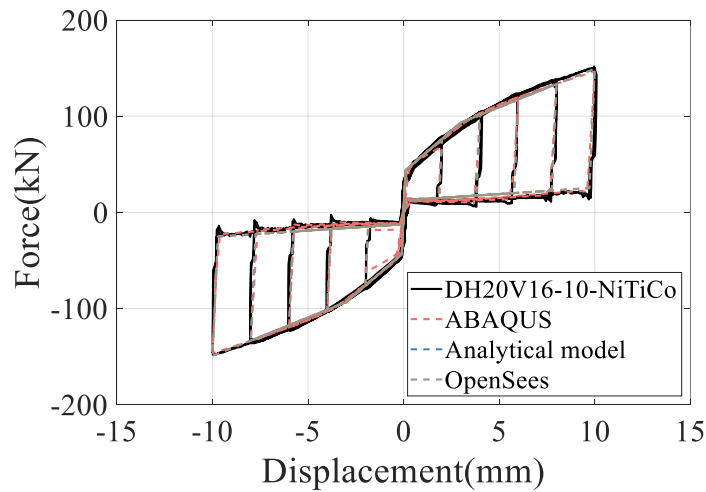


Fig. 4.33. Comparisons of hysteretic curves between various methods and test data for specimen DH20V16-10-NiTiCo

## **Chapter 5 Experimental programme for braced frame equipped with SMA-VFSD**

### **5.1 Introduction**

The previous chapter comprehensively validated the feasibility of the SMA-VFSD via analytical, experimental, and numerical methods. The damper exhibited a multistage energy-dissipation mechanism and improved design flexibility, indicating its potential to enhance the seismic resilience in engineering structures. This chapter commenced with an illustration of the potential structural applications of the SMA-VFSD. Then, an experimental programme investigating the cyclic behaviour of a one-bay and one storey braced frame equipped with the SMA-VFSD was conducted. Six frame tests were performed to study the effects of design parameters, including the preload of the SMA bolts and the sloping angle of the friction pairs, on structural behaviour. The test results, including experimental observations, hysteretic behaviour, energy-dissipation capacities, and self-centring abilities were discussed in section 5.3. Additionally, the repeatability and stability of the cyclic behaviour of the braced frame were also demonstrated through multiple-round tests. Following this, a simplified numerical model, which can consider initial gaps due to fabrication tolerances, was developed to predict the cyclic behaviour of the tested braced frame. This model was then validated against the test results of the specimens in section 5.3. Specifically, comparisons between the predictions of the model and test results of the frame specimens (e.g., hysteretic behaviour and energy-dissipation capacity) were conducted to demonstrate the accuracy and reliability of the proposed simplified mode. These validated modelling techniques will be employed in the next chapter to

assess the seismic performance of structures equipped with the SMA-VFSD at the system level.

## **5.2 Engineering applications of SMA-VFSD**

The SMA-VFSD offers extensive adaptability and can be applied in various structural contexts to improve seismic resilience. Fig. 5.1 illustrates potential applications of the proposed damper in common structural configurations, such as beam-column connections, rocking column bases, and braced structures. It is important to note that in these applications, nonlinear energy dissipation mainly occurs within the SMA-VFSD, while the other structural elements remain elastic during excitations. Therefore, the nonlinear hysteretic characteristics of such components or structures are primarily governed by the structural behaviour and performance of the SMA-VFSD, which is expected to exhibit a consistent multistage energy-dissipation mechanism. To illustrate this, a one-bay one-storey braced frame equipped with the SMA-VFSD was designed according to the lab equipment capacity. The configuration of the braced frame is depicted in Fig. 5.2. As depicted in Fig. 5.2, a damper brace was proposed, comprising the SMA-VFSD and an extended steel segment (a rectangular steel tube in this thesis). This brace was positioned diagonally within the frame to withstand lateral forces. The cyclic performance of the braced frame was thoroughly examined through both experimental and numerical methods.

## **5.3 Test of braced frame equipped with SMA-VFSD**

### **5.3.1 Material test**

For the braced frame, the seismic energy is absorbed by the SMA-VFSD and thus,

the remaining structural members (i.e., column, beam, and extended steel segment) stay elastic during loadings. In this test programme, Q345 grade steel was employed to fabricate these main structural members. To determine the material constants (i.e., elastic modulus and yielding strength) for the steel at various thickness (i.e., 8 mm, 10 mm, 12 mm and 14 mm), material coupon tests were performed using an INSTRON machine. The test setup and the dimensions of the material coupons are shown in Fig. 5.3. Each coupon specimen had a nominal gauge length of 50 mm and a nominal gauge width of 12.5 mm, as per the standard specifications (Chinese standard (GB/T228-2021)). For each thickness, three coupons were fabricated. The strain along the loading direction was measured by an extensometer with a 50-mm gauge length and the results are presented in Fig. 5.4. The material constants were calculated as the average value of three coupons. The measured elastic modulus and yielding strength for steel with thickness of 8 mm, 10 mm, 12 mm and 14 mm are as follows: 186 GPa and 435 MPa, 214 GPa and 492 MPa, 226 GPa and 425 MPa, and 210 GPa and 455 MPa, respectively.

### 5.3.2 Specimen design

The primary aim of the braced frame test is to demonstrate the effectiveness of the SMA-VFSD in enhancing structural resilience, while accounting for the connection boundaries in its applications. Additionally, the test seeks to evaluate whether the structural hysteretic behaviour can exhibit a multistage energy-dissipation mechanism similar to that observed in the individual damper tests. In the test programme, pin connections were utilised to connect the damper brace to the columns. It is worthy to note that in the previous damper test, the boundaries imposed on the SMA-VFSD by the wedge-shaped fixtures of the INSTRON machine (i.e., all degrees of freedom were constrained) were rigid and may not accurately reflect the conditions encountered in

real structural applications. Hence, stability-related concerns regarding the damper configuration might not be fully represented and therefore warrant necessary investigation in the frame test.

In this frame test, the maximum storey drift was set at 2%, based on the constraints of lab facilities and limitations of the current damper configuration. To meet the deformation requirements of the braced frame (i.e., 2% interstorey drift), the maximum deformation of the damper was increased from 10 mm (as discussed in Chapter 4) to 20 mm for this test. This necessitated the use of a disc spring group with more units in series for the disc spring systems and longer SMA bolts for the variable friction systems in the SMA-VFSD. Specifically, the disc spring system utilised 17 units in series (Fig. 5.5), while the variable friction system employed 290-mm long SMA bolts. Based on the previous tests on the disc spring group (see section 4.2.2.1) and the disc standard (Chinese standard (GB/T1972-2023)), the axial stiffness of each updated disc spring group system was reduced from 1.75 kN/mm to 1.13 kN/mm (i.e., from 11 units to 17 units). The hysteretic behaviour of the longer SMA bolts was investigated through cyclic tension-release tests, as illustrated in Fig. 5.6(a). The dimensions of the SMA bolt and the loading protocol are provided in Figs. 5.6(b) and (c) respectively, while the results are shown in Fig. 5.6(d). The material constants describing the hysteretic behaviour of the SMA bolt were also determined using the Auricchio's approach and the test data, listed in Table 5.1. The predicted hysteretic curve from the approach is compared against the test results in Fig. 5.6(d). The satisfactory consistency demonstrated the accuracy of Auricchio's approach integrated in ABAQUS.

The variable parameters examined in this test programme included the preload of the SMA bolts and the sloping angle of the wedge-shaped friction plates. The interior and exterior wedge-shaped friction plates with three inclinations ( $\theta_a = 7^\circ, 10^\circ, \text{ and } 13^\circ$ )

were employed. During the damper test (see section 4.3), it was observed that steel-brass friction pairs exhibited stable energy-dissipation capacity with only a slight increase in the friction coefficient under multiple tests. Therefore, the wedge-shaped friction plates for the damper test were reused in the frame test to further confirm the stability of the steel-brass friction pairs when subjected to multiple excitations. The span and storey height of the tested frame specimen were 1600 mm and 1640 mm, respectively, and the total length of the damper brace was 1759 mm. The structural members and the extended steel segment were welded using Q345 steel, designed to remain elastic and free of damage during the tests. The detailed dimensions of each member are provided in Fig. 5.7. It's worth noting that the dimensions of the damper components were not shown and can be referred to section 4.3. To accommodate the longer SMA bolts, additional block washers were used during the installation of the SMA bolts, as shown in Fig. 5.2. The extended steel segment was bolted to one end of the damper via a transition plate. Pin connections were used for all the beam-to-column connections and column bases.

A total of six frame tests were carried out. Simply use a full label as an example for naming convention: FH20V16 denotes that the preloads of the disc spring systems and SMA bolts are 20 kN and 16 kN, respectively. The detailed information on the test specimens is listed in Table. 5.2. Note that no friction system was installed for specimen FH20, and it was used to examine the hysteretic behaviour of the bare frame (i.e., without variable friction system). The test results of the specimens can be used to evaluate the level of friction presented in each pin connection and the contact surface (e.g., the lateral brace and the specimen). It is important to mention that all the potential contact surfaces were either lubricated or covered with Teflon sheets to minimise friction. Specimen FH20V16-R was a repeat test of specimen FH20V16, aimed at

demonstrating the repeatability and stability of the brace frame.

### 5.3.3 Test setup and instrumentation

The braced frame test was conducted using a self-balancing loading frame, as illustrated in Fig. 5.8. A photo of the test setup is presented in Fig. 5.9. Due to space limitations within the loading frame, no gravitational load was applied to the frame specimen, and thus the P-delta effect was not included in the test programme. The horizontal cyclic load was gradually applied using a manually controlled hydraulic jack. It is noteworthy that visual gaps in the pin connections, attributed to the fabrication tolerances, were observed after assembling the frame specimens, as depicted in Fig 5.10. Therefore, initial gaps were anticipated to possibly occur before the frame could withstand external loads. The impact of these initial gaps on the cyclic behaviour of the specimens will be elaborated in subsequent sections and further evaluated at the system level (i.e., a prototype structure) in the next chapter. To ensure the proper in-plane behaviour for the test specimens, lateral brace systems were installed, as shown in Fig. 5.9.

The measuring instrumentations for the braced frame test are depicted in Fig. 5.11. Two pairs of LVDTs (LVDTs 1/2 and LVDTs 3/4) were installed to monitor the lateral deformation of the specimen. The relative displacement between the average readings of LVDTs 1/2 and LVDTs 3/4 was recorded as the relative interstorey displacement of the specimen. Additionally, two more pairs of LVDTs (LVDTs 5/6 and LVDTs 7/8) were employed to measure the axial deformation of the damper and damper brace, respectively. Four donut load cells were installed to monitor the internal loads of the disc spring systems and the SMA bolts. The load applied by the hydraulic jack was recorded by a 50-ton load cell, as given in Fig. 5.10. Furthermore, for direct

measurement of the axial internal force in the damper brace, a customised 30-ton load cell was fabricated and utilised in the damper, as depicted in Fig. 5.11. The loading protocol for the frame test programme was a modified version based on the SAC project (SAC 1997), which is illustrated in Fig. 5.12. It comprised ten loading cycles with gradually increasing storey drift amplitudes at five levels (i.e., two cycles at each amplitude).

### 5.3.4 General observation

All specimens showed consistent experimental observations throughout the test. Specifically, as the drift amplitude increased, the frame specimen laterally shifted, causing the SMA-VFSD to either elongate (in the push direction) or shorten (in the pull direction). Fig. 5.13 depicts the deformation states of the damper and frame at the maximum drift amplitudes in the push and pull directions, respectively. According to the test observations, the SMA-VFSD in the frame specimens deformed effectively, exhibiting similar deformation modes (i.e., gap and relative slip patterns) as those observed in the previous damper test. Additionally, the damper's capability to function without stability-related issues was confirmed in realistic boundary conditions within structural applications. In general, with the increase of the storey drift amplitude, the total preloads (i.e., the sum of the preload of the disc spring groups and the friction force of the friction system) were exceeded, leading to the gradual development of a gap between the endplate and the exterior tube of the damper. The development trend of the gap in the damper under push direction was chosen and is illustrated in Fig. 5.14. The observed gap evolution aligned consistently with that observed in the damper test. Additionally, the relative movement of the exterior and interior friction plates can be visually identified, which was in line with the damper test. Upon the removal of the

external load, the frame specimen automatically returned to its original position, exhibiting slight residual deformation in the push direction while negligible deformation in the pull direction. This deformation was due to the initial gaps in the pin connections, as depicted in Fig. 5.10. An improvement in fabrication precision could reduce this residual deformation. Finally, during the testing process, intermittent noises were heard, possibly attributed to the rotation of the pin shafts within the pin connections.

### 5.3.5 Cyclic behaviour

Fig. 5.15 depicts the hysteretic responses of all frame specimens. As indicated in the figure, an initial gap was observed in the push direction for all specimens, consistent with the observed slight residual drifts in the push direction during the test. The expected trilinear flag-shaped hysteretic curves for the frame specimens with the SMA-VFSD were achieved. Specimen FH20 exhibited a bilinear behaviour with minimal energy dissipation, indicating that the disc spring group system solely provided the restoring force. It is worth noting that the slight energy dissipation was due to friction from the pin connections and between the specimens and the lateral brace. For the other frame specimens, the initial portion of the curves was linear, representing the decompression of the preload in the disc spring system and overcoming the static friction force in the SMA-VFSD friction system. The 1<sup>st</sup> "yielding point" in the curves (Figs. 5.15(b)-(e)) corresponded to the overcoming of the preload and friction force within the damper, subsequently causing relative sliding between the wedged friction plates in the SMA-VFSD. At this stage, the damper's stiffness decreased compared to the initial loading stage, resulting in a decrease in stiffness of the frame specimens. With a further increase in the storey drift amplitude, the damper brace, governed by the

damper's behaviour, either elongated or shortened (i.e., in push or pull directions), prompting the phase transformation of the SMA bolts in the SMA-VFSD. This led to a significant reduction in the stiffness of the damper brace and the emergence of a 2<sup>nd</sup> "yielding point" in the hysteretic curves of the frame specimens. To illustrate this variable stiffness pattern, the recorded hysteretic curves of the SMA-VFSD in the frame specimens are displayed in Figs. 5.16(b)-(e). It is evident that the damper exhibited a three-stage energy-dissipation mechanism, confirming consistency between damper and frame behaviour. Additionally, it is worth noting that the hysteretic characteristics of the damper observed in the frame test aligned with those seen in previous damper tests (see Chapter 4).

Figs. 5.17 (a)-(b) compare the cyclic behaviour of the tested frame specimens with different design parameters, and their respective SMA-VFSDs. It is evident from Fig. 5.17(a) that increasing the preload of the SMA bolts has a minimal effect on the hysteretic curves at both the damper and frame levels, contrary to the findings in the damper test. This may be caused by the slightly larger residual strain in the longer SMA bolts (290 mm long SMA bolts used in the frame test) compared to the shorter ones (used in the damper test in Chapter 4), as indicated in Fig. 4.4 and Fig. 5.6. This residual strain might result in a more obvious loss of the preload in the SMA bolts when a higher preload was applied. To illustrate this, Fig. 5.18 presents the loss of total preloads of the SMA bolts versus damper deformation at the last loading cycle of specimens FH20V8-10 and FH20V16-10. The figure also includes the initial preload values and the corresponding preload losses for the two specimens. The preload loss of specimens FH20V8-10 and FH20V16-10 was 7.1 kN and 2 kN, respectively. Therefore, a greater preload loss in the SMA bolts was observed for specimen FH20V16-10, leading to a similar force level of the SMA bolts in specimens FH20V16-10 and FH20V8-10 and

resulting the consistent hysteretic curves of the two specimens. Fig. 5.17(b) shows that the strength and energy-dissipation capacities of the specimens remarkably enhanced with the increase of the sloping angle of the friction plates ( $7^\circ$ ,  $13^\circ$ ) at both the damper and frame levels. However, for specimen FH20V16-10, a fuller hysteretic curve (the unloading path was closer to the X axis shown in Fig. 5.17(b)) was observed compared to the other specimens. This may be attributed to a slight increase in the friction coefficient due to the accumulation of friction slips (Fig. 4.8(f)), as the friction systems in specimen FH20V16-10 were reused more frequently than in the other two specimens. This frequent reuse likely led to a relatively higher friction coefficient and enhanced energy-dissipation capacities. Fig. 5.17(c) presents the results of specimen FH20V16-10 from two-round tests. The almost coincident hysteretic curves observed in two tests, both at the damper and frame levels, underscored the consistent performance of the damper with the reused friction system under subsequent loadings. In addition, Fig. 5.19 illustrates the comparisons of the hysteretic responses between the brace and damper for all specimens. The consistency in the hysteretic behaviour between the brace and damper is notable, suggesting that the elastic deformation of the extended steel segment in the brace under loading was minimal.

In general, the frame tests confirmed the feasibility of incorporating the proposed damper into braced frame structures. With the SMA-VFSD, these frames exhibit excellent self-centring behaviour, reliable energy dissipation capacity, and the anticipated multistage energy dissipation mechanism.

### **5.3.6 Energy-dissipation capacity**

The energy-dissipation capacity of the frame specimens was quantified using the absolute cumulative energy consumption ( $W_D$ ) and the equivalent viscous damping

(EVD,  $\zeta$ ) per cycle, as used in section 4.3.6. The calculated cumulative  $W_D$  and  $\zeta$  of the specimens and their comparisons are presented in Fig. 5.20 and Fig. 5.21, respectively. Note that the total energy dissipated by the frame specimens should theoretically equal the sum of the energy absorbed by the damper and by friction energy (e.g., between the lateral brace and the specimen). Additionally, the energy due to friction can be identified as the energy dissipated by the bare specimen (i.e., FH20). To illustrate this, the sum of the energy absorbed by each specimen's damper and the energy of specimen FH20 was calculated and compared to that of the corresponding specimen, as indicated in Fig. 5.20. The observed consistency in energy dissipation indicates that the primary source of energy dissipation in the specimens is the damper, with only a minor contribution from friction within the system. Fig. 5.21(a) shows the influence of the preload of the SMA bolts on the cumulated  $W_D$ . It was observed that increasing the preload of the SMA bolts only marginally enhances the energy-dissipation capacity of the damper. This minor improvement is attributed to the loss of the preload in the SMA bolts within the damper, as detailed in the previous section. As shown in Fig. 5.21(b), the cumulative  $W_D$  of specimen FH20V16-10 exceeded that of specimen FH20V16-13, contrary to the previous damper test results. This inconsistency arose from the relative increase in the friction coefficient of the friction pairs for specimen FH20V16-10, which was attributed to the accumulation of more friction slips. This observation was supported by a fuller hysteretic curve of specimen FH20V16-10 in Fig. 5.17(b). Notably, the slight increase in the friction coefficient with the cumulative slip further enhanced both energy dissipation and load-carrying capacities but had minimal impact on the self-centring behaviour of specimen FH20V16-10. Therefore, this beneficial and controllable increase in the friction coefficient can be considered a safety redundancy and reserve for structures. Additionally, the repeated tests on specimen FH20V16-10 demonstrated comparable dissipated energy, suggesting the reliable energy-dissipation capacity of the frame under sequent excitations. It is worth noting that the  $\zeta$  values of the frame specimens increased marginally and steadily over the loading stages. This suggests that the proposed damper can maintain a consistent and reliable energy-dissipation capacity even under varying levels of deformation in structures. The measured average  $\zeta$  of the frame specimens ranged from around 5% to 10%.

### 5.3.7 Self-centring behaviour

Fig. 5.22 illustrates the evolution of residual drift for all frame specimens in both positive (push) and negative (pull) directions. Note that the letters P and N are appended to each specimen's annotation to indicate the damper's behaviour in the positive and negative directions, respectively. It is evident that all specimens displayed a similar pattern of low-level residual drift (less than 0.2%). An abrupt increase in residual drift in the positive direction was observed and then remained stable over the loading stages, indicating that the residual drift was primarily caused by the above-mentioned fabrication tolerances rather than the plastic deformation in the main frame. Therefore, the impact of the initial gaps resulting from the fabrication tolerances was notable in the positive directions for all specimens, while in the negative direction, the residual deformation could be negligible. It should be noted that these gaps resulting from the fabrication tolerances are challenging to eliminate, particularly given the need for easy assembly of such pin connections on construction sites. The effects of such initial gaps on the seismic performance of structures equipped with the SMA-VFSD requires further attention and will be discussed in the next chapter.

## 5.4 Numerical analysis

As discussed in section 4.5.2, performing a refined numerical analysis for the frame equipped with the SMA-VFSD may be time-consuming, and convergence issues can further hinder computing efficiency. Moreover, accurately simulating the observed fabrication tolerances in the pin connections (illustrated in Fig. 5.10) could also lead to computational stability problems. In addition, employing a refined numerical analysis for evaluating the seismic performance of structures enhanced by the SMA-VFSD at the system level in the subsequent chapter is not feasible. Therefore, a simplified yet reliable numerical model for the test specimens was preferred in this section. This

simplified model was validated against the test data, with a focus on the hysteretic behaviour and energy dissipation capacity of the frame specimen.

#### **5.4.1 Establishment of simplified numerical model**

In this section, establishing the simplified numerical model for the frame specimens was conducted using the OpenSees platform. The effectiveness and accuracy of the newly developed uniaxial material (i.e., MGSC material) in predicting the hysteretic behaviour of the SMA-VFSD have been thoroughly validated, as detailed in section 4.5.2. The same modelling technique was utilised here, to simulate the damper behaviour. The numerical model for the frame specimens is depicted in Fig. 5.23, with some basic geometric dimensions between the centre lines of the specimens provided for reference.

Nonlinear force-based beam-column elements with fibre sections were employed to mesh the beams, columns, and extended rectangular tubes in the frame specimens. The material used was Steel01, with a post-yielding stiffness ratio of 0.02. Rigid beam elements were adopted to simulate the bracket of the pin connections between the damper brace and columns. A square-cross fibre section (100 mm × 100 mm) made of MGSC material was assigned to an element with a length of 550 mm to represent the hysteretic behaviour of the damper. Material constants for the MGSC material were determined based on the developed analytical model (or test data) and the geometric information of the fibre section. Specifically, the predicted force versus axial displacement curve of the damper was first converted to stress versus strain data, from which the material constants were then calculated. EqualDOF constraints were used to model all pin connections, while fixed constraints were applied to simulate the column bases in the specimens. It is important to note that the initial gaps among the pin

connections were not accounted for in the numerical model described above, which may result in discrepancies between the predictions and the test data. To address this issue, a simplified equivalent strategy was proposed. It was assumed that the initial gaps among all pin connections were integrated and represented by the hysteretic behaviour with an initial slip for the damper. This was achieved by employing a combination of MGSC material and multi-linear elastic material in series. The multi-linear elastic material exhibited bilinear behaviour, with an initial slip followed by rigid elastic behaviour in the positive direction, and rigid elastic behaviour in the negative direction. The magnitude of the slip strain could be determined from the test data. The behaviour of this material combination in series is illustrated in Fig. 5.24, was used to model the damper behaviour with initial gaps.

### 5.4.2 Numerical results

In Fig. 5.25, the hysteretic curves of interstorey drift obtained from the numerical models, both considering and not considering the initial gaps, are compared against the test data for specimen FH20V16-10. A more consistent agreement was observed between the numerical model accounting for the initial gaps and the test data. Therefore, the numerical model considering the initial gaps was used to predict the test results. Their comparisons of the hysteretic responses at the frame and damper levels are depicted in Fig. 5.15 and 5.16, respectively. The good agreement demonstrated the accuracy of the adopted numerical model in predicting the hysteretic behaviour of the specimens. Additionally, the comparisons of the cumulative  $W_D$  and EVD ( $\xi$ ) of the tests and numerical predictions are shown in Fig. 5.20. The good agreement of the above comparison results confirmed that the established numerical model can precisely trace the energy-dissipation capacity for structures equipped with the SMA-VFSD.

Therefore, the modelling technologies for the structures equipped with the damper can be reliably used in the subsequent seismic performance evaluation at a system level.

## 5.5 In summary

The primary objective of this chapter was to investigate the viability of integrating the proposed SMA-VFSD into structural applications. To achieve this, the chapter commenced with the potential structural applications of the proposed damper in several scenarios. Following this, experimental and numerical analyses were conducted to investigate the hysteretic behaviour of a specific structural application: a one-bay, one-storey braced frame equipped with the damper. Five frame specimens underwent quasi-cyclic testing, and the data obtained was compared with a simplified numerical model developed for this purpose. The main conclusions were outlined as below:

- The damper effectively provided lateral strength and energy-dissipation capacity for the braced frame when incorporated in the braced frame.
- The frame demonstrated a multistage energy-dissipation behaviour with flag-shaped hysteretic curves, mirroring the findings from the previous damper test. This indicated that the frame's hysteretic characteristics was governed by the damper and can be flexibly adjusted by altering the design parameters of the damper.
- The hysteretic behaviour of the frame specimens was basically not influenced by the loading history, indicating that the frame equipped with the SMA-VFSD has stable and reliable performance under multiple loadings.
- The frame exhibited excellent self-centring behaviour with minimal residual interstorey drifts. This residual drift resulted from the fabrication tolerance rather than the development of plastic deformation in the main frame. Additionally, the

test results showed that equivalent viscous damping (EVD) of the specimens was around 5%-10% and remained a steady increase over all loading stages.

- The effectiveness of the simplified frame model which could consider the initial gaps in tracing the hysteretic behaviour at both the frame and damper levels was validated, offering a highly efficient tool for evaluating the seismic performance of structures enhanced by the SMA-VFSD at the system level.

Table. 5.1 Material constants for longer SMA bolt

Material Constants	SMA
Forward transformation stress in tension, $\sigma_{Ms}$ (MPa)	300
Forward transformation stress in tension, $\sigma_{Mf}$ (MPa)	420
Reverse transformation stress in tension, $\sigma_{As}$ (MPa)	200
Reverse transformation stress in tension, $\sigma_{Af}$ (MPa)	100
Poisson ratio at austenite state, $\nu_A$	0.33
Poisson ratio at martensite state, $\nu_M$	0.33
Maximum transformation strain, $\epsilon_L$	0.025
Austenite modulus of elasticity, $E_A$ (GPa)	35
Martensite modulus of elasticity, $E_M$ (GPa)	30

Table. 5.2 Information on frame specimens

Specimens	Sloping angle( $\theta$ )	Preload of SMA bolts(kN)	Preload of disc spring system(kN)
FH20	-	-	
FH20V16-7	7	16	
FH20V8-10		8	20
FH20V16-10	10		
FH20V16-10- R		16	
FH20V16-13	13		

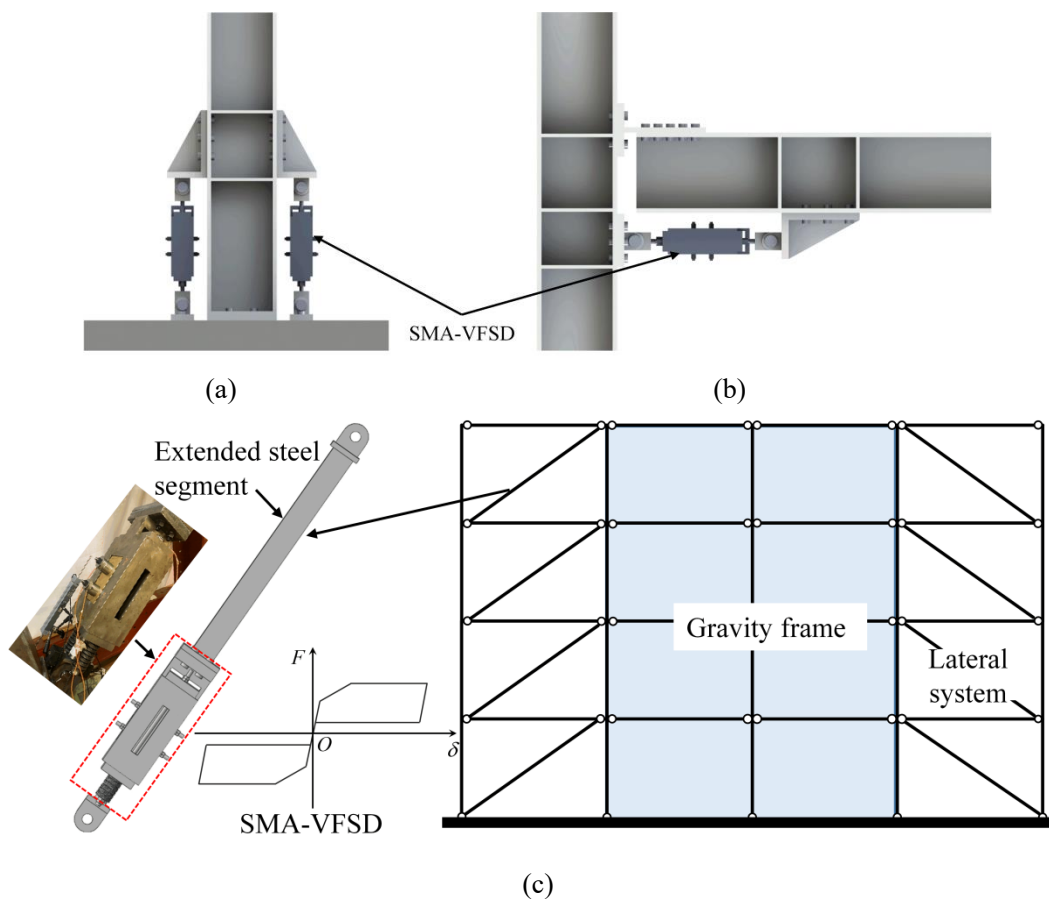


Fig. 5.1. Engineering applications of SMA-VFSD: (a) rocking column base; (b) beam-to-column connection; and (c) braced frame

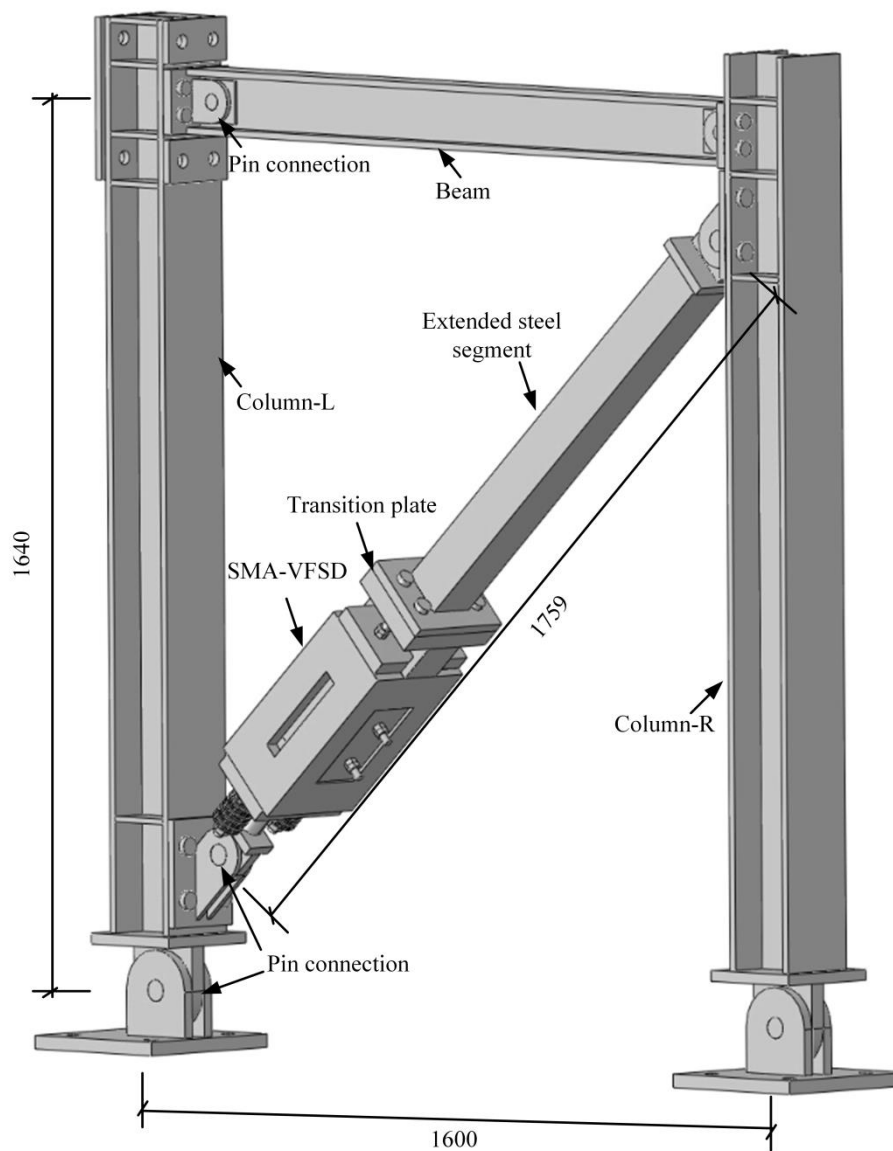
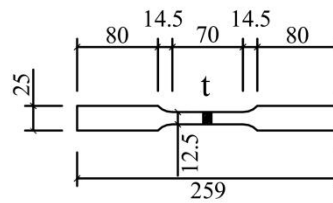


Fig. 5.2. Braced frame equipped with SMA-VFSD



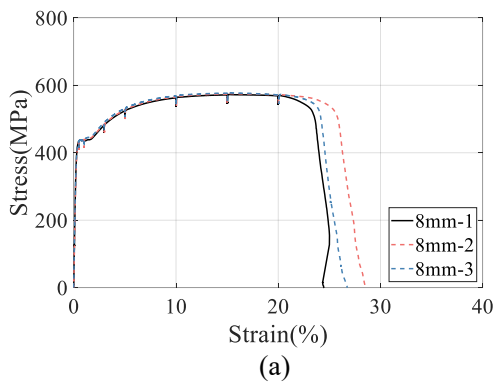
(a)



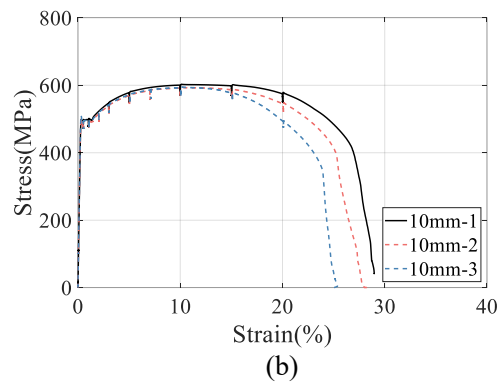
(b)

$t = 8/10/12/14$   
Unit: mm

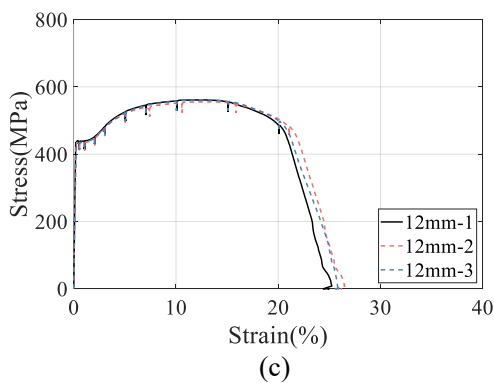
Fig. 5.3. Material test: (a) test setup; (b) dimension of coupon



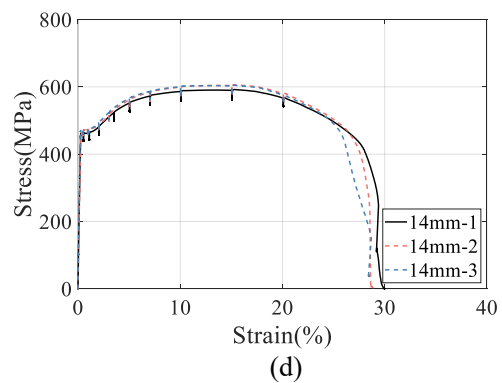
(a)



(b)



(c)



(d)

Fig. 5.4. Result of coupon test: (a) 8 mm; (b) 10 mm; (c) 12 mm; and (d) 14 mm

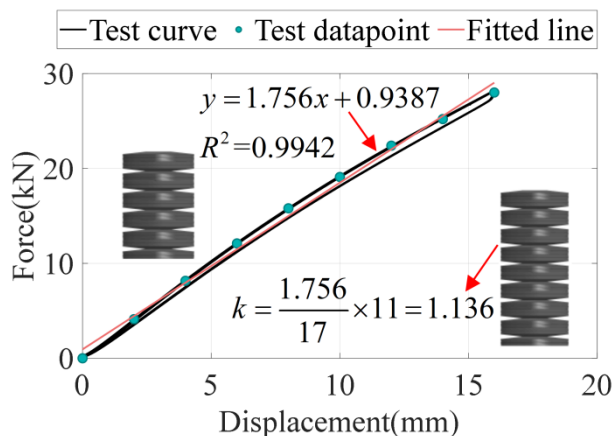


Fig. 5.5. Stiffness of disc spring group

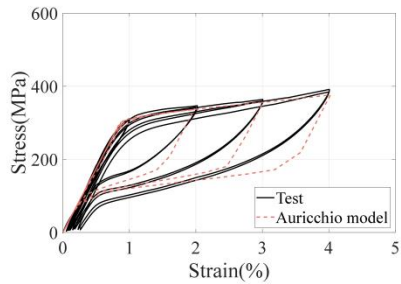
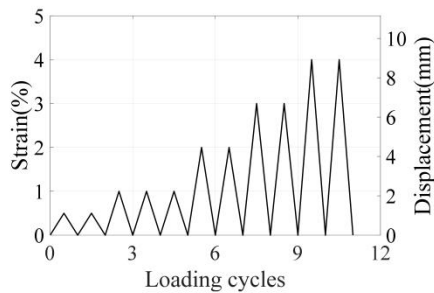
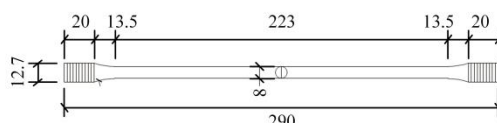
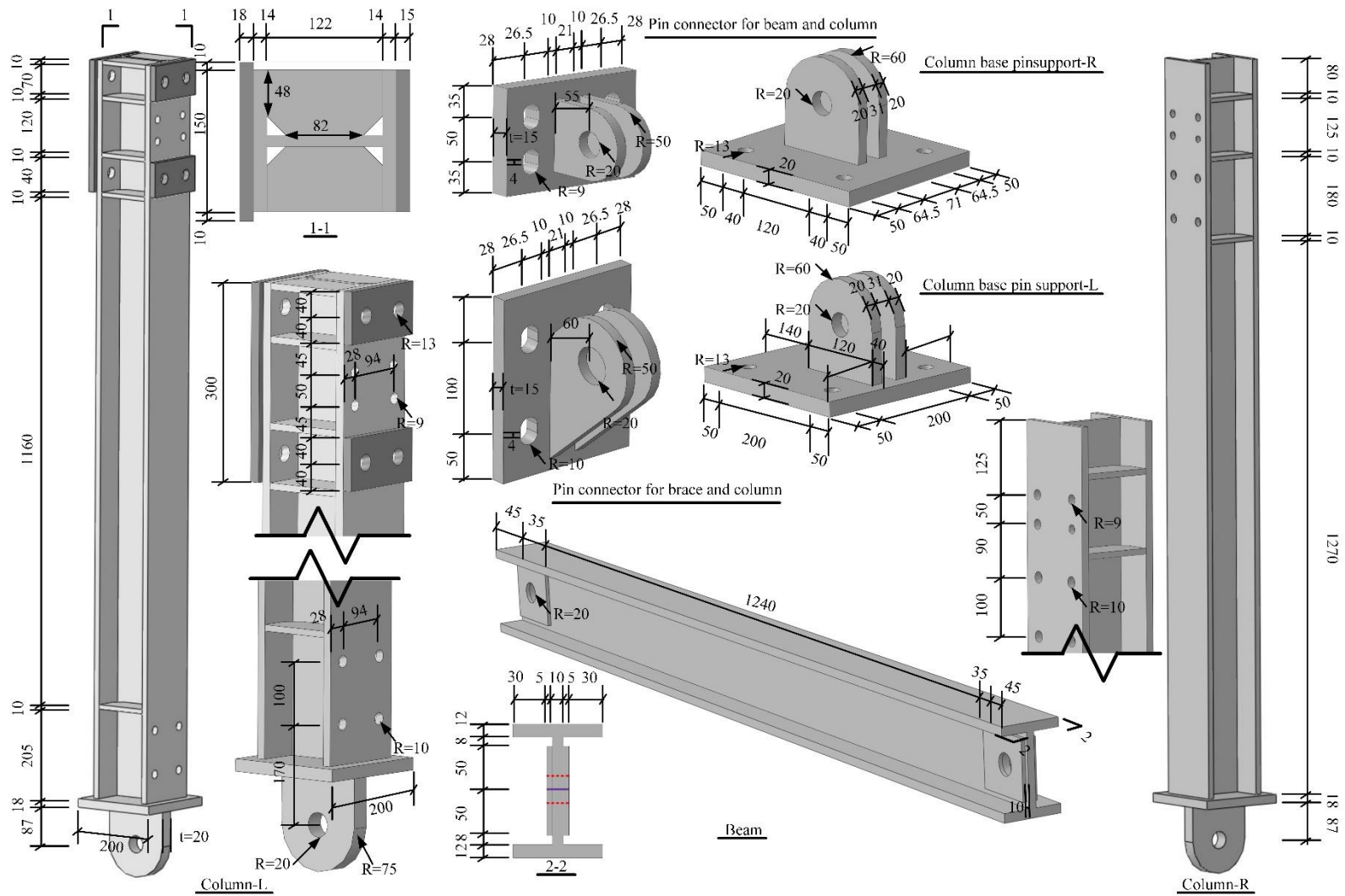


Fig. 5.6. SMA bolt test: (a) test setup; (b) dimension; (c) loading protocol; and (d) test result



(a)

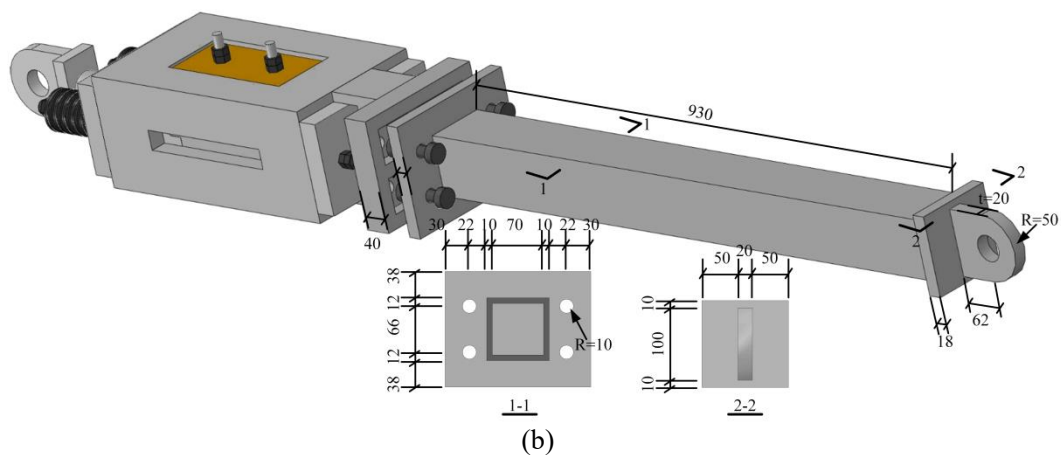


Fig. 5.7. Dimension of the frame specimen: (a) structural members; and (b) damper brace

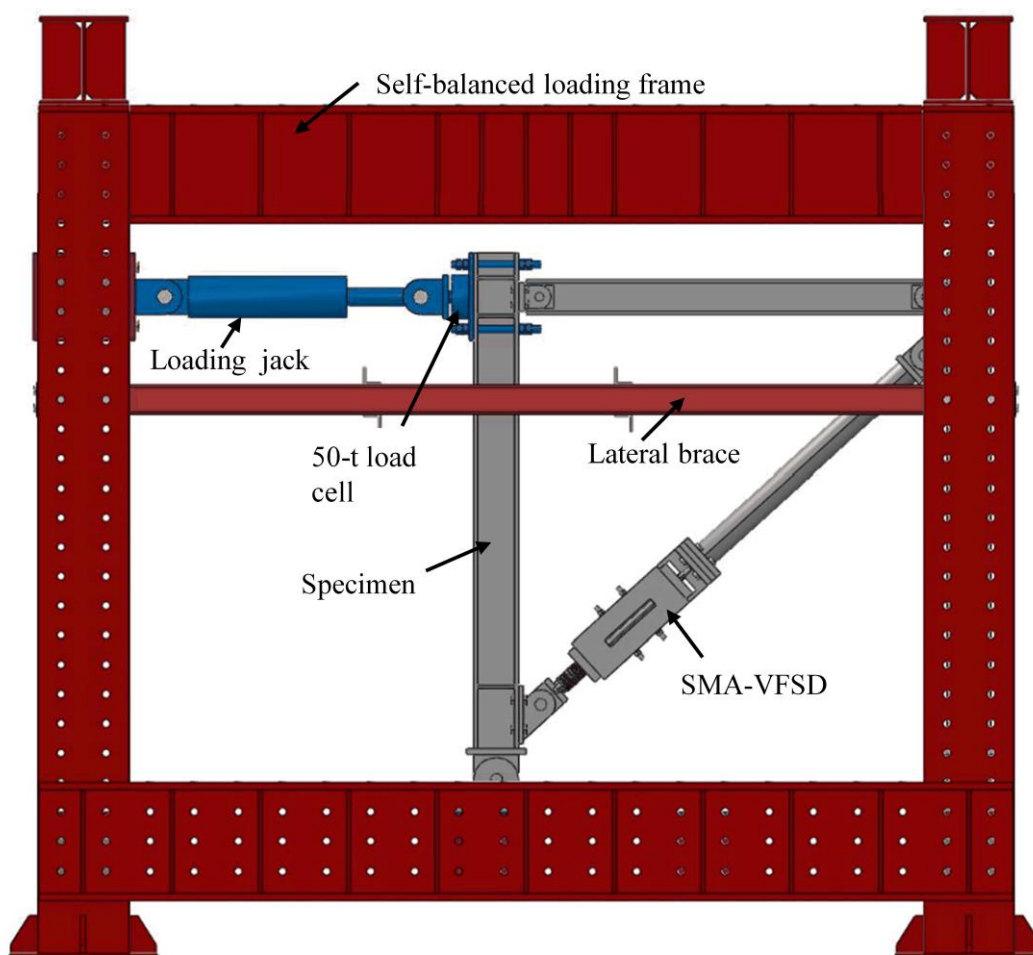


Fig. 5.8. Diagram of test setup for braced frame test

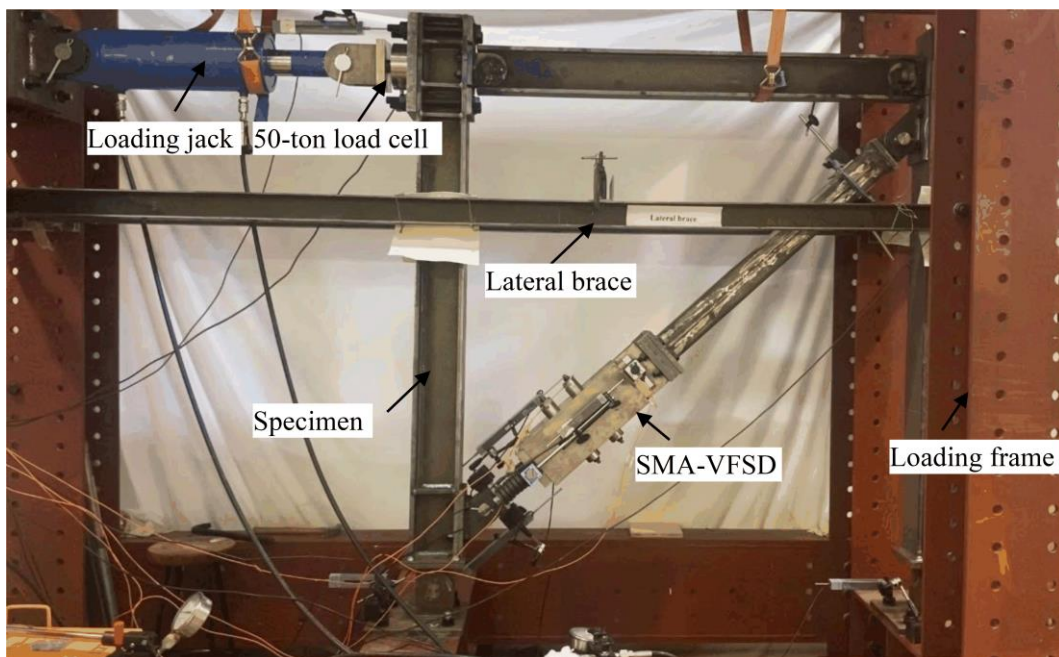


Fig. 5.9. Photo of braced frame test

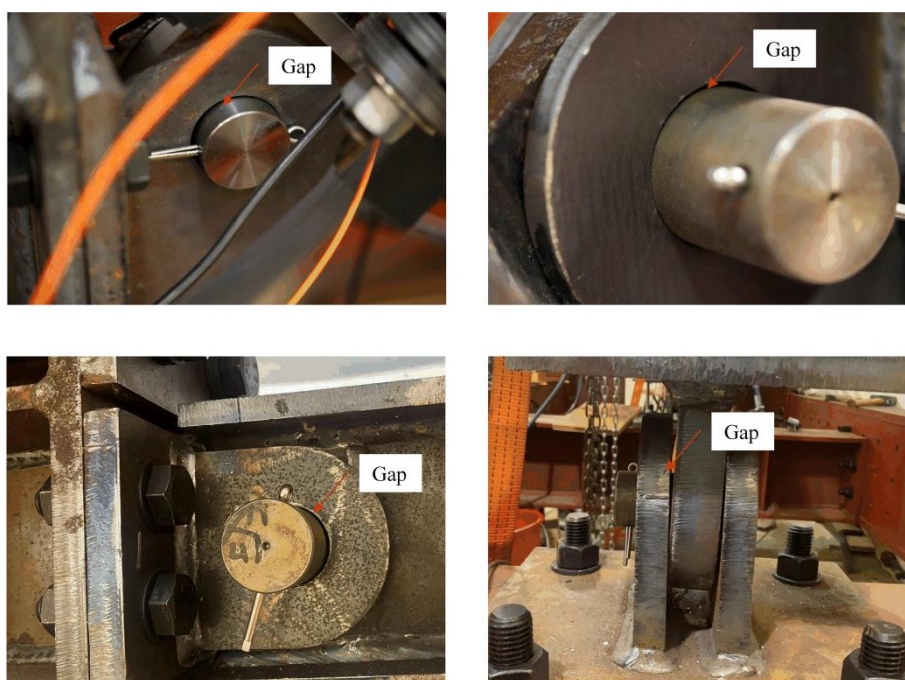


Fig. 5.10. Visible gap due to fabrication tolerances

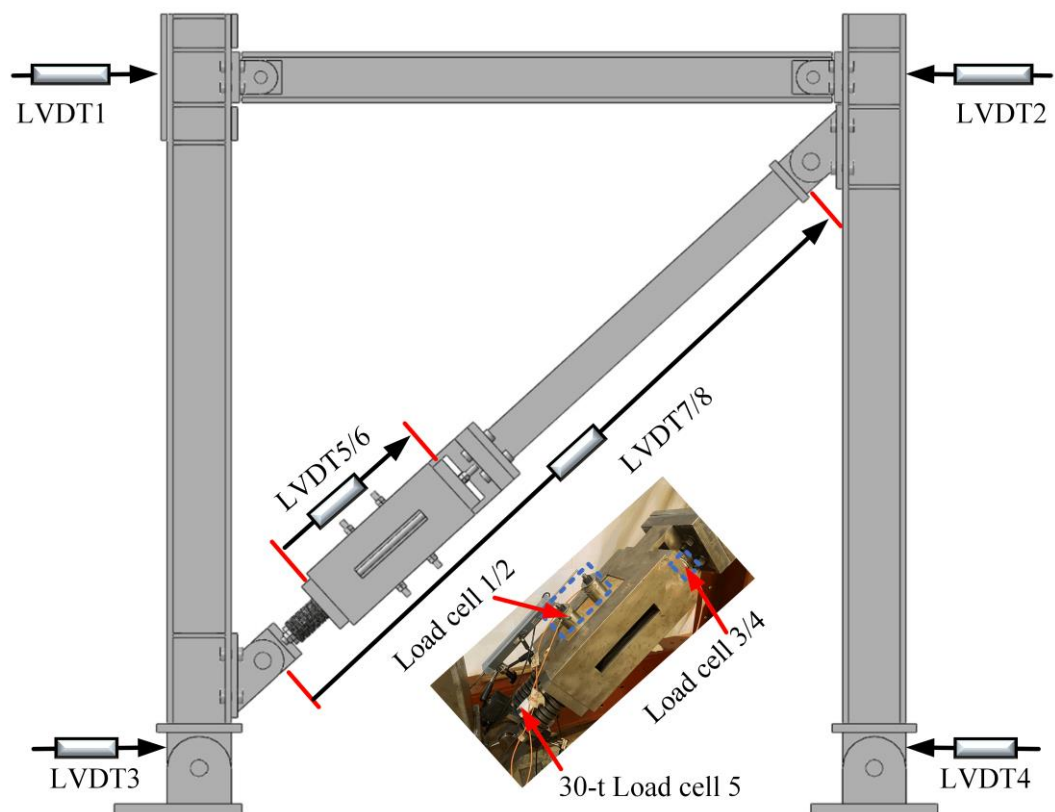


Fig. 5.11. Measurement plan

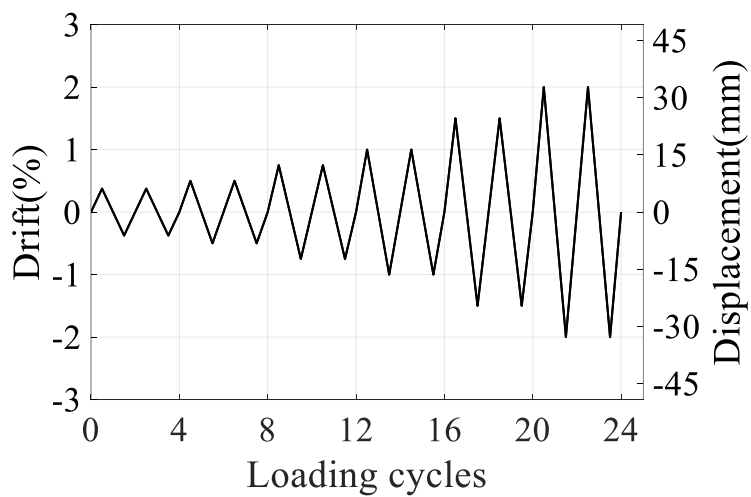
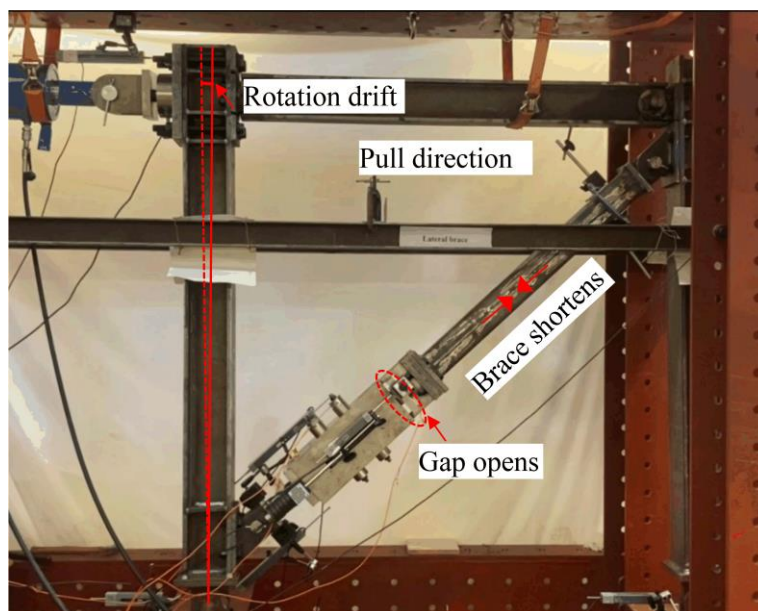
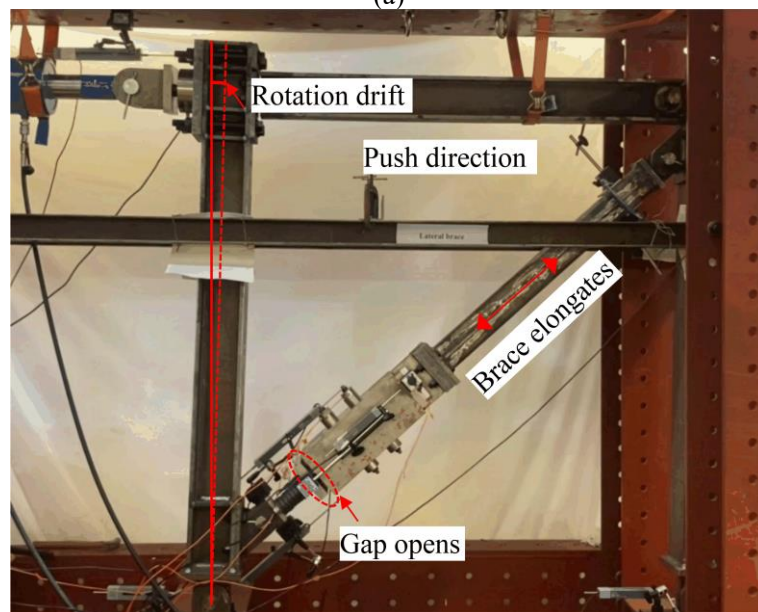


Fig. 5.12. Loading protocol



(a)



(b)

Fig. 5.13. Deformation states of the damper and frame at the maximum drift amplitudes in the pull and push directions: (a) Push direction; and (b) Pull direction

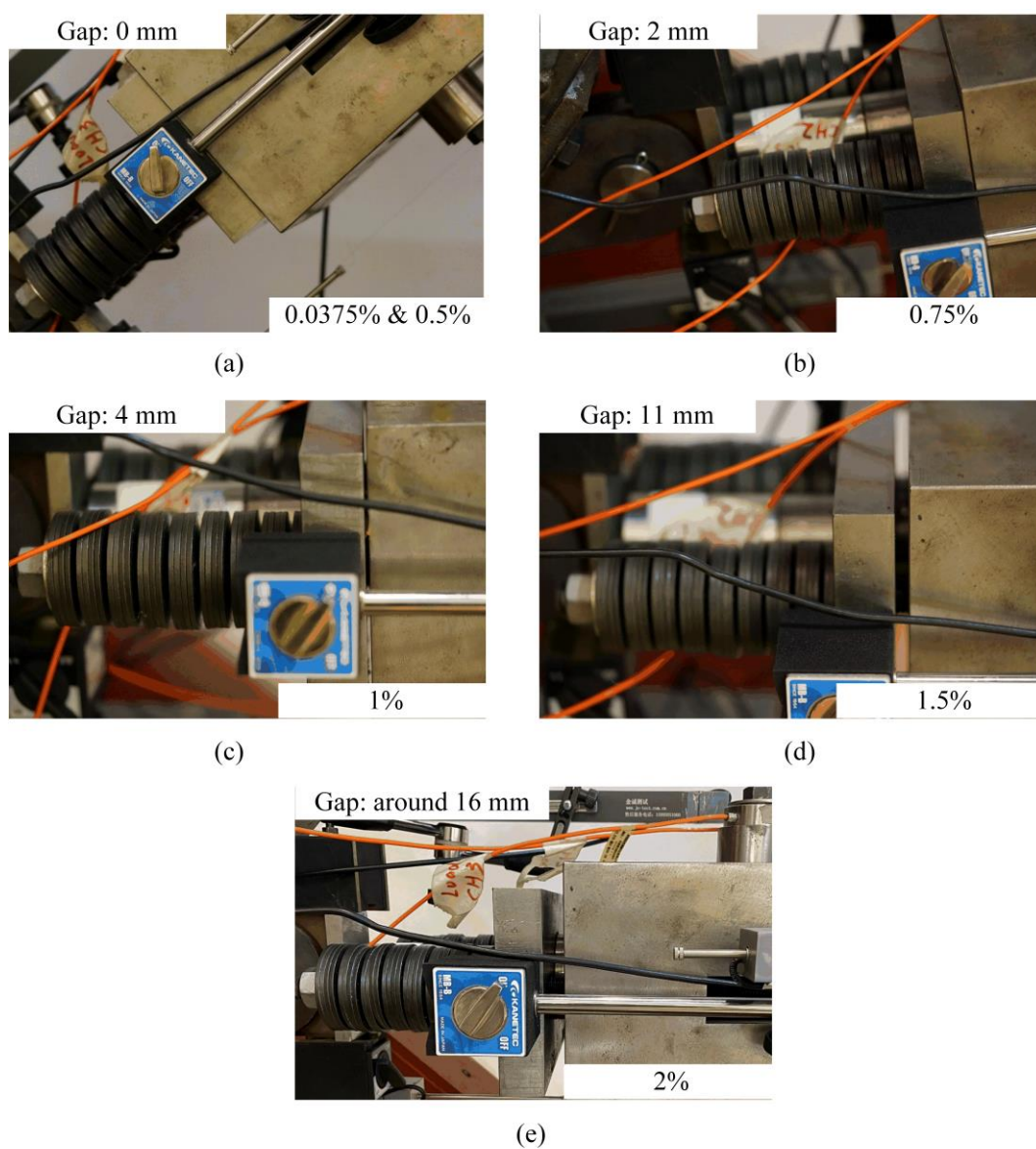
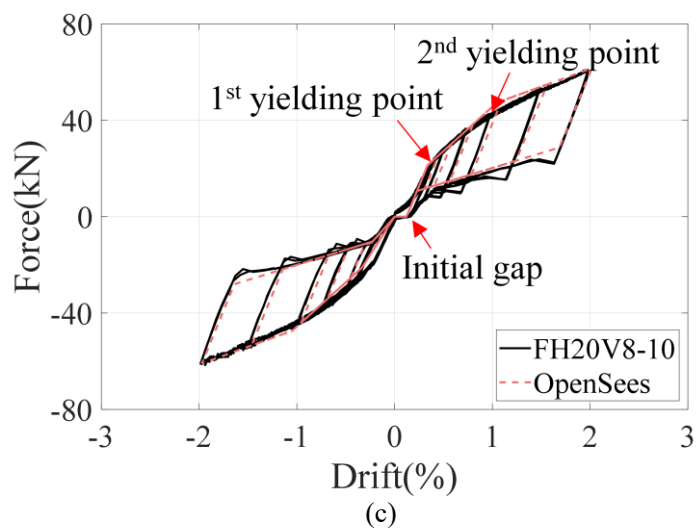
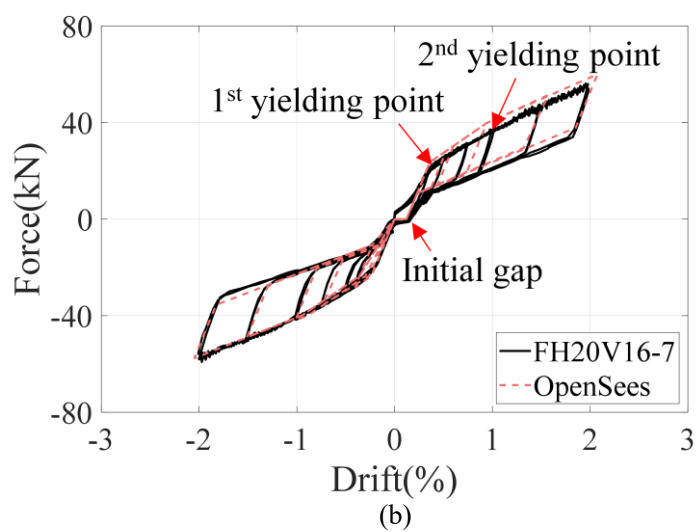
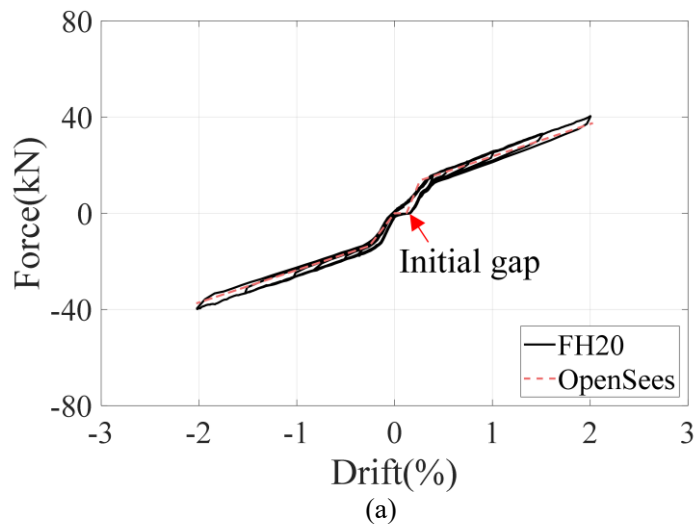


Fig. 5.14. Gap formation of the damper in the specimens:(a) 0.375% & 0.5%; (b) 0.75%; (c) 1%; (d) 1.5%; and (e) 2%



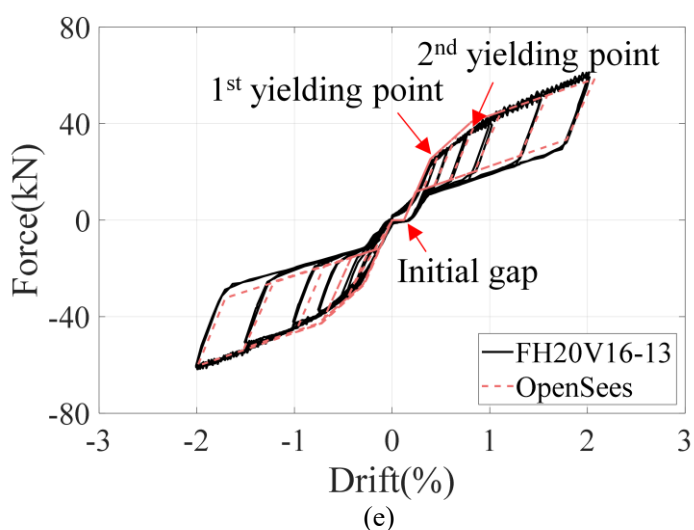
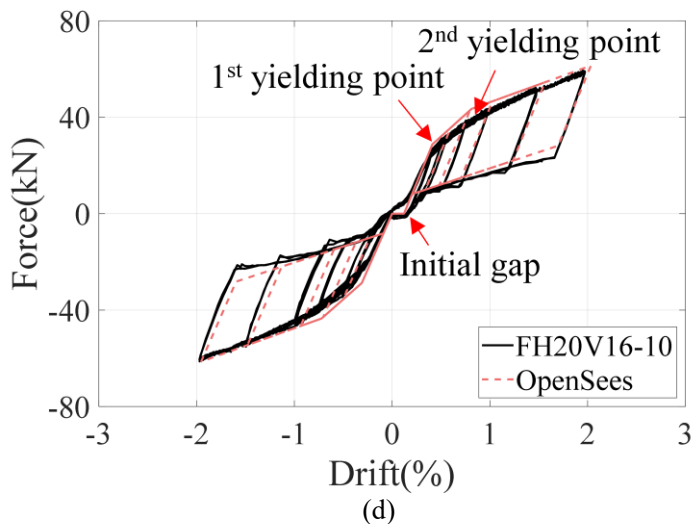
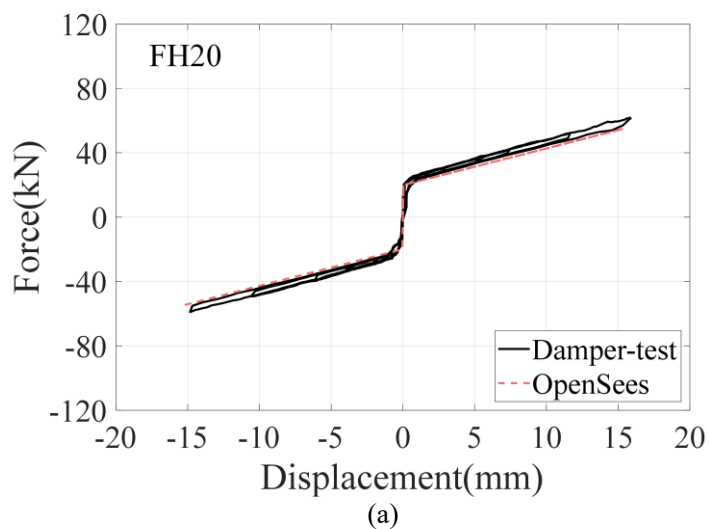
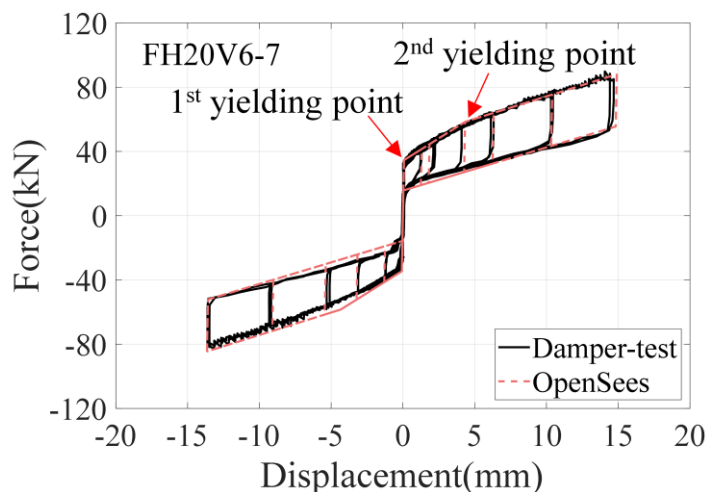
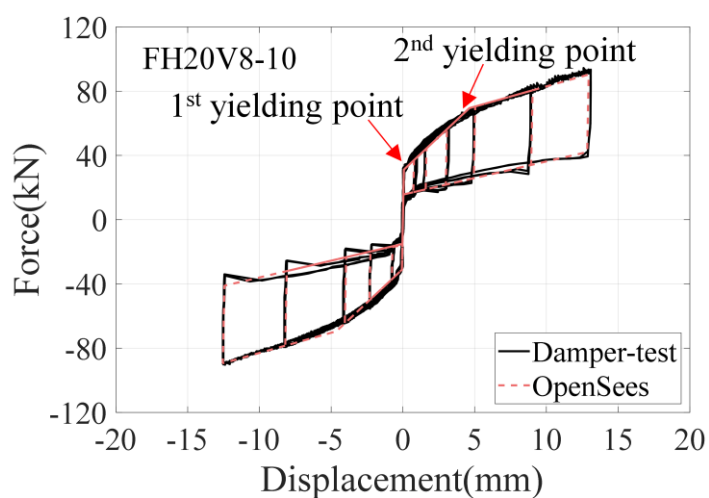


Fig. 5.15. Hysteretic curves for test specimens: (a) FH20; (b) FH20V16-7; (c) FH20V8-10; (d) FH20V16-10; (e) FH20V16-13

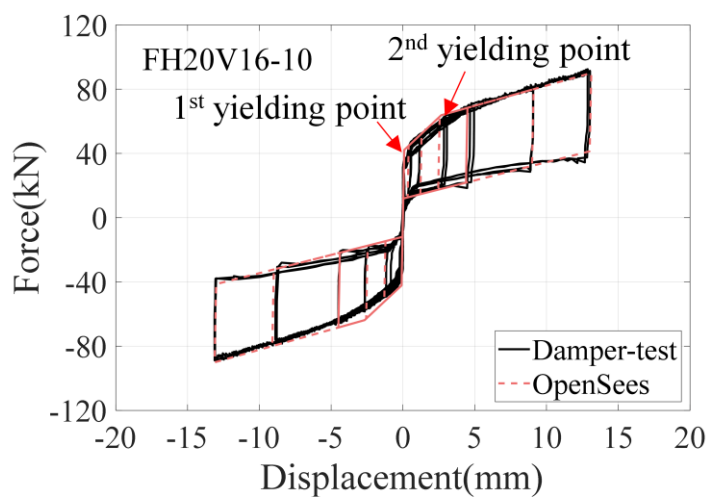




(b)



(c)



(d)

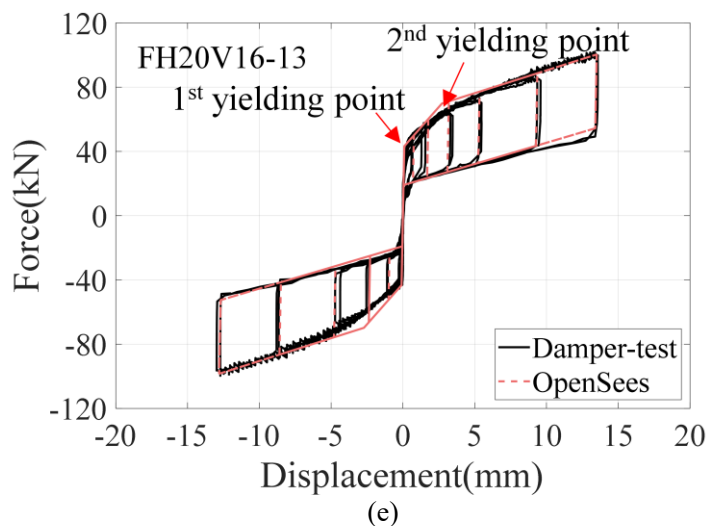
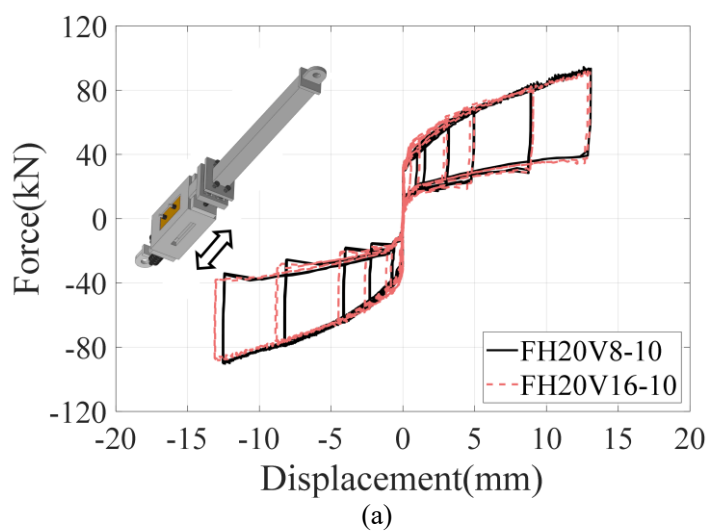
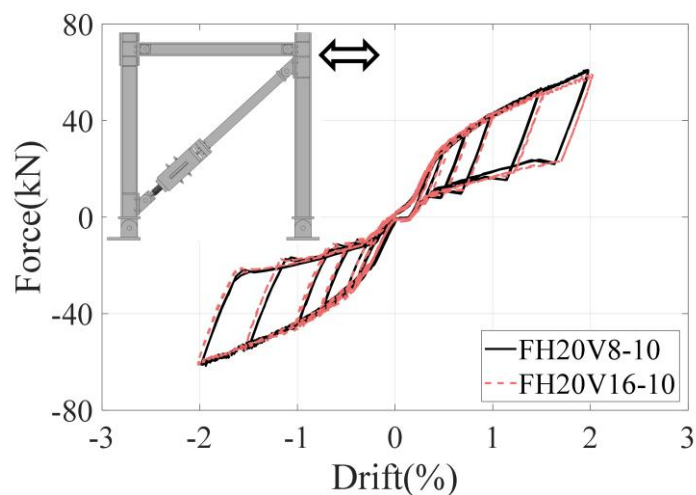
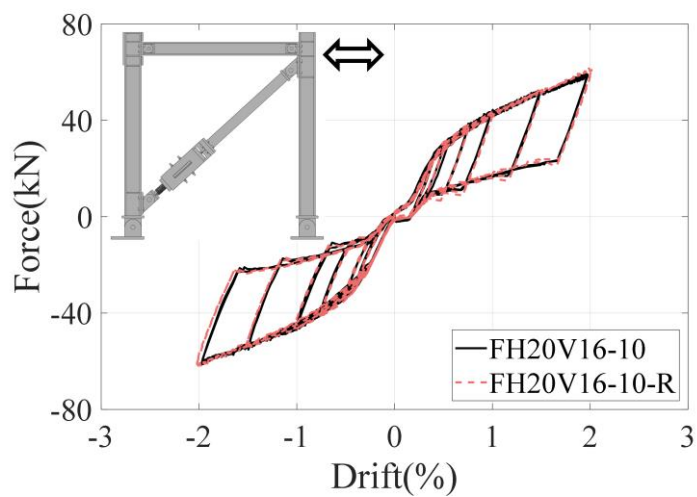
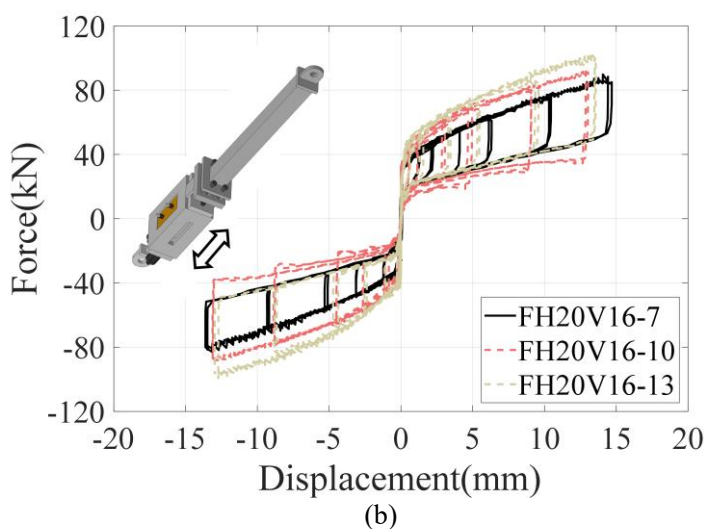
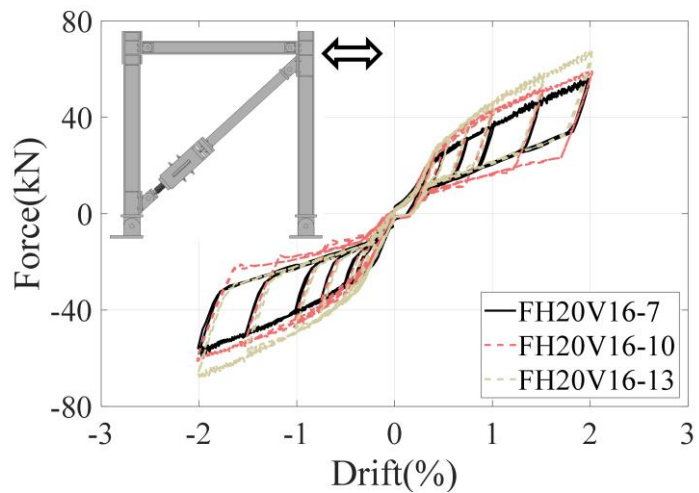


Fig. 5.16. Hysteretic curves of the SMA-VFSD for the test specimens: (a) FH20; (b) FH20V16-7; (c) FH20V8-10; (d) FH20V16-10; and (e) FH20V16-13





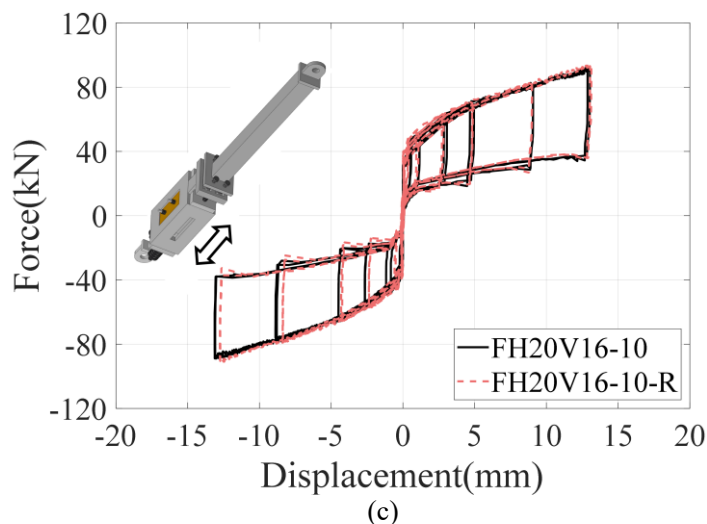


Fig. 5.17. Comparisons of the hysteretic curves of test specimens (frame and damper levels): (a) effect of preload, (b) effect of sloping angle, and (c) effect of repeated tests

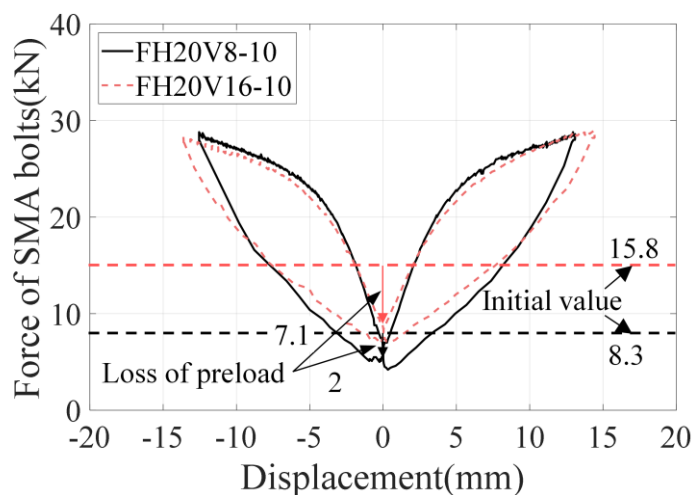
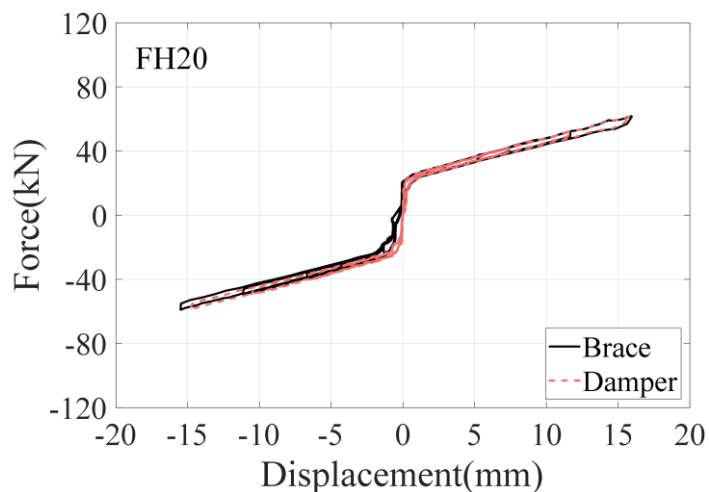
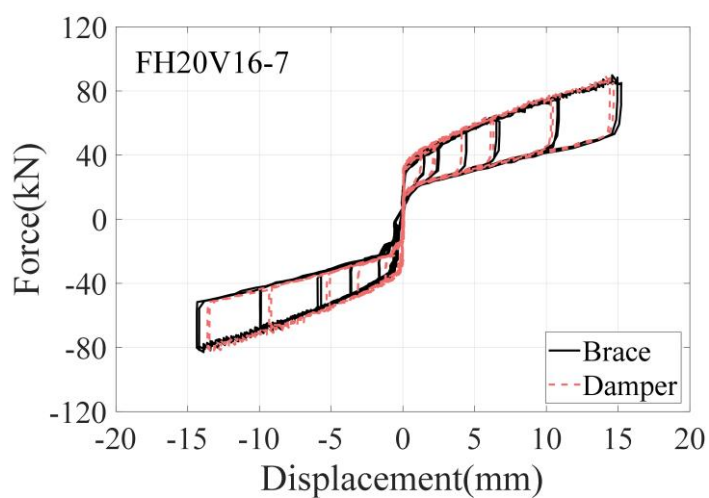


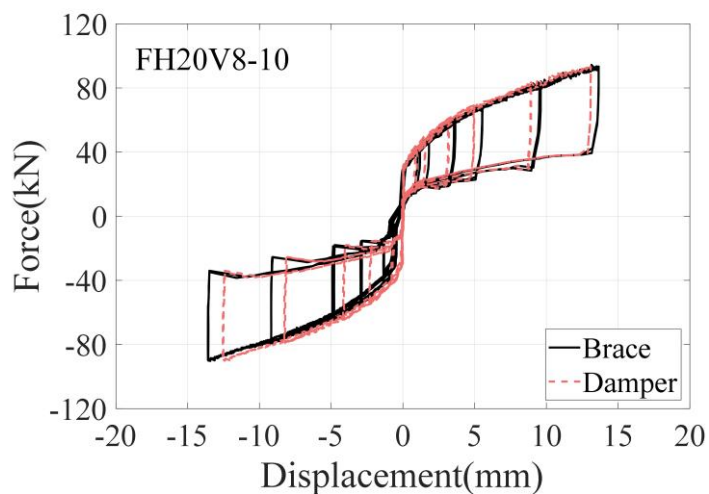
Fig. 5.18. Loss of total preloads of the SMA bolts during the last loading cycle of specimens FH20V8-10 and FH20V16-10



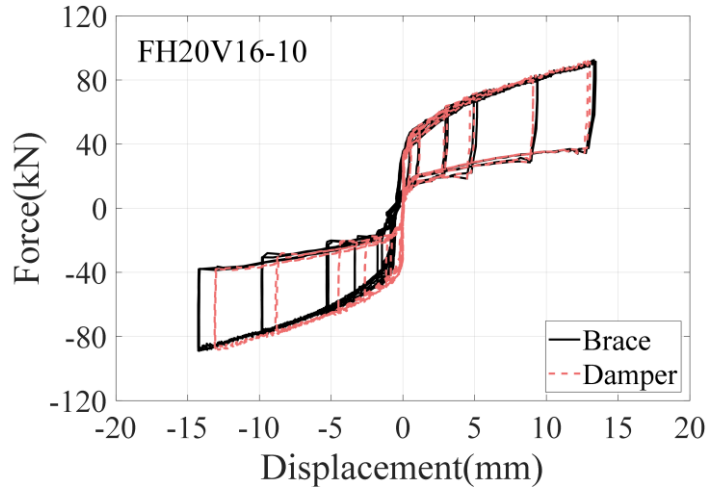
(a)



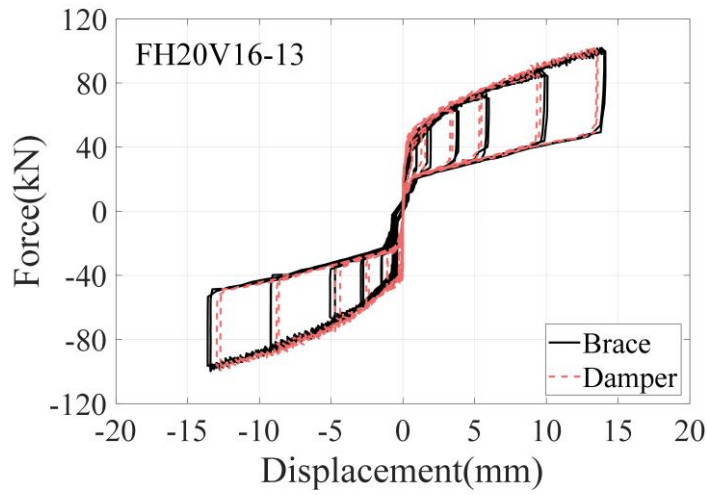
(b)



(c)

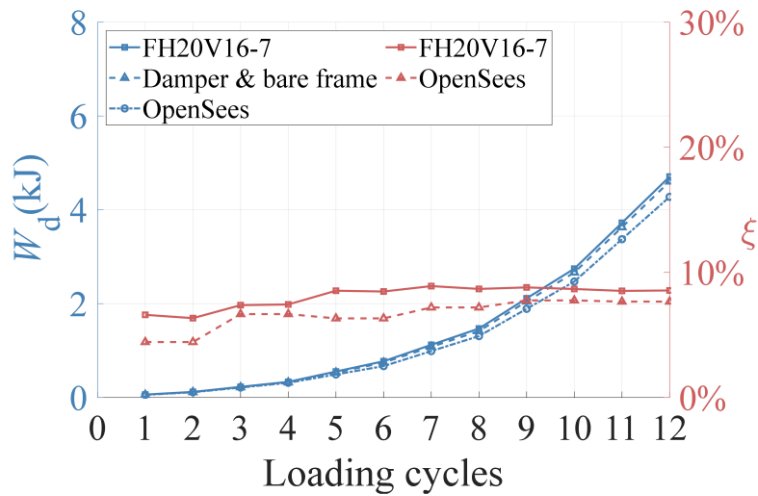


(d)



(e)

Fig. 5.19. Comparison of hysteretic curves of the brace and SMA-VFSD for the test specimens: (a) FH20; (b) FH20V16-7; (c) FH20V8-10; (d) FH20V16-10; and (e) FH20V16-13



(a)

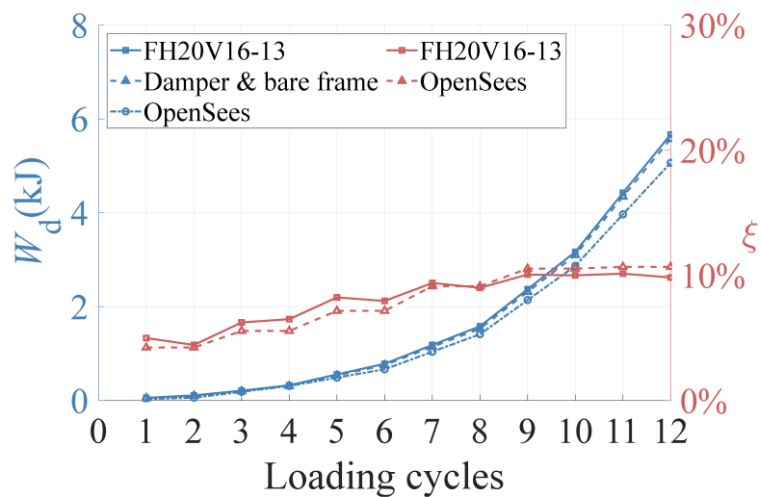
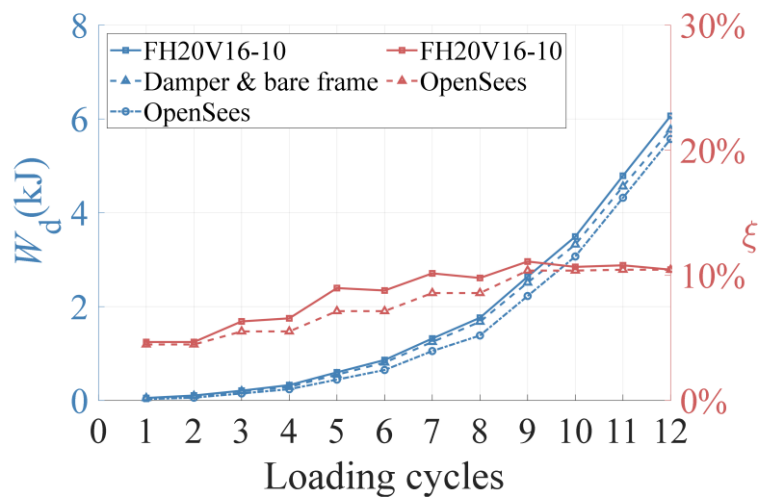
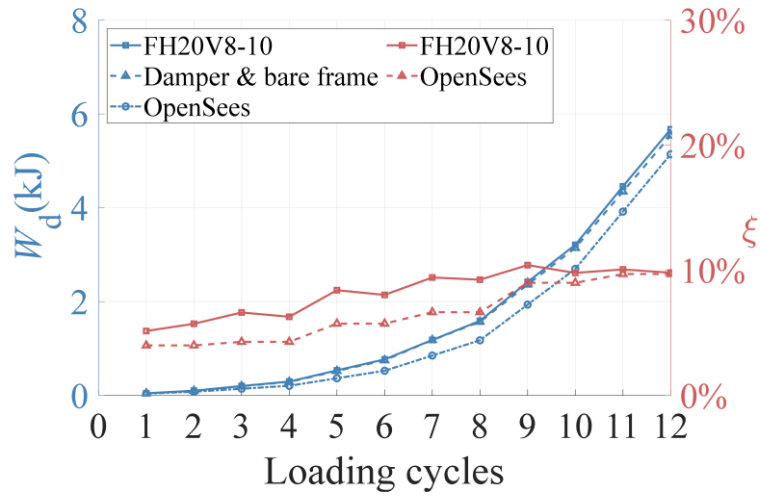


Fig. 5.20 Cumulative energy dissipation and  $\xi$  of test specimens: (a) FH20V16-7, (b) FH20V8-10, (c) FH20V16-10, and (d) FH20V16-13

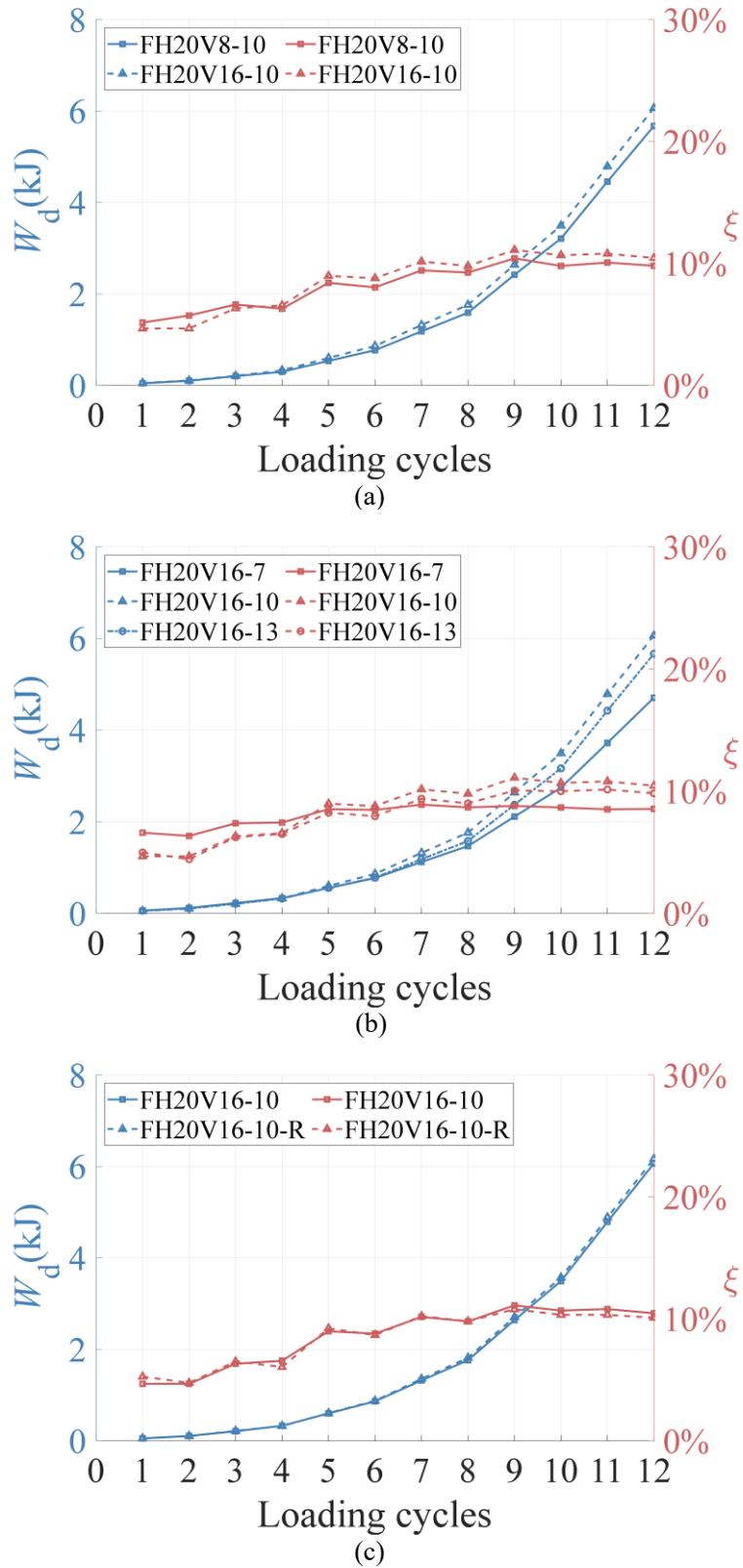


Fig. 5.21. Comparisons of the cumulative energy dissipation and  $\zeta$  of test specimens: (a) effect of preloads, (b) effect of sloping angles, and (c) effect of repeated tests

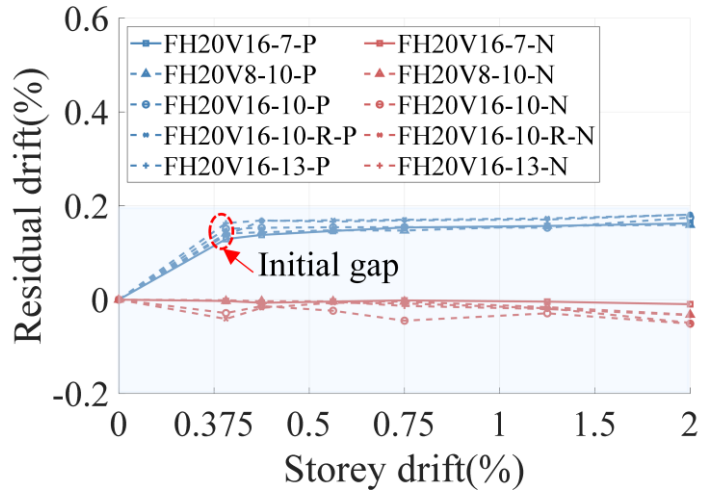


Fig. 5.22. Development of residual drift of test specimens

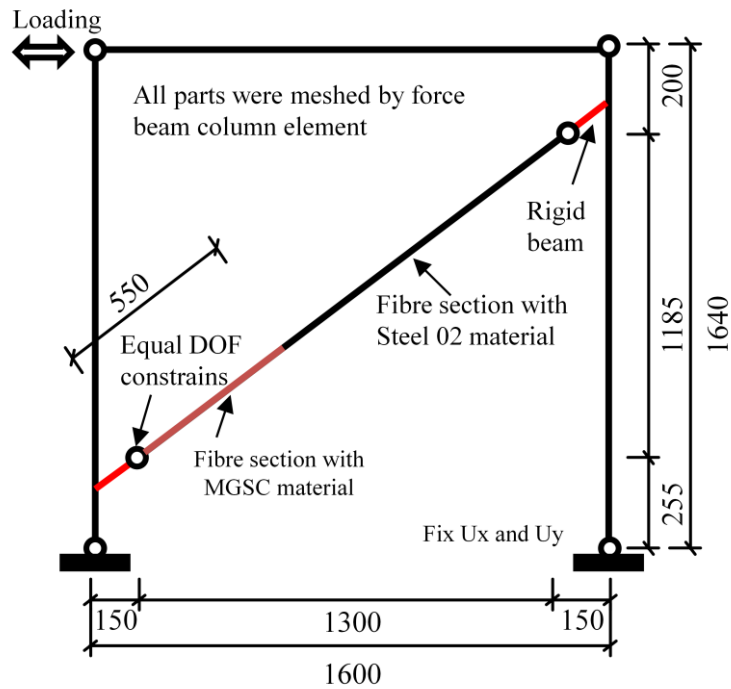


Fig. 5.23. Simplified numerical model for test specimens

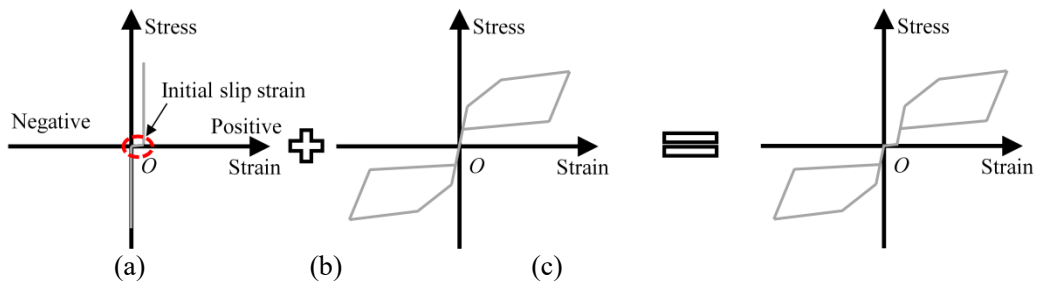


Fig. 5.24. Material behaviour: (a) multi-linear elastic material; (b) MGSC material; and (c) combination of multi-linear material and MGSC material in series

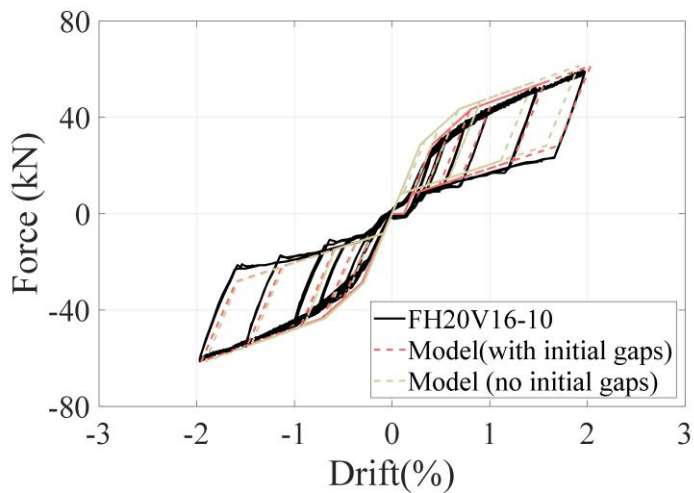


Fig. 5.25. Comparison of hysteretic curves obtained by numerical models and test data for specimen FH20V16-10

# Chapter 6 Seismic performance evaluation and demand analysis on braced frames<sup>1</sup>

## 6.1 Introduction

Chapter 5 demonstrated the feasibility of the proposed SMA-VFSD within a braced frame at the substructure level via detailed experimental and numerical studies. The braced frame specimens showcased consistent hysteretic characteristics, specifically, a multistage energy-dissipation mechanism as observed in the damper test. The seismic performance of braced structures equipped with the proposed damper was evaluated at the system level numerically and was presented in this chapter. Firstly, a prototype building equipped with the SMA-VFSD was designed and simulated using the validated modelling technologies provided in section 5.4.2. To demonstrate the effectiveness of the proposed damper in mitigating seismic responses, such as absolute peak floor accelerations (PFAs) and

---

<sup>1</sup>Chapter 6 is based on two published studies and is being reproduced with the permission of Elsevier. Zhang, P., Yam, M.C.H., Ke, K., Zhou, X.H., and Chen, Y.H. (2022). Steel moment resisting frames with energy-dissipation rocking columns under near-fault earthquakes: Probabilistic performance-based-plastic-design for the ultimate stage. *Journal of Building Engineering*, 54104625 & Ke, K., Yam, M.C.H., Zhang, P., Shi, Y., Li, Y., and Liu, S. (2023). Self-centering damper with multi-energy-dissipation mechanisms: Insights and structural seismic demand perspective. *Journal of Constructional Steel Research*, 204 107837.

overstrength-related issues in structures, a comparative study was conducted on structures equipped with the SMA-VFSD and a previous type of damper (referred to as PD for comparison, Hu et al. 2022), as shown in Fig. 6.1(b). The PD exhibited bilinear flag-shaped hysteretic curves without a dual-stiffness reduction mechanism. Following this, the seismic behaviour of structures with and without initial gaps in the proposed damper braces was examined to evaluate the effect of fabrication tolerances (i.e., clearance among pin connections) on the structural performance. Finally, using a self-developed calculation programme, nonlinear constant-ductility spectral analyses were conducted on a Single Degree of Freedom (SDOF) system, representing self-centring structures showing multistage energy-dissipation characteristics. The spectral analyses aimed to explore the seismic demands of structures equipped with the SMA-VFSD under different combinations of hysteretic parameters and earthquake records.

## **6.2 Seismic performance evaluation on braced frame equipped with SMA-VFSD**

### **6.2.1 Design of prototype building**

In this section, the viability of the SMA-VFSD in mitigating seismic performance for structures was validated through a case study. A prototype braced office building, equipped with the SMA-VFSD (referred to as BF-SMA-VFSD), was designed for a stiff soil site according to the Chinese code (GB50011-2011, Jiangsu province, China). Cyclic pushover and dynamic analyses were conducted to evaluate its behaviour under static loads and earthquakes. The damper brace configuration, depicted in the structural elevation (Fig. 6.1(b)), basically remained consistent with that used in Chapter 5. It comprised the SMA-VFSD and an extended steel segment (i.e., a circular steel tube

instead of a rectangle steel tube utilised in this chapter, as illustrated in Fig. 6.1(b)). The damper brace was positioned diagonally within the structure to withstand lateral forces. The beams and columns were connected using simple connections, and all column bases were fixed. H-shaped beams and box-shaped columns (with a nominal yielding strength of the adopted steel material is 345 MPa) were utilised. As confirmed in chapter 5, it is noteworthy that the braced frame demonstrated a consistent multistage energy-dissipation mechanism similar to that observed in the damper. As this is a novel braced structure showcasing a different hysteretic behaviour, there is no established design methodology to follow. Therefore, a trial-and-error design approach was employed based on the Chinese code (Chinese standard (GB50011-2011)). Initially, SAP2000 software was utilised to perform the elastic capacity design for the columns, beams, and damper braces under various load combinations (i.e., frequently occurred earthquakes (FOE), dead/live load, and wind). The information on the loads can be found in the reference (Chinese standard (GB50011-2011)). Following the critical load combination, the 1<sup>st</sup> yielding strength of the damper braces at the 1<sup>st</sup>, 2<sup>nd</sup>, and 3<sup>rd</sup> stories was determined. Finally, direct nonlinear dynamic analyses were conducted to examine the story drifts of structures under design basis earthquake level (DBE) and maximum considered earthquake level (MCE), respectively. Iterative designs were employed until the storey drifts satisfied the target requirements. Based on previous research recommendations, the drift limits for structures with simple beam-to-column connections under DBE level and MCE level were set at 2% and 4%, respectively in this study (Fahnestock et al. 2007; Qiu et al. 2017). This decision was supported by the satisfactory ductility observed in structures using simple connections. It should be noted that the current study did not propose a comprehensive design and evaluation framework for structures equipped with SMA-VFSD according to the multi-

performance-level targets under earthquake loading. This area requires further investigation in future research. The design guidelines for achieving these multi-performance-level targets in structures equipped with SMA-VFSDs should follow that the damper braces remain elastic up to the first yielding under the FOE level, function between the first and second yielding stages under the DBE level, and fully activate upon reaching the second yielding under the MCE level. After the iterative design process, the 1<sup>st</sup> yielding strength of the damper braces at the 1<sup>st</sup>, 2<sup>nd</sup>, and 3<sup>rd</sup> stories were determined as 280 kN, 220 kN, and 140 kN, respectively. Additionally, to meet the 4% storey drift limit under MCE level, the allowable axial deformation of the damper brace in this design was set at 100 mm for all storeys. Based on the yielding strength and deformation demand of the damper braces, the adopted SMA bolts and other mechanical design parameters of the damper for each storey were determined utilising the analytical hysteretic model developed in Chapter 3, and the results are outlined in Table 6.1. With these mechanical parameters established and the SMA bolts selected, subsequent detailed design of the damper configuration and each component can proceed accordingly. For the preliminary structural analyses, the temporary length of the damper was approximately considered as 1 m. The dimensions of the beams, columns and extended steel segments are also provided in Fig. 6.1(b).

### **6.2.2 Numerical model of prototype building and results**

Using the validated modelling technologies presented in section 5.4.1, a 2D representative braced frame was modelled in OpenSees, shown in Fig. 6.2. The centreline model of the braced frame was established, and the analysis also accounted for the P-delta effect. After the iterative design process, the first mode of the braced frame was 0.49 s. Two ensembles of earthquake ground motion records (LA1-LA20

and LA21-LA 40, respectively) developed by Somerville (Somerville 1997) were selected as input excitations, and their 5% damped spectral acceleration are shown in Fig. 6.3(a)-(b), respectively. The mean spectral acceleration of the two selected earthquake assembles were comparable to the DBE level and MCE level, respectively, in accordance with American codes (ASCE7-16). In addition, to illustrate the control of the overstrength of the SMA-VFSD, a previous type of damper (PD) proposed by Hu et al. (2022), exhibiting an improved bilinear flag-shaped hysteretic behaviour (shown in Fig. 6.1(b)), was also considered for comparison in the braced frame (labelled as BF-PD). The seismic behaviour of the structures with the two types of dampers was directly compared. It is important to note that the difference between the SMA-VFSD and the PD lies in whether stiffness and strength are decoupled through a multi-yielding mechanism. Before the dynamic analyses, modal cyclic pushover analyses (i.e., 1<sup>st</sup> mode) were conducted to gain insight into the fundamental characteristics of BF-SMA-VFSD and BF-PD. Fig. 6.4 illustrates a comparison of cyclic pushover results, presenting the dimensionless ratio ( $V/W$ ) of base force to seismic weight alongside roof drift for the BF-SMA-VFSD and BF-PD. Both structures demonstrated satisfactory self-centring behaviour up to the target roof drift (i.e., 4%). A slight residual drift was observed in the BF-PD, potentially resulting from minor plastic deformation in the structural members due to the higher overstrength of the PD under significant deformation levels. In contrast, the BF-SMA-VFSD displayed a multistage energy-dissipation mechanism, and its dual-stiffness reduction effectively decouples the damper's stiffness and strength. This reduces the strength demand on adjacent structural members, thus lowering the risks of the potential local failures. However, the decreased strength of structures due to the dual-stiffness-reduction mechanism (e.g., BF-SMA-VFSD) can result in the increased peak drift responses compared to structures with no

strength reduction (e.g., BF-PD). Assessing the performance of a structure solely based on peak drift responses may be insufficient. Additional engineering demand parameters, such as peak floor acceleration (PFA) responses, are necessary for a comprehensive evaluation for structures. The detailed discussion will be subsequently given in the dynamic analyses.

Based on the dynamic analyses, the comparison of distributions of mean maximum interstorey drifts between the BF-SMA-VFSD and BF-PD under DBE level and MCE level are given in Figs. 6.5(a)-(b), respectively. Both the BF-SMA-VFSD and the BF-PD showed consistent peak drift responses under DBE level, with the BF-SMA-VFSD exhibiting slightly larger drift responses under MCE level. This can be explained by the fact that the 2<sup>nd</sup> yielding stage of the damper in the BF-SMA-VFSD was not activated under the DBE level, leading to the similar damper performance and drift responses between both structures. However, under the MCE level, the multistage energy-dissipation mechanism of the SMA-VFSD was fully activated in the BF-SMA-VFSD. Conversely, the BF-PD, equipped with the PD of higher strength (see Fig. 6.1(b)), more effectively controlled the structural drift responses. To illustrate this, the comparison of the hysteretic behaviour of the damper at the 1<sup>st</sup> storey between the BF-SMA-VFSD and BF-PD subject to LA8 record (DBE level) and LA28 record (MCE level) are shown in Figs. 6.6(a)-(b), respectively. As shown in Fig. 6.6(a), the consistent cyclic responses of the dampers were observed for both the BF-SMA-VFSD and BF-PD subject to the DBE level, while the dampers in the BF-PD exhibited higher strength under MCE level. In addition, negligible residual drifts were observed for both the BF-SMA-VFSD and BF-PD, even under MCE level, as depicted in the Figs. 6.7(a)-(b), respectively. This suggested that the damper braces dissipated all seismic energy, while the main structural members remained elastic, aligning with the structural design principles.

As mentioned earlier, additional EDPs are required to assess the seismic performance of structures equipped with different dampers. Absolute PFAs, recognised as a crucial index for assessing damage to non-structural elements or instruments within structures, were calculated in the analyses. Fig. 6.8 compares the distributions of maximum interstorey PFAs between the BF-SMA-VFSD and BF-PD under both DBE and MCE levels. The results show comparable PFA patterns for the BF-SMA-VFSD and BF-PD under DBE level. However, the BF-SMA-VFSD demonstrated better control of the PFAs at the top storey under MCE level. To illustrate this, the time versus floor acceleration (FA) curves for the 3<sup>rd</sup> storey of both structures under LA8 (DBE level) and LA28 (MCE level) records are compared in Figs. 6.9(a)-(b), respectively. For clarity, curves showing significant responses during specific durations highlighted in blue shade (Figs. 6.9(a)-(b)) are also provided. The comparison of FA curves demonstrated that the 2<sup>nd</sup> yielding of the damper in the BF-SMA-VFSD was not triggered under DBE level, resulting in no observed PFA control. However, the effective FA control of the damper was confirmed after the full development of the 2<sup>nd</sup> yielding under MCE level. In the LA28 record, the PFAs of the 3<sup>rd</sup> storey in the BF-SMA-VFSD was reduced by 20% compared to that in the BF-PD.

Moreover, the multistage energy-dissipation mechanism of the SMA-VFSD is believed to decouple the stiffness and strength of the damper, thereby reducing damper overstrength. To demonstrate this, the overstrength factor  $\Omega$ , defined as the ratio of the maximum force of the damper to the 1<sup>st</sup> yielding force of the damper during earthquakes, was employed. The comparisons of  $\Omega$  values for the dampers in each storey between the BF-SMA-VFSD and BF-PD under all records are presented in Figs. 6.10(a)-(c), respectively. The above comparisons showed that comparable  $\Omega$  values of the dampers in each storey for both structures were observed under DBE level, while the  $\Omega$  values

of the dampers in all storeys of the BF-PD were significantly higher than those in the SMA-VFSD under MCE level. Note that a significant overstrength in the damper can increase the strength demand on their adjacent structural members or connections, thereby posing the risk of local failures at extreme cases. This finding confirmed the effectiveness of the multistage energy-dissipation mechanism in addressing damper overstrength, as identified in previous investigations (Chen et al. 2022; Qiu et al. 2022; Ke et al. 2023a). It is worth mentioning that the proposed SMA-VFSD, featuring a multistage energy-dissipation mechanism, offers an alternative to tackle concerns related to PFAs and overstrength for structures, although it may involve a minor compromise on peak drift control.

### **6.2.3 Effect of initial gaps on performance of braced frames equipped with SMA-VFSD**

As observed in the braced frame test in Chapter 5, utilising pin connections to join structural members (e.g., damper brace) inevitably introduces fabrication tolerances to facilitate assembly on the construction site. Before bearing loads, the damper braces, serving as lateral resisting members, may initially experience slippage due to the existing gaps among the connections. This initial imperfection could affect the structural dynamic responses by potentially altering the dynamic properties of structures (e.g., fundamental period and vibration modes). Although its effect is rarely investigated, undereating its impact on the seismic performance of structures is essential.

To examine the effect of the initial gaps in the pin connections on the seismic performance of the BF-SMA-VFSD, a 1 mm gap in both positive and negative directions was assumed for each damper brace. The validation of the numerical

strategies considering these initial gaps was demonstrated in section 5.4.1. Using the validated modelling technologies, a numerical model of BF-SMA-VFSD considering the initial gaps was developed. To avoid numerical convergence issues, a low stiffness value was assigned to the damper braces to represent the initial gaps during this stage. Modal cyclic pushover analyses (1<sup>st</sup> mode) were conducted to understand the fundamental behaviour of the BF-SMA-VFSD with the initial gaps. It is worth noting that the initial gaps in the damper brace could prolong the structural fundamental period and consequently alter structural dynamic properties. To maintain consistency in the lateral load pattern used in the modal pushover, the load pattern was aligned with the distribution of  $m\phi_1$  of the BF-SMA-VFSD without considering the initial gaps, where  $m$  represents the mass matrix and  $\phi_1$  denotes the 1<sup>st</sup> mode vector. Fig. 6.11 compares the cyclic pushover results (i.e., roof drift vs  $V/M$ ) of the BF-SMA-VFSD with and without the initial gaps. The hysteretic curves almost overlapped, with only a slight difference observed at the beginning (i.e., close to coordinate origin). The analysis results showed that structures considering the initial gaps performed comparably to those not considering them under static lateral loads.

To explore the effect of the initial gaps on the dynamic behaviour of the structures, Figs. 6.12(a)-(b) compares the distribution of the maximum peak drift responses of the structures with and without the initial gaps under DBE level and MCE level, respectively. Despite the small initial gaps, the peak drift responses were significantly increased, particularly for the upper stories of the structures. Similarly, an evident increase in PFAs was observed, especially for the lower storeys, as depicted in Fig. 6.13. The above unexpected yet important findings should be thoroughly examined and understood. It is crucial to address why even the small initial gaps among pin connections can noticeably elevate structural responses under earthquakes. To elucidate

this phenomenon, the detailed structural responses under LA28 were selected and discussed herein. Figs. 6.14(a)-(b) illustrate the complete and truncated acceleration record of LA28, respectively, with its spectral acceleration shown in Fig. 6.14(c). Two significant acceleration pulses were observed from 3 s to 5 s, with periods of 0.36 s and 0.42 s, respectively. It is worth noting that due to these acceleration pulses, the period corresponding to the peak spectral acceleration of LA28 was approximately 0.35 s, which was close to the structural fundamental period (i.e., 0.49 s) and thus may cause obvious structural responses. Fig. 6.15(a) illustrates the comparisons of the relative FAs of each storey for the structures with and without the initial gaps among pin connections. To provide clarity, the corresponding responses during the interval with significant acceleration pulses (i.e., from 3 s to 5 s) are also presented in Fig. 6.15(b). Additionally, Fig. 6.16(a) and Fig. 6.17(a) show the comparisons of the relative floor velocities (FVs) and interstorey drift response of each storey for the structures with and without the initial gaps, with their responses over the interval with significant acceleration pulses displayed in Fig. 6.16 (b) and Fig. 6.17(b), respectively. According to the relative FAs and FVs comparisons in Fig. 6.15(b) and Fig. 6.16(b), the structure with initial gaps showed increased relative PFA at each story, especially in the lower stories, along with higher relative FVs compared to the structure without gaps. The increased structural responses can be attributed to the fact that the structure with initial gaps may absorb more seismic energy due to initial stiffness reduction (caused by the fabrication tolerance) during lateral shaking under the same earthquake record. This additional energy absorption was reflected in the increased relative FV observed at each storey of the structure with the initial gaps (i.e., larger velocity indicated more kinematic energy in the structure, which is shown in Fig. 6.16). Furthermore, the structure with initial gaps accumulated more kinematic energy, which led to larger drift responses at each

storey, as indicated in Fig. 6.17. Additionally, a noticeable jump point was observed in the relative acceleration curves for the lower stories of the structure with the initial gaps when a change in movement direction occurred, whereas this phenomenon was not observed for the top storey. This jump point may be attributed to interstorey interaction during the transition of structural movement.

Due to the increased kinematic energy at each storey for the structure with the initial gaps under LA28, the damper braces may experience larger deformation to resist structural drifts and absorb this additional energy. To illustrate this, Fig. 6.18(a) compares the hysteretic curves of the damper at each storey for the structures with and without the initial gaps under LA28. Additionally, Fig. 6.18(b) shows their responses over the significant acceleration-pulse interval (from 3 s to 5 s) of LA28 for clarity. All dampers at the same storey for both the BF-SMA-VFSD with and without the initial gaps exhibited similar multistage hysteretic behaviour. However, the dampers in the structure with the initial gaps experienced larger elongation and higher strength during the significant acceleration-pulse interval of LA28. Neglecting this amplified effect caused by the initial gaps in structural design may pose the risks of structural damage (i.e., failure of damper braces) or collapse. Similar patterns in structural and damper responses were observed under other earthquakes, indicating consistent behaviour across different seismic events.

The discussions regarding the structures with the initial gaps in pin connections revealed that although these gaps may have minimal impact on static behaviour, they significantly affect structural dynamic responses under earthquakes. Observations indicated substantial increases in the peak drift responses, PFVs and PFAs for such structures, underscoring the importance of this seismic concern. This issue has been scarcely investigated but warrants attention, particularly for structures relying on

members using pin connections for lateral resistance.

### **6.3 Seismic demand analysis on braced frames equipped with SMA-VFSD**

The preceding section demonstrated the viability of the SMA-VFSD in mitigating seismic responses via a structural case study from the perspective of structural evaluations. It also highlighted the necessity of considering fabrication tolerances in pin connections during seismic dynamic analyses, particularly when the pin connections are used to join lateral-resisting structural members. In this section, the viability of the SMA-VFSD in mitigating seismic nonlinear structural demands was examined. The inelastic energy demand and acceleration demand of a low-to-medium structure equipped with the SMA-VFSD (labelled as S-SMA-VFSD) were explored and investigated. It is important to note that the BF-SMA-VFSD mentioned in section 6.2 is one of the structural applications of the proposed damper. As demonstrated in the braced frame test at the sub-structural level (Chapter 5) and the case study at the system level (section 6.2), when the lateral-resisting systems are mainly provided by the SMA-VFSD braces, the S-SMA-VFSD exhibits a consistent hysteretic behaviour similar to that observed in the SMA-VFSD test. The hysteretic behaviour and its parameters are illustrated in Fig. 6.19, showcasing the multistage energy-dissipation hysteretic characteristics. To thoroughly assess the seismic demands of structures exhibiting such hysteretic behaviour, it is essential to consider various structural periods and combinations of different hysteretic parameters, while also considering earthquake uncertainties. For this purpose, spectral analyses of an equivalent Single Degree of Freedom (SDOF) system representing S-SMA-VFSD were conducted. For a low-to-medium S-SMA-VFSD, its dynamic nonlinear behaviour can be dominated by its

fundamental vibration, allowing for an effective quantification of its seismic response using an equivalent SDOF system. (Zahrah et al. 1984; Leelataviwat et al. 2002; Song et al. 2007; Ucar et al. 2012; Qiu et al. 2016; Qiu et al. 2017b; Karatzetzou et al. 2018; Ke et al. 2018a; Zhou et al. 2021; Ke et al. 2022; Zhang et al. 2022). Therefore, the non-linear spectral analyses of an equivalent SDOF system denoting an S-SMA-VFSD was carried out.

The seismic behaviour of the equivalent SDOF system can be characterised by the multistage hysteretic rule (shown in Fig. 6.19) as well as the dynamic features of its fundamental mode including the effective equivalent mass ( $M$ ), the structural fundamental period ( $T$ ) and the damping ratio ( $\zeta$ ). In the nonlinear spectral analyses of the SDOF system, an expanded range of hysteretic parameter matrix and a wide variety of structural periods were considered. The parameter matrix under consideration included: 1) three levels of  $\bar{\alpha}_1$  (i.e., 0.05, 0.2, 0.35); 2) three levels of  $\bar{\beta}$  (i.e., 0.1, 0.3, 0.5); 3) three levels of  $\bar{\zeta}$  (i.e., 5, 8, 11) and six levels of  $\bar{\mu}$  (i.e., from 11 to 26 with an interval of 3). It is worthy of noting that the range of the hysteretic parameters  $\bar{\alpha}_2$  and  $\bar{\alpha}_4$  was relatively small at the system level, echoed in section 6.2. Therefore, for the current analyses, they were considered as zero to reduce computational costs. However, for steel hybrid structures equipped with the SMA-VFSD (i.e., the SMA-VFSDs are placed in the energy-dissipation bays(EDB), while main frame is made of high-strength steel), these parameters may have a significant impact on seismic performance, which is beyond the scope of the current study. For each combination of hysteretic parameters, the period of the SDOF system was varied from 0.1 s to 5 s, with increments of 0.1 s. Additionally, a unit mass and a damping ratio ( $\zeta$ ) of 5% were assigned to the SDOF system.

Two dimensionless indices were introduced and used to evaluate the energy and

acceleration demands of S-SMA-VFSD. To quantify the seismic energy demand, the energy modification factor ( $\gamma$ ) was used (Ucar et al. 2012; Qiu and Zhu 2016; Qiu and Zhu 2017; Qiu et al. 2017; Karatzetzou and Pitilakis 2018; Ke et al. 2018a; Zhou et al. 2021; Ke et al. 2022; Zhang et al. 2022a). Following the energy balance concept (shown in Fig. 6.20), the energy modification factor ( $\gamma$ ) can be determined by the ratio of the covered area of the peak skeleton response of the equivalent SDOF system denoting an S-SMA-VFSD (i.e., the nominal energy of the system,  $E_a$ ) to that of the corresponding elastic SDOF system ( $E_{ae}$ ) under an earthquake, given by

$$\gamma = \frac{E_a}{E_{ae}} = \chi \lambda_1^T \phi \lambda_2 \quad 6.2$$

$$\chi = \left( \frac{V_y}{V_e} \right)^2 = \frac{1}{R^2} \quad 6.3$$

$$\lambda_1 = [1, \bar{\zeta}, \bar{\mu} - \bar{\zeta}] \quad 6.4$$

$$\lambda_2 = [2\bar{\mu} - 1, 2\bar{\mu} - \bar{\zeta}, \bar{\mu} - \bar{\zeta}] \quad 6.5$$

$$\phi = \begin{bmatrix} 1 & 0 & 0 \\ 0 & \bar{\alpha}_1 & 0 \\ 0 & 0 & \bar{\alpha}_2 \end{bmatrix} \quad 6.6$$

where  $E_a$  = peak nominal energy of the equivalent SDOF system;  $E_{ae}$  = peak nominal energy of the corresponding elastic SDOF system;  $M$  = total mass of the equivalent SDOF system;  $\chi$  = damage-control coefficient;  $V_e$  = base force of the corresponding elastic system,  $R$  = strength reduction factor;  $\bar{\delta}_y$  and  $\bar{\delta}_p$  = displacement where the 1<sup>st</sup> and 2<sup>nd</sup> pseudo yielding of the equivalent SDOF system starts, respectively; and  $\bar{\delta}_e$  = maximum displacement of the corresponding elastic SDOF system. The other symbols can be found in Fig. 6.19.

Pertaining the acceleration demand, a dimensionless acceleration factor ( $\eta$ ) was used, defined as the ratio of the maximum absolute acceleration of the equivalent SDOF system to that of the corresponding elastic SDOF system during an earthquake. Figure

6.21 shows a flowchart guiding the constant-ductility spectral analyses of systems. Twenty-two far-field ground motions (44 earthquake records) specified in FEMA P695 were selected as input excitations (FEMA P695-2009), which is indicated in Fig. 6.21(c). To improve the computing efficiency, a self-developed calculating programme called BTESPEC was used to perform the constant-ductility non-linear spectral analyses. The accuracy of the calculation programme has been validated and can be referenced in previous related research (Ke et al. 2018a; Zhou et al. 2021; Ke et al. 2022; Zhang et al. 2022a). A data point was selected from the spectral results of the equivalent SDOF system representing an S-SMA-VFSD (i.e.,  $T = 1.5$  s,  $\bar{\alpha}_1$ ,  $\bar{\alpha}_2$ ,  $\bar{\alpha}_4$ ,  $\bar{\beta}$ ,  $\bar{\zeta}$ , and  $\bar{\mu} = 0.2, 0, 0, 0.3, 11, 20$ , respectively) under one earthquake record (i.e., Kocaeli record was randomly selected from the above earthquake motion set). Following this, a time history analysis was performed, and the results were compared with those obtained from the SDOF system developed using the OpenSees platform. Figure 6.22 presents the comparison of hysteretic curves and dynamic displacement responses, which confirmed the validity of the developed calculation programme. Additionally, these dynamic analyses validated the proposed model's effectiveness in predicting the dynamic behaviour of structures. For comparison, two additional equivalent SDOF systems representing two more types of self-centring structures were considered. One structure exhibited bilinear flag-shaped behaviour, labelled as S-BFS (Fig. 6.21(b)), while the other displayed an improved bilinear flag-shaped behaviour, labelled as S-IBFS (Fig. 6.21(b)) (Qiu et al. 2022; Chen et al. 2022). In contrast to the S-SMA-VFSD, the strength and stiffness of S-BFS and S-IBFS are coupled. Additionally, in comparison to S-BFS, S-IBFS, characterised by a fuller hysteretic curve, exhibited an enhanced energy-dissipation capacity.

### 6.3.1. Energy modification factor demand

Figure 6.23(a) illustrates representative mean energy modification factor spectra for the equivalent SDOF systems with the aforementioned hysteretic characteristics. In general, Overall, the three structural types (S-SMA-VFSD, S-BFS, and S-IBFS) with comparable ductility and energy modification factor spectra exhibited similar trends. For low-to-medium structures, where structural periods ranged from approximately 0.5 s to 2.5 s, this period range was identified as the target range requiring closer examination. For low-to-medium structures, where structural periods ranged from approximately 0.5 s to 2.5 s, this period range was identified as the target range requiring closer examination. To enhance clarity, the mean energy modification factor spectra within this target period range are displayed in Fig. 6.23(b). It can be seen that as  $\bar{\alpha}_1$  increased, the mean energy modification factor for all three structures also increased, indicating a corresponding rise in energy demand, which was consistent with previous findings (Ke et al. 2016). Importantly, the energy modification factor for S-SMA-VFSD remained consistently lower than that of the other two self-centering systems (S-BFS and S-IBFS), a trend that became more pronounced with higher target structural ductility.

### 6.3.2. Acceleration factor demand

Figure 6.24(a) presents the representative mean acceleration factor spectra for the equivalent SDOF systems representing the three structural types (S-SMA-VFSD, S-BFS, and S-IBFS). An overall declining trend in the mean acceleration factor was observed. Notably, the decrease in the mean acceleration factor spectra was steep for very short structural periods (less than approximately 0.5 seconds), while this trend was

less pronounced in longer period ranges. To provide a clearer view, the mean acceleration factor spectra within the target period range (0.5 s to 2.5 s) are depicted in Figure 6.24(b). Within this range, an evident upward trend in the mean acceleration factor for all three structural types was observed as  $\bar{\alpha}_1$  increased. Furthermore, when comparing S-SMA-VFSD with S-BFS and S-IBFS, the acceleration demand for the S-SMA-VFSD oscillators was consistently lower, particularly at high ductility levels.

In conclusion, these positive findings indicate that S-SMA-VFSD is more effective in reducing seismic demands (both energy and acceleration demands) compared to S-BFS and S-IBFS. These findings further underscore the potential of SMA-VFSD as a superior option for mitigating structural responses from a structural seismic demand perspective.

## 6.4 Summary

This chapter primarily focused on evaluating the seismic mitigation effectiveness of the proposed SMA-VFSD from a system-level perspective, considering both capacity and demand aspects. First, a three-storey prototype building equipped with the SMA-VFSD was designed. This was followed by a thorough comparative analysis with structures equipped with the previous type of damper (PD) through nonlinear dynamic simulations. Next, the effect of fabrication tolerances in pin connections on seismic performance was investigated. Finally, to assess the effectiveness of SMA-VFSD in optimising seismic performance, an equivalent SDOF system representing a low-to-medium S-SMA-VFSD was used to create a database of inelastic seismic demand indices, including the energy modification factor and acceleration factor. Additionally, demand comparisons were made with two other self-centering systems (S-BFS and S-IBFS) that exhibit different hysteretic behaviours. The main conclusions were

summarised as follows:

- The comparative analyses of a structural case demonstrated the effectiveness of the SMA-VFSD in optimising structural performance. This was particularly obvious in the substantial reduction of acceleration responses and the alleviation of damper overstrength-induced issues under strong earthquakes, albeit with a slight increase in drift responses.
- The effect of structural stiffness reduction at the beginning due to the initial gaps was discussed. The discussions highlighted that while these gaps may have minimal impact on static behaviour, they significantly affect the dynamic responses of structures under earthquakes. Observations indicated substantial increases in peak drift responses, PFVs and PFAs for such structures, underscoring the importance of this concern.
- The inelastic seismic demands, as measured by the energy modification factor and acceleration factor for equivalent SDOF systems, were consistently lower compared to those of two other self-centring systems (S-BFS and S-IBFS) with different hysteretic behaviours. This confirmed the effectiveness of SMA-VFSDs in reducing inelastic seismic demands. Thus, the potential of SMA-VFSDs for improving structural seismic performance was validated.

Table 6.1. Mechanical design parameters of dampers for case structure

Storey	$\mu_1$	$\mu_2$	NiTiCo SMA bolts (Number $\times$ Diameter $\times$ Length, unit: mm)	$\theta$	Preloads of disc spring systems (kN)	Stiffness of disc spring systems (kN/mm)	Preloads of SMA bolts (kN)
1			4 $\times$ 14 $\times$ 500		130	2.00	135
2	0.46	0.18	4 $\times$ 12 $\times$ 500	4°	100	1.5	110
3			4 $\times$ 10 $\times$ 500		75	1.10	70

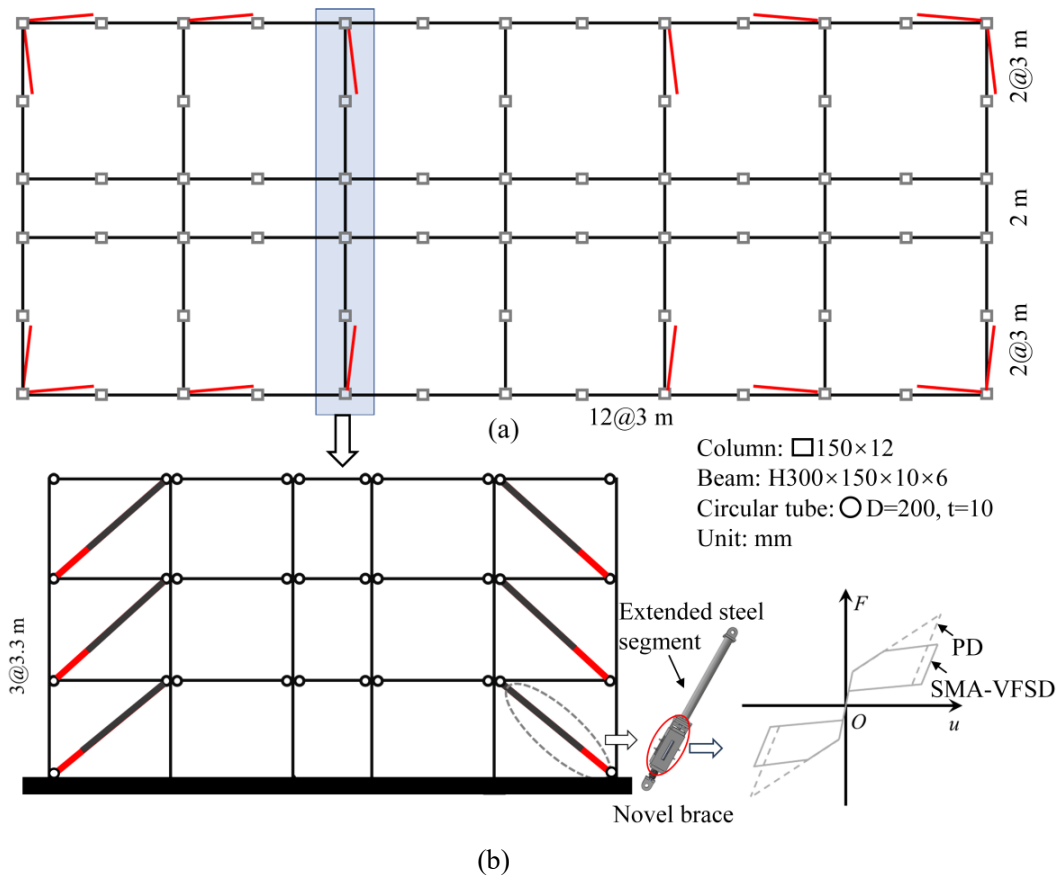


Fig. 6.1. Information on case structure: (a) structural plan, and (b) structural elevation and brace configuration

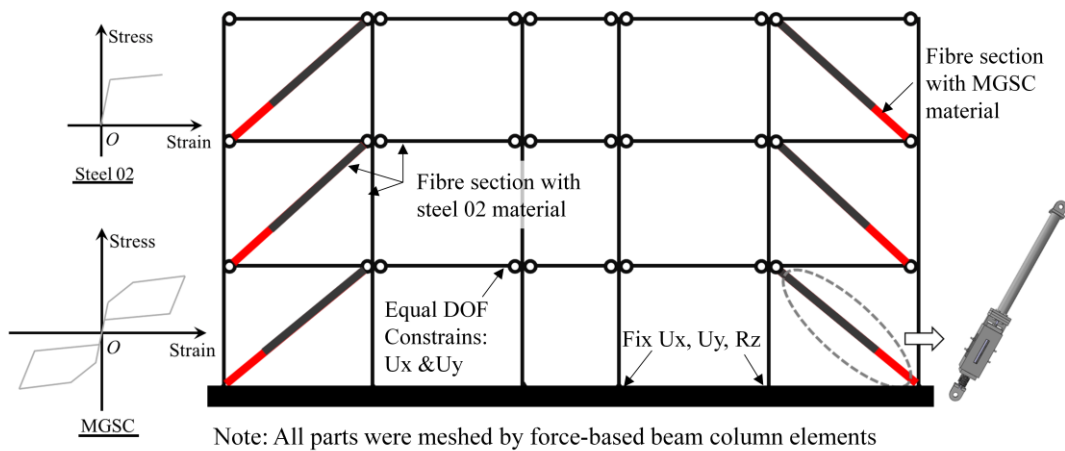
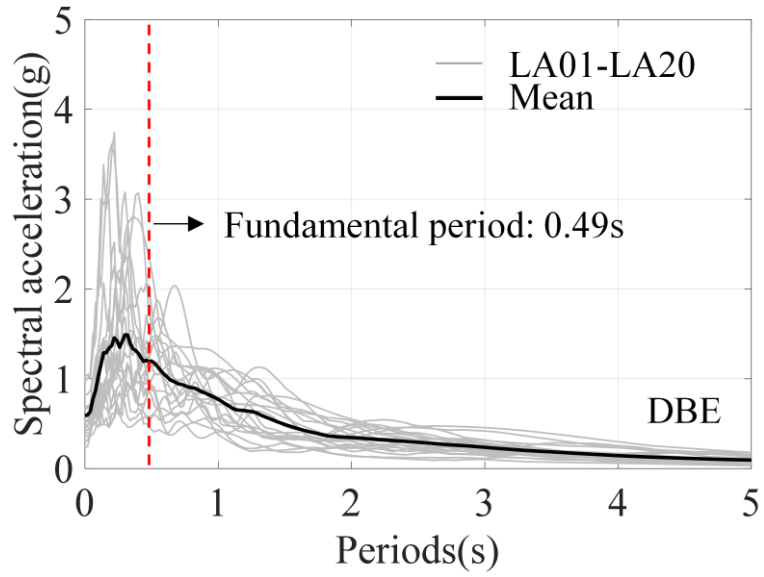
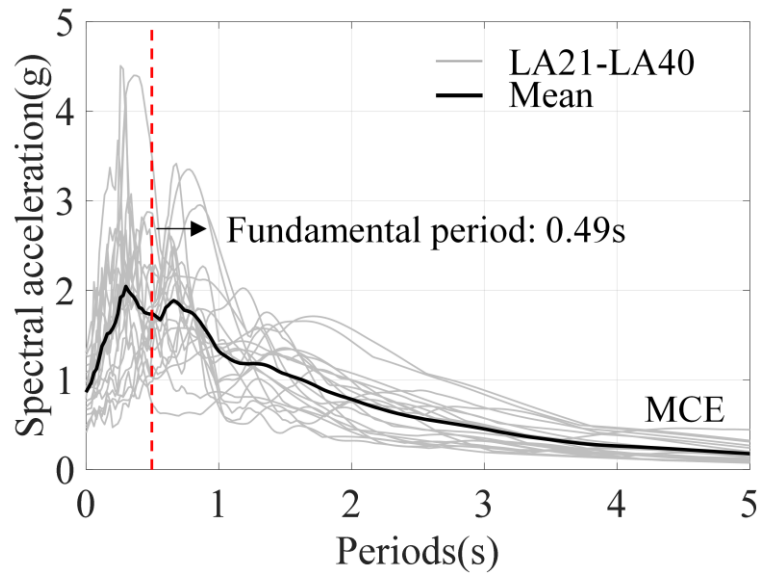


Fig. 6.2. Numerical model of braced frame



(a)



(b)

Fig. 6.3. Spectral acceleration of earthquake records: (a) DBE level, (b) MCE level

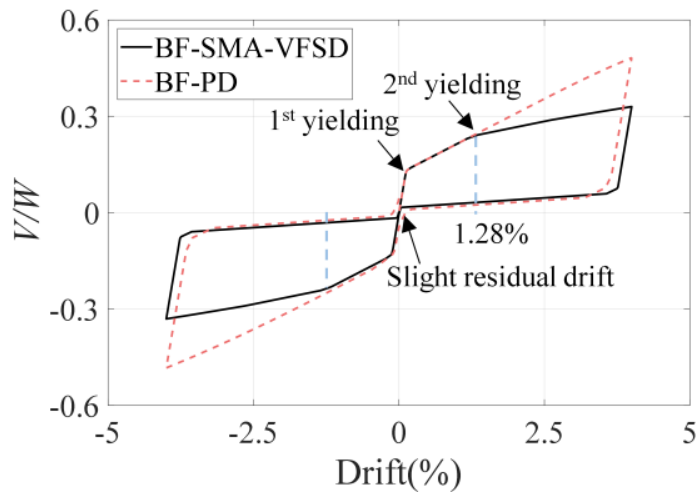
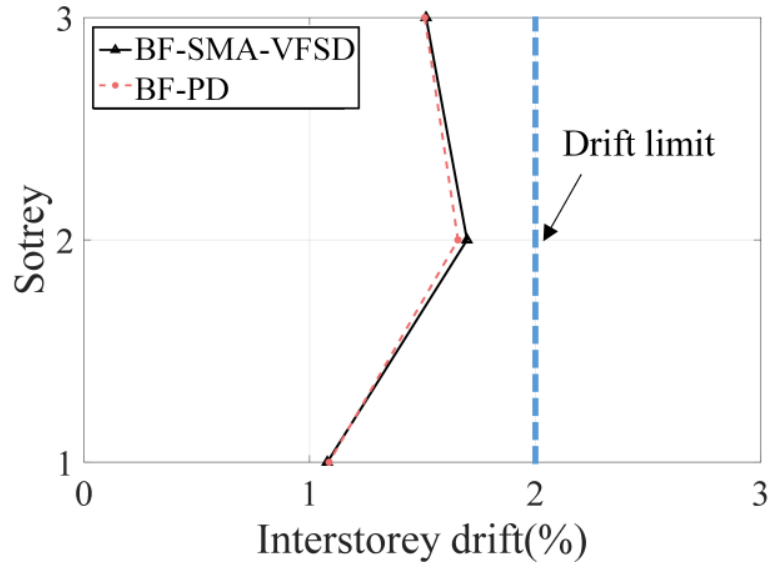
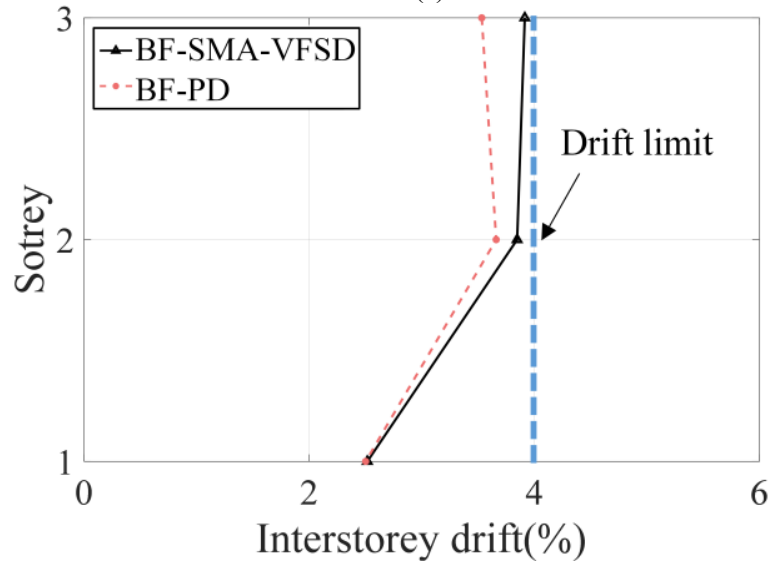


Fig. 6.4. Comparisons of cyclic pushover for structures equipped with SMA-VFSD and PD

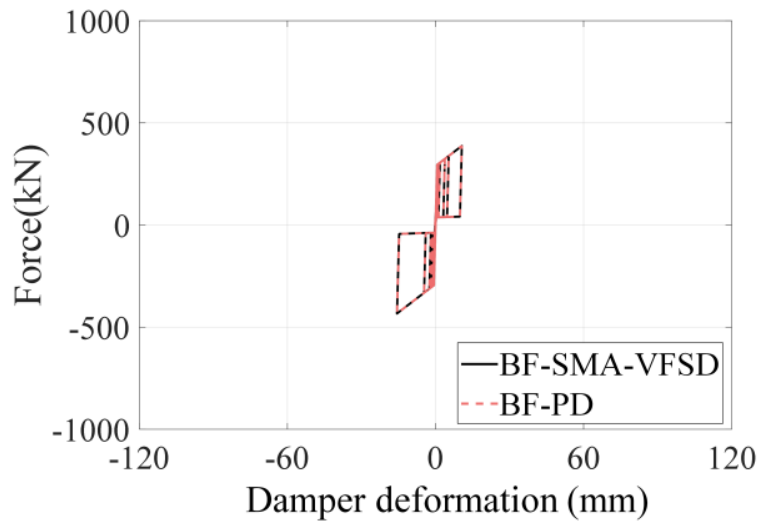


(a)



(b)

Fig. 6.5. Distributions of mean maximum interstorey drifts: (a) under DBE level, and (b) under MCE level



(a)

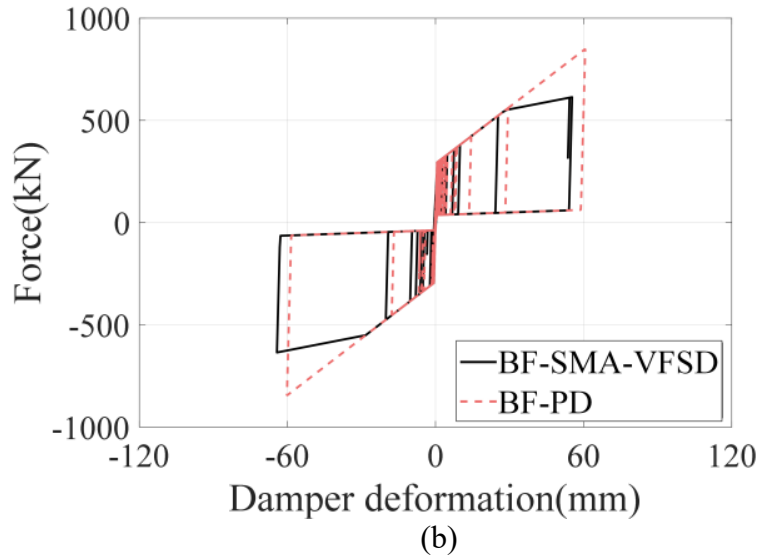


Fig. 6.6. Hysteretic responses of brace at 1<sup>st</sup> storey: (a) under LA8, (b) under LA28

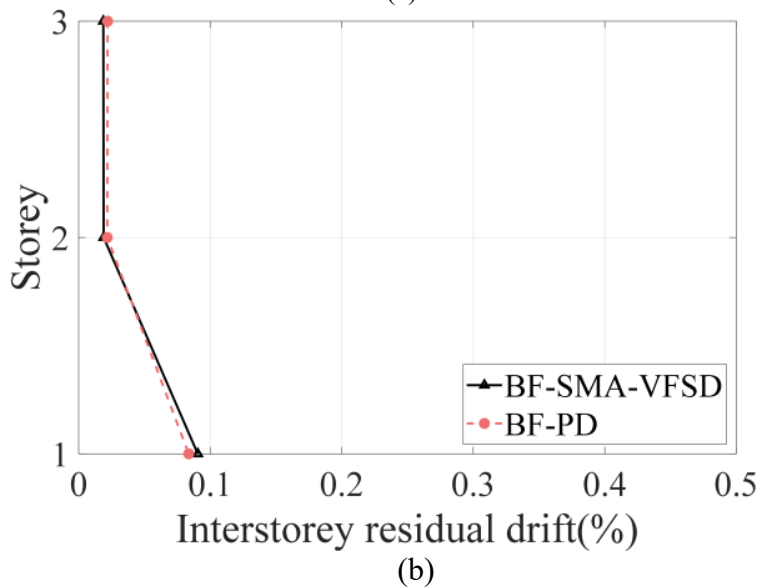
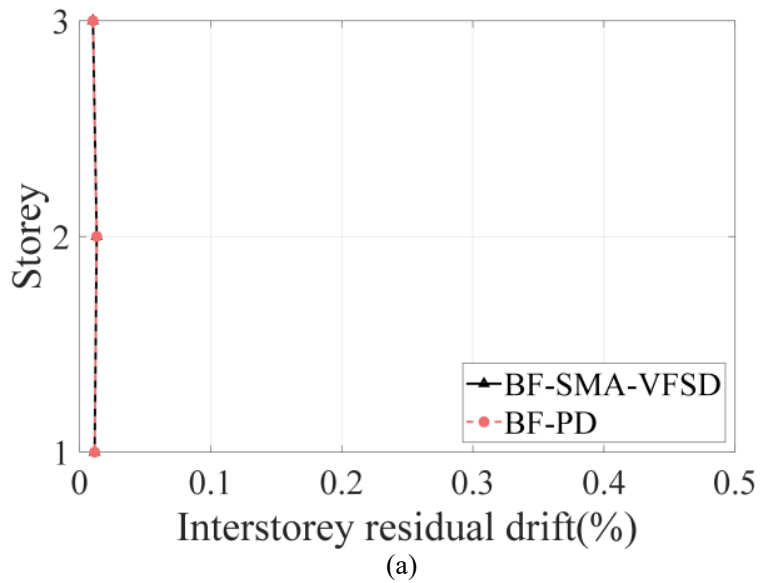


Fig. 6.7. Distributions of mean maximum interstorey residual drifts: (a) under DBE level, and (b) under MCE level

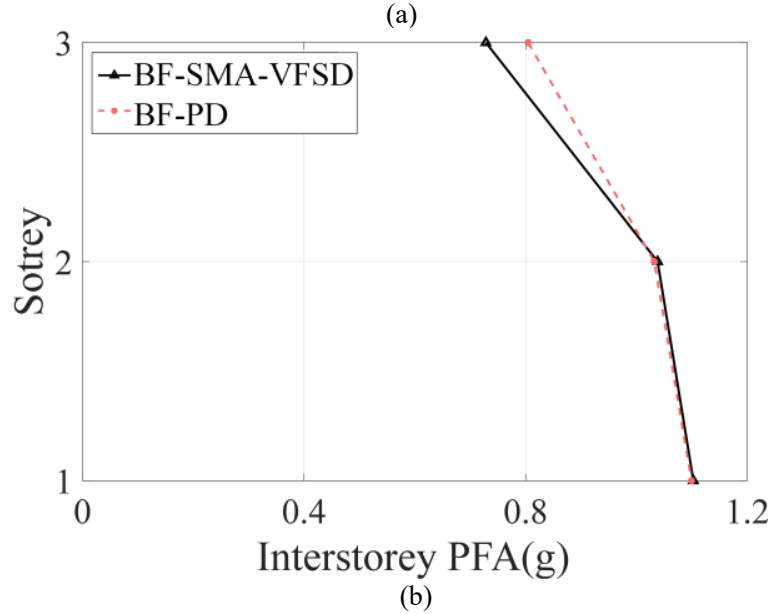
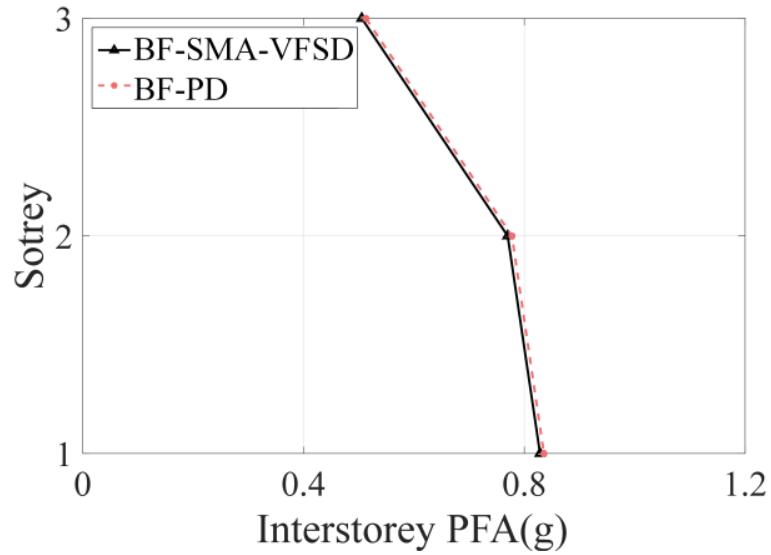
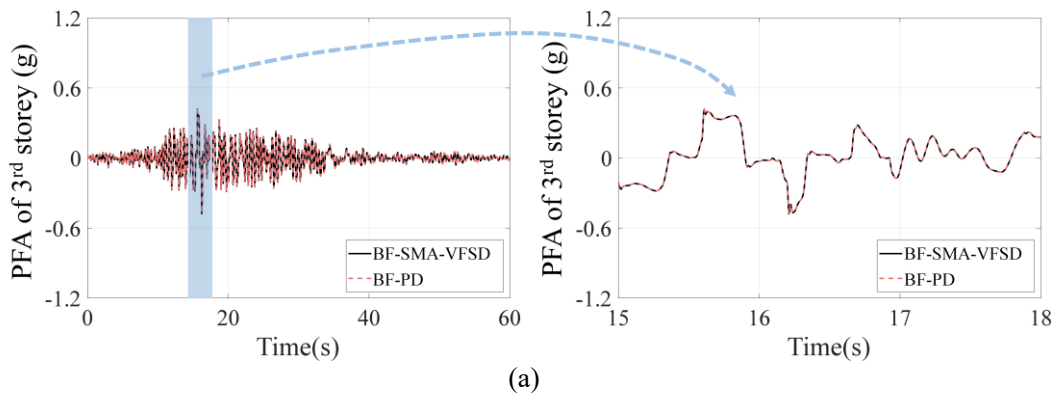


Fig. 6.8. Distributions of mean maximum interstorey PFAs: (a) under DBE level, and (b) under MCE level



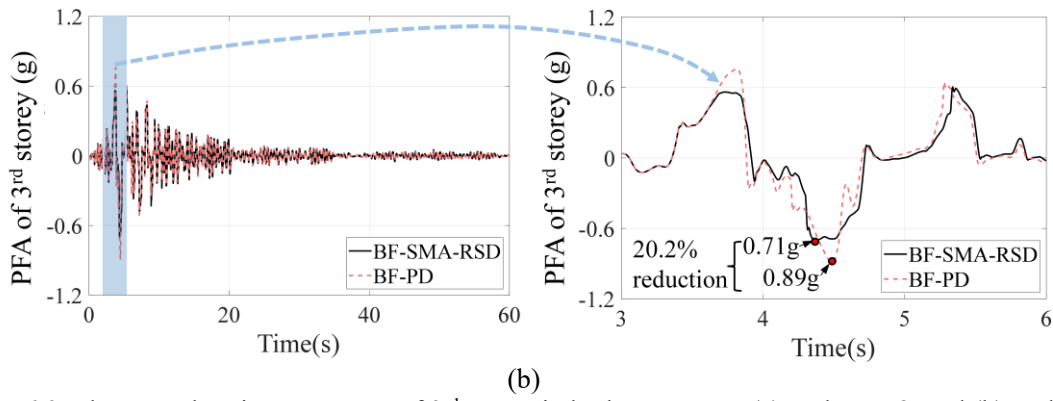
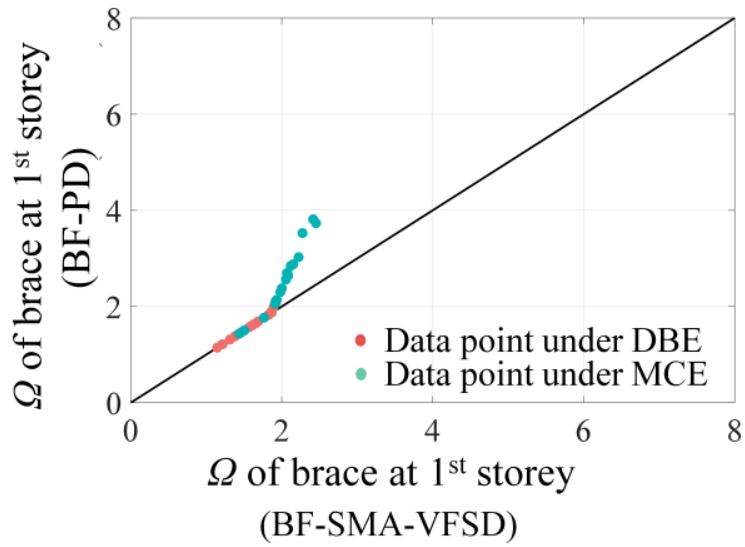
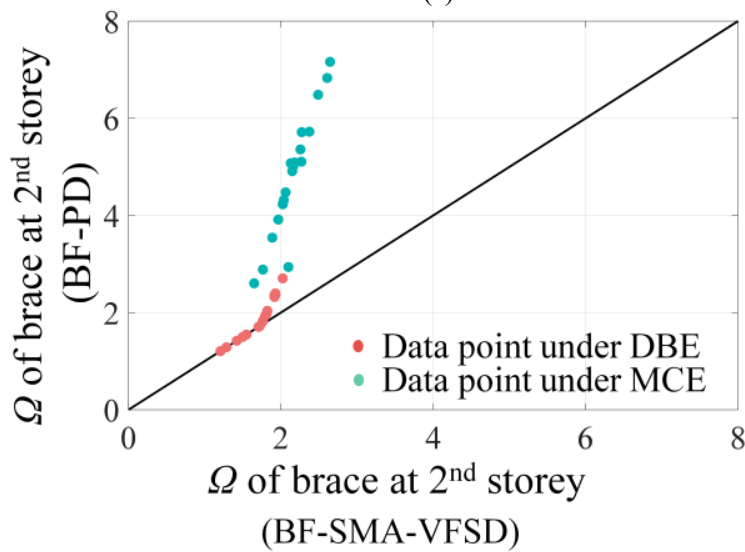


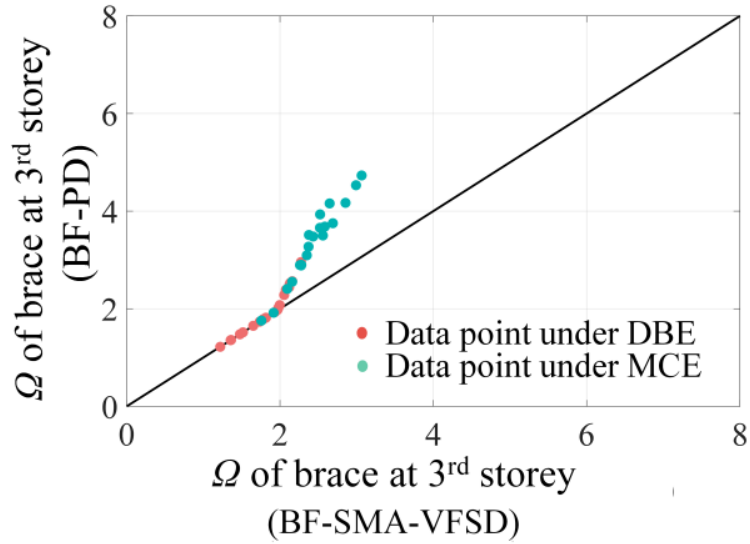
Fig. 6.9. Floor acceleration responses of 3<sup>rd</sup> storey in both structures: (a) under LA8, and (b) under LA28



(a)

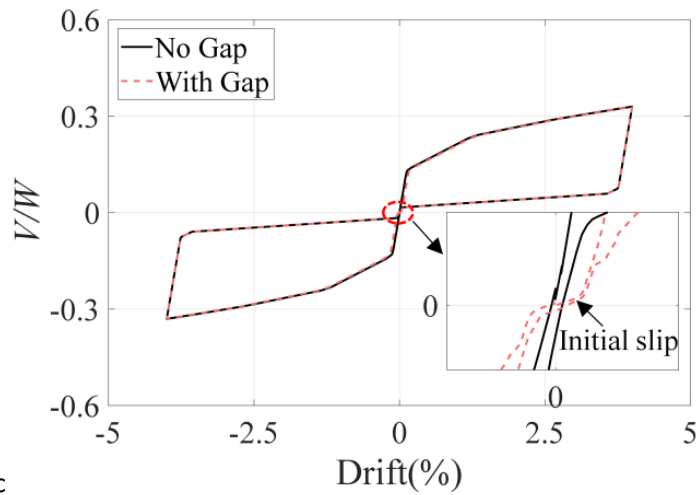


(b)



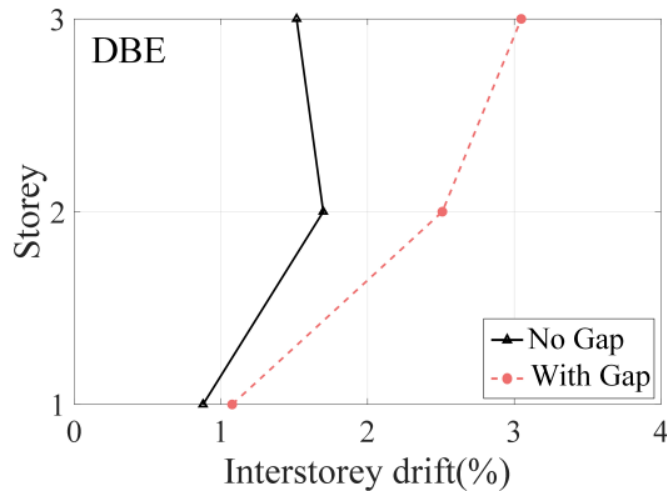
(c)

Fig. 6.10. Comparisons of calculated overstrength of brace at each storey under earthquakes for two structures: (a) 1<sup>st</sup> storey, (b) 2<sup>nd</sup> storey, and (c) 3<sup>rd</sup> storey



c

Fig. 6.11. Comparisons of cyclic pushover for BF-SMA-VFSD with and without initial gaps



(a)

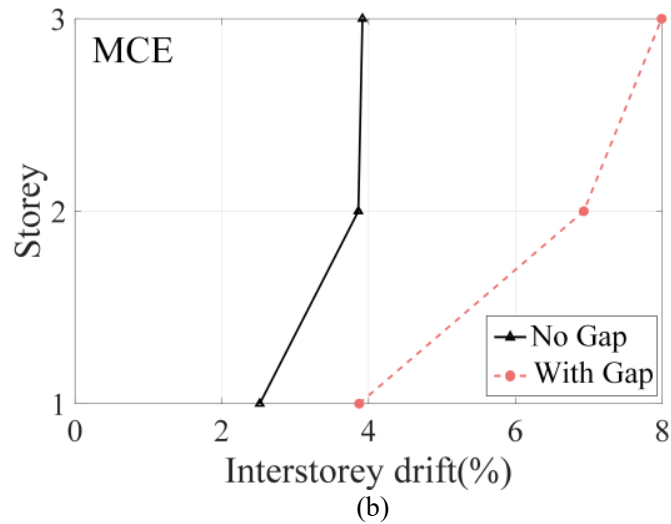


Fig. 6.12. Comparisons of distributions of mean maximum interstorey drifts for structures with and without the initial gaps: (a) under DBE level, and (b) under MCE level

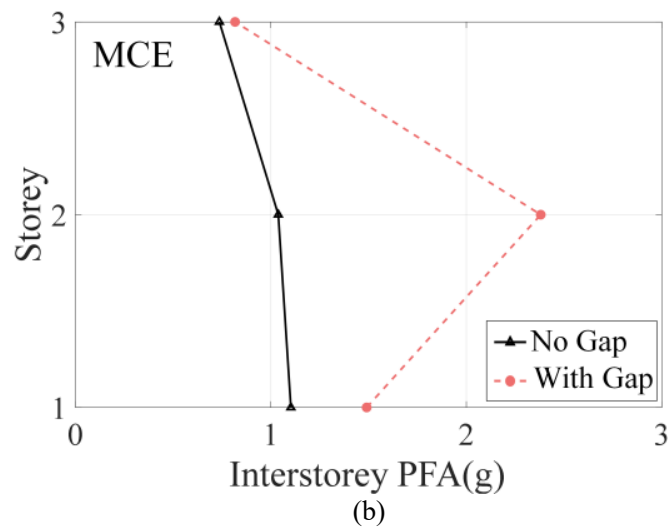
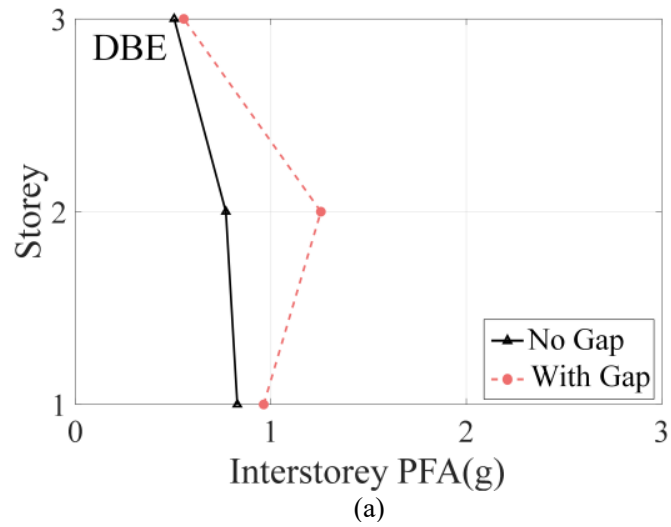


Fig. 6.13. Comparisons of distributions of mean maximum interstorey PFAs: (a) under DBE level, and (b) under MCE level

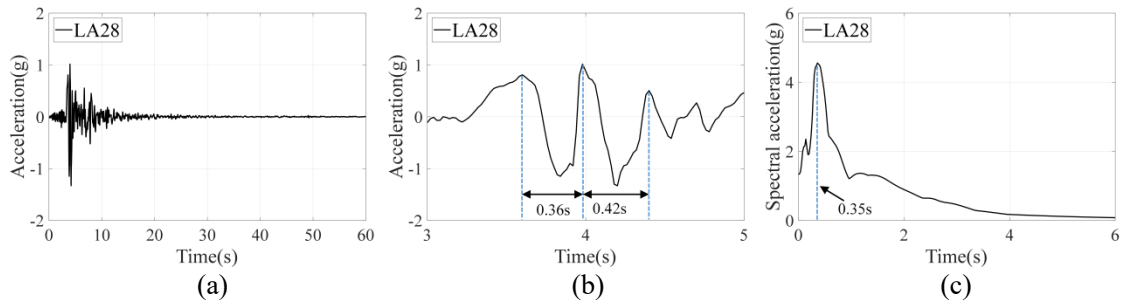


Fig. 6.14. Information on LA28: (a) full acceleration record, (b) over acceleration-pulse interval (i.e., 3 - 5s), and (c) spectral acceleration of LA28

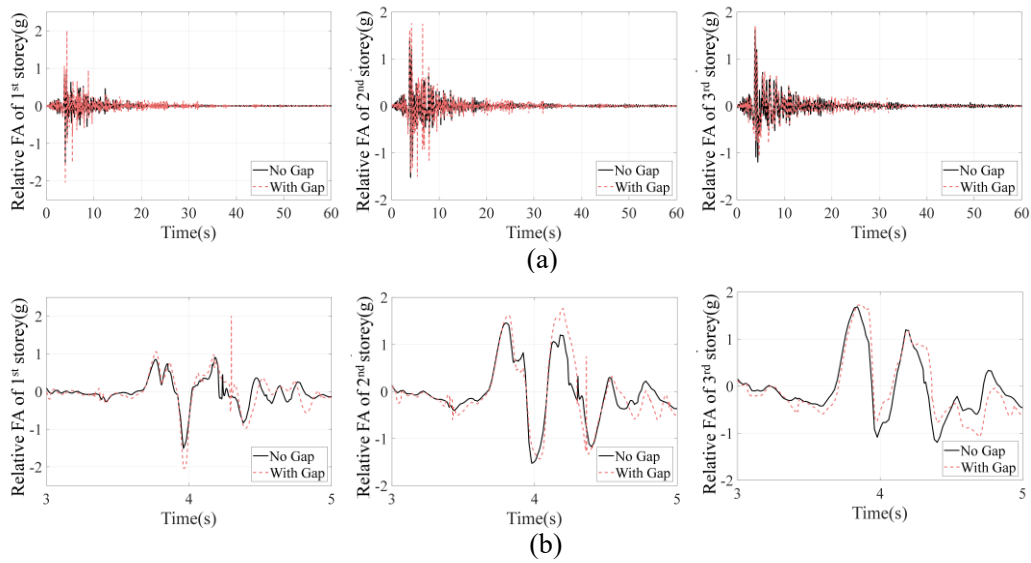


Fig. 6.15. Comparisons of relative FA of each storey for structure with and without the initial gaps: (a) under complete record, and (b) over acceleration-pulse interval (i.e., 3 - 5s)

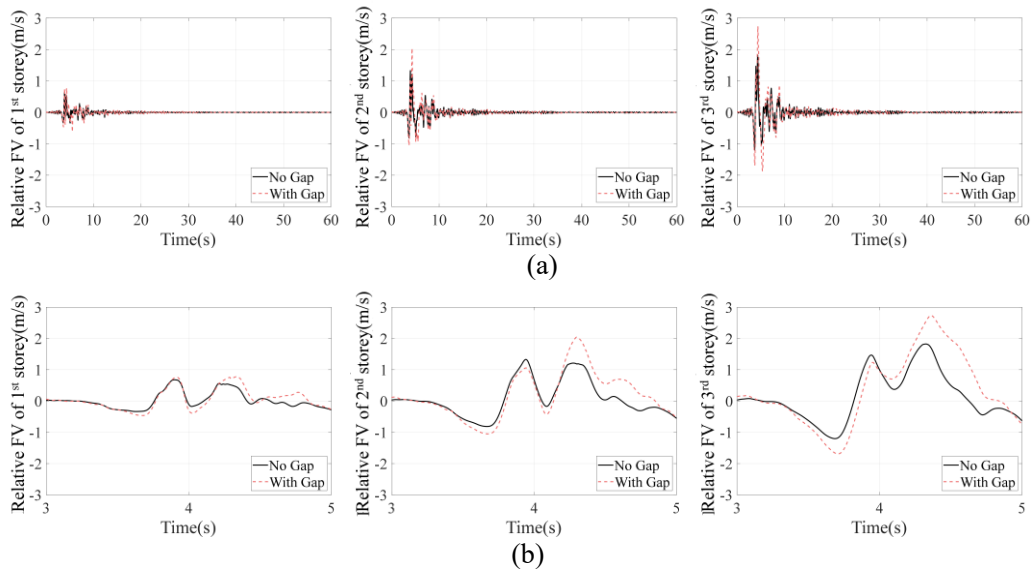


Fig. 6.16. Comparisons of relative FV of each storey for structure with and without the initial

gaps: (a) under complete record, and (b) over acceleration-pulse interval (i.e., 3 - 5s)

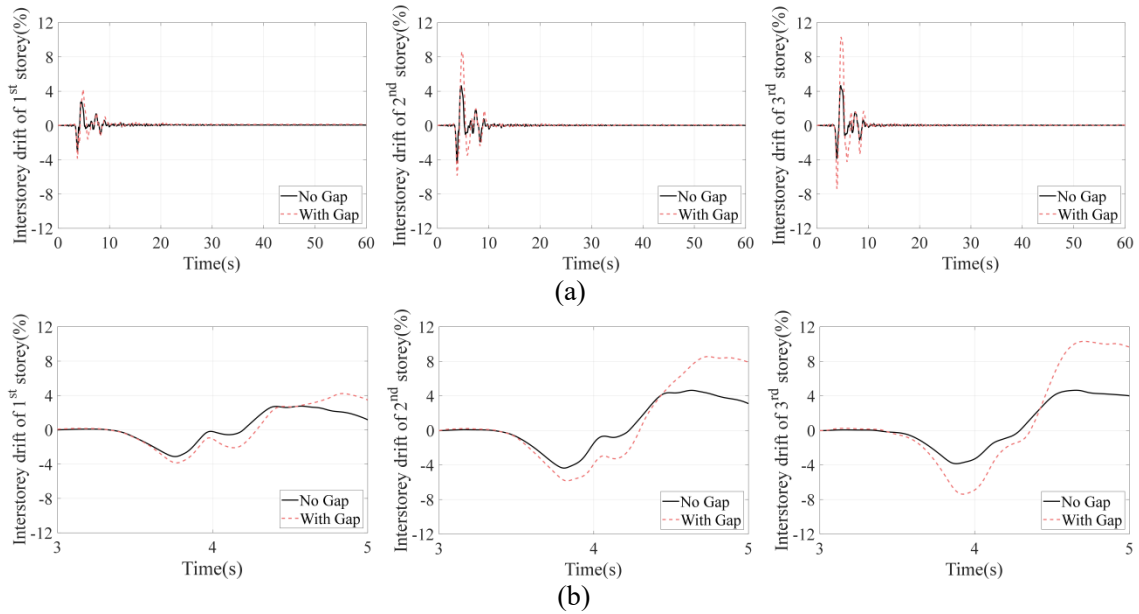


Fig. 6.17. Comparisons of interstorey drift responses of each storey for structure with and without the initial gaps: (a) under complete record, and (b) over acceleration-pulse interval (i.e., 3 - 5s)

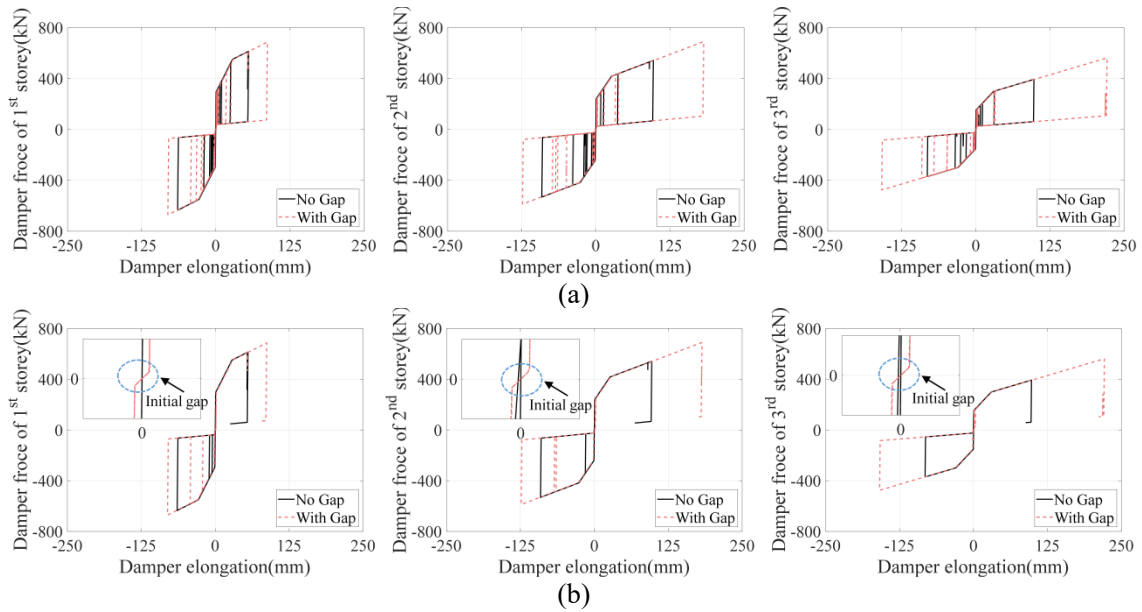


Fig. 6.18. Comparisons of hysteretic damper behaviour at each storey for structure with and without the initial gaps: (a) under complete record, and (b) over acceleration-pulse interval (i.e., 3 - 5s)

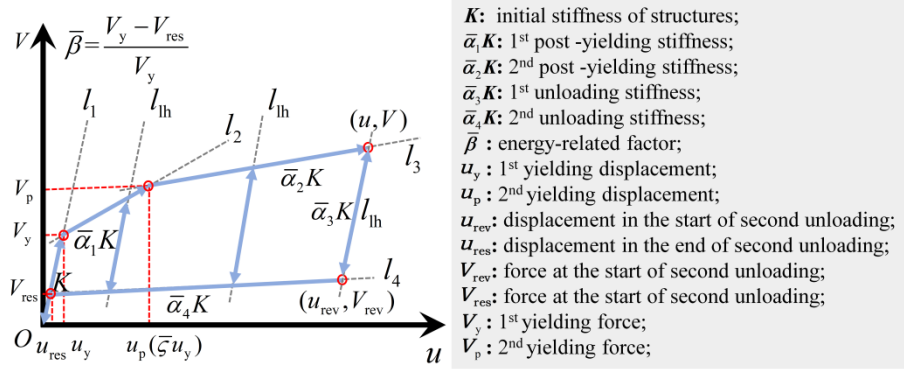


Fig. 6.19. Hysteretic behaviour of structure equipped with SMA-VFSD and implications of hysteretic parameters

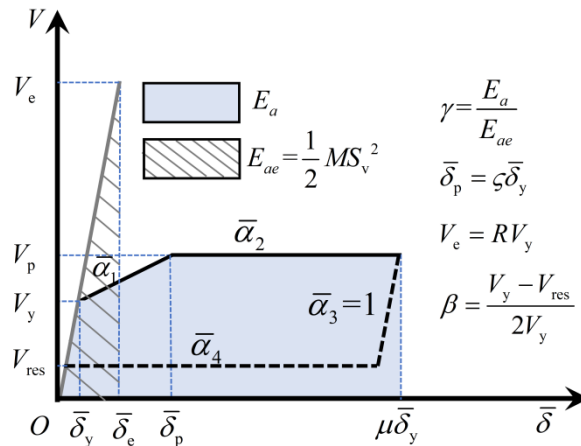


Fig. 6.20. Energy balance concept of systems

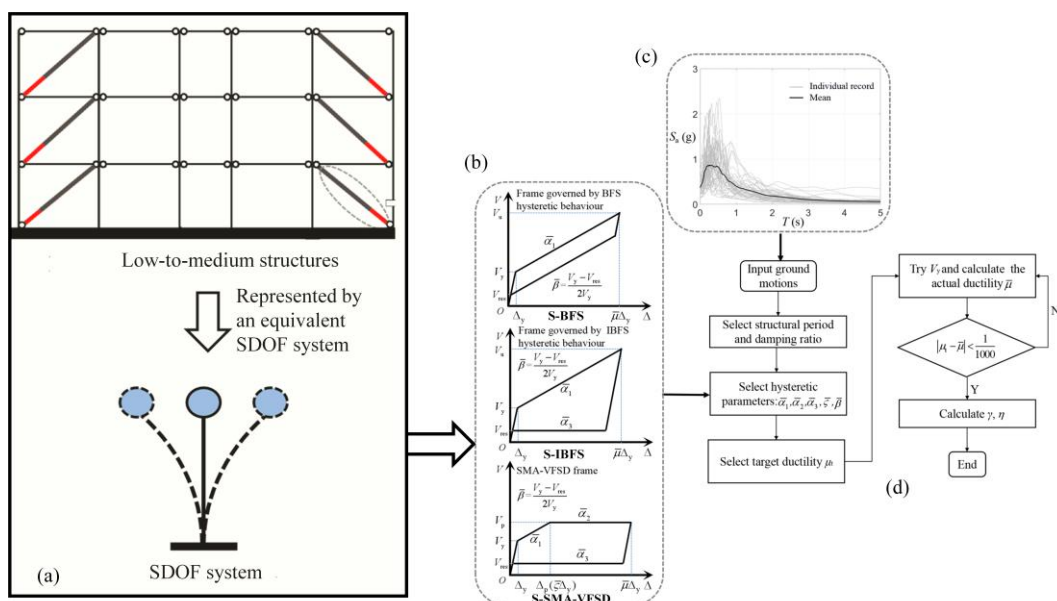
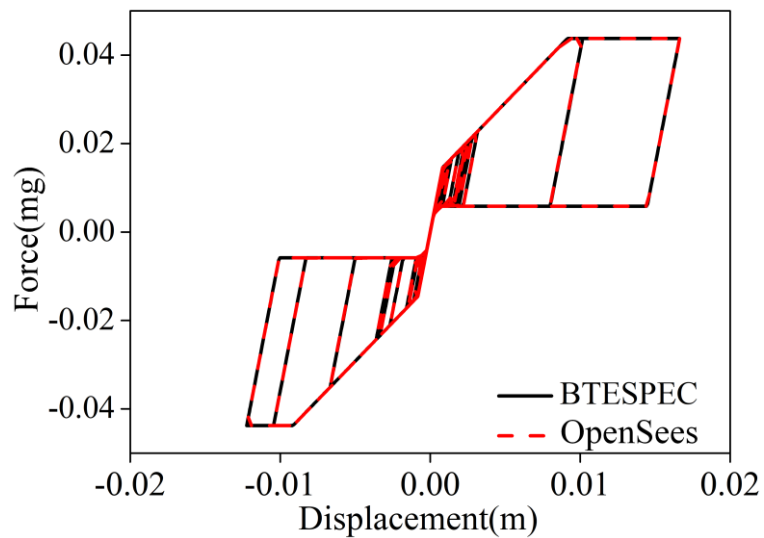
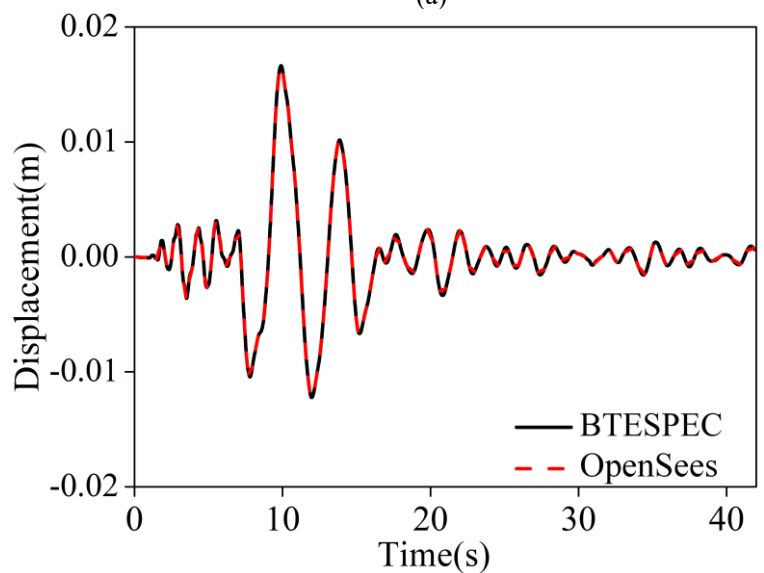


Fig. 6.21. Spectral analyse: (a) Equivalent Single Degree of Freedom (SDOF), (b) hysteretic law, (c) ground motions (0.05 damping ratio), and (d) flow chart.



(a)



(b)

Fig. 6.22. Comparison results of BTESPEC and OpenSees under Kocaeli record:  
 (a) Hysteretic responses; and (b) Displacement responses

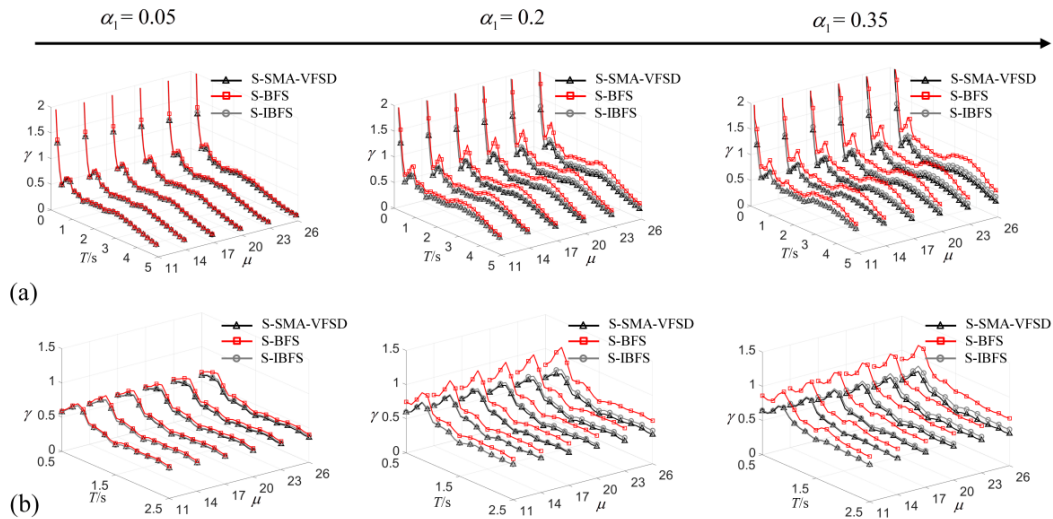


Fig. 6.23. Comparison of the mean energy modification factor spectra: (a) 0.1 s - 5 s, and (b) 0.5 s - 2.5 s.

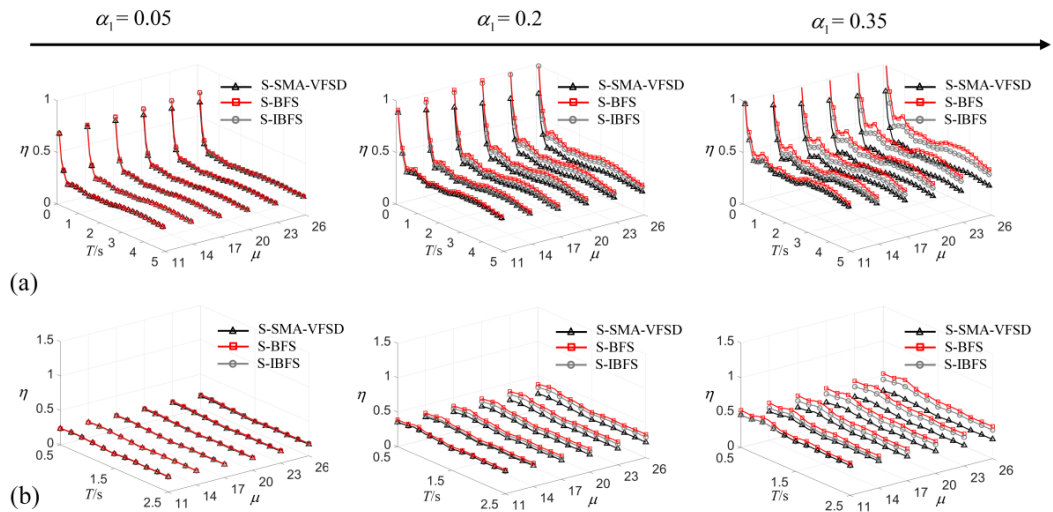


Fig. 6.24. Comparison of the mean acceleration factor spectra: (a) 0.1 s - 5 s, (b) 0.5 s - 2.5 s.

## Chapter 7 Summary and conclusions

### 7.1 Summary

The challenge of limited natural resources in the face of growing human populations underscores the urgent need for sustainable development across various societal realms. Post-earthquake investigations in civil engineering have shown that while conventional structures designed to current seismic standards may withstand earthquakes, the resulting damage often leads to high repair costs. In some cases, proposed repair strategies prove economically unviable compared to rebuilding, posing a threat to sustainable development. This issue stems from the lack of resilient concept in current design methodologies. Specifically, primary structural members in such structures, including beams, columns, and braces, not only provide strength and stiffness but also dissipate seismic energy. This coupling of energy-dissipation and strength-related elements undermines structural resilience, causing uncontrolled damage mechanisms and often resulting in significant residual deformation of structures after earthquakes.

Recently, self-centring technologies have been proposed to enhance structural resilience. These strategies aim to separate energy-dissipation-related elements from strength-related elements, at either the material or member level, enabling controlled structural damage and enhancing resilience.

In this thesis, to further improve seismic performance for self-centring structures, an innovative damper (SMA-VFSD) following the multistage energy-dissipation mechanism was proposed. In this damper, it combines the characteristics (i.e., superelastic effect and phase transformation) of shape memory alloys (SMAs), disc

spring systems, and a variable friction mechanism and integrate them into a specific configuration. Supported by the restoring force from the disc spring systems, the SMA-VFSD decouples the interdependence between the friction coefficient and the sloping angle of friction pairs, a phenomenon known as self-locking in previous research. This decoupling enables the multistage energy-dissipation mechanism and enhances the performance for the damper.

A comprehensive experimental programme on the SMA-VFSD was conducted at the damper level. Specifically, to verify the stable and predictable behaviour of the SMA-VFSD's constituent components, cyclic tests were performed on the SMA bolts, steel-brass friction pairs, and disc spring groups. The cyclic behaviour of these components was then discussed in detail. Then, eight damper specimens were tested under cyclic loadings. The test results, including experimental observations, hysteretic behaviour, and energy-dissipation capacities, were discussed, and the effect of the design parameters (i.e., SMA bolt type, sloping angle of friction pairs and preload of SMA bolts) on damper performance was investigated. Based on test data, the effectiveness of the developed analytical model in predicting the hysteretic responses for the SMA-VFSD was verified. Utilising the analytical model, further exploration was conducted to investigate the effects of an extended range of the design parameters on the damper behaviour. To provide a comprehensive the damper's performance, a detailed refined numerical model was developed and validated against test data. Finally, to enhance computational efficiency, a simplified model for quantifying damper behaviour was developed and its accuracy was also demonstrated.

Further, to validate the feasibility of the damper' application in braced frames, an experimental programme investigating the cyclic behaviour of a one-bay and one storey braced frame equipped with the SMA-VFSD was conducted at the sub-structural level.

Six frame tests were performed to study the effects of design parameters, including the preload of the SMA bolts and the sloping angle of the friction pairs, on structural behaviour. The test results, including experimental observations, hysteretic behaviour, energy-dissipation capacities, and self-centring abilities were discussed in detail. Following this, a simplified numerical model, which can consider initial gaps due to fabrication tolerances, was devised to predict the cyclic behaviour of the tested braced frame. This model was then validated against the test results of the specimens. Specifically, comparisons between the predictions of the developed model and the test results of the frame specimens (e.g., hysteretic behaviour and energy-dissipation capacity) were conducted to demonstrate the accuracy and reliability of the proposed simplified mode.

Finally, to verify the effectiveness of the proposed damper in mitigating seismic performance and enhance structural resilience at the system level, a prototype building equipped with the SMA-VFSD was designed and simulated using the validated modelling technologies. A comparative study was conducted on structures equipped with the SMA-VFSD and a previous type of damper (referred to as PD for comparison). Following this, the seismic behaviour of structures with and without initial gaps in the proposed damper braces was examined to evaluate the effect of fabrication tolerances (i.e., clearance among pin connections) on the structural performance. Finally, using a self-developed calculation programme, nonlinear constant-ductility spectral analyses were conducted on a Single Degree of Freedom (SDOF) system, representing structures showing multistage energy-dissipation characteristics. The aim of the spectral analyses was to explore the seismic demands of structures equipped with the SMA-VFSD under different combinations of hysteretic parameters and earthquake records.

## **7.2 Conclusions**

The main conclusions of this thesis, based on the theoretical, experimental, and numerical analyses of the proposed damper and its structural applications, can be summarised as follows.

Firstly, based on the damper component's test results, both NiTi SMA and NiTiCo SMA demonstrated stable hysteretic behaviour with minimal residual deformation but lower energy dissipation. The friction behaviour of the steel (GCr15)-brass(H62) friction pair under three normal force levels was consistent, confirming the reliable and predictable performance of the friction pair under variable normal forces. The disc spring group were shown stable and linear cyclic responses. At the damper-level test, the main conclusions can be drawn: 1) The mechanical behaviour of the tested dampers was consistent with the conceptual design. Furthermore, the decoupled relationship of design parameters was confirmed; 2) The tested SMA-VFSD exhibited a multistage energy-dissipation behaviour with flag-shaped hysteretic curves, where the key hysteretic parameters can be flexibly adjusted by varying the design parameters, making the damper adaptable to different engineering demands; 3) The hysteretic behaviour of the SMA-VFSD was basically not influenced by the loading history and loading rate, indicating that the proposed damper has stable and reliable performance; 4) The SMA-VFSD demonstrated a full self-centring behaviour and good energy-dissipation capacity; 5) The test results showed that equivalent viscous damping (EVD) of the specimens was around 16%-20% and remained consistent in all loading stages; 6) The damper behaviour prediction of the developed analytical model agreed well with the experimental results; 7) The refined and simplified numerical model accurately replicated the damper's behaviour, encompassing deformation modes and hysteretic responses.

Subsequently, according to the sub-structural test results, main conclusions

included: 1) The frame demonstrated a multistage energy-dissipation behaviour with flag-shaped hysteretic curves, mirroring the findings from the previous damper test; 2) The hysteretic behaviour of the frame specimens was basically not influenced by the loading history, indicating that the frame equipped with the SMA-VFSD has stable and reliable performance under multiple loadings; 3) The frame exhibited excellent self-centring behaviour with minimal residual interstorey drifts. This residual drift resulted from the fabrication tolerance rather than the development of plastic deformation in the main frame; 4) The test results showed that equivalent viscous damping (EVD) of the specimens was around 5%-10% and remained a steady increase over all loading stages; 5) The effectiveness of the simplified frame model which could consider the initial gaps in tracing the hysteretic behaviour at both the frame and damper levels was validated.

Finally, at the system level, the comparative dynamic analyses of a structural case demonstrated the effectiveness of the SMA-VFSD following the multistage energy-dissipation mechanism in optimising structural performance. The discussion on the effect of initial gaps causing structural stiffness reduction emphasised that, although these gaps had minimal effect on static behaviour, they significantly influenced the dynamic response of structures during earthquakes. Observations indicated substantial increases in peak drift responses and PFAs for the structures considering the initial gaps, underscoring the importance of this seismic concern. The inelastic seismic demands quantified by the constant-ductility-based energy modification factor and the acceleration factor of equivalent SDOF systems representing low-to-medium structures equipped with the SMA-VFSDs were always lower when compared to two additional self-centring systems (i.e., S-BFS and S-IBFS) that exhibit different hysteretic behaviour. Therefore, the promise of the SMA-VFSDs was justified from a structural seismic demand perspective.

### 7.3 Future work

Based on current research findings made in this thesis, the suggestions for future work were outlined as follows:

- **Exploration of Alternative Solutions to SMA Bolts:** The decoupling of strength and stiffness and the multistage energy-dissipation mechanism in the proposed SMA-VFSD are achieved through the introduction of SMA bolts, which enhances the design flexibility and overall performance of the damper. However, the cost of SMA bolts may limit the engineering applications of the damper, which indicates a need to explore alternative solutions. This research direction is promising for making the damper more practical and cost-efficient. The author is currently exploring potential options, such as combined disc spring systems with different configurations and preloads, which will be investigated further.
- **Enhancement of Friction Pair Combinations:** The friction pair used in this thesis provides a stable and reliable energy-dissipation mechanism for the damper. The friction behaviour of the selected pair appears to be insensitive to the tested range of normal forces. To further improve damper performance, additional friction pair combinations with customisable friction coefficients should be explored. Future research should extend the types of friction pair configurations and test a wider range of friction pairs.
- **Broader Structural Applications:** The braced frame equipped with the SMA-VFSD demonstrated the expected hysteretic behaviour, confirming its potential for structural applications. To explore the potential of the damper in a wider range of engineering applications, such as beam-to-column connections and rocking energy-dissipation columns, additional tests are needed to validate their feasibility.
- **Impact of Fabrication Tolerances on Seismic Performance:** The effect of

fabrication tolerances in pin connections on seismic performance was initially investigated, and dynamic analyses confirmed increased seismic demands due to initial gaps. Further research is required to fully understand how these initial gaps, caused by fabrication tolerances, amplify seismic responses in structures. The issue of the impact of fabrication tolerances on seismic performance is particularly important given the growing use of pin connections as primary structural elements in various structures.

- **Further Validation through Shaking Table Tests:** A comprehensive experimental programme was conducted to evaluate the performance of the damper, its constituent components, and the braced frame equipped with the damper. The test results provide valuable design considerations for the research community. To further validate the potential of the damper in structural applications, shaking table tests of structures equipped with the SMA-VFSD are recommended to assess their behaviour under dynamic loading conditions.

## Appendix A

The added new uniaxial material (MGSC material) in OpenSees contains two files (i.e., MGSCMaterial.h and MGSCMaterial.cpp). The detailed codes are given as below:

### Codes in MGSCmaterial.h:

```
#ifndef MGSCMaterial_h
#define MGSCMaterial_h
// Written: ZHANG Ping
// Created: MAY 2021
// Description: This file contains the class definition for MGSC (Multi-linear general
self-centering) Material. MGSCMaterial provides the abstraction for a one-dimensional
rate-independent flag-shaped hysteresis.
#include <UniaxialMaterial.h>
// #include <Matrix.h>
class MGSCMaterial : public UniaxialMaterial
{
public:
    MGSCMaterial(int tag, double k1, double k2, double k3, double k4, double k5,
        double ActF, double beta, double anta );
    MGSCMaterial();
    ~MGSCMaterial();
    const char* getClassType(void) const { return "MGSCMaterial"; };
    int setTrialStrain(double strain, double strainRate = 0.0);
    double getStrain(void);
    double getStress(void);
    double getTangent(void);
    double getInitialTangent(void) {return k1; };
    int commitState(void);
    int revertToLastCommit(void);
    int revertToStart(void);
    UniaxialMaterial* getCopy(void);
    int sendSelf(int commitTag, Channel& theChannel);
    int recvSelf(int commitTag, Channel& theChannel,
        FEM_ObjectBroker& theBroker);
    void Print (OPS_Stream& s, int flag = 0);
protected:
private:
    // Material parameters (from input)
    double k1; // Precompression Stiffness
    double k2; // Prestress Stiffness
    double k3;
    double k4;
    double k5;
```

```

double ActF; // Activation Stress/Force
double beta; // Flag-Shape Parameter
double anta;
double ActDef; // Actvation Strain/Deformation
double diffStrain; // Difference of strain from last step
// Committed history variables
double CDyna1p;
double CDyna2p;
double CDyna3p;
double CDyna1n;
double CDyna2n;
double CDyna3n;
// Trial history variables
double TDyna1p;
double TDyna2p;
double TDyna3p;
double TDyna1n;
double TDyna2n;
double TDyna3n;
// Trial state variables
double Tstrain; // Trial strain
double Tstress; // Trial stress
double Ttangent; // Trial tangent
// Committed State Variables
double Cstrain; // Committed Strain
double Cstress; // Committed Strain
double Ctangent; // Committed Strain
};
#endif

#pragma once

```

Codes in MGSCMaterial.cpp:

```

#include <MGSCMaterial.h>
#include <Vector.h>
#include <Channel.h>
#include <Matrix.h>
#include <Information.h>
#include <Parameter.h>
#include <math.h>
#include <float.h>
#include <elementAPI.h>
void* OPS_MGSCMaterial()
{
int numdata = OPS_GetNumRemainingInputArgs();
if (numdata < 9) {

```

```

opserr << "WARNING: Insufficient arguments\n";
opserr << "Want: uniaxialMaterial MGSCMaterial tag? k1? k2? k3? k4? k5 ";
opserr << "ActF? beta? anta?" << endl;
return 0;
}
int tag;
numdata = 1;
if (OPS_GetIntInput(&numdata, &tag) < 0) {
opserr << "WARNING invalid tag\n";
return 0;
}
double data[8] = { 0,0,0,0,0,0,0,0 };
numdata = OPS_GetNumRemainingInputArgs();
if (numdata > 8) {
numdata = 8;
}
if (OPS_GetDoubleInput(&numdata, data)) {
opserr << "WARNING invalid double inputs\n";
return 0;
}
UniaxialMaterial* mat = new MGSCMaterial(tag, data[0], data[1], data[2],
data[3], data[4], data[5], data[6], data[7]);
if (mat == 0) {
opserr << "WARNING: failed to create MGSC material\n";
return 0;
}
return mat;
}
MGSCMaterial::MGSCMaterial(int tag, double K1, double K2, double K3, double K4,
double K5,
double fa, double b, double Anta)
: UniaxialMaterial(tag, MAT_TAG_MGSCMaterial),
k1(K1), k2(K2), k3(K3), k4(K4), k5(K5), ActF(fa), beta(b), anta(Anta) {
// Find Equivalent Slip Force
ActDef = ActF / k1;
// Initialize variables
this->revertToStart();
}
MGSCMaterial::MGSCMaterial()
: UniaxialMaterial(0, MAT_TAG_MGSCMaterial),
k1(0.0), k2(0.0), k3(0), k4(0), k5(0), ActF(0.0), beta(0.0), anta(0) {
// Initialize variables
ActDef = 0;
this->revertToStart();
}
MGSCMaterial::~MGSCMaterial()
{
}
int
MGSCMaterial::setTrialStrain(double strain, double strainRate)

```

```

{
diffStrain = strain - Cstrain;
if (fabs(diffStrain) < DBL_EPSILON)
return 0;
// Set total strain
Tstrain = strain;
// Middle Elastic Portion (outside any upper or lower activation)
// Entirely elastic response
if (fabs(Tstrain) <= ((1 - beta) * ActF / k1)) {
TDyna1p = ActDef * (1 - beta);
TDyna2p = ActDef;
TDyna3p = anta * ActDef;
TDyna1n = -ActDef * (1 - beta);
TDyna2n = -ActDef;
TDyna3n = -anta * ActDef;
Tstress = k1 * Tstrain;
Ttangent = k1;
}
else {
// Positive Quadrant (Top Right) where strain >= 0
// Linear range movement (no upper or
// lower activation)
if (Tstrain >= 0) {
if ((Tstrain >= CDyna1p) &&
(Tstrain <= CDyna2p)) {
TDyna1p = CDyna1p;
TDyna2p = CDyna2p;
TDyna3p = CDyna3p;
TDyna1n = CDyna1n;
TDyna2n = CDyna2n;
TDyna3n = CDyna3n;
if (CDyna1p == (1 - beta) * ActDef)
{
Tstress = k1 * Tstrain;
Ttangent = k1;
}
else {
Tstress = k5 * TDyna1p + (k1 - k5) * (1 - beta) * ActDef + k4 * (Tstrain - TDyna1p);
Ttangent = k4;
}
}
else if (Tstrain > CDyna2p) {
if (Tstrain >= ActDef && Tstrain <= anta * ActDef) {
TDyna1p = (k4 * Tstrain - k2 * Tstrain - (k1 - k2) * ActDef - k5 * ActDef * (1 - beta)
+ k1 * ActDef * (1 - beta)) / (k4 - k5);
TDyna2p = Tstrain;
TDyna3p = anta * ActDef;
TDyna1n = CDyna1n;
TDyna2n = CDyna2n;
TDyna3n = CDyna3n;
}
}
}
}

```

```

Tstress = k2 * Tstrain + (k1 - k2) * ActDef;
Ttangent = k2;
}
else if (Tstrain < ActDef) {
TDyna1p = (k4 * Tstrain - k1 * Tstrain - k5 * ActDef * (1 - beta) + k1 * ActDef * (1
- beta)) / (k4 - k5);
TDyna2p = Tstrain;
TDyna3p = anta * ActDef;
TDyna1n = CDyna1n;
TDyna2n = CDyna2n;
TDyna3n = CDyna3n;
Tstress = k5 * TDyna1p + (k1 - k5) * ActDef * (1 - beta) + k4 * (Tstrain - TDyna1p);
Ttangent = k4;
}
else if (Tstrain > anta * ActDef) {
TDyna1p = (k4 * Tstrain - k2 * anta * ActDef - (k1 - k2) * ActDef - k3 * (Tstrain -
anta * ActDef) - k5 * ActDef * (1 - beta) + k1 * ActDef * (1 - beta)) / (k4 - k5);
TDyna2p = Tstrain;
TDyna3p = Tstrain;
TDyna1n = CDyna1n;
TDyna2n = CDyna2n;
TDyna3n = CDyna3n;
Tstress = k2 * anta * ActDef + (k1 - k2) * ActDef + (Tstrain - anta * ActDef) * k3;
Ttangent = k3;
}
}
else {
if (Tstrain > (k4 * anta * ActDef - k2 * anta * ActDef - (k1 - k2) * ActDef - k5 *
ActDef * (1 - beta) + k1 * ActDef * (1 - beta)) / (k4 - k5))
{
TDyna1p = Tstrain;
TDyna2p = (k4 * Tstrain - k5 * Tstrain - (k1 - k5) * ActDef * (1 - beta) - k3 * anta *
ActDef + k2 * anta * ActDef + (k1 - k2) * ActDef) / (k4 - k3);
TDyna3p = (k4 * Tstrain - k5 * Tstrain - (k1 - k5) * ActDef * (1 - beta) - k3 * anta *
ActDef + k2 * anta * ActDef + (k1 - k2) * ActDef) / (k4 - k3);
TDyna1n = CDyna1n;
TDyna2n = CDyna2n;
TDyna3n = CDyna3n;
Tstress = k5 * Tstrain + (k1 - k5) * ActDef * (1 - beta);
Ttangent = k5;
}
else if (Tstrain >= (k4 * ActDef - k1 * ActDef - k5 * ActDef * (1 - beta) + k1 * ActDef
* (1 - beta)) / (k4 - k5) && Tstrain <= (k4 * anta * ActDef - k2 * anta * ActDef - (k1 -
k2) * ActDef - k5 * ActDef * (1 - beta) + k1 * ActDef * (1 - beta)) / (k4 - k5))
{
TDyna1p = Tstrain;
TDyna2p = (k4 * Tstrain - k5 * Tstrain - (k1 - k5) * ActDef * (1 - beta) - k2 * ActDef
+ k1 * ActDef) / (k4 - k2);
TDyna3p = anta * ActDef;
TDyna1n = CDyna1n;

```

```

TDyna2n = CDyna2n;
TDyna3n = CDyna3n;
Tstress = k5 * Tstrain + (k1 - k5) * ActDef * (1 - beta);
Ttangent = k5;
}
else {
TDyna1p = Tstrain;
TDyna2p = (k4 * Tstrain - k5 * Tstrain - (k1 - k5) * ActDef * (1 - beta)) / (k4 - k1);
TDyna3p = anta * ActDef;
TDyna1n = CDyna1n;
TDyna2n = CDyna2n;
TDyna3n = CDyna3n;
Tstress = k5 * Tstrain + (k1 - k5) * ActDef * (1 - beta);
Ttangent = k5;
}
}
}
else {
if (Tstrain <= CDyna1n && Tstrain >= CDyna2n)
{
TDyna1p = CDyna1p;
TDyna2p = CDyna2p;
TDyna3p = CDyna3p;
TDyna1n = CDyna1n;
TDyna2n = CDyna2n;
TDyna3n = CDyna3n;
if (CDyna1n == -(1 - beta) * ActDef)
{
Tstress = k1 * Tstrain;
Ttangent = k1;
}
else
{
Tstress = k5 * CDyna1n - (k1 - k5) * (1 - beta) * ActDef + k4 * (Tstrain - CDyna1n);
Ttangent = k4;
}
}
else if (Tstrain < CDyna2n)
{
if (Tstrain <= -ActDef && Tstrain >= -anta * ActDef)
{
TDyna1p = CDyna1p;
TDyna2p = CDyna2p;
TDyna3p = CDyna3p;
TDyna1n = (k4 * Tstrain - k2 * Tstrain + (k1 - k2) * ActDef + k5 * (1 - beta) * ActDef
- k1 * (1 - beta) * ActDef) / (k4 - k5);
TDyna2n = Tstrain;
TDyna3n = -anta * ActDef;
Tstress = k2 * Tstrain - (k1 - k2) * ActDef;
Ttangent = k2;
}
}
}
}
}

```

```

}
else if (Tstrain >= -ActDef)
{
TDyna1p = CDyna1p;
TDyna2p = CDyna2p;
TDyna3p = CDyna3p;
TDyna1n = (k4 * Tstrain - k1 * Tstrain + k5 * (1 - beta) * ActDef - k1 * (1 - beta) *
ActDef) / (k4 - k5);
TDyna2n = Tstrain;
TDyna3n = -anta * ActDef;
Tstress = k5 * TDyna1n - (k1 - k5) * (1 - beta) * ActDef + k4 * (TDyna2n - TDyna1n);
Ttangent = k2;
}
else if (Tstrain < -anta * ActDef)
{
TDyna1p = CDyna1p;
TDyna2p = CDyna2p;
TDyna3p = CDyna3p;
TDyna1n = (k4 * Tstrain + k2 * anta * ActDef + (k1 - k2) * ActDef - k3 * (Tstrain +
anta * ActDef) + k5 * (1 - beta) * ActDef - k1 * (1 - beta) * ActDef) / (k4 - k5);
TDyna2n = Tstrain;
TDyna3n = Tstrain;
Tstress = k5 * TDyna1n - (k1 - k5) * (1 - beta) * ActDef + k4 * (TDyna2n - TDyna1n);
Ttangent = k3;
}
}
else {
if (Tstrain < -(k4 * anta * ActDef - k2 * anta * ActDef - (k1 - k2) * ActDef - k5 *
ActDef * (1 - beta) + k1 * ActDef * (1 - beta)) / (k4 - k5))
{
TDyna1p = CDyna1p;
TDyna2p = CDyna2p;
TDyna3p = CDyna3p;
TDyna1n = Tstrain;
TDyna2n = (k4 * Tstrain - k5 * Tstrain + (k1 - k5) * ActDef * (1 - beta) + k3 * anta
* ActDef - k2 * anta * ActDef - (k1 - k2) * ActDef) / (k4 - k3);
TDyna3n = (k4 * Tstrain - k5 * Tstrain + (k1 - k5) * ActDef * (1 - beta) + k3 * anta
* ActDef - k2 * anta * ActDef - (k1 - k2) * ActDef) / (k4 - k3);
Tstress = k5 * Tstrain - (k1 - k5) * ActDef * (1 - beta);
Ttangent = k5;
}
else if (Tstrain >= -(k4 * anta * ActDef - k2 * anta * ActDef - (k1 - k2) * ActDef - k5
* ActDef * (1 - beta) + k1 * ActDef * (1 - beta)) / (k4 - k5) && Tstrain <= -(k4 * ActDef
- k1 * ActDef - k5 * ActDef * (1 - beta) + k1 * ActDef * (1 - beta)) / (k4 - k5))
{
TDyna1p = CDyna1p;
TDyna2p = CDyna2p;
TDyna3p = CDyna3p;
TDyna1n = Tstrain;

```

```

    TDyna2n = (k4 * Tstrain - k5 * Tstrain + (k1 - k5) * ActDef * (1 - beta) + k2 * ActDef
- k1 * ActDef) / (k4 - k2);
    TDyna3n = -anta * ActDef;
    Tstress = k5 * Tstrain - (k1 - k5) * ActDef * (1 - beta);
    Ttangent = k5;
}
else {
    TDyna1p = CDyna1p;
    TDyna2p = CDyna2p;
    TDyna3p = CDyna3p;
    TDyna1n = Tstrain;
    TDyna2n = (k4 * Tstrain - k5 * Tstrain + (k1 - k5) * ActDef * (1 - beta)) / (k4 - k1);
    TDyna3n = -anta * ActDef;
    Tstress = k5 * Tstrain - (k1 - k5) * ActDef * (1 - beta);
    Ttangent = k5;
}
}
}
}
return 0;
}
double
MGSCMaterial::getStress(void)
{
    return Tstress;
}
double
MGSCMaterial::getTangent(void)
{
    return Ttangent;
}
double
MGSCMaterial::getStrain(void)
{
    return Tstrain;
}
}

int
MGSCMaterial::commitState(void)
{
    CDyna1p = TDyna1p;
    CDyna2p = TDyna2p;
    CDyna3p = TDyna3p;
    CDyna1n = TDyna1n;
    CDyna2n = TDyna2n;
    CDyna3n = TDyna3n;
    Cstrain = Tstrain;
    Cstress = Tstress;
    Ctangent = Ttangent;
}

```

```

return 0;
}
int
MGSCMaterial::revertToLastCommit(void)
{
    Tstrain = Cstrain;
    Tstress = Cstress;
    Ttangent = Ctangent;
    return 0;
}
int
MGSCMaterial::revertToStart(void)
{
    // Reset committed history variables
    CDyna1p = ActDef*(1-beta);
    CDyna2p = ActDef;
    CDyna3p = anta*ActDef;
    CDyna1n = -ActDef * (1 - beta);
    CDyna2n = -ActDef;
    CDyna3n = -anta * ActDef;
    // Reset trial history variables
    TDyna1p = ActDef * (1 - beta);
    TDyna2p = ActDef;
    TDyna3p = anta * ActDef;
    TDyna1n = -ActDef * (1 - beta);
    TDyna2n = -ActDef;
    TDyna3n = -anta * ActDef;
    // Initialize state variables
    Tstrain = 0.0;
    Tstress = 0.0;
    Ttangent = k1;
    Cstrain = 0.0;
    return 0;
}
UniaxialMaterial*
MGSCMaterial::getCopy(void)
{
    MGSCMaterial* theCopy =
        new MGSCMaterial(this->getTag(), k1, k2,k3,k4,k5,ActF,beta,anta
        );
    // Copy committed history variables
    theCopy->CDyna1p = CDyna1p;
    theCopy->CDyna2p = CDyna2p;
    theCopy->CDyna3p = CDyna3p;
    theCopy->CDyna1n = CDyna1n;
    theCopy->CDyna2n = CDyna2n;
    theCopy->CDyna3n = CDyna3n;
    // Copy trial history variables
    theCopy->TDyna1p = TDyna1p;
    theCopy->TDyna2p = TDyna2p;

```

```

theCopy->TDyna3p = TDyna3p;
theCopy->TDyna1n = TDyna1n;
theCopy->TDyna2n = TDyna2n;
theCopy->TDyna3n = TDyna3n;
// Copy trial state variables
theCopy->Tstrain = Tstrain;
theCopy->Tstress = Tstress;
theCopy->Ttangent = Ttangent;
theCopy->Cstrain = Cstrain;
return theCopy;
}
int
MGSCMaterial::sendSelf(int cTag, Channel& theChannel)
{
int res = 0;
static Vector data(20);
data(0) = this->getTag();
data(1) = k1;
data(2) = k2;
data(3) = k3;
data(4) = k4;
data(5) = k5;
data(6) = ActF;
data(7) = beta;
data(8) = anta;
data(9) = ActDef;
data(10) = CDyna1p;
data(11) = CDyna2p;
data(12) = CDyna3p;
data(13) = CDyna1n;
data(14) = CDyna2n;
data(15) = CDyna3n;
data(16) = Tstrain;
data(17) = Tstress;
data(18) = Ttangent;
data(19) = Cstrain;

res = theChannel.sendVector(this->getDbTag(), cTag, data);
if (res < 0)
opserr << "MGSCMaterial::sendSelf() - failed to send data\n";
return res;
}
int
MGSCMaterial::recvSelf(int cTag, Channel& theChannel,
FEM_ObjectBroker& theBroker)
{
int res = 0;
static Vector data(20);
res = theChannel.recvVector(this->getDbTag(), cTag, data);
if (res < 0) {

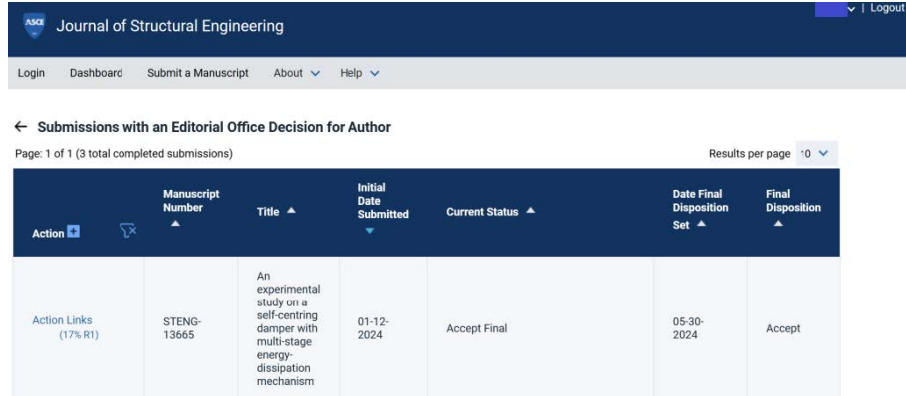
```

```
opserr << "MGSC::recvSelf() - failed to receive data\n";
this->setTag(0);
}
else {
this->setTag((int)data(0));
k1 = data(1);
k2 = data(2);
k3 = data(3);
k4 = data(4);
k5 = data(5);
ActF = data(6);
beta = data(7);
anta = data(8);
ActDef = data(9);
CDyna1p = data(10);
CDyna2p = data(11);
CDyna3p = data(12);
CDyna1n = data(13);
CDyna2n = data(14);
CDyna3n = data(15);
Tstrain = data(16);
Tstress = data(17);
Ttangent = data(18);
Cstrain = data(19);
}
return res;
}
void
MGSCMaterial::Print(OPS_Stream& s, int flag)
{
s << "MGSCMaterial, tag: " << this->getTag() << endl;
s << " k1: " << k1 << endl;
s << " k2: " << k2 << endl;
s << " k3: " << k3 << endl;
s << " k4: " << k4 << endl;
s << " k5: " << k5 << endl;
s << " ActF: " << ActF << endl;
s << " beta: " << beta << endl;
s << " anta: " << anta << endl;
}
```

## Appendix B

The below is the copyright of the publications used in this thesis:

### 1. Journal paper used in Chapter 3 and Chapter 4:



Action	Manuscript Number	Title	Initial Date Submitted	Current Status	Date Final Disposition Set	Final Disposition
Action Links (17% R1)	STENG-13665	An experimental study on a self-centring damper with multi-stage energy dissipation mechanism	01-12-2024	Accept Final	05-30-2024	Accept

### 2. Journal paper used in Chapter 6:

Journal of Constructional Steel Research 204 (2023) 107837

Contents lists available at ScienceDirect



Journal of Constructional Steel Research

journal homepage: [www.elsevier.com/locate/jcsr](http://www.elsevier.com/locate/jcsr)



Self-centring damper with multi-energy-dissipation mechanisms: Insights and structural seismic demand perspective

Ke Ke<sup>a</sup>, Michael C.H. Yam<sup>b,c</sup>, Ping Zhang<sup>a,b,c,\*</sup>, Yu Shi<sup>a,d</sup>, Yong Li<sup>a</sup>, Sijia Liu<sup>a</sup>

<sup>a</sup> School of Civil Engineering, Chongqing University, Chongqing, China  
<sup>b</sup> Department of Building and Real Estate, The Hong Kong Polytechnic University, Hong Kong, China  
<sup>c</sup> Chinese National Engineering Research Centre for Steel Construction (Hong Kong Branch), The Hong Kong Polytechnic University, Hong Kong, China  
<sup>d</sup> National Centre for International Research of Low-carbon & Green Buildings, Ministry of Science & Technology, and the Joint International Research Laboratory of Green Buildings and Built Environments, Ministry of Education, China



### 3. Journal paper used in Chapter 6:

Journal of Building Engineering 54 (2022) 104625

Contents lists available at ScienceDirect



Journal of Building Engineering

journal homepage: [www.elsevier.com/locate/jobee](http://www.elsevier.com/locate/jobee)



Steel moment resisting frames with energy-dissipation rocking columns under near-fault earthquakes: Probabilistic performance-based-plastic-design for the ultimate stage

Ping Zhang<sup>a,b</sup>, Michael C.H. Yam<sup>a,b</sup>, Ke Ke<sup>c,d,\*</sup>, Xuhong Zhou<sup>c,d</sup>, Yonghui Chen<sup>c,d</sup>

<sup>a</sup> Department of Building and Real Estate, The Hong Kong Polytechnic University, Hong Kong, China  
<sup>b</sup> Chinese National Engineering Research Centre for Steel Construction (Hong Kong Branch), The Hong Kong Polytechnic University, Hong Kong, China  
<sup>c</sup> School of Civil Engineering, Chongqing University, Chongqing, China  
<sup>d</sup> Key Laboratory of New Technology for Construction of Cities in Mountain Area (Chongqing University), Ministry of Education, Chongqing, China



### 4. Journal's approval for reusing the published material in Chapter 3 and

### Chapter 4:

发件人: PERMISSIONS permissions@asce.org  
收件人: ZHANG, ping828 [Student] ping828.zhang@  
日期: 2024年6月14日 周五, 上午10:25

**CAUTION:** This email is not originated from PolyU. Do not click links or open attachments unless you recognize the sender and know the content is safe.

Thank you for your inquiry. ASCE Publications employs [Copyright Clearance Center](#), an online permission service, to enable customers to request permission for licensing content directly. You will be able to obtain permission for most journals, proceedings, books and standards content requests, directly through Copyright Clearance Center.

**Author requests:** As an original author of an ASCE journal article or proceedings paper, you are permitted to reuse your own content (including figures and tables) for another ASCE or non-ASCE publication (including your thesis), provided it does not account for more than 25% of the new work.

1 / 2

---

Authors may post the final draft of their work on open, unrestricted Internet sites or deposit it in an institutional repository when the draft contains a link to the bibliographic record of the published version in the ASCE Library or Civil Engineering Database. "Final draft" means the version submitted to ASCE after peer review and prior to copyediting or other ASCE production activities; it does not include the copyedited version, the page proof, or a PDF of the published version.

**Institutional Repository requests:** If you are contacting us about your institution's repository. Authors may post a PDF of the ASCE-published version of their work on their employers' Intranet with password protection. Please add the statement: "This material may be downloaded for personal use only. Any other use requires prior permission of the American Society of Civil Engineers. This material may be found at [URL/link of abstract in the ASCE Library or Civil Engineering Database]."

For **Open Access Options and Rights**, visit <https://ascelibrary.org/author-center/rights-permissions#open-access-forms>.

For more information on ASCE Permissions refer to <https://ascelibrary.org/author-center/rights-permissions>.

For all other inquiries, we will review your request and respond within 7-10 business days.

### 5. Journal's approval for reusing the published material in Chapter 6:

**Re: Include the article in my PhD thesis [240612-009443]**

---

发件人: Permissions Helpdesk [permissionshelpdesk@elsevier.com](mailto:permissionshelpdesk@elsevier.com)

收件人: ZHANG, ping828 [Student] [ping828.zhang@](mailto:ping828.zhang@)

日期: 2024年6月13日 周四, 下午4:35

**CAUTION:** This email is not originated from PolyU. Do not click links or open attachments unless you recognize the sender and know the content is safe.

Dear Dr. Zhang,

Thank you for contacting us.

**RE: Self-centring damper with multi-energy-dissipation mechanisms: Insights and structural seismic demand perspective, Journal of Constructional Steel Research, Volume 204, May 2023, 107837.**

**Proposed use: PhD thesis.**

As an Elsevier journal author, you retain the right to Include the article in a thesis or dissertation (provided that this is not to be published commercially) whether in full or in part, subject to proper acknowledgment; see <https://www.elsevier.com/about/policies/copyright> for more information. **As this is a retained right, no written permission from Elsevier is necessary.**

As outlined in our permissions licenses, this extends to the posting to your university's digital repository of the thesis provided that if you include the published journal article (PJA) version, it is embedded in your thesis only and not separately downloadable.

Thank you.

Kind regards,

**Thomas Rexson Yesudoss**

Copyrights Specialist

**ELSEVIER** | HCM - Health Content Management

## 6. Journal's approval for reusing the published material in Chapter 6:

**Re: Include the journal article in a thesis or dissertation [240612-009299]**

---

发件人: Permissions Helpdesk [permissionshelpdesk@elsevier.com](mailto:permissionshelpdesk@elsevier.com)

收件人: ZHANG, ping828 [Student] [ping828.zhang@](mailto:ping828.zhang@)

日期: 2024年6月13日 周四, 下午4:41

**CAUTION:** This email is not originated from PolyU. Do not click links or open attachments unless you recognize the sender and know the content is safe.

Dear Dr. Zhang,

Thank you for contacting us.

**RE: Steel moment resisting frames with energy-dissipation rocking columns under near-fault earthquakes: Probabilistic performance-based-plastic-design for the ultimate stage, Journal of Building Engineering, Volume 54, 15 August 2022, 104625.**

**Proposed use: PhD thesis.**

As an Elsevier journal author, you retain the right to Include the article in a thesis or dissertation (provided that this is not to be published commercially) whether in full or in part, subject to proper acknowledgment; see <https://www.elsevier.com/about/policies/copyright> for more information. **As this is a retained right, no written permission from Elsevier is necessary.**

As outlined in our permissions licenses, this extends to the posting to your university's digital repository of the thesis provided that if you include the published journal article (PJA) version, it is embedded in your thesis only and not separately downloadable.

Thank you.

Kind regards,

**Thomas Rexson Yesudoss**

Copyrights Specialist

**ELSEVIER** | HCM - Health Content Management

Visit [Elsevier Permissions](#)

## References

- Auricchio, F., Taylor, R.L., and Lubliner, J. (1997). Shape-memory alloys: macro-modelling and numerical simulations of the superelastic behavior. *Computer Methods in Applied Mechanics and Engineering*, 146(3), 281–312.
- Auricchio, F., Marfia, S., and Sacco, E. (2003). Modeling of SMA materials: training and two-way memory effects. *Computers and structures*, 81(24), 2301–2317.
- Alavi, B., and Krawinkler, H. (2004). Strengthening of moment-resisting frame structures against near-fault ground motion effects. *Earthquake Engineering and Structural dynamics*, 33, 707–722.
- Abolmaali, A., Treadway, J., Aswath, P., Lu, F., McCarthy, E. (2006). Hysteresis behavior of t-stub connections with superelastic shape memory fasteners. *Journal of Constructional Steel Research*, 62(8), 831-8.
- AISC. Seismic provisions for structural steel buildings. ANSI/AISC 341-10. Chicago, 2010.
- Araki, Y., Maekawa, N., Shrestha, K.C., Yamakawa, M., Koetaka, Y., Omori, T., and Kainuma, R. (2014). Feasibility of tension braces using Cu–Al–Mn superelastic alloy bars. *Structural Control and Health Monitoring*, 21(10), 1304–1315.
- Araki, Y. and Kshitij, C. (2016). Shaking table tests of steel frame with superelastic Cu–Al–Mn SMA tension braces. *Earthquake Engineering and Structural dynamics*, 45, 297–314.
- ASCE7-16. Minimum design loads for buildings and other structures. American Society of Civil Engineers, 2016.
- ABAQUS Analysis User's Manual, ABAQUS Standard, Version 2022.

- Bellouard, Y. (2008). Shape memory alloys for microsystems: a review from a material research perspective. *Materials Science and Engineering: A*, 481–482, 582–589.
- Christopoulos, C., Filiatrault, A., Uang, C.M., and Folz, B. (2002a). Post-tensioned energy dissipating connections for moment-resisting steel frames. *Journal of Structural Engineering*, 128(9), 1111–1120.
- Christopoulos, C., Filiatrault, A., and Folz, B. (2002b). Seismic response of self-centring hysteretic SDOF systems, *Earthquake Engineering and Structural dynamics*, 31 (5), 1131–1150.
- Clifton, C. (2005). Semi-rigid joints for moment-resisting steel framed seismic-resisting systems. PhD thesis, New Zealand: University of Auckland.
- Christopoulos, C., Tremblay, R., Kim, H.-J, and Lacerte, M. (2008). Self-centering energy dissipative bracing system for the seismic resistance of structures: development and validation. *Journal of Structural Engineering*, 134, 96–107.
- Chinese standard. (2010). Code for seismic design of building (GB50011–2010). China Architecture and Building Press.
- Charney, F.A., and Atlayan, O. (2011). Hybrid moment-resisting steel frames, *Engineering Journal*, 48 (3), 169–182.
- Clayton, P.M., Berman, J.W., and Lowes, L.N. (2012). Seismic design and performance of self-centering steel plate shear walls. *Journal of Structural Engineering*, 138, 22–30.
- Chang, W.S., and Araki, Y. (2016). Use of shape-memory alloys in construction: a critical review. *Proceedings of the Institution of Civil Engineers*, 169(2), 87–95.
- Cladera, A., Weber, B., Leinenbach, C., Czaderski, C., Shahverdi, M., Motavalli, M. (2016). Iron-based shape memory alloys for civil engineering structures: an overview. *Construction and Building Materials*, 63, 281–293.

- Chancellor, N.B., Sause, R., Ricles, J.M. (2017). Design and validation of steel self-centering concentrically-braced frames. 16th World Conference on Earthquake, 16WCEE.
- Chen, J., Wang, W., and Fang, C. (2022). Manufacturing, testing and simulation of novel SMA-based variable friction dampers with enhanced deformability. *Journal of Building Engineering*, 45, 103513.
- Chinese standard. (2010). Code for Seismic Design of Buildings (GB50011-2010). Chinese Building Press, Beijing, China, 2010.
- Chinese standard. (2023). Code for disc spring (GB/T 1972-2023). State Administration for Market Regulation of China.
- Chinese standard. (2021). Code for metallic materials-Tensile testing-Part 1: Method of test at room temperature (GB/T 228.1-2021). State Administration for Market Regulation of China.
- Chen, Y., and Ke, K. (2019). Seismic performance of high-strength-steel frame equipped with sacrificial beams of non-compact sections in energy dissipation bays. *Thin-Walled Structures*, 139, 169–185.
- Chou, C., and Chen, Y. (2015). Development of steel dual-core self-centering braces: quasi-static cyclic tests and finite element analyses. *Earthquake Spectra*, 31(1), 247-272.
- Chu, G.L., Wang, W., and Zhang, Y.F. (2020). Nonlinear seismic performance of beam-through steel frames with self-centering modular panel and replaceable hysteretic dampers. *Journal of Constructional Steel Research*, 170, 91-106.
- Chen, P., Xu, L., Xie, and X. Xie. (2023). Enhanced design and experimental investigation of disc spring-based self-centering buckling-restrained braces with a compounded combination mode, *Earthquake Engineering and Structural*

- dynamics*, 52 (10), 3053–3073.
- DesRoches, R., McCormick, J., and Delemont, M. (2004). Cyclic properties of superelastic shape memory alloy wires and bars. *Journal of Structural Engineering*, 130, 38–46.
- Dusicka, P., and Iwai, R. (2007). Development of linked column frame system for seismic lateral loads, In: Proceedings of the SEI structures congress.
- DesRoches, R., Taftali, B., and Ellingwood, B.R. (2010). Seismic Performance Assessment of Steel Frames with Shape Memory Alloy Connections. Part I — Analysis and Seismic Demands. *Journal of Earthquake Engineering*, 14, 471–486.
- Deierlein, G., Krawinkler, H., Ma, X., Eatherton, M., Hajjar, J., Takeuchi, T., and Midorikawa, M. (2011). Earthquake resilient steel braced frames with controlled rocking and energy dissipating fuses. *Steel Construction*, 4(3), 171–175
- Dowden, D.M., Purba, R., and Bruneau, M. (2012). Behavior of self-centering steel plate shear walls and design considerations. *Journal of Structural Engineering*, 138, 11–21.
- Dougka, G., Dimakogianni, D., and Vayas, I. (2014). Innovative energy dissipation systems (FUSEIS 1-1)-experimental analysis. *Journal of Constructional Steel Research*, 96, 69–80.
- Dimakogianni, D., Dougka, G., and Vayas, I. (2015). Seismic behavior of frames with innovative energy dissipation systems (FUSEIS1-2). *Engineering Structures*, 90, 83–95.
- Di Cesare, A., Ponso, F.C., Lamarucciola, N., and Nigro, D. (2020). Experimental seismic response of a resilient 3-storey post-tensioned timber framed building with dissipative braces. *Bulletin of Earthquake Engineering*, 18(15), 6825–6848.

## References

---

- Engelhardt, M.D., Sabol, T.A., Aboutaha, R.S., Frank, K.H. (1995). Testing connections, an overview of the AISC Northridge moment connection test program. *Modern Steel Construction*, 36-44.
- Eatherton, M.R. (2010). Large-scale cyclic and hybrid simulation testing and development of a controlled-rocking steel building system with replaceable fuses, Ph.D. Dissertation, University of Illinois at Urbana-Champaign, 2010.
- Erochko, J., Christopoulos, C., Tremblay, R., and Choi, H. (2011). Residual drift response of SMRFs and BRB frames in steel buildings designed according to ASCE 7-05. *Journal of Structural Engineering*, 137, 589-599.
- Eatherton, M.R., Hajjar, J., Deierlein, G., Ma, X., and Krawinkler, H. (2010). Hybrid simulation testing of a controlled rocking steel braced frame system, in: 9 Th US Natl. 10th Conference of Earthquake and Engineering. Toronto, Canada.
- Eatherton, M.R., Ma, X., Krawinkler, H., Deierlein, G.G., and Hajjar, J.F. (2014a). Quasi-static cyclic behavior of controlled rocking steel frames. *Journal of Structural Engineering*, 140(11), 04014083.
- Eatherton, M.R., Ma, X., Krawinkler, H., Mar, D., Billington, S., Hajjar, J.F., and Deierlein, G.G. (2014b). Design concepts for controlled rocking of self-centering steel-braced frames. *Journal of Structural Engineering*, 140(11), 04014082.
- Eatherton, M.R., LFahnestock, L.A., Miller, D.J. (2014c). Computational study of self-centering buckling-restrained braced frame seismic performance. *Earthquake Engineering and Structural Dynamics*, 431897–914.
- FEMA. State of the Art Report on Systems Performance of Steel Moment Frames Subject to Earthquake Ground Shaking. Report No. FEMA-355C, prepared by the SAC Joint Venture for the Federal Emergency Management Agency, Washington, DC, 2000.
- Fahnestock, L.A., Ricles, J.M., Sause, R. (2007). Experimental evaluation of a large-

- scale buckling-restrained braced frame. *Journal of Structural Engineering*, 133(9), 1205–14.
- FEMA. (2009). FEMA P695, Quantification of building seismic performance factors. Washington, DC, Federal Emergency Management Agency.
- Fang C., Yam, M.C.H., Lam, A.C.C., and Xie, L.K. (2014). Cyclic performance of extended end-plate connections equipped with shape memory alloy bolts. *Journal of Constructional Steel Research*, 94, 122–36.
- Fang, C., Yam, M.C., Lam, A.C., and Zhang, Y. (2015). Feasibility study of shape memory alloy ring spring systems for self-centring seismic resisting devices. *Smart Materials and Structures*, 24 (7), 075024.
- Fang, C., Wang, W., He, C., and Chen, Y.Y. (2017). Self-centering behaviour of steel and steel-concrete composite connections equipped with NiTi SMA bolts. *Engineering Structures*, 150, 390–408.
- Fang, C., Yam, M. C.H. et al. (2018). A study of hybrid self-centring connections equipped with shape memory alloy washers and bolts. *Engineering Structures*, 164,155-168.
- Grigorian, C.E., Yang, T-S., and Popov, E.P. (1993). Slotted bolted connection energy dissipators. *Earthquake Spectra*, 9, 491-504.
- Gupta, A and Krawinkler, H. (1999). Seismic Demands for Performance Evaluation of Steel Moment Resisting Frame Structures. John A Blume Earthquake Engineering Center Technical Report 132.
- Garlock, M.M. (2002). Design, analysis, and experimental behaviour of seismic resistant post-tensioned steel moment resisting frames, Ph.D. dissertation, Dept. of Civil and Environmental Engineering, Lehigh Univ., Bethlehem, PA.
- Garlock, M.M., Ricles, J.M., and Sause, R. (2003). Cyclic load tests and analysis of

- bolted top and-seat angle connections. *Journal of Structural Engineering*, 129 (12), 1615–162.
- Garlock, M.M., Ricles, J.M., and Sause, R. (2005). Experimental studies of full-scale posttensioned steel connections. *Journal of Structural Engineering*, 3(438), 438–448.
- Garlock, M.M., Sause, R., and Ricles, J. M. (2007). Behaviour and design of posttensioned steel frame systems, *Journal of Structural Engineering*, 133(3), 389–399.
- Guo, Y.B., Klink, A., Fu, C.H. (2013). Machinability and surface integrity of Nitinol shape memory alloy. *CIRP Annals -Manufacturing Technology*.
- Gerami, M., and Abdollahzadeh, D. (2015). Vulnerability of steel moment-resisting frames under effects of forward directivity. *The Structure Design of Tall and Special Buildings*, 24, 97–122.
- Ganey, R., Berman, J., Akbas, T., Loftus, S, Daniel Dolan, J., Sause, R., and Blomgren, H.E. (2017). Experimental investigation of self-centering cross-laminated timber walls. *Journal of Structural Engineering*, 143(10), 04017135.
- Ghowzi, A.F., and Celik, O.C. (2022). Soil-structure interaction effects on the seismic response of steel frames with BRBs, SC-BRBs, and hybrid bracing systems, 3rd European Conference on Earthquake Engineering and Seismology, 3ECEES. Romania: Bucharest.
- Housner, G.W. (1963). The dynamic behavior of water tanks. *Bulletin of the Seismological Society of America*, 53 (2), 381–387.
- Hashemi, A., Yousef-Beik, S.M.M., Mohammadi, Darani. F., Clifton, G.C., Zarnani, P., and Quenneville, P. (2019). Seismic performance of a damage avoidance self-centering brace with collapse prevention mechanism. *Journal of Constructional*

- Steel Research*, 155, 273-285.
- Hashemi, A., Zarnani, P., Masoudnia, R., and Quenneville, P. (2017). Experimental Testing of Rocking Cross-Laminated Timber Walls with Resilient Slip Friction Joints. *Journal of Structural Engineering*, 144(1), 04017180.
- Haide,r S.M.B., and Lee, D. (2021). A review on BRB and SC-BRB members in building structures. *Structural Engineering and Mechanics*, 80, 609–23.
- He, X.Z., Chen, Y.Y., Ke K., Shao, T.F., Yam, M.C.H. (2022). Development of a connection equipped with fuse angles for steel moment resisting frames. *Engineering Structures*, 265, 114503.
- Hu, S., Zhu, S., Wang, W., and Shahria Alam, M. (2022a). Structural and nonstructural damage assessment of steel buildings equipped with self-centering energy-absorbing rocking core systems: A comparative study. *Journal of Constructional Steel Research*, 198, 107559.
- Hu, S., Zhu, S., Shahria Alam, M., and Wang, W. (2022b). Machine learning-aided peak and residual displacement-based design method for enhancing seismic performance of steel moment-resisting frames by installing self-centering braces. *Engineering Structures*, 271, 114935.
- Hu, S., Zhu, S., and Wang, W. (2022c). Machine learning-driven probabilistic residual displacement-based design method for improving post-earthquake reparability of steel moment-resisting frames using self-centering braces. *Journal of Building Engineering*, 61, 105225.
- Hassanzadeh, A., Moradi, S., Burton, H.V. (2024). Performance-based optimum seismic design of self-centering steel moment frames with SMA-based connections. *Earthquake Engineering and Structural dynamics*, 1–25.

- Issa, A.S., and Alam, M.S. (2019). Experimental and numerical study on the seismic performance of a self-centring bracing system using closed-loop dynamic (CLD) testing. *Engineering Structures*, 195, 144–155.
- Kim, H. J., and Christopoulos, C. (2009). Seismic design procedure and seismic response of post-tensioned self-centring steel frames, *Earthquake Engineering and Structural dynamics*, 38(3), 355–376.
- Ke, K., and Chen, Y. (2014). Energy-based damage-control design of steel frames with steel slit walls. *Structural Engineering and Mechanics*, 52(6), 1157–1176.
- Ke, K., Chuan, G., and Ke, S. (2016). Seismic energy factor of self-centering systems subjected to near-fault earthquake ground motions. *Soil Dynamics and Earthquake Engineering*, 84, 169–173.
- Ke, K., Yam, M.C.H., and Ke, S. (2017). A dual-energy-demand-indices-based evaluation procedure of damage-control frame structures with energy dissipation fuses. *Soil Dynamics and Earthquake Engineering*, 95, 61–82.
- Ke, K., and Yam, M.C.H. (2018). A performance-based damage-control design procedure of hybrid steel MRFs with EDBs. *Journal of Constructional Steel Research*, 143, 46–61.
- Ke, K., Zhao, Q., Yam, M.C.H., and Ke, S. (2018). Energy factors of trilinear SDOF systems representing damage-control buildings with energy dissipation fuses subjected to near-fault earthquakes. *Soil Dynamics and Earthquake Engineering*, 107, 20–34.
- Ke, K., Yam, M.C.H., Zhang, H.Y., Lam, A.C.C., and Zhou, X.H. (2020). High-strength steel frames with SMA connections in self-centring energy-dissipation bays: insights and a multimodal nonlinear static procedure. *Smart Materials and Structures*, 29, 125020.

- Ke, K., Zhou, X., Zhu, M., Yam, M.C.H., Wang, Y., and Zhang, H. (2022). Seismic evaluation of industrial steel moment resisting frames with shape memory alloys using performance-spectra-based method. *Journal of Building Engineering*, 48, 103950.
- Ke, K., Yam, M.C.H., Zhang, P., Shi, Y., Li, Y., and Liu, S. (2023a). Self-centering damper with multi-energy-dissipation mechanisms: Insights and structural seismic demand perspective. *Journal of Constructional Steel Research*, 204, 107837.
- Ke, K., and Chen, Y. (2016). Seismic performance of MRFs with high strength steel main frames and EDBs. *Journal of Constructional Steel Research*, 126, (2016) 214-228.
- Ke, K., Zhou, X., Zhu, M., Yam, M.C.H., and Zhang, H. (2023b). Seismic demand amplification of steel frames with SMAs induced by earthquake sequences. *J. Construct. Steel. Res*, 207, 107929.
- Karatzetzou, A., and Pitilakis, D. (2018). Reduction factors to evaluate acceleration demand of soil-foundation-structure systems. *Soil Dynamics and Earthquake Engineering*, 109, 199–208.
- Kazantzi, A.K., Righiniotis, T.D., and Chryssanthopoulos, M.K. (2008). Fragility and Hazard Analysis of a Welded Steel Moment Resisting Frame. *Journal of Earthquake Engineering*, 12, 596–615.
- Ke, K., Yam, M.C.H., Deng, L., Zhao, Q. (2018b). A modified DEB procedure for estimating seismic demands of multi-mode-sensitive damage-control HSSF-EDBs. *Journal of Constructional Steel Research*, 150, 329–345.
- Ke, K., Chen, Y., Zhou, X., Yam, M.C.H., and Hu, S. (2023c). Experimental and numerical study of a brace-type hybrid damper with steel slit plates enhanced by friction mechanism. *Thin-Walled Structures*, 182, 110249.

- Leelataviwat, S., Goel, S.C., and Stojadinović, B. (2002). Energy-based Seismic Design of Structures using Yield Mechanism and Target Drift. *Journal of Structural Engineering*, 128, 1046–1054.
- Leonardo, W., and Cortes, P. (2017). SMA tension brace for retrofitting concrete shear walls. *Palermo/Engineering Structures*, 140, 177-188.
- Li, Y.W., Li, G.Q., Jiang, J., and Wang, Y.B. (2019a). Seismic performance improvement of tension-only-braced frames with Energy-Dissipative Rocking Columns. *Engineering Structures*, 196, 109286.
- Li, Y.W., Li, G.Q., Jiang, J., and Wang, Y.B. (2019b). Experimental study on seismic performance of RC frames with Energy-Dissipative Rocking Column system. *Engineering Structures*, 194, 406–419.
- Li, Y.W., Li, G.Q., Jiang, J., and Wang, Y.B. (2019c). Use of energy-dissipative rocking columns to enhance seismic performance of buckling-restrained braced frames. *Journal of Constructional Steel Research*, 159, 548–559.
- Li, Y.W., Li, G.Q., Jiang, J., and Sun, F.F. (2018). Mitigating seismic response of RC moment resisting frames using steel energy-dissipative columns. *Engineering Structures*, 174, 586–600.
- McCormick, J., Barbero, L., and DesRoches, R. (2005). Effect of mechanical training on the properties of superelastic shape memory alloys for seismic applications. *Smart Structures and Materials- Smart Structures and Integrated Systems*, International Society for Optical Engineering, Bellingham, WA, p 430-439.
- McCormick, J. (2006). *Cyclic Behavior of Shape Memory Alloys: Material Characterization and Optimization*. Georgia Institute of Technology.
- McCormick, J., Aburano, H., Ikenaga, M., and Nakashima, M. (2008). Permissible residual deformation levels for building structures considering both safety and

- human elements. 14th world conference on earthquake engineering, Beijing: Seismological Press of China.
- Ma, X., Borchers, E., Peña, A., Krawinkler, H., Deierlein, G. (2010). Design and behavior of steel shear plates with openings as energy-dissipating fuses. Internal Report, John A. Blume Earthquake Engineering Center, Stanford University, 2010.
- Ma, X.H., Krawinkler, G., and Deierlein, G. (2011). Seismic design and behaviour of self-centering braced frames with controlled rocking and energy dissipating fuses. Report No. 174. Stanford, CA: Stanford University.
- Mohammad, M. (2012). Seismic response evaluation of the linked column frame system, PhD. Dissertation, University of Washington.
- Malakoutian, M., Berman, J.W., and Dusicka, P. (2013). Seismic response evaluation of the linked column frame system. *Earthquake Engineering and Structural dynamics*, 42 (6), 795–814.
- Mohammad, A.F., Mehdi, G. (2017). Steel beam-to-column connections equipped with SMA tendons and energy dissipating devices including shear tabs or web hourglass pins. *Journal of Constructional Steel Research*, 135, 30-48.
- Moroder, D., Smith, T., Dunbar, A., Pampanin, S., and Buchanan, A. (2018). Seismic testing of post-tensioned Pres-Lam core walls using cross laminated timber. *Engineering Structures*, 167, 639–654.
- Mazzoni, S., McKenna, F., Scott, M., and Fenves, G. (2006). Open system for earthquake engineering simulation (OpenSees). User command language manual: Pacific Earthquake Engineering Research Center, University of California, Berkeley.
- Nakamura, H., Ono, Y., Sugiyama, S., Wada, A., Baba, M., and Miyabara, T. (1997). Passive control system using steel slit damper, part 1: test of steel slit damper.

- Summaries of Technical Papers of Annual Meeting AIJ, Kanto, Japan, 843-844 (in Japanese).
- Newcombe, M.P., Pampanin, S., Buchanan, A., and Palermo, A. (2008). Section analysis and cyclic behavior of post-tensioned jointed ductile connections for multi-story timber buildings. *Journal of Earthquake Engineering*, 12(S1), 83–110.
- Nia, M.M., Moradi, S., Yang, T.Y. (2023). Performance-based seismic design of self-centering steel moment frames with SMA-bolted connections. *Journal of Constructional Steel Research*, 208 107990.
- Otsuka, K., Sakamoto, H., and Shimizu, K. (1997a). Successive stress-induced martensitic transformations and associated transformation pseudo-elasticity in Cu-Al-Ni alloy. *Acta Metallurgica*, 27(4), 585–601.
- Otsuka, K., and Wayman, C.M. (1997b). Shape memory materials. Cambridge University Press.
- Ocel, J., DesRoches, R., Leon, R. T., Hess, W. G., Krumme, R., Hayes, J. R., and Sweeney, S. (2004). Steel beam-column connections using shape memory alloys. *Journal of Structural Engineering*, 130, 732–40.
- Priestley, M.J.N., Evison, R.J., and Carr, A.J. (1978). Seismic response of structures free to rock on their foundations. *Bulletin of the New Zealand Society for Earthquake Engineering*, 11(3), 141–150.
- Priestley, M.J.N., and Tao, J.R. (1993). Seismic response of precast prestressed concrete frames with partially debonded tendons. *PCI Journal*, 38(1), 58–69.
- Priestley, M.J.N., and MacRae, G. (1994). Precast post-tensioned ungrouted concrete beam-column subassemblage tests. Report No. SSRP-94/10. San Diego, CA: University of California, San Diego.

- Priestley, M.J.N., Sritharan, S., Conley, J.R., and Pampanin, S. (1999). Preliminary results and conclusions from the PRESSS five-story precast concrete test-building. *PCI J*, 44(6), 42–67.
- PEER/ATC. Modeling and Acceptance Criteria for Seismic Design and Analysis of Tall Buildings. Technical Report No. PEER/ATC 72-1, prepared by Applied Technology Council for the Pacific Earthquake Engineering Center, Redwood City, CA, 2010
- Qian, H., Li, H., Song, G., and Guo, W. (2013). Recentering Shape Memory Alloy Passive Damper for Structural Vibration Control. *Mathematical Problems in Engineering*, 963530.
- Qiu, C.-X., and Zhu, S. (2016). High-mode effects on seismic performance of multi-story self-centering braced steel frames. *Journal of Constructional Steel Research*, 119, 133–143.
- Qiu, C.-X., and Zhu, S. (2017). Performance-based seismic design of self-centering steel frames with SMA-based braces. *Engineering Structures*, 130, 67–82.
- Qiu, C.-X., Li, H., Ji, K., Hou, H., and Tian, L. (2017). Performance-based plastic design approach for multi-story self-centering concentrically braced frames using SMA braces. *Engineering Structures*, 153, 628–638.
- Qiu, C.X., Fang, C., Liang, D., Du, X., Yam, M.C.H. (2020a). Behavior and application of self-centering dampers equipped with buckling-restrained SMA bars. *Smart Materials and Structures*, 29(3), 035009.
- Qiu, C.X., Wang, H., Liu, J., Qi, J., Wang, Y. (2020b). Experimental tests and finite element simulations of a new SMA-steel damper. *Smart Materials and Structures*, 29(3), 035016.
- Qiu, C., Liu, J., and Du, X. (2022). Cyclic behavior of SMA slip friction damper.

- Engineering Structures*, 250, 113407.
- Ricles, J.M., Sause, R., Garlock, M.M., and Zhao, C. (2001). Post-tensioned seismic resistant connections for steel frames. *Journal of Structural Engineering*, 127(2), 113–121.
- Ricles, J., Sause, R., Peng, S., and Lu, L. (2002). Experimental evaluation of earthquake resistant post-tensioned steel connection. *Journal of Structural Engineering*, 7(850), 850-859.
- Rojas, P., Ricles, J.M., and Sause, R. (2005). Seismic performance of post-tensioned steel moment resisting frames with friction devices. *Journal of Structural Engineering*. 131(4), 529–540.
- Roke, D., Sause R., Ricles J.M., Seo, C.-Y., and Lee, K.-S. (2006). Self-Centering Seismic-Resistant Steel Concentrically-Braced Frames. Proceedings of the 8th U.S. National Conference on Earthquake Engineering, San Francisco, California, USA.
- Roke D., Sause R., Ricles J.M., and Chancellor N.B. (2010). Damage-Free Seismic-Resistant Self-Centering Concentrically-Braced Frames. ATLSS Report 10-09, Lehigh University, Bethlehem, PA.
- SAC Joint Venture. (1997). Protocol for fabrication, inspection, testing, and documentation of beam-column connection tests and other experimental specimens. Rep No SAC/BD-97/02.
- Somerville, P. (1997). Development of Ground Motion Time Histories for Phase 2 of the FEMA/SAC Steel Project. SAC Background Document SAC/BD-91/04, SAC Joint Venture, Sacramento, Calif.
- Song, J., Chu, Y.-L., Liang, Z., and Lee, G.C. (2007). Estimation of peak relative velocity and peak absolute acceleration of linear SDOF systems. *Earthquake*

- Engineering and Engineering Vibration*, 6, 1–10.
- Speicher, M.S., DesRoches, R., and Leon, R.T. (2011). Experimental results of a NiTi shape memory alloy (SMA)-based recentering beam–column connection. *Engineering Structures*, 33, 2448-57.
- Sarti, F., Palermo, A., and Pampanin, S. (2016). Development and testing of an alternative dissipative posttensioned rocking timber wall with boundary columns. *Journal of Structural Engineering*, 142, E4015011.
- Sun, G., Liu, H., Liu, W. Yang, W. (2022). Development, simulation, and validation of sliding self-centering steel brace with NiTi SMA wires. *Engineering Structures*, 256, 114069.
- Tamai, H., Kitagawa, Y., and Fukuta, T. (2004). Application of SMA rods to exposed-type column bases in smart structural system. *Proceedings of 13th world conference on earthquake engineering*, Vancouver, B.C., Canada. Paper ID: 1884.
- Taftali, B. (2007). Probabilistic seismic demand assessment of steel frames with shape memory alloy connections. PhD dissertation, Georgia Institute of Technology.
- Tenchini, A., D’Aniello, M., Rebelo, C., Landolfo, R., Da Silva, L.S., and Lima, L. (2014). Seismic performance of dual-steel moment resisting frames, *Journal of Constructional Steel Research*, 101, 437–454.
- Ucar, T., Merter, O., and Duzgun, M. (2012). A study on determination of target displacement of RC frames using PSV spectrum and energy-balance concept. *Structural Engineering and Mechanics*, 41, 759–773.
- Wang, W., Zhou, Q., Chen, Y.Y., Tong, L.W., and Chan, T.M. (2013). Experimental and numerical investigation on full-scale tension-only concentrically braced steel beam-through frames, *Journal of Constructional Steel Research*, 80, 369-385.

- Wang, W., Chan, T.M., and Shao, H.L. (2015). Seismic performance of beam-column joints with SMA tendons strengthened by steel angels. *Journal of Constructional Steel Research*, 109, 61-71.
- Wang, W., Fang, C., and Liu, J. (2017a). Self-centering beam-to-column connections with combined super-elastic SMA bolts and steel angels. *Journal of Structural Engineering*, 143(2), 04016175.
- Wang, W., Du, X. L., Zhang, Y. F., and Chen, Y. Y. (2017b). Experimental investigation of beam-through steel frame with self-centering modular panels. *Journal of Structural Engineering*, 04017006.
- Wang, W., Kong, J.H., Zhang, Y.F., and Chu, G.L. (2018). Seismic behavior of self-centering Modular panel with slit steel plate shear walls: Experimental testing. *Journal of Structural Engineering*, 144(1).
- Wang, B., Zhu, S.Y., Qiu, C.X., Jin, H. (2019). High-performance self-centering steel columns with shape memory alloy bolts: Design procedure and experimental evaluation. *Engineering Structures*, 182, 446-458.
- Xu, L.H., Fan, X.W., and Li, Z.X. (2016a). Development and experimental verification of a pre-pressed spring self-centering energy dissipation brace. *Engineering Structures*, 127, 49-61.
- Xu, L.H., Fan, X.W., and Li, Z.X. (2016b). Cyclic behavior and failure mechanism of self-centering energy dissipation braces with pre-pressed combination disc springs.” *Earthquake Engineering and Structural dynamics*, 46, 1065-80.
- Xie, Q., Zhou, Z., Huang, J.H., and Meng, S.P. (2016). Influence of tube length tolerance on seismic responses of multi-storey buildings with dual-tube self-centering buckling-restrained braces. *Engineering Structures*, 116, 26-39.

- Xie, Q., Zhou, Z., and Meng, S.P. (2020). Experimental investigation of the hysteretic performance of self-centering buckling-restrained braces with friction fuses. *Engineering Structures*, 203, 109865.
- Yam, M.C.H., Fang, C., Lam, A.C.C., and Zhang, Y.Y. (2015). Numerical study and practical design of beam-to-column connections with shape memory alloys. *Journal of Constructional Steel Research*, 104, 177–92.
- Yam, M.C.H., Ke, K., Huang, Y., Zhou, X.H., and Liu, Y. (2022). A study of hybrid self-centering beam-to-beam connections equipped with shape-memory-alloy-plates and washers. *Journal of Constructional Steel Research*, 198, 107526.
- Zahrah, T.F., and Hall, W.J. (1984). Earthquake energy absorption in SDOF Structures. *Journal of Structural Engineering*, 110, 1757–1772.
- Zhao, B., Taucer, F., and Rossetto, T. (2009). Rossetto, Field investigation on the performance of building structures during the 12 May 2008 Wenchuan earthquake in China. *Engineering Structures*, 31, 1707-1723.
- Zhai, Z., Guo, W., Li, Y., Yu, Z., Cao, H., and Bu, D. (2019). An improved performance-based plastic design method for seismic resilient fused high-rise buildings. *Engineering Structures*, 199, 109650.
- Zhang, H., Zhou, X., Ke, K., Yam, M.C.H., He, X., and Li, H. (2022a). Self-centring hybrid-steel-frames employing energy dissipation sequences: Insights and inelastic seismic demand model. *Journal of Building Engineering*, 105451.
- Zhou, X.H., Zhang, H.Y., Ke, K., Guo, L.H., and Yam, M.C.H. (2021). Damage-control steel frames equipped with SMA connections and ductile links subjected to near-field earthquake motions: A spectral energy factor model. *Engineering Structures*, 239, 15, 112301.
- Zhang, P., Yam, M.C.H., Ke, K., Zhou, X.H., and Chen, Y.H. (2022b). Steel moment

- resisting frames with energy-dissipation rocking columns under near-fault earthquakes: Probabilistic performance-based-plastic-design for the ultimate stage. *Journal of Building Engineering*, 54104625.
- Zhou, X.H., Tan, Y.C., Ke, K., Yam, M.C.H., Zhang, H.Y., and Xu, J.Y. (2023). An experimental and numerical study of brace-type long double C-section steel slit dampers. *Journal of Building Engineering*, 105555.
- Zhou, Z., Xie, Q., Lei, X.C., He, X.T., and Meng, S.P. (2015). Experimental investigation of the hysteretic performance of dual-tube self-centering buckling-restrained braces with composite tendons. *Journal of Composites for Construction*, 19, 04015011.
- Zhang, H.Y., Zhou, X.H., Ke, K., Yam, M.C.H., Shi, Y., and Zhang, H.B. (2023a). Hybrid Self-Centering Connection Employing Energy Dissipation Sequences: Experimental Study and a Structural Seismic Demand Perspective. *Journal of Structural Engineering*, 49 (11), 12306.
- Zhang, C., Guo, X., Zong, S., and Chen, S. (2023b). Seismic performance of an assembled self-centering buckling-restrained brace with controllable initial stiffness. *Engineering Structures*, 286, 116111.
- Zhang, P., Yam, M.C.H., Ke, K., Song, Y.C., and Zhu, M. (2024). Experimental study of a self-centering damper with multistage energy-dissipation mechanism. *Journal of Structural Engineering*, 150 (11).